

ON ROTOR INTERNAL DAMPING INSTABILITY

A thesis submitted to the University of London for the degree of
Doctor of Philosophy

by
Mohamed A Kandil
Department of Mechanical Engineering
Imperial College London

December 2004

To my Father and Mother

Abstract

Rotor Internal Damping (RID) was the first recognised cause of rotordynamic self-induced vibration over a century ago. Hardware fixes (special dampers, redesigned rotor fits, modified bearings, etc.) are used empirically to overwhelm its destabilising effect. Such fixes will generally avoid absolute instability, if occasionally not bounded whirling, but do not allow for a proper understanding of mechanisms at play. Analytically, material RID was the more commonly studied, with models ranging from linear viscous to non-linear stiffness/damping hysteresis; thus allowing for the more philosophical research of simple shafts. Rotors' couplings are agreed to be the prominent RID sources, but were seriously researched during the last two decades, modelling rotor joints with macroslip friction. Although more realistic than material RID, such models could have been much improved had it not been for the geometric modelling approach limitations. This, on account of their very case-specific experimental and modelling particularities, and limitations of time-marching analysis render them inadequate for industrial applications.

This work was motivated by the virtual absentia of easily-applicable yet accurately-representative industrial techniques, when RID is becoming a more potential problem source. The scope of novel contributions is developing a valid and functional basis for the design, analysis and testing of rotor systems with RID. Three main basis for industrially-applicable techniques are developed, along with their numerous peripheral contributions, herein. Analytical techniques are adapted from control engineering to tackle the localised nonlinear RID system that is feedback-setup as linear and nonlinear subsystems. Linear hysteretic, along with viscous, RID is properly introduced and analysed, yielding representative Eigen-solutions and forced response. Analysis are mainly conducted in the rotating frame to accommodate the predominantly frequency domain models used. An experimentally applicable stability test is developed to assess safely the stability of a possibly unstable target system, whilst included in an overall stable system.

Acknowledgements

I am grateful to my supervisor Professor David J. Ewins, whose valuable advice, interest, and patience made this work a truly rewarding experience on so many levels. I am also thankful to my friends and colleagues at the dynamics section for their friendship as well as interesting and informative discussions. Particularly, I am indebted to Janito Vaqueiro Ferreira for his utterly selfless help. I am equally grateful to my former chairman Capt. Amir Riad, for his backing and time facilitated to carry out this work.

To all my friends: Thank you for standing by me during the past difficult times. As for Moustafa Ghanem, Rana Zako, Christabel Manickam, Tina and John Chandris, AbdulNaser Sayma, Ahmed ElGhazouli and Hani ElSakkout: You were there for me when really needed, and I am yours forever.

Nomenclature

Rotordynamics nomenclature

\mathbf{S}	Dynamic system, possibly nonlinear and time-varying
t	Time
$i = \sqrt{-1}$	Imaginary constant
$\Omega, \Omega_c, \Omega_{c_u}$	Constant speed of rotation, Critical speed, Critical speed of undamped system
ω, ω_e	Frequency of oscillations, Frequency of excitation
$\tau = \omega t, \tau_\Omega = \Omega t$	Frequency angle, Speed angle
n	Number of system's <i>degrees of freedom</i> (DOFs)
m, \mathcal{G}, k	Linear mass, gyroscopic and stiffness coefficients
c, c_i	External and internal linear viscous damping coefficients
d, κ	Hysteretic linear damping coefficient as used in complex $k(1 + i\kappa), \kappa = \frac{d}{k}$
..... <i>Time domain: Instantaneous real vectors</i> $\mathbf{v} = \mathbf{v}(t) \Leftarrow$ Bold Upright	
$F(\cdot); \mathbf{F}(\cdot, \cdot)$	Scalar ; Vector Function ${}_{2n \times 1}$ of parenthesised variable/s
\mathbf{x}, \mathbf{y}	X-, Y-directional coordinate vectors: $\frac{n}{2} \times 1$
$\mathbf{q} = \{\mathbf{x} \ \mathbf{y}\}^T$	Displacement vector: $n \times 1$
$\mathbf{f} = \{\mathbf{f}_x \ \mathbf{f}_y\}^T$	External Force (input) vector: $n \times 1$
$\mathbf{p} = \{\mathbf{q} \ \dot{\mathbf{q}}\}^T$	State phase vector $2n \times 1$
$\mathbf{q}_r = \{\xi \ \eta\}^T$	Displacement vector in rotating coordinates: 2×1
\mathbf{p}_r	State (phase) vector in rotating coordinates: 4×1
..... <i>Rotordynamic real LTI system matrices: Stationary frame of reference</i>	
$\mathbf{M}, \mathbf{C}, \mathbf{K}$	Mass (positive definite), Damping, Stiffness $n \times n$ matrices
$\mathbf{G}, \mathbf{K}_{cc}$	Gyroscopic, Circulatory skew-symmetric matrices
$\mathbf{A}, \mathbf{B}, \mathbf{O}$	State, Input, Output matrices of state-space
$\mathbf{S}(\mathbf{A}, \mathbf{B}, \mathbf{O})$	State-Space representation of LTI dynamic system \mathbf{S}
..... <i>Complex Coordinate/System notation</i>	
$\mathbf{M}_c, \mathbf{C}_c, \mathbf{K}_c$	complex representation of isotropic rotors $\mathbf{M}, \mathbf{C}_g, \mathbf{K}_g$
$\mathbf{z} = \mathbf{x} + i\mathbf{y}$	complex displacement vector representing $\{\mathbf{x}, \mathbf{y}\}$
$\mathbf{f}_c = \mathbf{f}_x + i\mathbf{f}_y$	complex force vector representing $\{\mathbf{f}_x, \mathbf{f}_y\}$
..... <i>Transformation Stationary \Leftrightarrow Rotating coordinate systems</i>	
\mathbf{T}	coordinate Transformation matrix at constant speed Ω
$x, y; \xi, \eta$	2 DOF planar coordinates in stationary ; rotating frames
$z = x + iy; \zeta$	complex coordinate in stationary ; rotating frames
$\mathbf{C}_r, \mathbf{K}_r$	general Damping & Stiffness matrices in rotating coordinates
\mathbf{I}, \mathbf{N}	Identity, Unit anti-symmetric matrices

Eigen analysis nomenclature

λ_i	i^{th} eigenvalue
$\omega_i, \hat{\omega}_i$	i^{th} (damped) modal frequency, natural frequency
γ_i	i^{th} modal damping factor
$\hat{m}, \hat{k}, \hat{c}$	Modal mass, stiffness, damping
$\mathbf{r}_i, \hat{\mathbf{r}}_i$	i^{th} (right) eigenvector, modal vector
$\mathbf{l}_i, \hat{\mathbf{l}}_i^*$	i^{th} left eigenvector, adjoint (complex-conjugate left) modal vector
\mathbf{R}, \mathbf{L}	Modal matrix of (right) eigenvectors, matrix of left eigenvectors
$\lambda_{f:i}; \omega_{f:i} > 0$	Eigenvalue of $i^{th}_{\in\{1,\dots,n\}}$ FWD mode ; with +ve modal frequency
$\lambda_{b:i}; \omega_{b:i} < 0$	Eigenvalue of $i^{th}_{\in\{1,\dots,n\}}$ BWD mode ; with -ve modal frequency
$\mathbf{\Lambda}$	Canonical form of \mathbf{A} , usually $\text{diag}\{\lambda_{i \in \{1 \dots 2n\}}\}$

Frequency domain nomenclature

s	Laplace variable
$\mathbf{q}(s), \mathbf{f}(s)$	Laplace transform of \mathbf{q}, \mathbf{f}
\mathbf{q}, \mathbf{f}	Complex Amplitude of sinusoidal \mathbf{q}, \mathbf{f}
$\mathbf{H}(s)$	Transfer Function Matrix (TFM) of stable \mathbf{S}
$\mathbf{G}(s)$	TFM of possibly-unstable \mathbf{S} (RID or other mechanism)
$\mathbf{H}_r(s)$	TFM in rotating coordinates
$H_{ij}(s)$	Individual Transfer Function (TF) in $\mathbf{H}(s)$ indexed ij
$G_{ij}(s)$	Individual TF in the possibly-unstable $\mathbf{G}(s)$ indexed ij
g_{ij}^d, p, o	Gain, a pole and a zero of $H_{ij}(s)$
$\mathbf{H}(\omega)$	Frequency Response Matrix (FRM)
$\mathbf{H}^d(\omega)$	Receptance FRM
$\mathbf{H}^v(\omega)$	Mobility FRM
$H_{ij}(\omega)$	Individual frequency response function (FRF) in $\mathbf{H}(\omega)$
\mathbf{S}, \mathbf{V}	Dynamic Stiffness = $\text{inv } \mathbf{H}^d$, Impedance = $\text{inv } \mathbf{H}^v$
$\Re(\cdot), \Im(\cdot)$	Real, Imaginary parts of parenthesised complex entity
$(\cdot)^*$	Complex conjugate of complex variable, vector or matrix
\vec{X}	Complex amplitude of sinusoidal $x(t) = \Re(\vec{X}e^{i\tau})$
$\bar{X} = \vec{X} $	Absolute amplitude of $x(t) = \Re(\vec{X}e^{i\tau}) = \bar{X} \cos(\tau + \psi_x)$

Mathematical abbreviation symbols

\equiv	Equivalent, Identically equal
\simeq, \approx, \neq	Semi-equivalent, Approximately equal, Not equivalent
$A : [a \triangleright b]$	Closed range of A increasing from a to b
$A : [a \triangleright \rangle$	Open-ended range of A increasing from a onwards
\nearrow, \searrow	Increase, decrease with specified range direction
$\circlearrowright, \circlearrowleft$	Clockwise, Counter-clockwise
$\stackrel{\text{def}}{=}$	Defined as
\forall	For all
\in	Belongs to, Element of, in
$\overset{s}{\subset}, \overset{s}{\supset}$	Sub-system of , Sup-system of subsystems
\exists	There exists
\rightarrow	Tends to
\Rightarrow	Implies, leads to
$a \Leftrightarrow b$	a leads to b and b leads to a
\sum	Summation
\prod	Product
$ \cdot $	Absolute value of (\cdot)
$\ \mathbf{p}\ $	Euclidean norm of vector \mathbf{p}
\mathbb{R}^l	The l -dimensional Euclidean space

Nonlinear analysis nomenclature

\mathcal{N}	Nonlinear element characteristic, possibly multi-valued input-output relationship
x	generic input to \mathcal{N} , usually $x = x(t)$ is a sinusoid
\mathcal{N}_M	Modified nonlinear element, equivalent to \mathcal{N} with more than one input
\mathcal{F}	Nonlinear force/Output of nonlinear element $\mathcal{N}, \mathcal{N}_M$
$\mathcal{F}^1 = \mathcal{F}^1(t)$	First (fundamental) harmonic component of $\mathcal{F} = \mathcal{F}(t)$
$\vec{\mathcal{F}}^1$	Complex amplitude of $\mathcal{F}^1(t) = \Re(\vec{\mathcal{F}}^1 e^{i\tau})$
$\bar{\mathcal{F}}^1 = \vec{\mathcal{F}}^1 $	Absolute amplitude of $\mathcal{F}^1(t) = \bar{\mathcal{F}}^1 \cos(\tau + \theta_1)$
$\vec{\xi}$	Complex amplitude of sinusoidal $\xi(t) = \Re(\vec{\xi} e^{i\tau})$
$\bar{\xi} = \vec{\xi} $	Absolute amplitude of sinusoidal $\xi(t) = \bar{\xi} \cos(\tau + \psi_\xi)$
\mathcal{S}_{NL}	Separable nonlinear \mathcal{S} into LTI and NL/time-varying subsystems
$\mathcal{S}_L, \mathcal{S}_N$	LTI and NL/time-varying $\overset{S}{\subset} \mathcal{S}_{NL}$
\mathcal{F}	Internal Nonlinear force vector
\mathcal{N}	Matrix of Nonlinearities \mathcal{N} s
\mathbb{k}	First order Describing Function of \mathcal{N}
\mathbb{k}_M	Describing Function of \mathcal{N}_M
\mathbb{K}	Matrix of \mathbb{k} s

Terminology abbreviations and acronyms

RID	Rotor Internal Damping
EAST	Experimentally Applicable Stability Test
LTI, LTV, NL	Linear Time-invariant, Linear Time-varying, Nonlinear
SISO, MIMO	Single-input-single-output, Multi-input-multi-output \equiv Multivariable
LC	Limit Cycle, e.g. RID precession
SVNL	Single-valued Nonlinearity
DVNL, MVNL	Double-valued, and Multi-valued Nonlinearity
EOMs	Equations of motion
DOFs	Degrees of Freedom
SDOF, MDOF	Single DOF, Multi DOF
FR, FRF	Frequency Response, Frequency Response Function
TFM, FRM	Transfer function matrix, Frequency response matrix
DFM, HBM	Describing Function Method, Harmonic Balance Method
TMA, FEA	Time Marching Analysis, Finite Element Analysis
PR, SPR	Positive real, Strictly positive real
PD, PSD	Positive Definite, Positive Semi-Definite
ROSTADYN	ROtor STAtor interaction DYNamics. BRITE/EURAM project no. 5463, 1994-97

Contents

1. Introduction	15
1.1. Statement of the problem	16
1.1.1. Problem overview	16
1.1.2. Factors influencing RID instability	19
1.1.3. State-of-the-art gaps	23
1.2. Research scope and thesis description	29
1.2.1. Research scope and problem-solving philosophy adopted	29
1.2.2. Thesis Description and Layout	30
2. Review of significant RID research	32
2.1. Overview of available literature	32
2.2. Historical preview	34
2.3. Experimental observations	35
2.3.1. Newkirk, Kimball, Taylor and Robertson (1924-1935)	35
2.3.2. Chaevskii & Olimpiev (1953-1959)	38
2.3.3. Kushul (1954-1965)	38
2.3.4. Tondl (1953-1965)	39
2.3.5. Mechanical Technology Incorporated (1983-1990)	41
2.4. Different models and analysis techniques	42
2.4.1. Introductory notes	43
2.4.2. The logic and physical reasoning of a RID follower force	45
2.4.3. A simple Jeffcott rotor model with RID	48
2.4.4. The Jeffcott rotor with RID on asymmetric bearings	61
2.4.5. RID sources models	66
2.4.6. Industrial tools	74
3. RID systems modelling and characteristics	92
3.1. Linear rotordynamic characteristics	92
3.1.1. EOMs of Linear Rotor-Bearing MDOF system	93
3.1.2. Linear system model representations	96
3.1.3. Modal analysis in stationary & rotating frames	101

3.1.4.	Characteristics of rotordynamic TFM/FRM	109
3.2.	RID characteristics and modelling	114
3.2.1.	Models of general nonlinear joints with friction damping	115
3.2.2.	RID Modelling: Concept, assumptions and EOMs	127
3.3.	Concluding remarks	134
4.	Analysis of linear RID system	137
4.1.	Modal analysis and frequency response of stable rotor without RID	137
4.1.1.	Analytical modal analysis	138
4.1.2.	Frequency response of analytical rotordynamic models	141
4.2.	Linear-RID-augmented system: Modal analysis and frequency response	156
4.2.1.	Effect of linear viscous RID on stability characteristics	156
4.2.2.	Effect of linear viscous RID on analytical forced response	165
4.2.3.	Appropriate use of ideal Hysteretic RID model	172
4.3.	Experimentally-Applicable Stability Test: EAST	176
4.3.1.	EAST overview	177
4.3.2.	Concept of EAST	178
4.3.3.	Ideal Use: System modes	179
4.3.4.	Analytical background and application of EAST	180
5.	Nonlinear analysis: Stability, Limit Cycles and Forced Response	184
5.1.	Aspects of nonlinear behaviour	184
5.1.1.	Stability Concepts	184
5.1.2.	Harmonic response peculiarities	185
5.2.	Nonlinear analysis suitable for the RID problem	186
5.2.1.	Various types of nonlinearities	187
5.2.2.	Overview: Nonlinear systems stability analysis	188
5.3.	Describing Function Method for RID problem	191
5.3.1.	DFM suitability for RID precession and forced response	191
5.3.2.	Graphical predictions with complex SISO RID problem	196
6.	Experimental validations	207
6.1.	Experimental Set-up	207
6.1.1.	Safety, applicability and limitations	208
6.1.2.	Test pieces	208
6.1.3.	Rotordynamic Test rig	209
6.1.4.	Hardware	210
6.2.	Experimental Modal Analysis and Testing	212
6.2.1.	Standard Modal Testing	212

6.2.2. Rotordynamic Modal Testing	213
6.2.3. Systematic experimentation	216
6.2.4. Future plan for flexible experimentation	219
7. Conclusions and Future work	230
7.1. Developments and Contributions	230
7.1.1. Main industrially-applicable techniques basis	230
7.1.2. Peripheral contributions to main techniques	232
7.1.3. Experimental contributions	233
7.1.4. Fundamentals' elaboration	234
7.2. Proposed future work	235
7.2.1. Extended Nyquist criterion with modified nonlinearities	236
7.2.2. Dither system linearisation and stabilisation	237
A. Reference material	240
A.1. Complex formulations	240
A.1.1. General complex EOMs	240
A.1.2. Complex formulation for isotropic rotors	240
A.1.3. Formula for the square root of a complex quantity	241
A.2. Adapted Control theorems and applications	241
A.2.1. The Principle of the Argument: A Mapping application	241
A.2.2. The general Nyquist criterion	242
A.2.3. Practical Absolute stability criteria	243
A.2.4. The approximate Describing Functions Method	245

List of Figures

2.1. Plane vibration of: a) visco-elastic beam b) elastic beam with hub friction	45
2.2. Stresses in a rotating visco-elastic shaft cross-section displaced downwards	46
2.3. Follower force due to an arbitrary displacement of the shaft cross-section	47
2.4. Ω -dependant lead/lag angles of neutral stress and strain axis of anelastic shaft	48
2.5. Stationary xy and \odot rotating $\xi\eta$ frames of reference	49
2.6. Simple elliptic precession	49
2.7. The Jeffcott rotor	51
2.8. Particular solution to gravity: Balanced Jeffcott rotor with viscous RID	53
2.9. Particular solution to gravity: Balanced Jeffcott rotor with hysteretic RID	56
2.10. The effect of cross-coupling on the eigenvalues of a 2DOF system	63
2.11. A simplified model, of a rotor coupling, for component damping	69
2.12. Visual example showing the oscillatory motion of a shaft section	71
2.13. Oscilloscope pictures of the stable and unstable (bounded self-induced whirling) motions below and above the threshold of instability respectively	77
2.14. A waterfall plot of a typical industrial rotordynamic instability	77
2.15. Spline coupling RID-induces whirling of the MAKILA engine tie-bolt	78
2.16. The MAKILA engine main components	78
2.17. Tie-bolt of the MAKILA engine at turbine section	79
2.18. Friction producing joints in the SSME turbines	80
2.19. Photographs of whirling rotor (textile spindle) orbits, above critical speed	81
2.20. Tondl's experimental Rotors	82
2.21. Tondl, 1965: Friction RID whirling frequency's varying amplitude with rpm	83
2.22. Tondl, 1965. Varying frequency and amplitude of friction RID precession when gyroscopes are effective—rotor with seven discs	84
2.23. MTI, 1990. FFT plots showing the sub and supercritical operation of rotordynamic test rig with axial spline	85
2.24. MTI, 1990. Waterfall plot showing the varying amplitude of instability—loss of spline friction	86

2.25. MTI 1990. FFT & waterfall plot showing the time varying nature of the interference-fit-induced subsynchronous vibrations	87
2.26. MTI, 1990; Time transient analysis for predicting the motion of the rotor-dynamic test rig with axial spline coupling	88
2.27. MTI, 1990; Predicted FFT plot based on the time transient analysis of the rotordynamic test rig with the axial spline coupling	89
2.28. MTI, 1990. The effect of imbalance and friction-torque product on the limit cycle orbits	90
2.29. MTI, 1990. The effect of bearing asymmetry on limit cycle orbits and ellipse sizes	91
3.1. Simple gyroscopic rotor on orthotropic bearings represented by 2 DOFs . .	93
3.2. Speed-dependent Single-valued Damping Models	123
3.3. Hysteresis loops of Macro-microslip and Micro-microslip joint models . . .	125
3.4. RID joint representation and modelling for 2DOF rotor	129
3.5. RID feedback setup in rotating frame	133
4.1. Modal frequencies $\omega_i = \Im(\lambda)_{i \in \{1, \dots, 4\}}$ of anisotropic rotor (3.2, 4.1) $\mathbf{C} = \mathbf{0}$. .	138
4.2. Eigenvalues $\lambda_{b,f}$ (3.45) of isotropic rotor (3.2, 3.10) with parameters (4.2) .	140
4.3. Eigenvalues $\lambda_{r:1,2}$ (3.47) of isotropic rotor (3.8, 3.11) with parameters (4.2)	141
4.4. Damping factors $\gamma_{1,2}, \gamma_{r:1,2}$ vs. Ω for stable rotor: parameters (4.2)	142
4.5. Example $\Delta\angle(i\omega_e - p), \Delta\angle(i\omega_e - o)$ contributing to $[\Delta\angle H_{ij}(\omega)]_{\omega: [\omega_{e:1} > \omega_{e:2}]}$	144
4.6. Modal contributions to point receptance in xy -frame at $\Omega = 500 \text{ rad/s}$	146
4.7. Point TF Pole-Zero maps at sub/supercritical speeds in xy - and $\xi\eta$ -frames	148
4.8. FRFs in stationary (1^{st} row) and rotating (2^{nd} row) at $\Omega < \Omega_c \Rightarrow \Omega < \omega_f$.	149
4.9. FRFs in stationary (1^{st} row) and rotating (2^{nd} row) at $\Omega > \Omega_c \Rightarrow \Omega > \omega_f$.	151
4.10. Partial Fractions of point FRF in $\xi\eta$ -frame at sub-critical speed	152
4.11. Partial Fractions of point FRF in $\xi\eta$ -frame at supercritical speed	153
4.12. FRFs of complex representations at $\Omega < \Omega_c$ in xy - and $\xi\eta$ -frames	155
4.13. FRFs of complex representations at $\Omega > \Omega_c$ in xy - and $\xi\eta$ -frames	156
4.14. $\Re(\lambda_{b,f})$: Effect of various viscous external/internal damping $c_i \cup c$	163
4.15. Damping factor $\gamma_{b,f}$ variation with Ω for rotors $c \cup c_i = 0, c = c_i, c_i \cup c = 0$	164
4.16. s -plane with stable and unstable poles based on $\frac{\text{internal}}{\text{external}}$ damping ratio . . .	168
4.17. Polar plots of stable/unstable (complex) rotor, based on $\frac{\text{internal}}{\text{external}}$ damping .	169
4.18. FRFs of rotor with stable/unstable FWD modes, based on $\frac{\text{internal}}{\text{external}}$ damping	171
4.19. Effect of hysteretic RID on modal stability	176
4.20. EAST illustration using a SDOF with possible hypothetical -ve damping .	180
4.21. A proposed experimental setup for EAST on a general rotor configuration .	182

4.22. FRFs of RID-unstable rotor derived from EAST	183
5.1. Real DFs of SVNL friction models for mobility FRFs	196
5.2. Complex DFs of DVNL friction models for receptance FRFs	197
5.3. Nyquist criterion adapted for <i>complex</i> linear viscous RID system <i>mobility</i> FRFs in $\xi\eta$ -frame: The effect of sub/supercritical speeds on instability . .	200
5.4. Adapted Nyquist criterion for complex <i>hysteretic</i> RID system <i>receptance</i> FRFs in $\xi\eta$ -frame: Infeasibility of instability at subcritical speeds	201
5.5. Graphical prediction of SVNL RID precession: Bounded and unbounded .	203
5.6. Graphical prediction of DVNL RID precession: Probable or unlikely	204
6.1. FE model and Campbell diagram of the test rotors' macro geometry	221
6.2. 1 st FWD Mode shape and frequency of reference rotor at various speeds: .	222
6.3. Plain and flange-coupled test rotors	223
6.4. Test rig, quill and rider bearing	224
6.5. FRFs of the test rotor at increasing speeds from stationary to supercritical	225
6.6. Flanged-rotor: Controlled FRFs exhibit typical friction damping behaviour	226
6.7. Overlaid Nyquist plots of stable and unstable mode-dominated FRFs . . .	227
6.8. \Re & \Im parts of stable and unstable mode-dominated FRFs at various speeds	228
6.9. Modal damping at various speeds: Curvic-coupling rotor controlled FRFs .	229
A.1. Sector bounded nonlinearity $\mathcal{N}(x, t)$	243
A.2. Letov-Lur'e problem: A nonlinear SISO feedback system	243

1. Introduction

Rotor internal damping (RID) refers to damping *within* a rotating structure (mechanical assembly) as opposed to external damping from the stator/support. RID can cause forward (FWD) whirling with a frequency close to that of a FWD mode (usually first) of the rotor when running supercritically, i.e. above first critical speed (*fig.6.1*). This subsynchronous precession is regarded as a self-excited vibration (of a particular mode, *fig. 2.15*), which can be bounded (*fig.2.13*) or can grow to result in an unstable system (*fig. 2.14*) should a combination of operating conditions exist. The most significant condition is speed, with whirling initiating at the *onset speed of instability*. Such self-induced whirling/instability is unlike resonance at a critical speed or a parametrically-excited instability causing high levels of vibration in a narrow range of speed that a rotor can pass through while accelerating or decelerating. If the onset of RID instability is reached, non-synchronous vibration is initiated and maintained, not passed through on further increase of speed. If whirling is bounded, its amplitude may fluctuate noticeably with increased speed, yet can be limited by the system's nonlinearities until the rotor or stator parts (seals, bearings, etc.) fail. Alternatively, whirling might not be bounded and its amplitude will increase monotonically, even at a constant speed until failure.

Turbine manufacturers, try to avoid severe RID-induced whirling by:

- Raising the onset speed of instability and decreasing the subsynchronous whirling amplitude via: a) introducing external damping, possibly through special dampers e.g. adaptive control dampers b) lowering friction coefficients in rotor joints—which are the major source of destabilising RID—via lubrication, tightness and minimising surfaces' relative motion; and locating these joints away from anti-nodes c) introducing support anisotropy.
- Avoiding operation much above the critical speed, whenever convenient

It will be seen that in order to increase operating speeds, a pre-requisite of increased turbine efficiency, the development of:

- A more in-depth understanding of the RID mechanism and instability phenomenon
- Accurate and efficient linear and nonlinear (NL) analytical techniques and models of RID, to predict its instability behaviour and perform parametric evaluations.

- Safe and conclusive experimental stability testing of operational rotor prototypes.

are required to be able to live comfortably with RID whirling, as opposed to totally avoiding the unpredictable unknown, which is the motivation of this research (§.1.2).

1.1. Statement of the problem

1.1.1. Problem overview

By the turn of the 20th century, turbine manufacturers had started to design and operate rotors supercritically. That was only after DeLaval’s experimental demonstration (1895) of the safely-sustained supercritical operation of a steam turbine. His experiment refuted Rankine’s hypothesis (“Indifferent Equilibrium”, 1869) that rotors, modelled with no Coriolis effect, cannot be stable if operated at speeds above the critical [63].

1.1.1.1. Realising the cause of and the quick-fix to RID instability

No sooner did turbine manufacturers start operating supercritical rotors than they encountered severe vibrations that were at first related to imbalance. The industry was bewildered by the successful supercritical operation of some units but not others of similar construction. A few researchers hypothesised on the possibility of RID being the cause, but took it no further until General Electric (GE) encountered severe problems with their blast furnaces’ compressors [80, 130]. In 1924, Kimball [80, 81, 82, 83] came to the then apparently illogical reasoning that RID caused such instability as it induced a “follower force” that is tangential to the rotor’s orbit, acts in its direction of precession and increases in magnitude with speed of rotation. He then argued that this force could overcome the stabilising external damping forces at a certain *supercritical onset speed*, thereby rendering the rotor unstable—see physical explanation in §2.4.2.

RID was the first recognised cause of self-induced instability, and oil-whip followed shortly after. Although the main source of RID was always agreed to be friction from rotor joints/fits, until recently, it was regularly modelled as linear viscous damping. Since its recognition, manufacturers have always appreciated the RID destabilising effect and accounted for it in their designs by implementing hardware fixes to overwhelm it. Such fixes (e.g. special external dampers, redesigning rotor fits and modifying bearings) or even operating below the predicted onset speed will generally avoid absolute instability but meanwhile do not allow for a proper understanding of the mechanisms at play.

1.1.1.2. Proper modelling of RID Vs. ease of modelling and analysis

Analytically, material hysteresis is the more commonly studied RID destabilising mechanism, with several models available for its representation. These range from linear viscous to non-linear stiffness and/or damping hysteresis; thus allowing for the more philosophical research of simple shafts [55, 57, 58, 59, 69, 122, 123, 124, 132, 148, 160], which included some mathematical muscle-flexing investigating double-Hopf bifurcations [159, 164, 165, 166], etc. but with few attempts at industrial applications [197, 198, 199].

Although friction at rotor joints has always been agreed [63, 64] to be the prominent source of destabilising RID, it has received minimal attention analytically and even less so experimentally, in the sixties [19, 41, 93, 177]. Recently (late 70's–early 90's), serious research efforts [7, 8, 13, 17, 90, 91, 104, 107, 108, 111, 127, 174, 175, 179, 185, 184] were invested in *geometrically-modelling* rotor joints with simple friction RID models and experimentally identifying their coefficients [88, 89], on the tails of the Space Shuttle Main Engine (SSME) RID instability problem [34]. Still, the knowledge of, and analytical capability for dealing with rotor joint friction are less than sufficient to use confidently at an industrial level. This is due to the experimental and modelling difficulties of their very case-specific behaviour. Turbine manufacturers usually suffice with Eigen-analysis results of linear (FEA) EOMs with cross-coupled equivalent viscous and/or hysteretic damping coefficient of RID (§.2.4.6.1) based on [200] and its extensions [31], which yield erroneous and unrepresentative results. Should any mode have a positive decay coefficient (unstable), then the onset speed of instability is concluded to be lower than the design operational speed, and a rotor redesign is effected.

Linear FEA is a simple approach to a complex problem, not only for friction damping, but even for material damping. The nature of material hysteresis causing damping is rather complicated with several factors affecting it. Limiting concern to metallic (particularly ferrous) rotors, authors make some simplifications and idealisations in developing material damping models. Factors such as mean stress, loading history, magnetism and even pre-stressing are amongst those usually ignored. Temperature effects, although important for turbine stages, are usually ignored along with amplitude-dependence in the case of linear RID. For the materials concerned, frequency can have a minimal effect on their damping capacity only at very low amplitudes and only on comparing frequencies of two-to-three orders of magnitude; a scenario of which the frequently-used viscous RID is not representative. A review of the damping literature [76] such as that provided by Pisarenko (1974), Lazan (1968) or Lincare (1954) reveals the complexity of damping mechanisms, the limitations of their models and, more importantly, the different opinions of authors on matters such as amplitude dependence and others. The different material damping models used for representing RID vary and sometimes results contradict.

1. Introduction

A specific material damping model representative of the damping magnitude and accounting for the various operative factors (mechanisms) affecting this magnitude would be too complicated and unnecessary. This is so since material damping—in metallic, non-composite rotors—may increase by an order of magnitude due to rotor operating conditions, yet will still be very small by comparison with friction damping from joints and couplings, provided that large shaft deformations are avoided. This latter condition is usually satisfied due to geometric constraints and yield safety factors.

1.1.1.3. The depth of recent in-depth research into friction RID

Although turbine manufacturers appreciated the destabilising effect of RID, its significance in comparison with other self-excited instabilities is noticeably minor and can usually be handled empirically, since rotors are usually lightly damped except in specific cases. Examples of such specific cases are the SSME turbopumps, on account of their built-up design, with several joints (*fig. 2.18*) that are capable of relative slippage resulting in friction within the rotating assembly. RID instability of the SSME turbopumps was of such significance that intensive research was commissioned and a better understanding of the phenomenon was made available for the more standard industries to adopt and apply. Still, research associated with such opportunities is usually focused on the particular problem at hand and will generally not go much further beyond recommending a solution or remedy tailored specifically for that case. For instance, the work associated with the SSME focused mainly on spline couplings, the main source of RID, and used a simplified friction damping model for illustration purposes. Much less work was associated with shrink fits, despite their marked destabilising influence since they were a lesser source of trouble. Negligible effort was invested in modelling RID of Curvic couplings, since they were deemed non-influencing to the specific RID problem at hand due to their location close to the anti-nodes of the first mode. The models developed demonstrated the possibility of a limit cycle instability that resembled the experiments, conducted with a spline coupling, only qualitatively. See §.2.1 for an overview and critique of previous work on RID instability. Works on Curvic couplings' modelling and analysis include [13, 140, 194, 195, 196].

1.1.1.4. Current industrial problem

RID is becoming a more potential source of problems, not only for advanced turbines e.g. SSME turbopumps, but also for the more standard supercritically-operated industrial turbines as well as aero-engines (*figs. 2.16, 2.17*). This is due to the ever-increasing demand for lighter and more compact aero-engines that sustain higher flow rates inducing higher forces and encouraging joint slippage. Although industrial turbomachinery is not

necessarily of a highly built-up design as aero-engines; RID could be problematic as it can initiate a series of interactions of different self-induced instabilities, such as those resulting from rubs and oil whip in industrial steam power generators.

A thorough understanding of the RID destabilising phenomenon is not confidently at hand, which is of paramount importance to the implementation of increased performance/weight efficiency and safe operation of high speed rotors. Recent experimental work on RID sources is minimal and largely concentrated on axial spline couplings. Analytical work has been either too theoretical to apply industrially or over-simplified in most industrially-applicable cases. Representative RID models have not been incorporated properly in system analysis that include other self-induced instability mechanisms.

Examples of rotors below involve intricate designs. Such rotor-stator systems cannot be modelled adequately (for RID stability analysis) in FEA by merely utilising beam elements with dissipative capacity, spring-damper bearings and, on rare occasions, rotational spring-damper couplings; as is the current practice.

Mid-sized to large helicopters' engines are frequently of an intricately built-up design incorporating CurvicTM couplings, tie bolts, interference fits and, occasionally, spline couplings. They are good examples that can suffer serious damage from RID instability, thus causing financial loss or worse when lives are involved. They are also examples of a situation where hardware fixes to the RID problem are not always possible due to their rather compact design.

Large and heavy rotors as found in steam turbines, are examples at the other end of the spectrum. Due to the flexible rotor design and special couplings linking shaft segments, such sagging rotors are inherently heavily damped. The RID follower force effect (resulting from alternating bending moments due to gravity sag) will tend to displace the rotors horizontally, hence rendering them prone to radial rubs—another source of self-induced instability.

1.1.2. Factors influencing RID instability

Operational and experimental observations can generally characterise the RID instability behaviour and identify the factors affecting it under different circumstances. Analytical models can predict some such observations due to the different mechanisms modelled as well as postulate on the effect of others that cannot be easily observed.

1.1.2.1. RID instability behaviour

The behaviour of RID instability can vary considerably, even in cases of almost identical conditions. However, there are some general characteristics of said behaviour:

1. RID instability has never been observed below the first critical speed. RID analysis models that predict instability/precession at subcritical speeds are considered erroneous, usually on account of inappropriate modelling and/or analysis. Linearisation (5.2) with a NL hysteretic RID model (2.18) may predict subcritical-speed instability (2.24), which is blamed on Taylor series truncation (§.2.4.3.4). Also, a linear hysteretic model [200] that is inappropriately implemented will yield instability on rotation commencement (§.2.4.6.1), which has never been reported.
2. Should RID whirling appear, it can be sustained up to higher speeds at a quasi-constant frequency that is close to that of the FWD bending mode for each speed (*fig. 2.15*). The speed up to which RID whirling can be accommodated is rather case-specific.
3. Should it appear, the whirling amplitude can increase and decrease (possibly to unnoticeable) several times with increased speed, before a semi-constant amplitude of this subsynchronous component is established (*fig. 2.21*).
4. At a constant operating speed, the whirling amplitude may vary (*fig. 2.25*) or even disappear totally, (*fig. 2.24*), as in the case of an axial-spline coupling locking due to loss of the instability-inducing friction forces.
5. If whirling is accommodated over a wide speed range that extends beyond the second critical speed, its frequency can suddenly jump from that of the first FWD bending mode up to that of the second FWD bending mode (*fig. 2.19*).
6. Whirling does not have to start with a frequency close to that of the first FWD mode. It can start with a frequency close to any of the FWD modes provided it is subsynchronous; as represented *linear*-analytically in [45].
7. The more common appearance of instability in industrial rotor cases is an increasing level of the subsynchronous component (at the first bending frequency) with speed until failure. Shrink fits and/or spline couplings are virtually always involved. However, as observed experimentally, an increased whirling amplitude does not necessarily imply an increased destabilising effect (§.5.3.2.2), provided it does not provoke other destabilising mechanisms.

1.1.2.2. Factors affecting instability behaviour

From literature reviews, factors that influence RID instability are summarised below:

State and method of operation

1. Operating speed: Whirling initiation, reoccurrence and imbalance-beating occur at specific operating speeds. Such speeds, especially instability onset, may well vary for the same rotor depending on factors to follow. Also, as the operating speed varies, it will affect whirling patterns and amplitude.
2. Acceleration: The rate of acceleration, particularly just after resonance, and that of deceleration from a speed where whirling was established, will affect the whirling amplitude and sustainability over varying speed spectra.
3. Load: Lightly loaded shafts with small inertia are more susceptible to RID instability than those with higher loads. That can be due to the need for stronger disturbances to influence the steady operation of rotors with higher inertia and load, which can consequently initiate instability.
4. Rotor orientation: Vertical orientation can make a rotor more prone to instability than a horizontal one, which is demonstrated experimentally and analytically [177]. Furthermore, industrial vertical rotors utilise tilt pad bearings which introduce less external damping and have different characteristics to oil film bearings.

Damping source and operative mechanisms Friction joint damping resulting from surfaces' relative tangential motion is significantly more pronounced than that from their perpendicular motion, and the latter is usually ignored. The micro/macro slip behaviour dictates an increased damping capacity up to a maximum that decreases after a certain amplitude of relative motion; as depicted by describing functions (*fig.5.2*). A friction damper is thus characterised by the surfaces' properties and their relative motion.

Friction damping mechanisms in rotors

- Rotors/shafts Couplings: axial splines, flanges, Curvic™ couplings
- Shrink fits: discs on hubs or sleeves.
- Tie bolts and keys in key-ways
- Blade root fixation to wheels.
- Heavy horizontal rotor segments' shear slippage.

Three generic types of couplings exist, at least [47], which are used to join rotors of individual subassemblies, components or rotating machinery subsystems:

1) The single fixed joint (solid coupling) is often a high precision spline connection that is locked up tightly on a combination of pilot diameters (hence the name: *piloted spline*) and tooth contact surfaces with provisions for shimming or clocking adjustments. The result is a solid shaft effect, yet allowing for sufficiently small angular misalignment and radial eccentricities, so as to maintain vibrations below allowable limits. When locked securely, contact surfaces' relative motion is largely inhibited.

2) The single working joint, which is splined with crowned teeth and a crowned tip diameter, can allow large relative axial motion and modest angular misalignment. It is common practice to lubricate such an *un-piloted spline* joint to suppress RID whirling.

3) The distance piece with a joint at either end—capable of accommodating all misalignments—is an additional rotordynamic element with balancing requirements, etc.

Factors affecting friction damper characteristics are:

- Contact pressure.
- Surface geometry, material, hardening condition and machining.
- Lubrication (wet or dry) film thickness and material characteristics.

Minimising friction between rotating parts' surfaces can avoid RID instability well beyond the range of operating speed. Friction effects can be minimised by decreasing the slipping surface areas as in piloted splines, decreasing friction coefficients as in un-piloted splines, and increasing contact pressure as in Curvic couplings. Depending on the friction joint, its placement relative to bending amplitude (and rate) peaks plays a major role. For instance, placing tight joints away from vibration nodes has a favourable effect on account of decreased specific energy dissipation (*fig.5.2*). While material hysteresis is hardly of significance in aero-engines, it should be appreciated in composite rotors [187].

Mode of mechanism operation Not all RID is undesirable since its effects vary with source and mechanism—see radial RID follower forces from couplings and fits §.2.4.5.2 for comparison. For instance, friction is intentionally introduced into blade roots as a vibration damper. While blade root dampers function in a similar fashion to spline couplings, the most prominent cause of RID instability by far, there is hardly any bending at the root, thus hardly any radial restoring force (§.2.4.2). Also, disc dynamics are decoupled from shaft dynamics except in the disc's one-nodal-diameter mode which gives rise to the gyroscopic moments. On the other hand, shearing of short modular rotor segments, as found in helicopter powerplants at elevated temperatures, does produce radial forces.

The effect of friction forces hence resulting on stability ought to be afforded some serious considerations, which is planned for future work.

Stator damping, anisotropy and nonlinearity Support flexibility, damping and anisotropy, as well as side loads tend to enhance stability by raising the onset speed of instability, and decreasing the subsynchronous whirl orbit size [20, 21, 24, 46, 65, 191]. Childs [33], based on his experimental research, contests the literature-exaggerated significance of stator asymmetry in suppressing RID instability. On the other hand, *Rotor asymmetry* is argued [187] to counteract the destabilising effect of RID, since it can induce backward precession—parametric instability at certain speeds. Stiffness asymmetry will also modify the rotor orbits at different sections thus influencing the operative damping mechanisms. *A different argument based on multiple frequencies is presented on p.193.*

Imbalance has a nontrivial influence on whirling initiation, particularly around the critical speed, and maintenance. It introduces a static displacement into the friction joint thus influencing its characteristics; yielding a non-symmetric joint and a more complex problem to analyse. In this work, time simulations have shown a significant beating effect between imbalance and whirling vibrations. The magnitude of imbalance has a marked effect on the growth or limitation of whirling and will affect its behaviour as speed is increased or decreased.

Gyroscopic effects enhance rotor stability; a fact observed in the lab (vertical rotor running without bearings) and proven here analytically (*p.162*). The gyroscopic effects on stability in non-conservative systems have been researched well [6, 67, 68, 87, 193], but perhaps not specifically in conjunction with RID. Roseau [159], included the gyroscopic effects of thin discs in simulations of a nonlinear-stiffness shaft with *linear viscous* RID. It was shown that there is an optimum combination of: a) The number and location of discs, and b) the amount of RID for an enhanced stability of motion.

1.1.3. State-of-the-art gaps

Although research into the effects of RID has been ongoing for over a century, there are some significant gaps in the current knowledge base as well as the analysis and testing techniques available. Reliable and industrially-applicable tools are one rather important category missing. To the author's knowledge, the industry has no analytical tool to predict regions of rotational speeds, above the first critical, for safe rotor operation with the coexistence of sustained yet tolerable RID whirling. This should be of significant importance to super-critical rotor manufacturers, in increasing the rotor operating speed

(and hence efficiency) while maintaining safety with confidence. Another category in need of attention is the experimental validation of various mathematical hypotheses.

1.1.3.1. Representative damping models for RID

Damping models used to date yield qualitative representations of RID instability/whirling.

Linear RID models be they viscous and/or hysteretic, are used in linear Eigen analysis that concludes on absolute stability/instability at an operating speed and thus can infer graphically (*fig.4.19*) an onset speed of instability. Such linear analysis cannot account for the largely nonlinear behaviour of RID instability or the factors affecting it (§.1.1.2.1, 1.1.2.2). As such, linear RID analysis serve as useful, albeit rough, initial stability estimates, or as a pass/fail test to avoid totally instability onset speed.

Nonlinear models of hysteresis and support characteristics give a better representation of the obviously nonlinear problem. Whirling existence, its varying amplitudes with speed, and even precession-frequency jumps can be theoretically demonstrated by nonlinear hysteresis models. However, such models are far more qualitative in nature than linear ones, with operating speeds regions where they are not even qualitatively representative. Nonlinear hysteresis and/or support characteristics models are also limited to rather simplified shaft-on-two-bearings rotors. An attempt [159] at a nonlinear shaft with *linear viscous* RID and several disc configurations, expanding on the double-Hopf bifurcations discussed in [164, 165, 166], demonstrated there is an optimum disc configuration to kerb instability, but is still a long way short of a representative model over a the whole speed-spectrum, let alone a real system.

Joints modelled with geometrically-distributed friction elements §.2.4.5.2, although primitive thus far, yield the better whirling representation over all the speed spectrum. However, the nature of geometric-modelling is virtually preventative of refined friction elements use, and simple Coulomb or bi-linear elements (3.68,3.69) are largely used. Accordingly, results fall short of accurately predicting the whirling: orbit, amplitude and amplitude's qualitative fluctuation with speed. Also, such models do not reflect the effect of whirling or forced response amplitude on stability. While increased whirling amplitude tends to settle down to a sustainable level in most joints, this is not the case where unpiloted spline couplings are concerned (*fig.5.6*). In such case, an element similar to the bi-linear one, only with an assumed model that troughs, e.g. parabolic friction (*fig.3.2*) in series with a spring, is suggested for future work.

Suitability of RID models There are numerous RID models used with several analyses techniques, some of which are straightforward, others have several reservations and sometimes results contradict. As such, the model selection procedure can be cumbersome and prone to error for the industrial engineer; a frequently recurring situation.

Analysis objective Consider the selection of an axial spline coupling RID model from: simple Coulomb damping vs. multi-parameter microslip vs. their equivalent linear damping model. For a simple/initial check of absolute stability and a rough estimate of its onset, an Eigen-analysis with equivalent viscous linear damping model would be adequate, provided operation is well below the predicted onset of instability. Thereafter, time integration with a Coulomb damping model, in conjunction with the collective teeth stiffness, will give a whirling orbit representation, which can be used in a parametric evaluation of the stabilising variables such as external damping, asymmetric bearings, side loads and imbalance. Still the whirling orbit's amplitude will be recognised in a non-dimensional form. In this example, the use of a geometrically-distributed microslip model is a totally unwarranted complication, as the coupling's dynamics are vaguely predictable anyway, and do not exhibit much microslip in the un-piloted case. Adopting a black box input-output model for this joint however, is probably the better way forward for a more realistic as well as expedient whirling prediction as implemented hereafter.

Proper implementation Even the choice of a linear damping model for Eigen-analysis can yield serious erroneous predictions. Nelson's RID model implementation [200] and its arguably improved sequels [31] are widely implemented with industrial in-house FEA packages, and constitute a combination of both viscous and hysteretic damping. The erroneous implementation of hysteretic RID allows for unstable modes from the outset, see §.4.2.3 for an appropriate implementation. Also, the linearised stability analysis (5.2) with nonlinear hysteretic RID yield different results and conditions for stability, one of which (2.24) erroneously allows for subcritical instability.

1.1.3.2. Refined friction models for the various types of rotor joints

Geometrically-derived friction joints models are arrived at by distributing simple friction elements over the joint's geometry. Spline joint models are available, and time-marched to predict the non-dimensional existence, stability and frequency of whirling. Usable friction models for other joints e.g. shrunk-on discs and hubs, flanged or Curvic couplings, etc. are practically non-existent. Should geometrically-derived models be deemed those of choice, models for these potentially destabilising joints are needed since they are widely incorporated in aero-engines.

Refined friction elements The limited-availability geometrically-derived friction joint models, use Coulomb friction and occasionally its slightly improved bi-linear version, with elasticity deriving from the coupling itself, see §.2.4.5.2. Although macroslip can be a viable representation in the case of un-piloted axial splines, it is rather inadequate to represent friction in shrink fits and Curvic couplings. One of the several macroslip elements (§.3.2.1.2), and their possible extensions to a contact area [161], is required for accurate whirling predictions, and explaining its amplitude variation whilst sustained.

Since sophisticated elements are more costly in terms of modelling and computation power, the level of sophistication for a friction joint model has to be justified in terms of accuracy vs. behavioural representation. This is undoubtedly, one reason why micro-microslip friction elements are not implemented in RID time-marching analysis, as opposed to the rather straightforward Coulomb damping that can be modelled as an ideal relay. As a general rule, joints with rigid surfaces that are not very highly-pressed together, e.g. unpiloted spline couplings, can suffice with a simple macroslip model, especially that a sophisticated model does not necessarily imply accurate numerical predictions. As surface elasticity (as opposed to joint elasticity) and normal forces are increased, the need to account for microslip behaviour becomes more significant in order to predict, more accurately, whirling characteristics.

Un-piloted spline couplings (p.22) are designed to tolerate misalignment. Their teeth are not heavily pre-stressed, do not share the torque load equally, and experience enough axial and radial (usually ignored) relative motion to keep them virtually continuously slipping. As such, a macroslip RID model can be adequate for qualitative whirling representation in axial splines. The adequacy verdict derives from considering the vaguely predictable axial splines' dynamics, their modelling approximations, and the means of assigning surface friction/stiffness coefficients, against the complexity of a microslip model and its parameters' sensitivity to the actual joint dynamics, etc. A macroslip model is also passable as it can represent loss of whirling in the case of axial splines locking (*fig. 2.24*) after a few revolutions at constant speed or on increasing speed.

Shrink fits on the other hand, are never totally slipping, almost always involve small partial interface slip due to shaft's flexibility, and their vibration patterns are far more well behaved and predictable in comparison with axial splines; (*figs. 2.24-2.25*); a case where a micro-microslip model is an ideal choice. This is especially true since shrink-fit RID whirling has not been observed to be *lost* with elapsed time at a constant speed or on increasing operating speed (*fig. 2.25*). A sophisticated microslip model can reflect on the experimentally-observed changing whirling amplitude at constant or with varying speed. Similar comments apply to Curvic couplings, although they seldom result in RID whirling on account of their high precision matching and tight clamping.

Input-Output models Hybrid analytical-experimental techniques-derived Masing's joints have not, to author's knowledge, been utilised to study the RID problem. Since:

- Friction joints characteristics are rather case-specific
- Masing's models are best suited to cyclic vibration analysis, hence are best used with approximate methods, thus avoiding their complex time-marching analysis.

such models incorporating microslip should prove ideal in tackling the RID problem.

1.1.3.3. Approximate nonlinear analysis and nonlinear coupling methods

The RID problem is inherently nonlinear, yet Eigen analysis are the typically used industrially. Lyapunov linearisations have been implemented academically [41, 93, 177] for simple rotors, to conclude only on absolute stability and may yield erroneous results.

Time marching for combined effects Time marching (typically fourth order Runge-Kutta) is the analysis used largely to tackle the nonlinear RID problem and is the ultimate analytical tool to check model performance. Although RID effects in simple rotors have been studied using relatively simple nonlinear damping models, this was in virtual isolation from other rotordynamic phenomena with the exception of rotor/stator asymmetry and imbalance. Rotor-stator interactions like dry friction rubs (blades/flexible stator, shaft/stator and seal, etc.), hydrodynamic bearings effects, labyrinth seal fluid coupling, etc., are usually not accounted for in RID instability analysis. These nonlinear mechanisms are potential sources of self-excited instability/subsynchronous whirling, which can be co-rotating or counter-rotating (forward or backward precession). These whirl-inducing mechanisms can all interact with the RID mechanism as well as each other: Exciting, emphasising or counteracting.

Although time marching is a very reliable technique, its brute force renders it:

- Too costly, computation wise, for a realistic system
- Unsuitable for parametric evaluations or behavioural patterns identification

The Harmonic Balance Method (HBM). Cumbersome implementation of HBM early variants¹ showed the possibility of a non-trivial supercritical solution, representing whirling [177] of an unforced simple rotor with nonlinear hysteretic RID. However, the author did not find any material of significance on applying the HBM/DFM for RID precession analysis. The HBM/DFM (see §.5.3) are neat, simplistic and straightforward alternatives

¹Near-periodic solutions of quasi-linear systems at multiple resonances; summarised in [93].

A method of solving quasi-linear systems [177]

to the lengthy time-marching analysis of precession, particularly in the case of the lack of, or the weak existence of, higher harmonics resulting from the nonlinearity. Experiments on rotors with shrink fits and axial splines do not exhibit higher harmonics of whirling (*figs. 2.24-2.25*); a situation that is reaffirmed by the analytical time marching of our simple rotors (*fig.3.1*) with friction joints (*fig.3.2*). Although the HBM/DFM are popular approximation tools for nonlinear vibrations, they are primarily used for forced response analysis and have not been used for RID stability analysis. An obvious hurdle for LC/precession analysis using the HBM/DFM is finding an initial guess (IG) for the iterative solution. This problem is solved herein (§.5.3.2.2) with meticulous caution exercised when using DF analysis with negative frequencies (5.14). Results thus achieved are reliable and in very good agreement with time-marching, hence the HBM/DFM for precession analysis are excellent tools for parametric studies in this specific case.

1.1.3.4. Gyroscopic effects on stability

The research conducted [159] in the gyroscopic effects on stability is highly theoretical for a nonlinear simple shaft rotor utilising double-Hopf bifurcation to study the stability of the first and second shaft modes, and the effect of disc location on stability. An extension of that to realistic rotors will prove useful (*p.162*).

1.1.3.5. The short-segmented rotor model

All rotordynamic models consider lateral vibrations that result in an alternating bending moment leading to axial relative motion of surfaces when addressing the friction RID problem. Several helicopter engines are relatively short in overall length, and are built-up of several short segments, whose diameters can be more than twice their lengths. The segments are held together with tie bolts whose tension can drop at elevated temperatures; a situation beam elements are not suited to represent, and shear forces ought to be accounted for, as they produce surface friction that can affect stability. Although radial shear friction in spline couplings is usually ignored, since it does not contribute much to friction RID and causes modelling complications e.g. EOMs nonlinear coupling [185], it ought not be ignored in the case of a short-segmented rotor and its effect on stability/whirling ought to be assessed.

1.1.3.6. Experimental investigations and prototype testing required

Experimental observations of the phenomenon thus far are far from being adequate to fully cover its various aspects. In general, no experimental work has been carried out whilst controlling the values and behaviour of RID and its mechanisms—see §.6.2.4 for suggested flexible experimentation. More experimentation on the effect of couplings

other than splines in different configurations is needed. Experimentation to validate the postulated stabilising gyroscopic effect and value of RID (*p.162*) is required. Validation of predicted whirling amplitudes is necessary to verify the accuracy of RID models if they are to be used with confidence; an exercise that has not been carried out.

Safe and conclusive prototype testing is an inherent part of turbine production. However, testing for possible instabilities under various conditions is merely part of performance testing within controlled environments, which can be rather hazardous. A properly structured means of modal-stability testing a possibly-unstable rotordynamic system, whilst insuring overall stability, is not available to the authors knowledge.

1.2. Research scope and thesis description

The main motivation for this research is to address the current industrial problem (§.1.1.1.4) with RID and cover most of its related gaps (§.1.1.3).

1.2.1. Research scope and problem-solving philosophy adopted

1.2.1.1. Research scope

‘To develop a valid and functional basis for the design, analysis and testing of rotor systems with RID’. The resulting analytical and experimental techniques can be expanded upon and further fine-tuned for industrial purposes as well as research. Rotor-dynamists will use the final reliable and industrial-applicable tools for:

- Design: Parametric evaluations for external damping, joint location, etc.
- Experimental: Safe and reliable prototype testing for operation and design validity
- Analysis of problematic rotors: RID whirling stability and possible fixes

The above yields decisions as to the avoidance or mild tolerance of RID whirling within predictable levels, without excessive modelling limitations or over simplifications.

1.2.1.2. Philosophy of tackling the RID problem

RID derives predominantly from friction joints that are physically localised on the rotating assembly. Accordingly, RID is localised, and joints with nonlinear stiffness and damping are modelled as localised nonlinearities in this work. To isolate and concentrate on the RID instability problem, only linear (possibly time-varying) rotordynamic systems are considered with both linear and nonlinear RID with characteristics ‘ \mathcal{N} ’.

System separation into linear and nonlinear parts A model for the overall NL system ‘ \mathbf{S}_{NL} ’ can be separated into a linear time-invariant (LTI) subsystem ‘ \mathbf{S}_L ’ model and a NL subsystem ‘ \mathbf{S}_N ’ model that is possibly time-varying; which is short-handed as $\{\mathbf{S}_L, \mathbf{S}_N\} \stackrel{S}{\subset} \mathbf{S}_{NL}$ (figs. 3.5, A.2). This scenario allows convenient models: *spatial* (3.1), *modal* (3.34) or *response* (fig. 4.9), for \mathbf{S}_L and \mathbf{S}_N to be acquired separately, and combined thereafter using nonlinear coupling techniques [51, 101, 151] to produce an overall model for \mathbf{S}_{NL} representing the rotordynamic system including NL RID. The model thus developed can be further fine-tuned by correlating analytical and experimental results under relevant conditions, which is to be followed by a model updating process [60, 149].

Nonlinear coupling techniques have been implemented successfully with spatial and FR models to predict steady-state forced-response of structures with localised nonlinearities using the HBM. However, such techniques have not been extended to stability and whirling analysis because MIMO mechanical systems *do not*: 1) Lend themselves naturally to such exercise and 2) exhibit instabilities frequently. Control engineering, on the other hand, offers well-developed analysis techniques specifically for such problems and mainly for models $\mathbf{S}_{NL} \stackrel{S}{\supset} \{\mathbf{S}_L, \mathbf{S}_N\}$ that are setup in a feedback formulation. The suitability of such analyses to handle the RID problem will depend on the characteristics of both $\mathbf{S}_L, \mathbf{S}_N$ presented in chapter 3.

Analytical and experimental techniques used are: Routh-Hurwitz criteria. State-space and TFM representations. Non-self-adjoint modal analysis of indefinite nonsymmetric matrices. FR and TMA of linear and nonlinear rotordynamic systems. Experimental modal analysis of nonlinear rotordynamic systems. Control/stability analysis, feedback formulations and conformal mapping. Stability theory and Lyapunov analysis. Masing’s rule for nonlinear friction joints. Describing function analysis.

1.2.2. Thesis Description and Layout

This work contributes the basis for three analytical techniques, along with their several leading contributions, which are corroborated experimentally. These techniques are:

A proper use of linear ideal Hysteretic RID model appropriately implemented with $\text{sgn } \omega$ for FR and Eigen-analysis in the rotating frame, which involve negative frequencies. Results are representative of experimental observations—*Chs. 4, 6*.

An Experimentally Applicable Stability Test EAST is developed to assess safely the modal stability (and its margins) of a target rotordynamic system, which may become

unstable. FRFs of the quasi-linearised target system, setup as a subsystem of an overall-stable system, reflect stable/unstable poles using conformal mapping—*Chs. 4, 6*.

The extended Nyquist criterion is a graphical FR method for RID whirling prediction, which is borrowed from control engineering, used in conjunction with the DFM, and modified to suit the complex SISO nonlinear RID problem in the rotating frame. Experimentally observed varying whirling/stability behaviour is corroborated by the choice of friction model, reflecting different RID joints—*Ch. 5*.

They are presented in this order, over the coming six chapters, described briefly as:

Chapter 2 Review of significant RID research and critique of industrial tools.

Chapter 3 Analysis foundation laid. Linear rotordynamic and friction models' characteristics presented using Masing's rule. Important modal expressions developed analytically. Parabolic friction model assumed. Localised RID modelled in feedback.

Chapter 4 Linear RID systems' analytical conditions for instability and gyroscopic effects on modal stability developed. Appropriate use of complex stiffness with negative-frequency analysis presented. Peculiarities exemplified numerically. Results compared to stable system. Effect of stable/unstable poles on polar plots elucidated.

Chapter 5 Nonlinear analysis overviewed. Suitable analysis identified. Nyquist criterion adapted for RID, validated against linear cases, and used with complex RID DFs.

Chapter 6 Experimental corroboration of the analytical work developed above. The follower force rationale demonstrated. RID micro-slip behaviour confirmed.

Chapter 7 Conclusions on analytical developments and experimental validations. Future plan for extending techniques' functionality, along with implementing dither system linearisation and stabilisation; being the logical consequence of NL analysis developed.

Appendix Reference material on complex formulations. Adapted Control theorems and applications such as the extensively used DFM.

2. Review of significant RID research

Important findings of the literature review, and their associated commentary are presented in this chapter. An overview of available literature since 1924, which is in numerous languages, pointing out philosophies of handling the problem as well as hurdles associated with reviewing literature on such an old and persistent problem is presented first. Then, a historical perspective, as to the phases when RID instability received significant attention, and their resulting findings, is summarised. Important Experimental observations by various researchers are detailed next. These are used as guides for developing RID models and analysis capable of reproducing such observations, as well as for comparison with this work's experimentation, which adopts the experimental modal analysis approach. Lastly, significant analytical work is presented. This includes physical reasoning of the RID destabilising effect, *linearised* modelling and analysis attempts at representing the experimentally-observed behaviour, and finally geometrically-derived joint models that may be linearised and used within FEA along with beam elements' linear RID.

2.1. Overview of available literature

High-speed rotating machinery manufacturers started having severe and destructive vibration problems as soon as they operated supercritically, which was by the turn of the 20th century. Then, RID was the first cause to be attributed to such phenomena, and was formally published in 1924 [80, 130]. Since its recognition, various approaches have been adopted by different researchers in assessing the effect of RID on rotor systems' dynamic behaviour and in refining their models to better represent the actual behaviour. These differences were largely due to the varying nature of the damping sources and mechanisms. Modelling, analysis and computing capabilities and the researchers' affiliation, also had a significant effect on shaping the progress and philosophy of handling the problem. The fact that research is still ongoing in several parts of the world reflects the importance of, and need for further understanding the RID problem. The result of circa one hundred years of research is a substantial amount of literature concerned with RID.

Since 1924, research on the RID destabilising effect has been ongoing in several parts of the world. As is the nature with an old persistent research problem, there are several schools of thought with different philosophies towards tackling the problem, to which

authors would affiliate. The literature fell in one of two obvious categories: an industrially-affiliated category, where authors—as much as the available computation and analytical capabilities would allow—would try to provide industrially useable tools to predict the existence of RID-induced instability and possibly avoid it; and a more academically-affiliated or theoretical category where authors would deal with the problem as a mathematical one, making several hypothetical assumptions and unrealistic conditions, yet solve the mathematical problem they posed. Examples of the results of the industrially-affiliated authors are: the early (1924-35) research results [80, 81, 82, 83, 154, 155, 156, 157, 170], the representation of the effect of RID on a shaft cross-section as a follower force derived from the viscous stress-strain relation [45, 63, 64, 65] (late '60s), the transfer-matrix method including hysteretic damping [103], rotor FE routines incorporating equivalent damping coefficients [31, 128, 129, 163, 200], and the models of friction-producing joints [7, 8, 88, 89, 90, 91, 104, 184, 185]. Examples of the academically-affiliated research are continuum shaft models with: nonlinear stress-strain-rate relation [25, 55, 56, 57, 58, 59, 123, 124], some looking at double-Hopf bifurcations [164, 165, 166], and lastly fitted with discs (via a delta function) and linear viscous damping [159]. Perhaps the early works of Dimentberg and Tondl [41, 177, 178] fell in-between, as they were serious at elaborating the marked effect of RID models, albeit for Jeffcott rotors, but then ended recently in a more academic guise [42, 43].

Literature concerned with the destabilising effect of RID is in several languages: Russian, Czech, English, Polish, German, French and recently Chinese. Most of the systematic experimental work was done in the former eastern block before the mid sixties. Valuable analytical work was also carried out there, explaining numerous such experimental findings. Only a few of those publications were translated to English years later, e.g. that of Tondl, Bolotin, Dimentberg and Kushul. The extensive work (especially experimental) of Chaevskii, Poznyak and Olimpiev could only be recognised from Tondl's translated text [177]. Authors who settled in the western world, e.g. Muszynska, include their previous research in their English publications and cite some works of researchers from their former part of the world. Publications in German and French are of a more recent nature (i.e. after mid sixties). German publications tend to be more industrially-applicable such as those of Kramer, Gasch, Pfutzner, Hasselgruber, Hassenpflug and Foppl. Luckily, the old German work on RID was not diverse and important modern publications have English equivalents. A few French publications are translated (like Roseau's text) or are reprinted in English, like Lalanne's and Ferraris's work.

2.2. Historical preview

Research into the effects of RID was mainly influenced by industrial interests and requirements as will be demonstrated. The mid 1920's, late 1940's and mid 1970's (and for a good twenty years to follow) are the major industrial drives' periods. Recently (1993), European aero-engines manufacturers developed more interest in RID, on account of whirling induced by spline joints, reflecting their need to further understand the phenomenon and other destabilising mechanisms' interactions.

The 1920's saw a trend reversing the rotor design concepts of the previous decade. Turbine manufacturers began to construct lighter weight rotors with shrink fits, having lower critical speeds and designed to operate above the first critical speed. "Flexible rotor design" manufacturers encountered severe operating difficulties at speeds above critical that were, at first, attributed to lack of proper balancing. Meanwhile, General Electric (GE) encountered a series of blast furnace compressors' failures that were operated supercritically. Shop men and engineers referred to the violent vibration "of unknown origin" at, the some times observable, lower than operating speed frequency as "shaft whipping" or "instability". This trend triggered considerable research interests since the absolute trust in high speed rotating shafts operating in aircrafts, power stations, factories and laboratories was being questioned. Rotor instabilities thus became the elite branch of vibration, and substantial research effort headed in that general direction. Initial significant research was carried out by Newkirk (1924), Kimball (1924, 25) and was concurrently carried on by Taylor (1925), Robertson (1933–35) and Smith (1933).

In Eastern Europe, energy industries and factories started relying heavily on high-speed rotating machinery by the late 1940's. Due to the lesser financial significance of research at the time in that part of the world, coupled with their mathematical excellence and dedication to research (as opposed to the western world particularly for the more taxing experimental research), valuable analytical and more so experimental results were achieved. Tondl's ten-year research (1953-63) at the National Research Institute of Heat Energy in Prague, and Kushul's work (1954-65), starting with high-speed textile spindles operating in the 'instability region', and his observation of the jump from whirling at the first to that at the second natural frequency, are examples of great works concerned with RID, that were not to be bettered or even reconstructed; this is probably due to the concentration on the more prominent causes of self-induced vibration in rotating machinery such as oil whip.

By the mid 1960's, the western world's research in RID picked up again (Ehrich, 1964; Gunter, 1966), building on its counterpart's—eastern block: Dimentberg, Bolotin, Kushul, Tondl—works that became available. The main drive for this research pick-up (starting with Ehrich, 1964) was NASA's interests (Gunter, 1966) in running supercritical aero-

engines and accounting for subsynchronous whirling—RID and oil whip were the known causes. The analytical results are more industrially-applicable and in simpler terms (as opposed to that of the eastern block) for the industry engineer to absorb. Such works as those of Ehrich and Gunter, formed the foundation for incorporating the effect of RID in industrially-applicable FE routines. A few Polish and Czech authors carried on with their nonlinear analytical research (Muszynska, 1968) and (Tondl, 1965) but, it was not to be compared with the previous research’s momentum in the eastern block.

The SSME turbopumps’ (HPFTP High Pressure Fuel Turbopump & HPOTP High Pressure Oxygen Turbopump) instabilities encountered by Rocketdyne (a division of Rockwell International that was developing the principal propulsion element SSME for NASA’s Space Shuttle) were the third major industrial drive for RID research in the mid 1970’s. This research was directed towards friction-induced instability due to the built-up design of the turbopumps that operated supercritically. A major research program was initiated by NASA (1983-1988) and concentrated mainly on spline couplings as they were experimentally-concluded to be the main source of significant friction damping. Internal hysteresis damping was consciously ignored as it was insignificant by comparison with friction regarding energy dissipation. Research and publications concerned with spline couplings’ dynamic coefficients and friction mechanisms are still ongoing till the present day [128].

2.3. Experimental observations

Some of the important experimental techniques and observations from the literature are summarised here. These experimental investigations were carried out by prominent researchers whose conclusions shaped their analytical approach and that of others. Their findings portray the characteristic behaviour of RID instability and give insight into what needs to be investigated further. Experimental findings and conclusions, from the experiments conducted by the Imperial College team working on ROSTADYN¹, are in general agreement with the experimental observations of previous research results.

2.3.1. Newkirk, Kimball, Taylor and Robertson (1924-1935)

B. L. Newkirk of the GE research laboratory investigated (1924) the nature of GE blast furnace compressors’ failures on site and later experimentally on a test rotor simulating a typical compressor unit. Although his methods were relatively crude, due to lack of probes at the time, he observed (and was the first to demonstrate) that above the first critical speed, rotors could enter into a violent whirling in which their centreline precessed

¹ROtor STAtor interaction DYNamics: BRITE/EURAM project no. 5463, 1994-97

2. Review of significant RID research

at a rate equal to the first critical speed. He also uncovered some very important facts (listed below) regarding the phenomenon.

1. Balancing did not affect the whirling onset speed or its amplitude
2. Whirling always occurred above the first critical speed, never below it.
3. Onset speed of instability varied widely between similarly-constructed machines.
4. Precession speed was constant regardless of operating speed.
5. Whirl was encountered only in built-up rotors.
6. Increasing foundation flexibility increased the whirl threshold speed.
7. Distortion or misalignment of bearing housing increased the threshold speed.
8. Introducing damping into the foundation increased the whirl threshold speed.
9. Increasing axial bearing thrust load increased the whirl threshold speed.
10. A disturbance was sometimes required to initiate whirling in well-balanced rotors.

Newkirk observed that if his experimental rotor was running smoothly near the threshold speed, a disturbance would cause it to go into whirl. The time required for this whirl to die away increased as the rotor approached threshold. Once whirling had developed above threshold, it would grow until limited by the protective ring, to a spiral motion that is somewhere between very gentle and extremely abrupt, depending on speed and on the type of shrink fit. Occasionally, he observed that under large deflections, instead of the motion becoming unbounded, a finite quasi-steady-state whirl pattern would develop. That suggested at a much later time that shaft stiffness nonlinearity could produce limit cycles.

Statement 6 above, left Newkirk at a loss to explain why foundation flexibility alone should improve rotor stability. Early in the experimental phase, his assistant, *H. D. Taylor* discovered that any looseness in the bearing support or clamps which held the test rotor had a strong tendency to prevent whirling. Following these experiments, special bearings incorporating flexibility and damping were designed for unstable turbo-compressors using a wide range of stiffness and damping values. In no case were these compressors made able to whirl, despite the lowering of the critical speed as was expected. It was also concluded that bearing damping was necessary to suppress whirling; a situation that was different while trying to suppress oil whip a year later.

Later, Kimball and Lovell et al (1925) performed extensive tests of the internal friction characteristics of various metallic and non-metallic materials. The experimental technique employed, to determine the ratio of internal friction forces to elastic shaft forces, adopted the “follower force” hypothesis due to RID. If the rotating horizontal shaft was loaded vertically (e.g. due to gravity), it would experience an alternating internal bending moment which would result in internal damping (due to material hysteresis) and hence, a follower force. This follower force has the same sense of direction as that of rotation, whence would displace the centre of the shaft in the same direction. The follower force would tend to rotate the centre of the shaft but, it is counter-acted by the gravity force. In other words, a vertical force on a rotating shaft where RID is active, will cause not only a vertical displacement in the direction of the force, but also a horizontal one in the direction of rotation. The angle of inclination, between the shaft-bearing centres’ plane (formed by the shaft centre axis and the bearing centre line) and the vertical, was the measure used to compare the damping forces with the elastic ones in that rotating shaft. Their measurements showed a ratio of 0.001 to 0.002 for most ferrous and non-ferrous materials they tried. In sight of Kimball and Lovell’s findings and in accordance with such small ratios, Newkirk concluded that it must have been the friction created by shrink fits of the impellers and spacers that was the predominant cause of whirl instability. He had observed that no whirl instability could be developed when all shrink fits were removed from his test rotor.

At Newkirk’s suggestion, Kimball experimentally investigated a special test rotor with rings on hubs shrunk on the shaft, and confirmed that the frictional effect of shrink fits is the more active cause of shaft whirl as opposed to the effect of internal friction (hysteresis) in the shaft itself. Taylor concluded, after numerous tests with various hub configurations, that axial contact length of shrink fits should be as short and tight as permissible without exceeding the yield strength of the material. Robertson reported that even short, highly-stressed shrink fits may induce instability, provided the rotor is given a sufficiently large initial disturbance e.g. displacement to initiate relative internal slippage in the fit. He showed several designs of hubs and bosses found to be beneficial in reducing the destabilising effect of internal friction. In general, if long shrink fits have to be employed, as in compressor wheels and impeller spacers, it is then necessary to undercut the pieces along the central region of the inner bore so as to restrict the contact area to the ends of the fit. *One of Robertson’s more important conclusions, was that similar effects could be produced by any friction which opposes a change of shaft’s deflection; e.g. friction existing at the connections of flexible couplings.*

2.3.2. Chaevskii & Olimpiev (1953-1959)

In the former eastern block, systematic experimental research was first conducted by Chaevskii (1955, 1957) followed by Olimpiev (1959). Chaevskii investigated both the effect of hysteretic damping and dry friction between hub and shaft in the horizontal and vertical rotor orientations. His test equipment consisted of a vertical shaft with a disk which could be immersed in fluid to a variable depth, thereby controlling the magnitude of external viscous damping. His conclusions on the effects of hysteretic damping were :

1. If the motion of the rotor was stable with the shaft in the vertical position, it was also stable in the horizontal position for the same external damping. The opposite need not be true.
2. If the motion of an unbalanced rotor became unstable in the region just above the critical speed, this does not signify that it will be unstable at higher speeds as is the case with perfectly-balanced rotors.
3. In as far as steady large amplitude vibrations are attained, the frequency of these vibrations will be approximately equal to the natural frequency of the rotor.

Olimpiev performed extensive tests on more than twenty models of rotors running in ball bearings. The rotors were of lengths and diameters from 705 to 1300 mm and 20 to 60 mm respectively. He found that the danger of self-excited vibrations being set up as a result of hysteretic damping diminished rapidly as the shaft dimensions (mainly diameter) were increased. Hence this danger would be practically non-existent in rotors of turbo-generators and other machinery without overhung discs. For such rotors (without overhung discs) of at least 35mm running in anti-friction bearings, self-excited vibrations did not exist until well beyond the second critical speed.

2.3.3. Kushul (1954-1965)

In his translated text, Kushul (1965) describes some experimental observations of the motion of some high speed textile spindles which exhibited self-excited whirling motion. The spindles were composed of built-up structures of a long wooden spindle inserted over a thin steel shaft (effectively a long shrink fit). He observed experimentally the “unstable” precessive rotor orbits above the stability threshold via an innovative optical system for that time. He attached a fine needle to the spindle end and obtained pictures by photographing (*fig. 2.19*) the resulting motion through a telescopic lens. The frequency of whirling was established from the relation between the speed and the number of stationary loops in the orbit pictured. Kushul is one of the few people who reported on RID instability

within the unstable region. Although he did not have access to linear capacitance probes to observe the rotor orbits, his work with the above-mentioned optical system verified and demonstrated important facts.

1. Self-excited vibration occurred only above the first critical.
2. The whirl frequency remained almost constant at all speeds and was close to that of the first natural frequency of the spindle.
3. In certain cases well above the threshold, the whirl frequency could abruptly change from that of the first to that of the second spindle natural frequency.
4. The use of an elastic support by itself with no increased damping did not reduce the self-excitation. (contrary to Newkirk and Taylor's experimental findings)
5. External damping improved the rotor stability.
6. The most effective means to control the instability was a spring-loaded bushing and damping sleeves.

2.3.4. Tondl (1953-1965)

Tondl (1965) conducted experiments on two types of rotor configurations (*fig. 2.20*) affecting RID and made use of a capacitance probe for vibration pickup and a camera for time history recording. The first type was a rotor with a single slit disk held together by screws and with conical apertures in the centres to mate with the hub on the shaft. Two configurations for the hub were used to demonstrate the difference in the effect of dry friction between hub and shaft, and internal friction (hysteretic damping). The first configuration was a double-ended conically- machined hub that was tightly shrunk onto the shaft so as to demonstrate the hysteresis effects. The second hub was composed of two small shrunk-on discs over which a double conically-ended sleeve was carried to mate with the disc. The second type of rotor carried seven discs with holes around their circumference shrunk onto a shaft of the same diameter as the former. Rods were loosely inserted through the holes of the central three discs and secured against slipping out. With the shaft deformed, slippage occurred at the contact surfaces of the holes and rods forced out by centrifugal forces.

When using the first configuration for the first type, instability was ascertained after the critical speed and was related to the imperfect shrink-fit of the disc that came almost totally loose during operation (*fig. 2.21*). When a proper shrink fit was effected, instability precession or transients were not encountered except after the operating speed was quadruple the critical speed. Material hysteresis was then ignored and attention

was concentrated on dry friction. Turning back to the first rotor and running the speed continuously up, self-excited precession was set up at above 4000 rev/min (1st critical at 1200 rev/min) and was practically constant in amplitude and frequency (first natural) on increasing rotational speed (*fig. 2.21*). He referred to the 4000 rev/min as the onset of instability before which several sub-harmonic resonances (at the 1st natural frequency) were encountered above the critical speed, the more significant of which was at a speed twice the critical speed. Other sub-harmonics were encountered between the critical speed and that at twice critical. A couple more sub-harmonics were observed at speeds between twice the critical and the onset speeds. Running up to and down from a speed above the onset had similar characteristics but did not follow exactly the same path, and the running down path had higher amplitudes of precession. The starting speed of precession seemed to depend on the acceleration after the critical speed has been crossed. Generally, if the first critical frequency component from unbalance at critical speed or that from self-induced precession was given enough time to die away, the onset would be delayed and would have lower amplitudes.

Tondl, in his translated text, makes no reference to the changing frequency—observed (*fig. 2.22*) for the seven-disc rotor's vibration—of precession with rotational speed. It is perhaps intriguing, why he did not extend his analysis to include, or comment on the gyroscopic effect of the discs; especially that it was demonstrated analytically (Dimentberg, 1961) that gyroscopes raise the natural frequency and hence, the critical speed and the onset of instability. Tondl's conclusions in brief were:

1. If very small diameter shafts are not of concern, the most important component of internal damping is that caused by friction set up at the contact surfaces of rotor parts during deformations of the rotor. Examples are friction between shaft and disk hub, rotor key-ways with keys inserted, etc. Above critical speed, this type of damping may cause instability as it could be excited by rotor unbalance.
2. The whirling frequency was practically the same as rotor natural frequency.
3. It was found experimentally that RID had an unfavourable effect on transitional vibrations of rotors passing more quickly through the critical speed. Just above resonance, the vibrations contain a very large component of the natural frequency. If the speed is rapidly decreased after self-excited vibrations are started, these vibrations are maintained as far as down to the critical speed, as opposed to the gradual increase or decrease of speed where the instability occurs at a speed above the critical. Hence, the most rapid crossing of critical speed was not the most favourable; rather, a fast crossing in the immediate resonance region followed by gradual increase of speed at a low acceleration just above the critical speed.

2.3.5. Mechanical Technology Incorporated (1983-1990)

MTI carried out a long-term project (1983-1987, and finally reported in 1990) to investigate the internal rotor friction instability problem for NASA G. C. Marshall Space Flight Centre. The project was mainly concerned with the instability of the SSME turbopumps (*fig. 2.18*) after being diagnosed to be due to RID in the early to mid 1970's by D. Childs et al (1976). MTI's research concentrated on RID produced by surface friction at joints and conducted traction, dynamic and rotordynamic tests (*figs. 2.23– 2.25*). Traction tests were carried out to determine coefficients of friction under various conditions of normal load, amplitude and frequency of vibration, surface materials, machining and lubrication, and temperature. Dynamic (forced 1st mode and free decay) testing was conducted for damping factor estimates on joint components with mating surfaces in the turbopumps namely: Curvic couplings, shrink fits and axial spline couplings. Rotordynamic tests were carried out, using both shrink fits and axial spline couplings, on rotating shafts to monitor their behaviour in a range of sub- and super-critical speeds. Analytical and experimental research was carried on, after the project's completion by its research team members and concentrated on friction in axial splines.

From their traction tests, MTI concluded that a constant coefficient of friction is not generally valid; particularly in the case of joint surfaces that are not lubricated and have very small relative motion. They still sufficed with using constant friction coefficients in their damping models, since even those interfaces with small relative motion were dry-film lubricated. They argued that a better understanding of the relation between the friction coefficients and the relative vibration amplitudes was required before incorporating a variable coefficient of friction damping in their models.

Forced dynamic testing revealed that Curvic couplings had a very low equivalent damping coefficient which, with little approximation, can be treated as a linear damper when properly fastened with high tension bolts. Hence Curvic couplings were not included in the rotordynamic test program, especially since their position on the turbopumps does not allow them to experience significant bending. The other two components tested, on the other hand, exhibited an equivalent damping coefficient that was amplitude-dependent—hence the damping force is nonlinear. The coefficients' dependence on amplitude in the case of a shrink-fit seemed to be a linear function of amplitude (nonlinear damping force) at relatively low amplitudes, quadratic at upper-mid range and cubic if the highest amplitude test point is taken into account. Spline couplings had a very strong (more than cubic) dependence on amplitude. The only model to their knowledge that emulated such behaviour was that of a lap joint undergoing micro slip, with its equivalent damping having a linear dependence on amplitude—nonlinear (quadratic) damping force with amplitude.

Rotordynamic testing showed that both axial-splines and interference-fits produced

subsynchronous components on the FFT spectrum shortly after the first critical has been passed. The experimental results of the spline coupling were not very repeatable due to their, intended, loose design which resulted in continually changing natural frequency and normal forces that in turn affect friction. The subsynchronous vibration (instability) levels grew to be unbounded (except only by safety rings) within a few hundred revolutions of initiation. The existence of the supercritical component starting at half its equivalent running speed was related to the gravity sag that produces a twice per rev component. The continued existence of the twice per rev supercritical vibration with increased speed was attributed to the broad-band noise produced by friction. It could have also been attributed to the supercritical harmonics produced by a strong nonlinearity. Interference-fits produced more repeatable and less vigorous patterns that were sustained further.

The rotordynamic test-rig was modelled analytically utilising the friction RID model of the axial spline-coupling developed under the program. The results (*figs. 2.26, 2.27*) were adequate for representing the frequency of the subsynchronous precession and demonstrated the possibility of a sustained limit cycle.

2.4. Different models and analysis techniques

This section is intended to acquaint the reader with modelling RID and demonstrate, with simplified examples, the effect of changing RID model in rotordynamic EOMs. Some of the simpler models compiled from the literature survey are reproduced in this section, along with the author's explanation, commentary and critique. The different analysis used for stability and response prediction are introduced alongside the models.

After introductory notes—looking at the development of RID models over the years—and elucidating the physical meaning of the follower force along, this section introduces the simplest Jeffcott rotor model supplemented with internal damping. Although the Jeffcott rotor is an oversimplification, it does help demonstrate the phenomenon, with minimal mathematical complication. Later, particular solutions from viscous and hysteretic RID models are extrapolated so as to comment on the experimental results obtained at Imperial (*figs. 6.5, 6.7, 6.9*). After introducing the RID instability behaviour with various RID models (viscous, hysteretic, friction), an analytical examination of damping sources is introduced; followed by stating the analysis conducted previously in studying RID in conjunction with rotor and/or stator asymmetry and their results. Finally, industrial tools for RID instability prediction are stated.

2.4.1. Introductory notes

During the course of his investigations, A.L. Kimball (1924) postulated that shaft hysteresis induced by alternating stress cycles could produce forces that are normal to the plane of the deflected shaft. He suggested that internal shaft friction could be responsible for shaft whirling and postulated that below the rotor critical speed, internal friction would damp out the whirl motion while above it will sustain whirl. Based on his observations, these forces could also be developed by shrunk-on discs. Newkirk (1924) was able to demonstrate, theoretically, the instability of a rotor with internal damping above the first critical speed, by including an additional *follower force* normal to the deflected rotor. Newkirk made no attempt to extend the Jeffcott model to include a flexible and damped foundation; hence he was not able to account for some of Kimball's observations, and particularly for his own observation (no.6 §.2.3.1) mentioned earlier, in his theoretical model.

The follower force is represented as cross-coupled stiffness coefficients in a non-symmetric stiffness matrix—Maxwell-Betti reciprocity theorem cannot be satisfied—of a linear analysis, resulting in a system that is potentially unstable and that has an instability onset. The whirling frequency resulting from such an analysis would be equal to one of the forward natural frequencies—usually the first—which was a good enough approximation to real situations. The cross-coupled terminology comes from the form of the force expression in a non-rotating co-ordinate system where a deflection of the rotor in one direction would cause a force in the orthogonal (tangential) direction that drives the rotor into an orbit. If the magnitude of the follower force is proportional to the instantaneous whirl velocity, the force is classified as a negative damper and as cross-coupled stiffness force if proportional to the instantaneous orbit radius.

Until the late 1950's, analytical models for RID emulated the so-called follower force by a cross-coupling of stiffness in the EOMs of a simple rotor, with no analytical reference to its source. By the late 1950's, this cross-coupling was presented as a result of including an internal damping force, that is operative on rotor flexing in a frame of reference rotating at a speed equal to the rotor spin speed (Dimentberg, 1959). Still, there was no analytical derivation as to the source of such an internal damping force. Tondl (1963) presented the effects of including this internal damping force, as one that can have a varying characteristic dependence on amplitude, in the EOMs of both, horizontal and vertical simple rotors.

Dimentberg (1959) was the first to examine analytically the source of EOMs cross-coupling. He represented stresses as, not only related to strain by Young's modulus, but also related to the strain-rate by a viscous coefficient. EOMs cross-coupling will occur on rotor flexing in the rotating frame of reference. He formulated the first continuum model

of a rotor as one that is based on a rotating simple beam and related the bending moments to the stresses resulting from the strain and the strain-rate. Bolotin (1961) and Tondl (1963) followed in Dimentberg's footsteps and represented the stress as a function of the varying amplitude of strain. The stability analysis of the above was largely by applying the Routh-Hurwitz criterion to the *linearised* EOMs. Ehrich (1964) and Gunter (1966) built on Dimentberg work by representing graphically (as force vectors) the forces resulting from the strain/strain-rate-dependent bending moment, and the stability was examined by examining the external damping force magnitude opposing that of internal damping. Although the different RID models—with varying amplitude-dependence—reflected the authors' efforts to better represent the nature of the destabilising damping, it was not until 1977 that Tecza investigated a realistic source of RID, i.e. the friction-producing spline coupling, and included its effect directly in the EOM.

Analytical investigations into the effect of RID on stability can be divided into two damping-source-dependent major categories under which researchers have tried to rationalise the phenomena namely: material hysteresis damping, be it visco-elastic or hysteretic under linear or non-linear regimes of motion; and friction-induced damping from interference fits, splines, flanges, tie bolts, etc. The latter reasoning is the more accepted (for metal rotors), due to the practical design of built-up rotors and the significant difference in the amount of energy dissipated (from one system or mode to another) via the two broad source-categories.

Although friction has always been recognised as *the* source of destabilising damping, analytical models for some of the friction-producing components (axial splines, interference fit and Curvic coupling joints) were developed fairly recently, acknowledging the macro slip behaviour of surfaces in contact, yet modelling their friction as Coulomb friction (continually slipping surfaces) for simplicity of analysis. A simplified model of macro-micro slip in a Curvic coupling was attempted by Lund (1986).

Presence of instability is predicted preliminary, by comparing the negative energy dissipated by friction at joints (integrating the moments produced over one complete whirl cycle) with the positive work from external damping, to give the whole system's (positive or negative) energy dissipated per whirl cycle at speeds above critical. At a later stage, non-linear time-transient analysis including the non-linear component models are employed to predict a non-dimensional orbit stability as a vibration amplitude that is diminishing or increasing or as a sustained limit cycle orbit. Previously, Tondl (1965) accounted for the overall internal rotor friction in analogy with Coulomb friction, yet attempted no modelling of the friction-producing joints.

Material (visco-elastic and hysteretic) damping models were the first sources and although they have not been very fashionable recently, especially in industrial research (e.g. NASA or aero-engine manufacturers), material damping models under non-linear motion

(nonlinear Green's strain tensor) analysis (frequently using the centre manifold method) still retain a portion of the current research on RID—which is not diverse anyway—in predicting general trends of stability, response and limit cycle behaviour. Equivalent Linear damping models using linear analysis are still largely employed for threshold speed of instability prediction in industrial rotordynamic analysis.

2.4.2. The logic and physical reasoning of a RID follower force

If a non-rotating shaft experiences lateral vibration, internal stresses are developed that

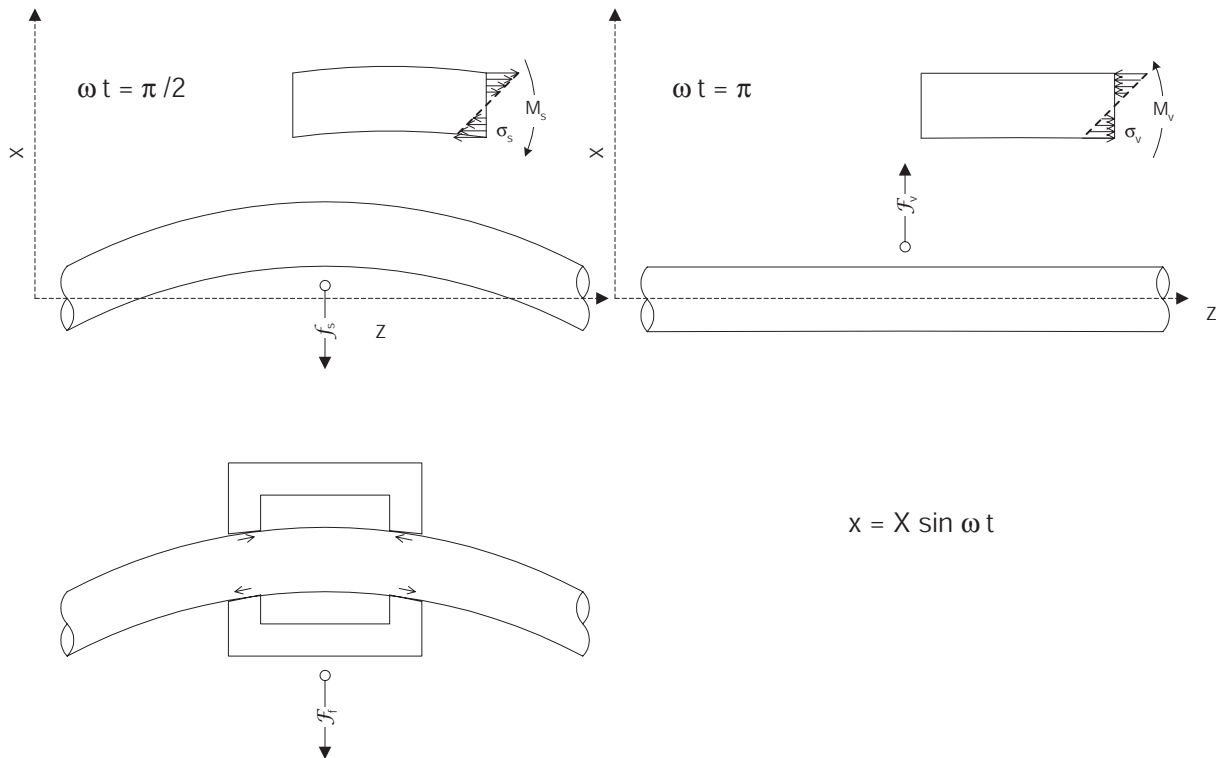


Figure 2.1.: Plane vibration of: a) visco-elastic beam b) elastic beam with hub friction

are related to the strain of the shaft fibres, which are, in turn, related to the deformation of the shaft. A metal shaft within linear stress-strain $\sigma_s = E\varepsilon$ range, has a bending moment $M_s = EIu''$ and a restoring force $f_s = -EIu''''$ at the section considered. If the shaft is of a viscous nature, additional stresses are developed due to the strain rate of change $\sigma_v = \mu\dot{\varepsilon}$, which are in quadrature phase leading strain-related stresses. As such, when the beam is at the equilibrium position (zero deflection) with the maximum $\dot{\varepsilon}$ there exists these strain-rate dependent stresses which oppose the flexing of the shaft. Because the shaft is not rotating, the neutral strain and neutral stress axis coincide, with the restoring force and the internal damping force vectors, resulting from the strain-dependent and strain-rate-dependent stresses respectively, are in the same direction perpendicular to the

2. Review of significant RID research

neutral stress axis, albeit in quadrature phase. A similar argument applies in the case of a purely elastic shaft with a shrink-fit (*fig. 2.1*). On replacing the moment resulting from the viscous stresses by the moment resulting from the surface friction, we obtain a force vector that is in the same direction and phase—in the case of Coulomb friction—as those of the restoring force. This analogy between friction damping and viscous damping should be in mind when considering the rational, which follows, of the RID follower force.

For RID to be operative, the shaft itself has to flex changing strain in its fibres, which produces viscous stresses (or surface friction) and consequently the related RID force. In a shaft with linear viscous characteristics, the infinitesimal stiffness and damping forces ($df_s = E\epsilon dA$ and $df_v = \mu\dot{\epsilon}dA$) result from multiplying elastic and viscous stresses with their corresponding infinitesimal areas dA . The simple example of a rotating shaft that is downward forced (e.g. gravity) and sagged, illustrates the changing strain effect in shaft fibers A, B, C, D (*fig. 2.2*) at a cross-section. For the loading shown, fibres A, B have

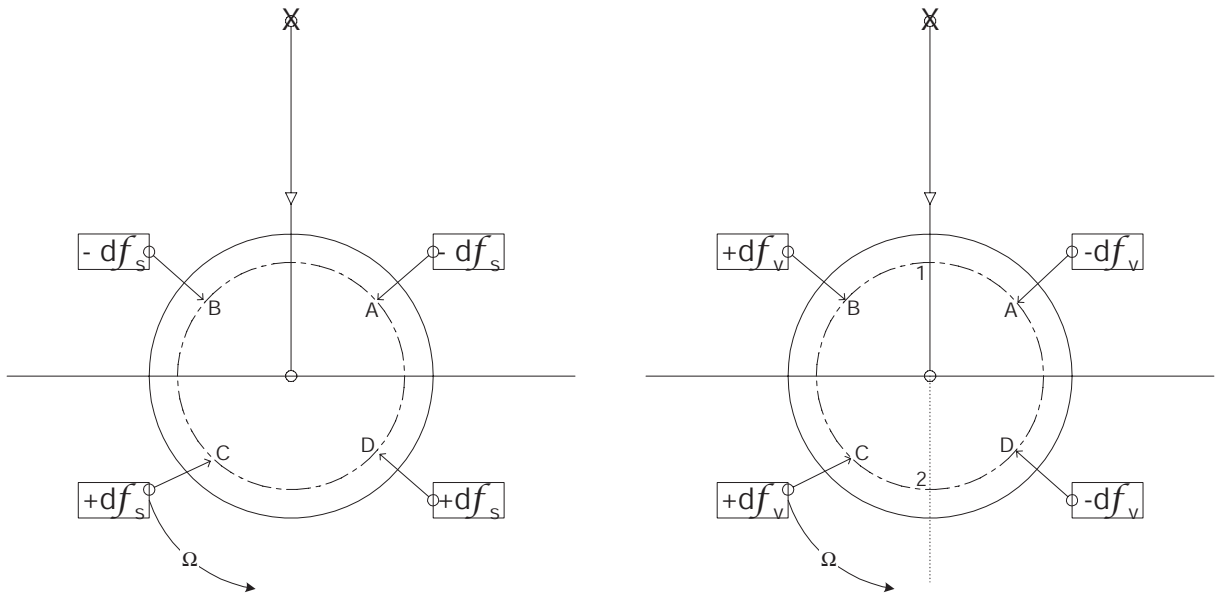


Figure 2.2.: Stresses in a rotating visco-elastic shaft cross-section displaced downwards

a negative strain $-\epsilon$, thus experience a compressive force $-df_s$. Fibres C and D have a positive strain $+\epsilon$ and experience a tensile force $+df_s$. These forces produce a moment $dM_s = 2df_s a$. The resulting moment for the whole cross-section is in equilibrium with the external moment due to the load applied (gravity).

Damping forces are shown in the right-hand diagram (*fig. 2.2*). Fibres travelling from point 1 to point 2, in the direction of rotation, will be extending; and those travelling from point 2 to point 1, will be shortening. Hence the strain in fibres B and C will have a positive rate of change $+\dot{\epsilon}$, and that in D and A will have a negative rate of change $-\dot{\epsilon}$. As such, the damping forces developed will have corresponding signs. Unlike the elastic (stiffness) forces, these added viscous forces—resulting from the added viscous stress—did

not result from a shaft deformation in the horizontal direction, in which the shaft can (and will) move until these forces are balanced by the shaft stiffness in the horizontal direction. The shaft section will move in the horizontal direction in an attempt to minimise its potential energy—by trying to annul viscous stresses—via straining the fibres in a manner producing elastic stresses of opposite sign to the existing viscous stresses.

From equilibrium (of stable operation), the damping forces must be opposed/counteracted by equal (and opposite) stiffness forces df_c as:

$$df_v + df_c = 0 = \mu \dot{\varepsilon} dA + E \varepsilon_c dA$$

whence the imposed strain

$$\varepsilon_c = -\frac{\mu \dot{\varepsilon}}{E}$$

Damping forces thus impose the strain $-\varepsilon_c$ in B and C, and $+\varepsilon_c$ in D and A. This strain is imposed in a similar manner over the whole of each half-cross-section; hence the shaft bends and gives rise to displacement in the horizontal direction, emulating the effect of applying a horizontal force which is tangential to the displacement of the rotor centre—“*follower force*”. Mathematically, the RID-induced horizontal displacement is part of the particular solution of rotordynamic EOMs with RID—the other part is the vertical displacement—as will be seen in the following section.

As with sagging that results in the RID-induced horizontal displacement, it is reasonable to accept that any random static lateral load resulting in a displacement r will induce a follower force (*fig. 2.3*). Extending the foregoing to general hysteresis anelasticity, which

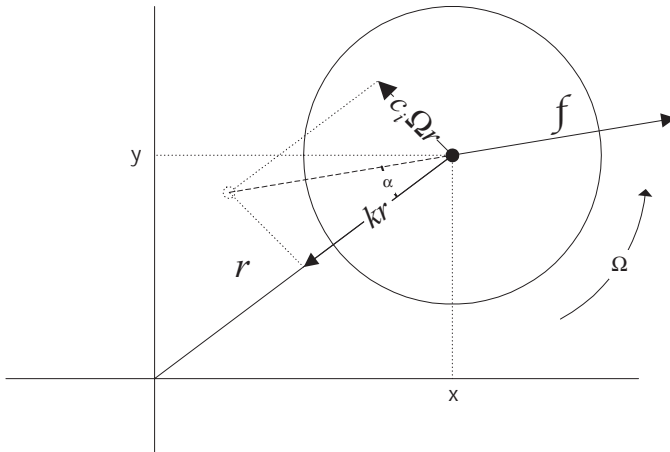


Figure 2.3.: Follower force due to an arbitrary displacement of the shaft cross-section

requires stress σ leads strain ε by a phase angle α *in forced response*, it is clear that hysteresis in a rotating shaft will cause a phase shift in the development of stress as the shaft fibres rotate around the through peak strain to the neutral strain ($\varepsilon = 0$) axis—

perpendicular to displacement vector r . The result is a neutral stress axis ($\sigma = 0$) that phase shifted by an angle α from the neutral strain axis. Accordingly, the force resultant of stress, which is perpendicular to the neutral stress axis is not in line with the deflection vector r , and hence this force resultant has a radial component (in line with r) and a tangential component perpendicular to r .

In the special case of circular whirling (2.4), when the rotational speed Ω is greater than the whirl frequency ω , a shaft fibre will travel in the same direction (as rotation) relative to the neutral strain axis. Since strain lags stress by angle α , the neutral stress axis must be ahead of the neutral strain axis. Thus, the force resultant of flexural stresses has a restoring component $kr \cos \alpha$ and a tangential component $kr \sin \alpha$, which is in the direction of the whirl acting as a *follower force*. If the shaft does not whirl, e.g. just sagging, this argument still holds since $\Omega > \omega = 0$; and the neutral stress axis will lead the neutral strain axis, yielding a stress resultant that has a restoring component in the direction opposite to displacement, and a tangential component that displaces the shaft centre in the horizontal direction according to sense of rotation.

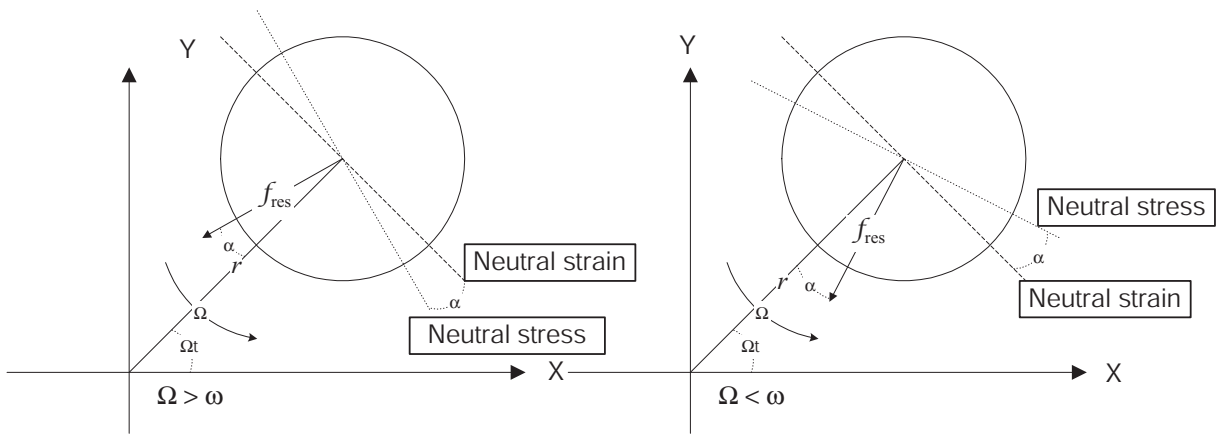


Figure 2.4.: Ω -dependant lead/lag angles of neutral stress and strain axis of anelastic shaft

However, if $\Omega < \omega$, a shaft fibre will travel in the opposite direction of Ω , relative to the neutral strain axis, and the position of the neutral stress axis is reversed. Therefore, the tangential force component will oppose whirling, acting in the direction of the stabilising external damping; in which case, it is not a follower force, or maybe a negative one.

2.4.3. A simple Jeffcott rotor model with RID

The Jeffcott rotor model (§.2.4.3.2) can demonstrate the possibility of instability due to simple linear viscous RID. LTI EOMs of the perfectly balanced and unexcited rotor include speed-dependent cross-coupled stiffness terms to represent the destabilising force.

Stability analysis is effected by examining eigenvalues of the general solution, as well as implementing Routh's criterion to assess stability conditions, thus identifying the threshold speed of instability. The particular solution demonstrates the follower force cross-coupling effect as displacing the rotor horizontally on applying a vertical force. Attention is drawn to the particular solution speed-dependence or independence in the hysteretic RID case, to confirm the forced response of the experimental rotor (*fig. 6.9*).

2.4.3.1. Complex kinematics and rotating vectors in xy - and $\xi\eta$ -frames

For RID analysis, it is essential to consider the $\xi\eta$ -frame of reference, which is rotating at shaft speed Ω with respect to the stationary xy -frame (*fig. 2.5*).

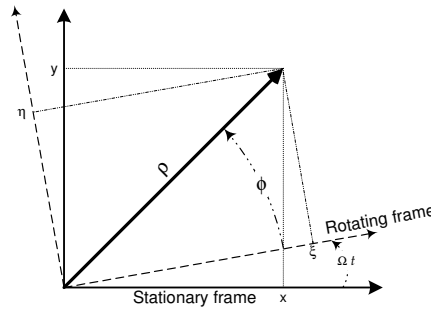


Figure 2.5.: Stationary xy and $\xi\eta$ rotating frames of reference

Furthermore, authors used polar coordinates (2.1) in the $\xi\eta$ -frame to analyse NL RID models (§.2.4.3.4) with ρ being length (magnitude) of the displacement vector, and ϕ its angle of rotation.

$$\rho e^{i\phi} = \zeta \quad (2.1)$$

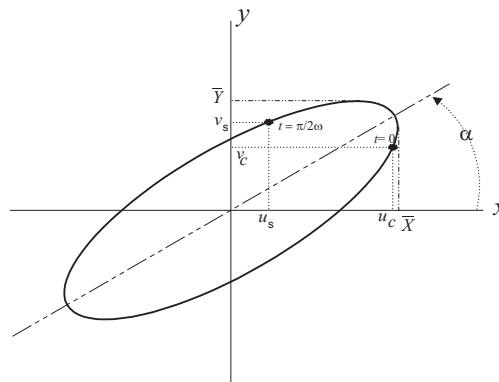


Figure 2.6.: Simple elliptic precession

Rotating vectors can be used to represent the possibly asynchronous ($\omega \neq \Omega$) single-

2. Review of significant RID research

frequency elliptic precession of *fig. 2.6*:

$$\mathbf{q} = \begin{Bmatrix} x(t) \\ y(t) \end{Bmatrix} = \begin{bmatrix} u_c & u_s \\ v_c & v_s \end{bmatrix} \begin{Bmatrix} \cos \tau \\ \sin \tau \end{Bmatrix} = \begin{Bmatrix} \bar{X} \cos(\tau + \alpha_x) \\ \bar{Y} \cos(\tau + \alpha_y) \end{Bmatrix} = \Re \left(\begin{Bmatrix} \bar{X} \\ \bar{Y} \end{Bmatrix} e^{i\tau} \right) \quad (2.2)$$

Elliptic precession can be co-rotating (FWD) or counter-rotating (BWD), i.e. in the same or opposite directions to that of rotation. Special cases of (2.2) are:

$$u_s = -v_c \cup u_c = v_s, \quad \Rightarrow \quad \alpha_u = \alpha_v + \pi/2 \quad \odot : \text{FWD circular precession} \quad (2.3a)$$

$$u_s = v_c \cup u_c = -v_s, \quad \Rightarrow \quad \alpha_u = \alpha_v - \pi/2 \quad \ominus : \text{BWD circular precession} \quad (2.3b)$$

when $\bar{X} = \bar{Y}$ and (2.3a)[(2.3b)] states that $x(t)$ leads [lags] $y(t)$ by $\pi/2$ resulting in FWD [BWD] circular precession.

EOMs resulting from (2.4) are used (*Chs. 2-5*) in conjunction with various analysis.

$$\mathbf{z} = \mathbf{x} + iy \quad \text{and} \quad \mathbf{f}_c = \mathbf{f}_x + i\mathbf{f}_y \quad (2.4)$$

If we treat the xy -plane as a complex one, (2.4) reduces to pre-multiplying (2.2) by $\{1, i\}$ and setting $z = x + iy$, two complex rotating vectors can represent this elliptic motion:

$$z = \bar{Z}_f e^{i\tau} + \bar{Z}_b e^{-i\tau} \quad (2.5)$$

of fixed amplitudes \bar{Z}_f, \bar{Z}_b representing FWD and BWD circular precessions respectively, where $\frac{\bar{Z}_f}{\bar{Z}_b} \begin{cases} >1 \Rightarrow \text{FWD} \\ <1 \Rightarrow \text{BWD} \end{cases}$ which, when added, result in an ellipse with semi-major axis a , semi-minor axis b , and attitude angle α :

$$a = |\bar{Z}_f| + |\bar{Z}_b| \quad (2.6a)$$

$$b = |\bar{Z}_f| - |\bar{Z}_b| = \frac{1}{a} \det \begin{bmatrix} u_c & u_s \\ v_c & v_s \end{bmatrix} \quad (2.6b)$$

$$2\alpha = \alpha_f + \alpha_b \quad (2.6c)$$

A positive [negative] value for the semi-minor axis b , indicates a FWD [BWD] whirling orbit. FWD [BWD] *circular* precession requires $\bar{Z}_b = 0$ [$\bar{Z}_f = 0$].

Similarly for the $\xi\eta$ -frame, $\zeta = \xi + i\eta$, where pre-multiplying (3.4) by $\{1, i\}$ gives:

$$z = \zeta e^{i\tau\Omega} = \rho e^{i(\tau\Omega + \phi)} \quad (2.7a)$$

$$\zeta = z e^{-i\tau\Omega} = \bar{Z}_f e^{i(\omega - \Omega)t} + \bar{Z}_b e^{-i(\omega + \Omega)t} \quad (2.7b)$$

In (2.7b) the complex rotating vector $\bar{Z}_b e^{-i(\omega + \Omega)t}$ is always rotating in the -ve direction

\odot , while the rotational direction of $\vec{Z}_f e^{i(\omega-\Omega)t}$ depends on $\text{sgn}(\omega - \Omega) \begin{cases} >0 \Rightarrow \odot \\ <0 \Rightarrow \ominus \end{cases}$.

2.4.3.2. The Jeffcott rotor

This is a simple single-disc rotor on an elastic shaft, mounted in two bearings. The mass of the shaft is considered negligible compared to that of the disc. The disc is not oblique with respect to the shaft and is centred between the bearings; hence no gyroscopic effect need be taken into account. The shaft rotates at a constant speed (angular velocity) Ω and, initially, in rigid bearings. Accordingly, the disc motion is considered a simple plane motion. x, y are the co-ordinates of the disc centre in the stationary frame of reference X, Y ; and ξ, η are the co-ordinates of the disc centre in the rotating frame of reference. ϵ is the centre of gravity eccentricity of the disc, m is the mass of the disc and k is the shaft stiffness (*fig. 2.7*). Assuming linear viscous external damping, the stationary frame

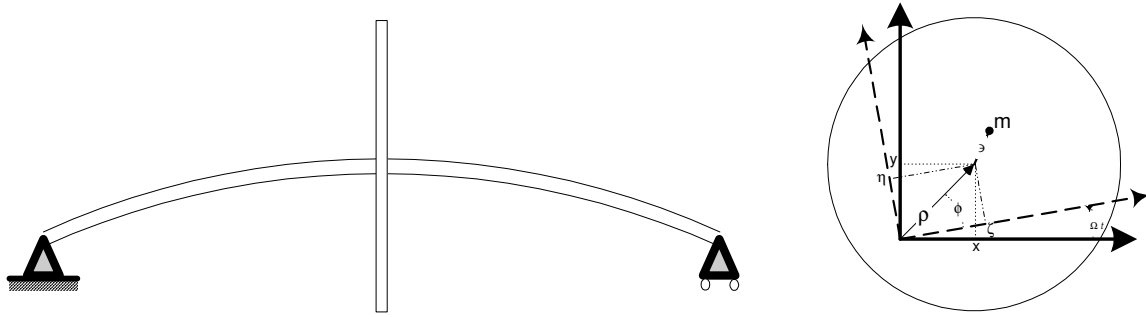


Figure 2.7.: The Jeffcott rotor

EOMs of the horizontal Jeffcott rotor without RID are:

$$\begin{aligned} m\ddot{x} + c\dot{x} + kx &= m\epsilon\Omega^2 \cos \Omega t \\ m\ddot{y} + c\dot{y} + ky &= m\epsilon\Omega^2 \sin \Omega t - mg \end{aligned}$$

which can be combined in the complex format as,

$$m\ddot{z} + c\dot{z} + kz = m\epsilon\Omega^2 e^{i\Omega t} - img \quad (2.8)$$

Using (2.7) to obtain EOMs expressed in the rotating frame of reference as:

$$m(\ddot{\zeta} + 2i\Omega\dot{\zeta} - \Omega^2\zeta) + c(\dot{\zeta} + i\Omega\zeta) + k\zeta = m\epsilon\Omega^2 - img e^{-i\Omega t} \quad (2.9)$$

RID force \mathcal{F} is introduced to the EOMs describing shaft flexing, in the rotating frame:

$$m(\ddot{\zeta} + 2i\Omega\dot{\zeta} - \Omega^2\zeta) + c(\dot{\zeta} + i\Omega\zeta) + k\zeta + \mathcal{F} = m\epsilon\Omega^2 - img e^{-i\Omega t} \quad (2.10)$$

2. Review of significant RID research

Changing the nature of \mathcal{F} will affect the solution behaviour and stability patterns, as well as impact type of analysis that should accommodate its nature.

2.4.3.3. Linear viscous internal damping

With $\mathcal{F} = \mathcal{F}_v = c_i \dot{\zeta}$, (2.10) can be written after normalising with mass m , as:

$$\ddot{\zeta} + 2i\Omega\dot{\zeta} - \Omega^2\zeta + \tilde{c}(\dot{\zeta} + i\Omega\zeta) + \tilde{c}_i\dot{\zeta} + \omega^2\zeta = \epsilon\Omega^2 - ig e^{-i\Omega t} \quad (2.11)$$

which, in the stationary frame of reference, translates to :

$$\ddot{z} + \tilde{c}\dot{z} + \tilde{c}_i(z - i\Omega z) + \omega^2 z = \epsilon\Omega^2 e^{i\Omega t} - ig \quad (2.12)$$

or in the real (non-complex) format as:

$$\begin{aligned} \ddot{x} + \tilde{c}\dot{x} + \tilde{c}_i\dot{x} + \tilde{c}_i\Omega y + \omega^2 x &= \epsilon\Omega^2 \cos \Omega t \\ \ddot{y} + \tilde{c}\dot{y} + \tilde{c}_i\dot{y} - \tilde{c}_i\Omega x + \omega^2 y &= \epsilon\Omega^2 \sin \Omega t - g \end{aligned} \quad (2.13)$$

with cross-coupled stiffness coefficients reflecting destabilising forces, according to Castilano's theorem: A neutrally stable elastic system must have a symmetric stiffness matrix.

EOMs complete solution is the sum of the general and particular solutions.

The particular solution of (2.13) to rotating imbalance at Ω and gravity g is:

$$z = Z_\epsilon e^{i\Omega t} + Z_g$$

Introducing this particular solution to eq. (2.12) we get:

$$\begin{aligned} Z_\epsilon &= \frac{\epsilon\Omega^2}{\omega^2 - \Omega^2 + i\tilde{c}\Omega} = R_\epsilon e^{-i\mu} \\ Z_g &= \frac{ig}{i\tilde{c}_i\Omega - \omega^2} = R_g e^{-i\nu} \end{aligned} \quad (2.14)$$

in which

$$\begin{aligned} R_\epsilon &= \frac{\epsilon\Omega^2}{\sqrt{(\omega^2 - \Omega^2)^2 + \tilde{c}^2\Omega^2}} \quad , \quad \tan \mu = \frac{\tilde{c}\Omega}{\omega^2 - \Omega^2} \\ R_g &= \frac{g}{\sqrt{\tilde{c}_i^2\Omega^2 + \omega^4}} \quad , \quad \tan \nu = \frac{\omega^2}{\tilde{c}_i\Omega} \end{aligned}$$

with R_ϵ , R_g , μ and ν being real constants. From (2.14), it follows that the disc centre is deflected by R_g due to gravity. Due to RID, this deflection is not in the direction of

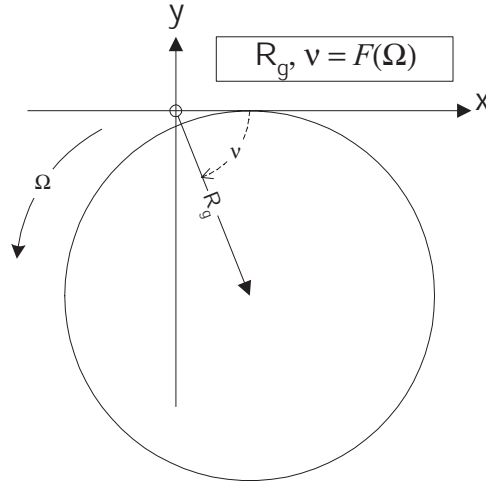


Figure 2.8.: Particular solution to gravity: Balanced Jeffcott rotor with viscous RID

gravity but is turned through an angle $(\pi/2 - \nu)$, in the sense of shaft rotation, from the negative Y axis (*fig. 2.8*). R_g and ν decrease with increased speed; $\lim_{\Omega \rightarrow \infty} R_g = 0$ and $\lim_{\Omega \rightarrow \infty} \nu = 0$. R_ϵ is the radius of the circular path that imbalance drives the shaft centre around at the same speed and in the direction of shaft rotation. Z_ϵ , the particular solution to imbalance, is identical to that of Jeffcott rotor without RID. *This is logical since the response to imbalance in a Jeffcott rotor is a synchronous circular precession, causing no periodic flexing of the shaft fibres, and hence no RID force is functional.*

The general solution of eq. (2.12), employed to study the stability of motion; is:

$$z = Z_1 e^{i\lambda_1 t} + Z_2 e^{i\lambda_2 t}$$

where Z_1, Z_2 are integration constants and λ_1, λ_2 are roots of the characteristic equation:

$$\lambda^2 - i\lambda(\tilde{c} + \tilde{c}_i) - \omega^2 + i\Omega\tilde{c}_i = 0 \quad (2.15)$$

resulting in the roots:

$$\lambda_{1,2} = \frac{i(\tilde{c} + \tilde{c}_i)}{2} \pm \sqrt{\omega^2 - \left(\frac{\tilde{c} + \tilde{c}_i}{2}\right)^2 - i\Omega\tilde{c}_i}$$

putting

$$\omega_c^2 = \omega^2 - \left(\frac{\tilde{c} + \tilde{c}_i}{2}\right)^2$$

2. Review of significant RID research

and while $\tilde{c}_i\Omega < \omega_c^2$ we can approximate

$$\sqrt{\omega_c^2 - i\Omega\tilde{c}_i} \simeq \omega_c - \frac{1}{2}i \left(\frac{\tilde{c}_i\Omega}{\omega_c} \right)$$

which results in

$$\begin{aligned} \lambda_1 &\simeq +\omega_c + \frac{1}{2}i \left(\tilde{c} + \tilde{c}_i - \frac{\tilde{c}_i\Omega}{\omega_c} \right) \\ \lambda_2 &\simeq -\omega_c + \frac{1}{2}i \left(\tilde{c} + \tilde{c}_i + \frac{\tilde{c}_i\Omega}{\omega_c} \right) \end{aligned}$$

which leads to the conclusion that $Z_2e^{i\lambda_2t}$ is always stable : BWD whirl

The stability of $Z_1e^{i\lambda_1t}$, and hence z , depends on the imaginary part of λ_1 which when multiplied by i gives the decay (non-oscillatory) component of the free vibration

$$\begin{aligned} Z_1e^{i\lambda_1t} &= Z_1e^{i(\omega_c + \frac{1}{2}i(\tilde{c} + \tilde{c}_i - \frac{\tilde{c}_i\Omega}{\omega_c}))t} \\ &= Z_1e^{(i\omega_c - \frac{1}{2}(\tilde{c} + \tilde{c}_i - \frac{\tilde{c}_i\Omega}{\omega_c}))t} \end{aligned}$$

With stability requiring a negative real part of the solution, the stability condition is:

$$\begin{aligned} \left(\tilde{c} + \tilde{c}_i - \frac{\tilde{c}_i\Omega}{\omega_c} \right) &> 0 \\ &\Downarrow \\ \Omega &< \omega_c \left(1 + \frac{\tilde{c}}{\tilde{c}_i} \right) \end{aligned} \quad (2.16)$$

Alternatively, stability conditions are determined using the Routh-Hurwitz criterion for equations with complex coefficients (*see p.161*) on (2.15), which result in the conditions:

$$\begin{aligned} (-) \begin{vmatrix} 1 & 0 \\ 0 & -(\tilde{c} + \tilde{c}_i) \end{vmatrix} &> 0 \Rightarrow \tilde{c} + \tilde{c}_i > 0 \quad , \text{ and} \\ \begin{vmatrix} 1 & 0 & -\omega^2 & 0 \\ 0 & -(\tilde{c} + \tilde{c}_i) & \tilde{c}_i\Omega & 0 \\ 0 & 1 & 0 & -\omega^2 \\ 0 & 0 & -(\tilde{c} + \tilde{c}_i) & \tilde{c}_i\Omega \end{vmatrix} &> 0 \Rightarrow \omega^2(\tilde{c} + \tilde{c}_i)^2 - \tilde{c}_i^2\Omega^2 > 0 \end{aligned} \quad (2.17)$$

Since $\tilde{c} > 0$ and $\tilde{c}_i > 0$ the first condition is always satisfied. Since $\omega^2 \gg (\tilde{c} + \tilde{c}_i)^2$ the second (2.17) requires $\Omega < \omega \left(1 + \frac{\tilde{c}}{\tilde{c}_i} \right)$, which is practically the same result from (2.16).

2.4.3.4. Hysteretic internal damping

RID force parallel to velocity vector This frequency-independent hysteretic RID force is generally nonlinear, amplitude- ($\max |\zeta|$) and pre-stress-dependent:

$$\mathcal{F} = \mathcal{F}_h = F[\max |\zeta|] \frac{\dot{\zeta}}{|\dot{\zeta}|}$$

$\frac{\dot{\zeta}}{|\dot{\zeta}|}$ is included not only to dictate direction, but also to render RID inoperative in the absence of $\xi\eta$ -frame vibration. The EOM with mass-normalised RID function \tilde{F} is:

$$\ddot{\zeta} + 2i\Omega\dot{\zeta} + (\omega^2 - \Omega^2)\zeta + \tilde{c}(\dot{\zeta} + i\Omega\zeta) + \tilde{F}[\max |\zeta|] \frac{\dot{\zeta}}{|\dot{\zeta}|} = -ige^{-i\Omega t} \quad (2.18)$$

Note that if the RID force, \mathcal{F}_h , is expressed as a function of amplitude (either linear or nonlinear) only, without the term $\frac{\dot{\zeta}}{|\dot{\zeta}|}$; it will not produce any cross-coupling in the EOMs as expressed in the stationary frame of reference, in a manner similar to kz and $k\zeta$ of eqs. (2.8, 2.9). This is because the cross-coupling in the stationary frame derives from transforming the rate-dependent terms, which are not cross-coupled, in the rotating frame; to the stationary frame, in a manner similar to eqs. (2.11, 2.12).

Introducing polar co-ordinates (2.1) $\rho e^{i\phi} = \zeta = \xi + i\eta = \sqrt{(\xi^2 + \eta^2)} e^{i\phi}$ we get:

$$\left\{ \ddot{\rho} - \rho\dot{\phi}^2 + i(\rho\ddot{\phi} + 2\dot{\rho}\dot{\phi}) + 2i\Omega(\dot{\rho} + i\rho\dot{\phi}) + (\omega^2 - \Omega^2)\rho + \tilde{c}(\dot{\rho} + i\rho\dot{\phi} + i\Omega\rho) + \tilde{F}[\max \rho] \frac{\dot{\rho} + i\rho\dot{\phi}}{\sqrt{\dot{\rho}^2 + \rho^2\dot{\phi}^2}} \right\} e^{i\phi} = -ige^{-i\Omega t} \quad (2.19)$$

which, on separating the real and imaginary terms, can be split into:

$$\begin{aligned} \ddot{\rho} - \rho\dot{\phi}^2 - 2\Omega\rho\dot{\phi} + (\omega^2 - \Omega^2)\rho \\ + \tilde{c}\dot{\rho} + \tilde{F}[\max \rho] \frac{\dot{\rho}}{\sqrt{\dot{\rho}^2 + \rho^2\dot{\phi}^2}} = -g \sin(\phi + \Omega t) \quad , \text{ and} \\ \rho\ddot{\phi} + 2\dot{\rho}\dot{\phi} + 2\Omega\dot{\rho} + \tilde{c}(\Omega + \dot{\phi})\rho \\ + \tilde{F}[\max \rho] \frac{\rho\dot{\phi}}{\sqrt{\dot{\rho}^2 + \rho^2\dot{\phi}^2}} = -g \cos(\phi + \Omega t) \end{aligned} \quad (2.20)$$

Particular solution These equations are satisfied by the particular solution: $\rho = R$ and $\phi = -\Omega t + \phi_o$ in the rotating frame of reference, where R and ϕ_o are constants defined

2. Review of significant RID research

by the equations:

$$\begin{aligned} R\omega^2 &= -g \sin \phi_o \\ \tilde{F}[R] &= g \cos \phi_o \end{aligned}$$

which yields,

$$\tan \phi_o = -\frac{R\omega^2}{\tilde{F}[R]} = -\frac{kR}{F[R]} = -\frac{1}{\Theta[R]}$$

The term $\frac{kR}{F[R]}$ is the dimensionless ratio of the elastic force—called forth by the deflection R —to the damping force, and is independent of speed, and hence is the angle ϕ_o . If the damping force—which is a monotonic increasing function of amplitude—was linear with amplitude (valid for small amplitudes), then ϕ_o does not change with the amplitude of vibration. From the above, ϕ_o is a negative angle i.e. clockwise from the stationary x-axis. It is more instructive to consider the angle $\check{\phi}_0$ as measured from the negative y-axis in

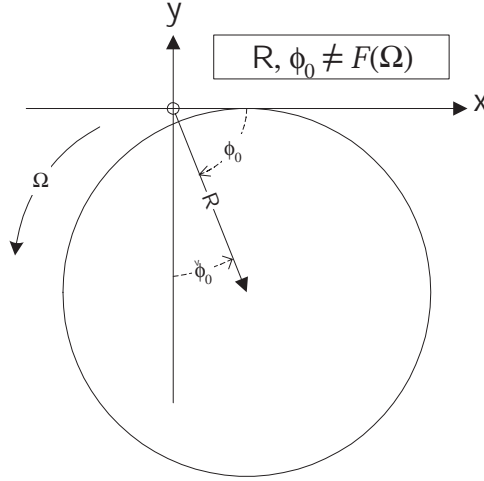


Figure 2.9.: Particular solution to gravity: Balanced Jeffcott rotor with hysteretic RID

the direction of rotation (*fig. 2.9*), in which case

$$\begin{aligned} R\omega^2 &= g \cos \check{\phi}_o \\ \tilde{F}[R] &= g \sin \check{\phi}_o \\ \tan \check{\phi}_o &= \Theta[R] \end{aligned}$$

The (-) sign is omitted as $\check{\phi}_0$ is measured from -ve Y-axis. Since $\check{\phi}_0$ is usually very small:

$$\begin{aligned} R &\simeq \frac{g}{\omega^2} \left(1 - \frac{1}{2}\check{\phi}_0^2\right) \simeq \frac{g}{\omega^2} \left\{1 - \frac{1}{2} \left(\Theta \left[\frac{g}{\omega^2}\right]\right)^2\right\}, \\ \check{\phi}_0 &\simeq \tan \check{\phi}_0 = \frac{\tilde{F}[R]}{R\omega^2} = \Theta[R] \simeq \Theta \left[\frac{g}{\omega^2}\right] \end{aligned} \quad (2.21)$$

The *speed-independent* shaft deflection R due to gravity is reduced by $\frac{1}{2} \left(\Theta \left[\frac{g}{\omega^2} \right] \right)^2$, and is diverted from the -ve Y-axis by an angle $\check{\phi}_0 \simeq \Theta \left[\frac{g}{\omega^2} \right]$ in the direction of rotation.

Linearised stability analysis (5.2) in the neighbourhood of particular solution R . We consider r to be the variation in variable ρ , and v the variation in variable ϕ . Since disturbing motion r is small compared to undisturbed motion R , we can replace the function $\tilde{F}[\max(R+r)]$ by the function $\tilde{F}[R+r]$. Using the expansions:

$$\tilde{F}[\rho+r] = \tilde{F}[\rho] + \tilde{F}'[\rho]r + \tilde{F}''[\rho]r^2 + \dots,$$

where,

$$\tilde{F}'[\rho] = \frac{d(\tilde{F}[\rho])}{d\rho}$$

and

$$\begin{aligned} & \frac{\dot{\rho} + \dot{r}}{\sqrt{(\dot{\rho} + \dot{r})^2 + (\rho + r)^2(\dot{\phi} + \dot{v})^2}} = \\ & \frac{\dot{\rho}}{\sqrt{\dot{\rho}^2 + \rho^2\dot{\phi}^2}} + \frac{\rho^2\dot{\phi}^2}{(\dot{\rho}^2 + \rho^2\dot{\phi}^2)^{\frac{3}{2}}}\dot{r} - \frac{\dot{\rho}\rho\dot{\phi}^2}{(\dot{\rho}^2 + \rho^2\dot{\phi}^2)^{\frac{3}{2}}}r - \frac{\dot{\rho}\rho^2\dot{\phi}}{(\dot{\rho}^2 + \rho^2\dot{\phi}^2)^{\frac{3}{2}}}v + \dots, \end{aligned}$$

and

$$\begin{aligned} & \frac{(\rho+r)(\dot{\phi} + \dot{v})}{\sqrt{(\dot{\rho} + \dot{r})^2 + (\rho + r)^2(\dot{\phi} + \dot{v})^2}} = \\ & \frac{\rho\dot{\phi}}{\sqrt{\dot{\rho}^2 + \rho^2\dot{\phi}^2}} - \frac{\dot{\rho}\rho\dot{\phi}}{(\dot{\rho}^2 + \rho^2\dot{\phi}^2)^{\frac{3}{2}}}\dot{r} + \frac{\dot{\rho}^2\dot{\phi}^2}{(\dot{\rho}^2 + \rho^2\dot{\phi}^2)^{\frac{3}{2}}}r + \frac{\dot{\rho}^2\rho}{(\dot{\rho}^2 + \rho^2\dot{\phi}^2)^{\frac{3}{2}}}v + \dots, \end{aligned}$$

Substituting $\rho+r$ for ρ and $\phi+v$ for ϕ in equations (2.20) and omitting the nonlinear terms in accordance with Lyapunov's theorem on the first approximation, we get:

$$\begin{aligned} \ddot{r} + \left(\tilde{c} + \frac{\tilde{F}[R]}{R\Omega} \right) \dot{r} + \omega^2 r + \tilde{F}[R]v &= 0, \text{ and} \\ R\ddot{v} + \tilde{c}R\dot{v} + R\omega^2 v - \tilde{F}'[R]r &= 0 \end{aligned}$$

The characteristic equation of which derives from,

$$\begin{vmatrix} \lambda^2 + \left(\tilde{c} + \frac{\tilde{F}}{R\Omega} \right) \lambda + \omega^2 & \tilde{F} \\ -\frac{\tilde{F}'}{R} & \lambda^2 + \tilde{c}\lambda + \omega^2 \end{vmatrix} = 0$$

2. Review of significant RID research

where $\tilde{F} = \tilde{F}[R]$. Evaluating the determinant we obtain the equation :

$$\lambda^4 + \left(2\tilde{c} + \frac{\tilde{F}}{R\Omega}\right) \lambda^3 + \left[2\omega^2 + \tilde{c} \left(\tilde{c} + \frac{\tilde{F}}{R\Omega}\right)\right] \lambda^2 + \omega^2 \left(2\tilde{c} + \frac{\tilde{F}}{R\Omega}\right) \lambda + \omega^4 + \frac{\tilde{F}\tilde{F}'}{R} = 0$$

The Routh-Hurwitz criterion for equations with real coefficients $a_{i \in 0 \dots 2n}$, requires $\forall a_i$ be of the same sign and different from zero, which is satisfied since $\tilde{c} > 0$, $\tilde{F} > 0$ and $\tilde{F}' > 0$; and also requires that $\Delta_{0, \dots, 3}$ (as defined below) be all greater than zero.

$$\begin{array}{cccc} \Delta_0 & \Delta_1 & \Delta_2 & \Delta_3 \\ \hline \left| \begin{array}{cccc} a_1 & a_0 & 0 & 0 \\ a_3 & a_2 & a_1 & 0 \\ 0 & a_4 & a_3 & a_2 \\ 0 & 0 & 0 & a_4 \end{array} \right| \end{array}$$

This results in the following inequalities, necessary to satisfy, for stability of motion:

$$\begin{aligned} \Delta_0 &= a_1 && > 0 \text{ true} \\ \Delta_1 &= a_1 a_2 - a_0 a_3 &= a_1 \left(\left[2\omega^2 + \tilde{c} \left(\tilde{c} + \frac{\tilde{F}}{R\Omega} \right) \right] \right) - \omega^2 a_1 &> 0 \text{ true} \\ \Delta_2 &= a_3(a_2 a_1 - a_0 a_3) - a_1^2 a_4 &\Rightarrow \tilde{c}\omega^2 \left(\tilde{c} + \frac{\tilde{F}}{R\Omega} \right) - \frac{\tilde{F}\tilde{F}'}{R} &> 0 \text{ condition} \\ \Delta_3 &= a_4 \Delta_2 &\Rightarrow \Delta_2 &> 0 \text{ condition} \end{aligned}$$

For the motion under investigation, the first two inequalities are always satisfied. The last two inequalities indicate that the condition for stability is $\Delta_2 > 0$ which requires:

$$\tilde{c}\omega^2 \left(\tilde{c} + \frac{\tilde{F}}{R\Omega} \right) - \frac{\tilde{F}\tilde{F}'}{R} > 0$$

or when rearranged

$$R\tilde{c}^2\omega^2 + \frac{\tilde{c}\omega^2\tilde{F}}{\Omega} > \tilde{F}\tilde{F}' \quad (2.22)$$

If either of the terms on the left-hand side of the inequality (2.22) is larger than the right-hand side, then the inequality is satisfied. Accordingly, if

$$R\tilde{c}^2\omega^2 > \tilde{F}\tilde{F}'$$

which contains no speed of rotation term, and can be rewritten as

$$\frac{\tilde{c}^2}{\omega^2} > \frac{\tilde{F}\tilde{F}'}{R\omega^4}$$

or on defining $D = \tilde{c}/\omega = \frac{c}{\omega m}$ as relative external damping, can be rewritten as,

$$D^2 > \Theta[R] (\Theta[R] + R\Theta'[R]) \quad (2.23)$$

is true, then motion is always stable, satisfying (2.23) and in turn (2.22) which is a sufficient condition for the stability. Since (2.23) does not contain a speed term, then (if satisfied) the motion is stable over the whole interval of speed Ω with no onset speed of instability. This could be achieved by increasing the external stabilising damping.

In the case of *linear* hysteretic RID, valid for small amplitudes, \tilde{F} is a linear function of $R \Rightarrow \tilde{F}[R] = R\tilde{F}_o$. Using this simplifying assumption, the (2.23) acquires the form:

$$D^2 > \frac{\tilde{F}_o^2}{\omega^2} = \Theta_o^2$$

On the other hand, if the inequality (2.23) is not satisfied, the stability criterion (inequality 2.22) implies that the motion will be stable up to a certain speed (dictated by the relative magnitudes of internal and external damping), after which the motion will be unstable as implied by the following, which is a restatement of inequality (2.22)

$$\begin{aligned} \Omega < \omega \frac{(\tilde{c}/\omega)(\tilde{F}/R\omega^2)}{(\tilde{F}/R\omega^2)(\tilde{F}'/\omega^2) - (\tilde{c}^2/\omega^2)} = \\ \omega \frac{(\tilde{c}/\omega)(F/kR)}{(F/kR)(F'/k) - (\tilde{c}^2/\omega^2)} = \\ \omega \frac{D\Theta[R]}{\Theta[R](\Theta[R] + R\Theta'[R]) - D^2}. \end{aligned} \quad (2.24)$$

Or, on implementing the reasonably valid simplifying assumption of linearity:

$$\Omega < \omega \frac{(\tilde{c}/\omega)(\tilde{F}_o/\omega^2)}{(\tilde{F}_o^2/\omega^4) - (\tilde{c}^2/\omega^2)} = \omega \frac{D\Theta_o}{\Theta_o^2 - D^2}.$$

Inequality (2.24) and its linear form suggest that instability will occur after an onset speed, which can be any multiple or fraction of the rotor's natural frequency; i.e. *the onset of instability can be a sub-critical speed*. Because this had never been verified experimentally, the model was deemed an erroneous representation by Tondl (1965). He argued this erroneous result was caused by replacing $\tilde{F}[\max(R+r)]$ with $\tilde{F}[R+r]$. Furthermore, he had assumed that RID force acts in a direction opposite to that of $\dot{\zeta}$, which is contradicted

2. Review of significant RID research

by simple reasoning showing it does not quite coincide with $\dot{\zeta}$.

RID force not parallel to velocity vector Expressing disc deflection ζ in polar coordinates ρ, ϕ , for a small change of the vector $\Delta\zeta$, we have:

$$\Delta\zeta = \frac{\partial(\rho e^{i\phi})}{\partial\rho}\Delta\rho + \frac{\partial(\rho e^{i\phi})}{\partial\phi}\Delta\phi = (\Delta\rho + i\rho\Delta\phi)e^{i\phi}$$

There are two components of change: 1) Radial component, $\Delta\rho$ of ρ ; and 2) Cross-radial component, $\Delta\phi$ of ϕ . Considering RID is nonlinear with amplitude: $\Delta\rho$ and $\Delta\phi$ will result in RID forces of unequal absolute values. RID force can thus be expressed by:

$$\mathcal{F}_h = \left(F_1[\max \rho] \frac{\dot{\rho}}{\sqrt{(\dot{\rho}^2 + \rho^2\dot{\phi}^2)}} + iF_2[\max \rho] \frac{\rho\dot{\phi}}{\sqrt{(\dot{\rho}^2 + \rho^2\dot{\phi}^2)}} \right) e^{i\phi}$$

and in analogy with equation (2.20) we get

$$\begin{aligned} \ddot{\rho} - \rho\dot{\phi}^2 - 2\Omega\rho\dot{\phi} + (\omega^2 - \Omega^2)\rho \\ + \tilde{c}\dot{\rho} + \tilde{F}_1[\max \rho] \frac{\dot{\rho}}{\sqrt{\dot{\rho}^2 + \rho^2\dot{\phi}^2}} &= -g \sin(\phi + \Omega t) \\ \rho\ddot{\phi} + 2\dot{\rho}\dot{\phi} + 2\Omega\dot{\rho} + \tilde{c}(\Omega + \dot{\phi})\rho \\ + \tilde{F}_2[\max \rho] \frac{\rho\dot{\phi}}{\sqrt{\dot{\rho}^2 + \rho^2\dot{\phi}^2}} &= -g \cos(\phi + \Omega t) \end{aligned} \quad (2.25)$$

Particular solution is $\rho = R$ and $\phi = -\Omega t + \phi_o$ as in (2.20) where R and ϕ_o are constants. $\check{\phi}_0$ which reflects the RID effect on the particular solution is defined by:

$$\check{\phi}_0 \simeq \tan \check{\phi}_0 = \frac{\tilde{F}_2[R]}{R\omega^2} = \Theta_2[R] \simeq \Theta_2\left(\frac{g}{\omega^2}\right)$$

which unlike (2.21), shows that, of the two RID force components, only the cross-coupled component is effective in displacing the rotor horizontally.

Stability analysis , applying Routh-Hurwitz criterion. For stability at any speed:

$$\tilde{F}_2[R]\tilde{F}'_2[R] < \tilde{c}^2 R\omega^2$$

which if not satisfied, the inequality

$$\Omega < \frac{\tilde{c}\omega^2 \tilde{F}_1[R]}{\tilde{F}_2[R] \tilde{F}_2'[R] - \tilde{c}^2 R \omega^2}$$

becomes the criterion for stability. From the foregoing, the radial component of internal damping acts in a manner similar to external damping in enhancing the stability and raising the onset speed of instability. On the contrary the cross-radial component of internal damping acts in an opposite manner and may cause instability.

2.4.4. The Jeffcott rotor with RID on asymmetric bearings

The use of energy dissipated, in one precession cycle, for assessing stability of extended Jeffcott rotor, on orthotropic bearings, is demonstrated and criticised. Energy dissipated or introduced by RID is calculated and added to that dissipated by external damping. If the total energy is negative [positive], then the system is stable [unstable]. The destabilising effect of rotor and/or stator asymmetry is ignored. The suppressing effect of RID on this parametric instability is hinted at.

2.4.4.1. Viscous RID model on orthotropic bearings

Stationary frame EOMs for a balanced jeffcott rotor on orthotropic bearings are:

$$\begin{aligned} m\ddot{x} + c_i(\dot{x} + \Omega y) + c\dot{x} + k_x x &= 0 \\ m\ddot{y} + c_i(\dot{y} - \Omega x) + c\dot{y} + k_y y &= 0 \end{aligned} \quad (2.26)$$

The solution at the threshold of instability will be in the form:

$$\begin{bmatrix} k_x - m\omega^2 + i\omega(c_i + c) & \Omega c_i \\ -\Omega c_i & k_y - m\omega^2 + i\omega(c_i + c) \end{bmatrix} \begin{Bmatrix} x \\ y \end{Bmatrix} = 0 \quad (2.27)$$

For a solution to exist, the determinant must be zero, resulting in

$$\begin{aligned} \omega &= \sqrt{\frac{k_x + k_y}{2m}} \\ \Omega_s^2 &= \omega^2 \left(1 + \frac{c}{c_i}\right)^2 + \frac{(k_x - k_y)^2}{4c_i^2} \end{aligned} \quad (2.28)$$

Instability sets in when the speed reaches Ω_s . The rotor is stabilised either by providing external damping c , or by making the supports anisotropic to raise the threshold speed

2. Review of significant RID research

Ω_s but will not eliminate instability. Energy dissipated by RID per whirl cycle is:

$$E_{\text{dis}} = d \int_0^{\tau=2\pi/\omega} [(\dot{x} + \Omega y)\dot{x} + (\dot{y} - \Omega x)\dot{y}] dt \quad (2.29)$$

which results in

$$E_{\text{dis}} = 2\pi d \left(\omega \frac{a^2 + b^2}{2} - \Omega ab \right)$$

stating that the dissipated energy will be negative when

$$\Omega > \omega \left(\frac{a^2 + b^2}{2ab} \right)$$

As defined, ω is the elliptic orbit single frequency (2.2), and a, b are its axis (2.6). It is what can be termed as the *mean natural frequency* of the rotor-bearing system, that has two natural frequencies, one in each of the two orthogonal directions. On substituting $x = x_0 e^{\lambda t}$, $y = y_0 e^{\lambda t}$; the undamped and de-coupled version of (2.26) has:

$$\begin{aligned} \lambda_{1,2} &= \pm i\omega_{ny} ; \omega_{ny} = \sqrt{\frac{k_y}{m}} \\ \lambda_{3,4} &= \pm i\omega_{nx} ; \omega_{nx} = \sqrt{\frac{k_x}{m}} \end{aligned}$$

where ω_{nx} and ω_{ny} are the two independent natural frequencies—one in the x and the second in the y directions—of the system, causing two critical speeds. The free vibration of the system is, thus, composed of two oscillations with the above frequencies.

We can define

$$\bar{k} = \frac{k_x + k_y}{2}, \Delta k = \frac{k_x - k_y}{2} > 0, \bar{\omega} = \sqrt{\frac{\bar{k}}{m}}, \check{k} = \frac{\Delta k}{\bar{k}}$$

where \bar{k} is the average stiffness and $\bar{\omega}$ is the mean natural frequency. After mass-normalisation, eq. (2.26) can be put in matrix form as:

$$\begin{Bmatrix} \ddot{x} \\ \ddot{y} \end{Bmatrix} + (\tilde{c} + \tilde{c}_i) \begin{Bmatrix} \dot{x} \\ \dot{y} \end{Bmatrix} + \begin{bmatrix} \bar{\omega}^2(1 + \check{k}) & \tilde{c}_i \Omega \\ -\tilde{c}_i \Omega & \bar{\omega}^2(1 - \check{k}) \end{bmatrix} \begin{Bmatrix} x \\ y \end{Bmatrix} = \{0\} \quad (2.30)$$

This system (eq. 2.30) differs from its undamped and de-coupled version in, as expected, the damping terms and the cross-coupling terms. The damping coefficients merely reduce the value of the natural frequency to that of the damped natural frequency e.g. ($\omega_{ny_d} = \sqrt{\omega_{ny}^2 - (c/2m)^2}$). The cross-coupling has a more interesting effect on the natural frequencies or eigenvalues (*fig 2.4.4.1*). As cross-coupling is introduced to the undamped and de-coupled system, the lower natural frequency ω_{ny} is raised (increases in value), and

the upper natural frequency ω_{nx} is lowered (decreases in value). The squares of both

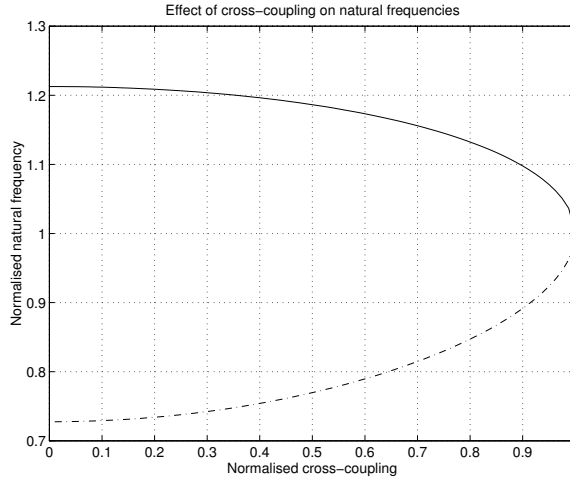


Figure 2.10.: The effect of cross-coupling on the eigenvalues of a 2DOF system with a single mass and orthotropic stiffness. The dotted (lower) curve represents the lower natural frequency as normalised by the mean frequency, i.e. $(\omega_{ny}/\bar{\omega})$; and the solid curve represents the normalised higher natural frequency. $\tilde{c}_i\Omega$ is normalised by Δk .

frequencies $(\omega_{ny}^2, \omega_{nx}^2)$ change by the same amount which depends on the strength of the cross-coupling relative to $\Delta k/m$. This approaching of natural frequencies increases with stronger cross-coupling, and continues until the cross-coupling coefficient equals Δk ; by which time, both squares of natural frequencies would have changed by an amount $\Delta k/m$ and both frequencies will equal the mean natural frequency $\bar{\omega}$. On strengthening the cross-coupling further, the natural frequencies will have the same oscillatory part yet, one will have a real part that is positive (unstable) and the other will have a stable negative real part. In this instance, using $(\bar{\omega})$ in eq. (2.29) is valid and will produce a negative E_{dis} only. A positive E_{dis} is not possible since the system would be unstable.

Eq. (2.30) yields the nondimensional characteristic equation

$$\hat{\lambda}^4 + 2(D + \Theta)\hat{\lambda}^3 + (2 + (D + \Theta)^2)\hat{\lambda}^2 + 2(D + \Theta)\hat{\lambda} + (1 + (\Theta N)^2 - \check{k}^2) = 0$$

where $\hat{\lambda} = \lambda/\bar{\omega}$, and $N = \Omega/\bar{\omega}$. Applying the Routh-Hurwitz criterion, we get the condition for stability as

$$(D + \Theta)^2 + \check{k}^2 - (\Theta N)^2 > 0$$

which is rewritten as

$$\Omega^2 < \bar{\omega}^2 \left[\left(1 + \frac{D}{\Theta}\right)^2 + \left(\frac{\check{k}}{\Theta}\right)^2 \right] \quad (2.31)$$

Eq. (2.31) is the same as eq. (2.28); only it is evident that $\bar{\omega}$ is neither a whirling frequency nor an eigenvalue—it serves merely as a reference frequency—which confirms its misuse

for calculating the energy dissipated by RID as in eq. (2.29).

The condition for stability obtained (inequality 2.31) for the extended Jeffcott rotor (on orthotropic bearings) is the same as that for the Jeffcott rotor on isotropic bearings (ineq. 2.17), except for the second term inside the square brackets—i.e. $(\check{k}/\Theta)^2$ which is equal to $(k_x - k_y)^2/4c_i^2$ as in eq. (2.28). This term is used as a secondary argument to support the claim—using this model—that bearing orthotropy enhances the stability by raising the onset of instability (Smith, 1933). This claim, however, is not entirely valid; since $(\check{k}/\Theta)^2$ raises the onset of instability, of the externally undamped system, to $\omega\sqrt{1+\check{k}}$ which is the higher natural frequency $\omega_{nx} = \sqrt{\frac{k_x}{m}}$ — \check{k} is corrected by Θ when the cross-coupling due to viscous RID is accounted for in the EOMs which brings the critical speeds closer together, hence reducing $\check{k} = \Delta k/\bar{k}$ of the undamped system. As such, according to this model, the instability due to linear viscous RID of a Jeffcott rotor can occur only at speeds above the second critical speed; which is a statement quite similar to the case of isotropic bearings. The possibility of instability occurring before the second critical speed is highly unlikely; since below the first critical, RID is stabilising and in-between the two critical speeds, the response to imbalance is a backward precessing elliptic orbit at a frequency equal to that of rotation Ω , which results in a stabilising RID.

The main mathematical argument, on which enhanced stability due to bearing orthotropy is based, is the fact that an undamped system (of EOMs) with isotropic stiffness terms will have $\Delta k = 0$. As such, any coefficient of stiffness cross-coupling will be greater than Δk ; a situation that results in two eigenvalues having the same imaginary part (oscillation frequency) and also having real parts that are of the same magnitude yet opposite signs. Accordingly, the undamped rotor system will be unstable—on application of any disturbance—regardless of it being rotating or not. If present, external damping can counteract and, possibly, eliminate the positive real part in one of the eigenvalues, depending on the relative value of the damping coefficients and the cross-coupling coefficients. However, Childs (1993) contests the effectiveness of introducing support orthotropy as a means of enhancing rotor stability; and claims, based on his experimental research, that its effect has been exaggerated in the literature.

2.4.4.2. Hysteretic RID model on orthotropic bearings

The basis for the following hysteretic RID model is there exists a phase angle α between the neutral stress and neutral strain axis of the shaft cross-section. The neutral stress axis either leads, or lags the neutral strain axis by the angle α depending on whether ω

is less than, or greater than Ω respectively.

$$\begin{aligned} m\ddot{x} + c\dot{x} + k_r x + \gamma k_r y &= 0 \\ m\ddot{y} + c\dot{y} + k_r y - \gamma k_r x &= 0 \end{aligned}$$

where k_r is the shaft radial stiffness, and

$$\begin{aligned} \gamma &= \sin \alpha \text{ when } \Omega > \omega \text{ or for negative } \omega \text{ —backward whirl} \\ \gamma &= -\sin \alpha \text{ when } \Omega < \omega \end{aligned} \quad (2.32)$$

In a similar analysis as in eqs. (2.27), the condition for stability is

$$\frac{\omega c}{k_r} > \gamma \quad , \quad \omega = \sqrt{\frac{k}{m}}$$

When the whirl frequency equals the critical speed, the rotor becomes potentially unstable with a positive γ : a situation that does not vary with increased speed. If, however, the bearings provide sufficient damping such that $\frac{\omega c}{k_r} > \gamma$, the rotor will be stable at all speeds—which is similar to the result from ineq. (2.23).

When the bearings are anisotropic, the whirl orbit becomes an ellipse with an instantaneous whirl frequency ω_t expressed as

$$\omega_t = \frac{\omega ab}{x^2 + y^2}$$

and the energy dissipated per whirl cycle is

$$E_{\text{dis}} = -k_r ab \int_0^{2\pi} \gamma d(\omega t)$$

If $\omega_t > \Omega$ at any time during the whirl cycle, then the energy dissipated is negative, corresponding to energy added to the rotor which becomes unstable.

2.4.4.3. Coulomb damping

The dry friction force of constant magnitude opposite to the direction of the relative sliding velocity, is represented in the stationary frame of reference as

$$\mathcal{F}_x = \left(\frac{-\dot{x} + \Omega y}{v} \right) \mu N \quad , \quad \mathcal{F}_y = \left(\frac{-\dot{y} - \Omega x}{v} \right) \mu N \quad \text{with} \quad v = \sqrt{(\dot{x} + \Omega y)^2 + (\dot{y} - \Omega x)^2}$$

where μ is the friction coefficient and N the normal force to the surfaces in contact.

2. Review of significant RID research

The energy thus dissipated per whirl cycle is

$$E_{\text{dis}} = \mu N \int_0^T \left[\left(\frac{\dot{x} + \Omega y}{v} \right) \dot{x} + \left(\frac{\dot{y} - \Omega x}{v} \right) \dot{y} \right] dt$$

2.4.5. RID sources models

2.4.5.1. Viscous stress

In a non-synchronous whirl circular orbit The simple case of a circular orbit with $\Omega > \omega$ is considered. A boundary value problem is formulated for an Euler beam and considering the added effect of viscosity-induced stresses on the bending moment.

We start from the stress-strain relation at a point in the cross-section of the shaft with a linear term relating stress to the rate of strain as

$$\sigma_z = E\varepsilon_z + \mu(d\varepsilon_z/dt) \quad (2.33)$$

from the linear beam theory, the strain at a point

$$\varepsilon_z = \varepsilon_o(r/r_o) \cos \gamma$$

with γ being the angular orientation of the shaft fibre from the plane of deflection, so

$$\sigma_z = \varepsilon_o(r/r_o)(E \cos \gamma - \mu \sin \gamma d\gamma/dt)$$

The resulting moments at any shaft cross-section are

$$\begin{aligned} M_{zy} &= \int \int_A \sigma_z r \cos \gamma dA = (\varepsilon_o/r_o)EI \\ M_{zx} &= \int \int_A \sigma_z r \sin \gamma dA = -(\varepsilon_o/r_o)\mu(d\gamma/dt)I \end{aligned} \quad (2.34)$$

The resultant forces from the moments are the radial restoring force

$$f_y = EI(d^4y/dz)$$

and the tangential destabilising force

$$f_x = -\mu I(d\gamma/dt)(d^4y/dz)$$

from the perpendicular moment (2.34) resulting from the viscous term in the stress-strain

relation. Shaft rotation with respect to the plane of deflection is given by

$$d\gamma/dt = \Omega - \omega$$

If we presume the existence of external viscous damping that is proportional to the shaft's vibration (at its natural frequency) and opposes it, the shaft motion is stable up to the point where the damping forces cancel each other

$$c\omega y = \mu I(\Omega - \omega)(d^4y/dz) \quad (2.35)$$

Turning back to the vibration modes, we have from the balance of the radial forces

$$EI(d^4y/dz) + \bar{\rho}\omega^2 y = 0$$

which is the classic equation for beam vibration where $\bar{\rho}$ here is the shaft mass per unit length, with a solution in terms of the mode shapes as

$$y = y_o \cos(n\pi z/l)$$

with n being the mode number, l the shaft length and z the shaft's axial co-ordinate. The conventional solution for critical speeds (natural frequencies) being

$$\omega^2 = EI n^4 \pi^4 / \bar{\rho} l^4 \quad (2.36)$$

which on substitution in stability criterion (2.35) yields the simplified expression

$$\Omega = \omega + (cE/\mu\bar{\rho})/\omega$$

Damping coefficients can be expressed as ratios to system critical damping as:

$$\zeta = \zeta_e + \zeta_i = (c/2\bar{\rho}\omega) + (\mu\omega/2E)$$

with a useful parameter expressing their relative effects as their relative ratio at a typical mode (e.g. the fundamental mode)

$$\frac{\zeta_{e1}}{\zeta_{i1}} = \frac{(cE/\mu\bar{\rho})}{\omega_1^2}$$

The stability boundary then becomes

$$\frac{\Omega}{\omega_1} = \frac{\omega}{\omega_1} + \frac{\zeta_{e1}/\zeta_{i1}}{\omega/\omega_1}$$

2. Review of significant RID research

For a given value of damping ratio parameter, it can be seen that the minimum rotational speed at which instability is encountered is *not necessarily* associated with whirl at the first natural frequency ω_1 . With the set of natural frequencies from (2.36)

$$\frac{\omega_n}{\omega_1} = n^2$$

The mode n associated with limiting stability is found to be relevant to the range

$$n^2(n-1)^2 < (\zeta_{e1}/\zeta_{i1}) < n^2(n+1)^2$$

with the stability criterion

$$\frac{\Omega}{\omega_1} = n^2 + (\zeta_{e1}/\zeta_{i1})/n^2$$

In a non-synchronous whirl general orbit A more general representation of the RID effect as induced by shaft fibres undergoing cyclic stress which is related to the fibre's strain and its rate (2.33), is obtained by considering the variation of the variable R_z —which is the shaft centre deflection at the axial location z of its length l .

$$\varepsilon_z = \varepsilon_o(r/r_o) \cos \gamma \quad , \quad \varepsilon_o = r_o \frac{d^2 R}{dz^2}$$

Since R_z is not constant, then ε_o also varies with time and consequently has a time derivative $d\varepsilon_o/dt$ which results in writing eq. (2.33) in the form

$$\sigma_z = \varepsilon_o \left(\frac{r}{r_o} \right) (E \cos \gamma - \mu \sin \gamma \dot{\gamma}) + \mu \frac{d\varepsilon_o}{dt} \left(\frac{r}{r_o} \right) \cos \gamma$$

which results in bending moments in the radial (denoted by M_R), and cross-radial (or tangential denoted by M_ϕ) directions

$$\begin{aligned} M_R &= \iint_A \sigma_z r \cos \gamma \, dA \\ &= \int_0^{2\pi} \int_0^r \left(\frac{r}{r_o} \right) \left\{ \left(\varepsilon_o E + \mu \frac{d\varepsilon_o}{dt} \right) \cos \gamma - \varepsilon_o \mu \sin \gamma \dot{\gamma} \right\} \cos \gamma \, r^2 \, dr \, d\gamma \\ &= \frac{I}{r_o} \left(\varepsilon_o E + \mu \frac{d\varepsilon_o}{dt} \right) \quad , \\ M_\phi &= \iint_A \sigma_z r \sin \gamma \, dA = -\frac{\varepsilon_o}{r_o} \mu I \dot{\gamma} \end{aligned} \tag{2.37}$$

The radial (restoring) and tangential forces developed per unit length are given by

$$\bar{f}_r = - \left[EI \frac{d^4 R}{dz^4} + \mu I \frac{d^4 \dot{R}}{dz^4} \right] \quad \text{and} \quad \bar{f}_\phi = -\mu I \frac{d^4 R}{dz^4} \dot{\gamma} \quad \text{where} \quad \dot{\gamma} = \Omega - \dot{\phi}$$

The unit tangential force can be either stabilising or destabilising (driving force) depending on whether rotor precession $\dot{\phi}$ is greater or less than the shaft speed Ω

The rotor deflection can be represented by the summation of its modes as

$$R(z) = \sum_{n=1}^{\infty} R_n \sin \frac{n\pi z}{l}$$

In the case of a single-mass (disc) rotor located symmetrically along the shaft axis, the deflection may be approximated by the first mode. The total radial and tangential force acting on the rotor is found by integration over the length of the rotor to obtain

$$f_r = \int_0^l \bar{f}_r dz = - \left(\frac{\pi}{l} \right)^3 EIR_m + \mu I \dot{R}_m \quad \text{and} \quad f_\phi = \left(\frac{\pi}{l} \right)^3 \mu I R_m (\dot{\phi} - \Omega) \quad (2.38)$$

where R_m is the deflection of the rotor mass centre.

2.4.5.2. Joint friction

In order to consider component damping in EOMs, we need the relation between the bending moment and the difference angle along the component. The simplified toothed coupling model of *fig. 2.11* is considered. The same method can be used for spline-couplings and shrink fits and can be modified slightly to deal with Curvic couplings.

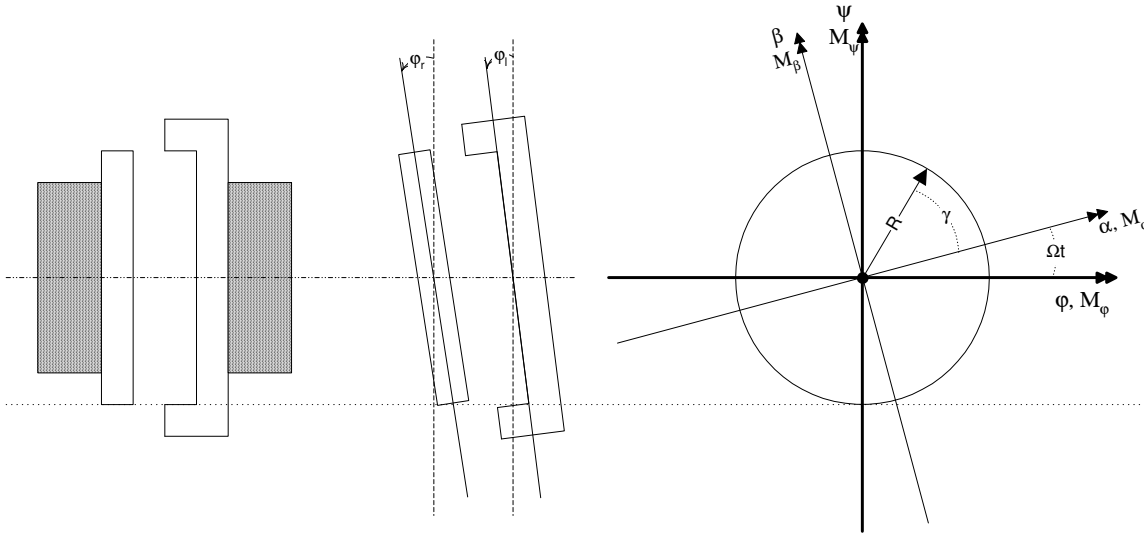


Figure 2.11.: A simplified model, of a rotor coupling, for component damping

Fig.2.11 shows the coupling's two halves in separate sketches. The angles of rotation (tilt) can be different and both will be assumed small and displayed as vectors. The components of the difference angles are $\Delta\varphi = \varphi_r - \varphi_l$ and $\Delta\psi = \psi_r - \psi_l$ the components

2. Review of significant RID research

of the bending moment are shown as M_φ and M_ψ . In the rotating co-ordinate system with angular velocity Ω , the corresponding notations are $\Delta\alpha$, $\Delta\beta$ and M_α, M_β .

Bending moment at the coupling arises from the tooth forces and their distance from the axis of rotation. We assume a linear force-displacement relationship such as applies to a spring and distribute the forces continuously around the circumference of the circle of radius R . For the difference angle γ , the relative displacement at the position R, γ is

$$x_\gamma = \Delta\alpha R \sin \gamma$$

and the elastic displacement force on the arc of length $R d\gamma$ is

$$df = \frac{k}{2\pi} \Delta\alpha R \sin \gamma d\gamma$$

where k is the axial stiffness of all teeth. The moment of this force about rotation axis

$$dM_\alpha = df R \sin \gamma .$$

By integration, the resulting moment is

$$M_\alpha = \int_0^{2\pi} \frac{k}{2\pi} \Delta\alpha (R \sin \gamma)^2 d\gamma = k \frac{R^2}{2} \Delta\alpha .$$

As such, the rotational stiffness is the amount of bending moment produced per unit angle of relative rotation (tilt)

$$\widehat{k} = \frac{M_\alpha}{\Delta\alpha} = k \frac{R^2}{2} \quad (2.39)$$

Viscous damping in joints can be similarly assumed as uniformly distributed over all teeth with a coefficient c_i . Then the moment produced for a rate of change of $\Delta\dot{\alpha}$ is

$$M_{\dot{\alpha}} = c_i \frac{R^2}{2} \Delta\dot{\alpha} = \widehat{c}_i \Delta\dot{\alpha}$$

From the foregoing, the resisting moment to the instantaneous relative angular rotation $\Delta\alpha(t)$ can be expressed as

$$\begin{aligned} M_\alpha &= \widehat{k} \Delta\alpha + \widehat{c}_i \Delta\dot{\alpha} \\ M_\beta &= \widehat{k} \Delta\beta + \widehat{c}_i \Delta\dot{\beta} \end{aligned} \quad (2.40)$$

which represent rotating-frame moment components, or stationary-frame at $\Omega = 0$. In a stationary frame, moment components can be expressed using (2.7) as:

$$\begin{aligned} M_\varphi &= \widehat{k} \Delta\varphi + \widehat{c}_i \Omega \Delta\psi + (\widehat{c}_i + \widehat{c}) \Delta\dot{\varphi} \quad , \\ M_\psi &= \widehat{k} \Delta\psi - \widehat{c}_i \Omega \Delta\varphi + (\widehat{c}_i + \widehat{c}) \Delta\dot{\psi} \end{aligned} \quad (2.41)$$

where \widehat{c} is the coefficient of external damping due to joint rotation. The EOMs cross-coupling reflects the existence of destabilising circulatory *moments* rendering the system potentially unstable, as in the previous case of shaft's linear-viscous material damping.

For absolute stability, work done by all forces and moments must be positive. As an illustration, we can calculate the work done by the above moments over one period of natural vibration. To avoid complications, we will consider the *circular* motion¹ of the

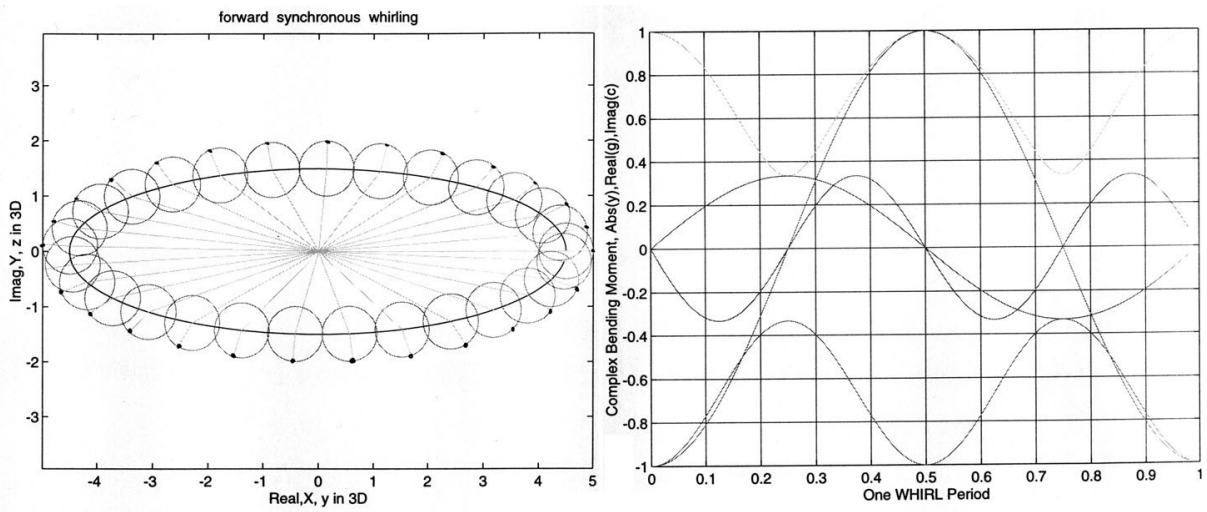


Figure 2.12.: Visual example showing the oscillatory motion of a shaft section relative to the rotating frame of reference and the resulting alternating bending moments

shaft centre with natural frequency ω_n , which results in the following rotations

$$\Delta\varphi = \widehat{\Delta\varphi} \cos \omega_n t \quad , \quad \Delta\psi = \widehat{\Delta\psi} \sin \omega_n t$$

and the work done by the moments in one period is

$$W_v = \int_0^{2\pi/\omega_n} (M_\varphi \Delta\dot{\varphi} + M_\psi \Delta\dot{\psi}) dt = 2\pi (\widehat{c}_i + \widehat{c}) \omega_n - \widehat{c}_i \Omega \widehat{\Delta\varphi}^2$$

¹with circular motion, the coupling (or shaft) experiences only one frequency ($\Omega - \omega_n$), as opposed to multiple frequencies (at least two, as in the case of a simple elliptic motion) when motion is not circular, and hence the damping force cannot be expressed simply in the case of viscous damping. Circular motion occurs if both the rotor and stator are perfectly symmetric and no gravity force functional; a situation that is not possible practically.

2. Review of significant RID research

With stability assured for positive W_v , its borderline is encountered at rotation speed

$$\Omega_{th} = \frac{\widehat{c}_i + \widehat{c}}{\widehat{c}_i} \omega_n$$

Speeds above Ω_{th} will cause the work done W_v by the moments to be negative, hence rendering the system (forward rotational mode) unstable. The above equation is similar to the ineq. (2.16) for the stability of the forward lateral vibration mode.

Friction damping in joints resulting from the relative motion (rotation) of coupling parts also can have a destabilising effect on rotor motion. Considering the (simplest) Coulomb RID model in a one-dimensional element, we have the force arising from a relative displacement $x(t) = \widehat{x} \sin \omega t$ expressed as

$$f(t) = \mathcal{F}_c \operatorname{sgn}(\dot{x})$$

with \mathcal{F}_c being a constant doing work W_c over one period expressed as

$$W_c = 4\mathcal{F}_c \widehat{x}$$

Similarly, the friction-induced moments due to relative rotation $\Delta\alpha$ at a joint are

$$M_\alpha(t) = M_c \operatorname{sgn}(\Delta\dot{\alpha})$$

and the work dissipated over one period is

$$W_c = 4M_c \widehat{\Delta\alpha}$$

For a flexible toothed coupling with a dry friction coefficient μ that is loaded by a turning moment M_T (producing normal forces on the teeth) and that experiences a relative axial displacement $x(t)$, the resulting axial friction force from all the teeth is

$$f(t) = \mu \frac{M_T}{R} \operatorname{sgn}(\dot{x})$$

For rotational vibration of this flanged coupling, we have the relative vibration velocities of the two halves as $\dot{\alpha}$ and $\dot{\beta}$ (in the rotating frame) resulting in a relative axial velocity \dot{x}_γ at the point on the circumference described by the angle γ and expressed as

$$\dot{x}_\gamma = R(\Delta\dot{\alpha} \sin \gamma - \Delta\dot{\beta} \cos \gamma) = R\sqrt{\Delta\dot{\alpha}^2 + \Delta\dot{\beta}^2} \sin(\gamma - \vartheta)$$

where

$$\cos \vartheta = \frac{\Delta \dot{\alpha}}{\sqrt{\Delta \dot{\alpha}^2 + \Delta \dot{\beta}^2}} \quad , \quad \sin \vartheta = \frac{\Delta \dot{\beta}}{\sqrt{\Delta \dot{\alpha}^2 + \Delta \dot{\beta}^2}}$$

by which \dot{x}_γ is: negative for $0 < \gamma < \vartheta$, positive for $\vartheta < \gamma < \pi + \vartheta$ and negative again for $\pi + \vartheta < \gamma < 2\pi$. Assuming uniformly distributed friction force at the teeth around the circumference, then for an element of arc this force is:

$$df = \frac{\mu M_T}{2\pi R} \operatorname{sgn}(\dot{x}_\gamma) d\gamma$$

which leads to the following components of moment in the rotating frame of reference

$$M_\alpha = \mu \frac{M_T}{2\pi} \int_0^{2\pi} \operatorname{sgn}(\dot{x}_\gamma) \sin \gamma d\gamma \quad , \quad M_\beta = -\mu \frac{M_T}{2\pi} \int_0^{2\pi} \operatorname{sgn}(\dot{x}_\gamma) \cos \gamma d\gamma$$

which—in accordance with the sign of \dot{x}_γ —on performing the integration result in

$$M_\alpha = \frac{2}{\pi} \mu M_T \cos \vartheta \quad , \quad M_\beta = \frac{2}{\pi} \mu M_T \sin \vartheta$$

or on using the values for $\cos \vartheta$ and $\sin \vartheta$ results in

$$M_\alpha = \frac{2}{\pi} \mu M_T \frac{\Delta \dot{\alpha}}{\sqrt{\Delta \dot{\alpha}^2 + \Delta \dot{\beta}^2}} \quad , \quad M_\beta = \frac{2}{\pi} \mu M_T \frac{\Delta \dot{\beta}}{\sqrt{\Delta \dot{\alpha}^2 + \Delta \dot{\beta}^2}} \quad (2.42)$$

Moments M_φ and M_ψ in the stationary frame are obtained by applying transformation (2.7) to the (above) moments in the rotating frame of reference, i.e. exchange

$$\Delta \dot{\alpha} = \Delta \dot{\varphi} + \Omega \Delta \psi \quad , \quad \Delta \dot{\beta} = \Delta \dot{\psi} - \Omega \Delta \varphi \quad .$$

The resulting moments will be

$$\begin{aligned} M_\varphi &= \frac{2}{\pi} \mu M_T \frac{\Delta \dot{\varphi} + \Omega \Delta \psi}{\sqrt{(\Delta \dot{\varphi} + \Omega \Delta \psi)^2 + (\Delta \dot{\psi} - \Omega \Delta \varphi)^2}} \\ M_\psi &= \frac{2}{\pi} \mu M_T \frac{\Delta \dot{\psi} - \Omega \Delta \varphi}{\sqrt{(\Delta \dot{\varphi} + \Omega \Delta \psi)^2 + (\Delta \dot{\psi} - \Omega \Delta \varphi)^2}} \end{aligned} \quad (2.43)$$

which exhibits a cross-coupling of the term $\Omega \Delta \varphi$, which will result in the potentially destabilising circulatory forces in analogy with (2.41).

Moments M_φ and M_ψ are nonlinear in their velocities, thus are not readily amenable to the linear stability analysis (e.g. Routh-Hurwitz criteria or eigen value examination) customary for LTI systems e.g. (2.13). Two approaches are customary in such case: a)

Implement numerical time integration to the system-governing nonlinear EOMs with the nonlinearities from the joints separated from the linear rotordynamic system, and residing on the right-hand side of the EOMs as nonlinear forcing functions. b) Use equivalent viscous damping coefficients to be plugged in the EOMs similar to eqs. (2.41). It has been shown that the work done by the friction moment over one period is $W_c = 4M_c \widehat{\Delta\alpha}$, and the work done by the viscous damping moment (expressed in terms of $\widehat{\Delta\alpha}$) is $W_{v_\alpha} = \pi \widehat{d} \omega \widehat{\Delta\alpha}$. With $M_c = \frac{2}{\pi} \mu M_T$, the equivalent dry friction coefficient is

$$\widehat{c}_c = \frac{4M_c}{\pi \omega \widehat{\Delta\alpha}} = \frac{8}{\pi^2} \mu \frac{M_T}{\omega \widehat{\Delta\alpha}}$$

or on using \widehat{x} at the radius R as

$$\widehat{c}_c = \frac{8}{\pi^2} \mu \frac{M_T R}{\omega \widehat{x}}$$

which can be plugged in eqs. (2.41) instead of \widehat{c}_i and apply the same stability analysis, the Routh-Hurwitz criterion or check the decay coefficient of the eigen values for stability conditions. The above expressions for \widehat{c}_c are rather questionable due to the uncertainties in ω and $\widehat{\Delta\alpha}$ (i.e. $\frac{\widehat{x}}{R}$). However, they can provide a rough first estimate of stability.

2.4.6. Industrial tools

Lund (1974) was arguably the first to include the RID destabilising effect in a realistic rotor-bearing system analysis. He extended the Myklestad-Prohl transfer matrix method (for critical speed calculation) to examine eigenvalues of the system which would incorporate journal bearings, internal (shaft) damping, aerodynamic excitation, etc. He represented the effect of hysteretic RID as an angle α (2.45) by which the stress leads the strain, and to which the energy dissipated is proportional. For current industrial applications however, incorporating joint RID in stiffness matrices of rotordynamic FEA is more realistic, even with viscous RID, and far more straightforward—see [47, 86].

2.4.6.1. Linear material damping representation in rotating beam FEA

Building on Lund's work, E. S. Zorzi, who was interested in RID, and H. D. Nelson, who had just published one of the first papers (1975) on rotor FEA, published a paper (1976) incorporating RID in Nelson's FE model via a constitutive (stress-strain) law. This law (2.46) known widely as Nelson's model, has viscous as well as hysteretic RID coefficients, and is utilised extensively in industrial FE routines. Adopting and building on Nelson's work, L. W. Chen and D. M. Ku developed (1991) a C^0 three-node isoparametric rotor finite element—as opposed to the C^1 two-node element—based on the Timoshenko beam. Their derived strain energy dP^e and dissipation function dD^e of a differential element—

ignoring transverse shear deformation—are stated here. Nelson’s model and conclusions are presented briefly from these two papers; and criticised for their limitations.

The EOM for the *undamped* rotor element without axial load is written as:

$$([M_T] + [M_R])\{\ddot{q}\} - \Omega[G]\{\dot{q}\} + ([K^e] - [A])\{q\} = \{Q_c\} \cos \Omega t + \{Q_s\} \sin \Omega t \quad (2.44)$$

where the 8×8 element matrices are: $[G]$ the skew symmetric gyroscopic matrix, $[M_T]$ the translational mass matrix, $[M_R]$ the rotary mass matrix, $[K^e]$ the stiffness matrix.

Nelson’s RID model has linear viscous RID simply represented by coefficient η_v , and hysteretic RID expressed by the loss factor η_h , which is related to the loss angle α_h :

$$\sin(\alpha_h) = \frac{\eta_h}{\sqrt{1 + \eta_h^2}} \quad (2.45)$$

Combined, the two RID models yield the axial stress-strain constitutive relationship:

$$\sigma_z = E \left\{ \frac{\varepsilon_z}{\sqrt{1 + \eta_h^2}} + \left(\eta_v + \frac{\eta_h}{\sqrt{1 + \eta_h^2}} \right) \dot{\varepsilon}_z \right\} \quad (2.46)$$

Incorporation Nelson’s model in (2.44) yields the moment-curvature relationships:

$$\begin{aligned} \begin{Bmatrix} M_x \\ M_y \end{Bmatrix} &= & (2.47) \\ EI \begin{bmatrix} \frac{1+\eta_h}{\sqrt{1+\eta_h^2}} & \left(\eta_v \Omega + \frac{\eta_h}{\sqrt{1+\eta_h^2}} \right) \\ \left(\eta_v \Omega + \frac{\eta_h}{\sqrt{1+\eta_h^2}} \right) & -\frac{1+\eta_h}{\sqrt{1+\eta_h^2}} \end{bmatrix} \begin{Bmatrix} u'' \\ v'' \end{Bmatrix} &+ EI \begin{bmatrix} \eta_v & 0 \\ 0 & -\eta_v \end{bmatrix} \begin{Bmatrix} \dot{u}'' \\ \dot{v}'' \end{Bmatrix} \end{aligned}$$

Coupled response in the x-z and y-z planes is clear through viscous and hysteretic RID effects; while viscous RID velocity-dependence produces additional de-coupled moment.

The Lagrangian EOM can be established for the damped finite rotating shaft element:

$$([M_T] + [M_R])\{\ddot{q}\} + (\eta_v[K^e] - \Omega[G])\{\dot{q}\} + (\eta_a[K^e] + \eta_b[K_c])\{q\} = \{Q(t)\} \quad (2.48)$$

where

$$[\eta] = \begin{bmatrix} \eta_a & \eta_b \\ -\eta_b & \eta_a \end{bmatrix} ; \quad \eta_a = \frac{1 + \eta_h}{\sqrt{1 + \eta_h^2}} ; \quad \eta_b = \eta_v \Omega + \frac{\eta_h}{\sqrt{1 + \eta_h^2}}$$

and

$$[K_c] = \int_0^l EI [\Gamma']^T \begin{bmatrix} 0 & 1 \\ -1 & 0 \end{bmatrix} [\Gamma'] ds$$

It is in this circulatory matrix $[K_c]$, where the RID-induced instability is characterised. These authors' results show that hysteretic RID is destabilising at all speeds; and that all FWD modes are unstable, while all BWD modes are stable, if only hysteretic RID is defined, since including viscous RID introduces the stabilising term $\eta_v[K^e]$.

2.4.6.2. Limitations of, and reservations on Nelson's model

There are several reservations regarding Nelson's work, most notably: The destabilising effect of hysteretic RID at all speeds.

The erroneous conclusion that a hysteretic RID model will cause instability as soon as rotation commences, is due to the invariant sign of the hysteretic angle α_h (2.45) at speeds above, and below the natural frequency of the mode concerned. An example of appropriate implementation is (2.32).

The nonfactual claim that Dimentberg (1959) reached the same conclusion about the destabilising effect of hysteretic RID at all speeds. Dimentberg states, very clearly, that hysteretic RID can be destabilising above the critical speed only, along with a condition of an insufficient stabilising external damping; which, if exists, the rotor will be always stable. Also, Dimentberg did not use an angle α_h (the cause of this erroneous conclusion) to characterise hysteretic RID; in fact his model was similar to that of (2.25) used by Tondl (1963) which stemmed from Dimentberg's model.

The constitutive law assumed resembles Dimentberg's (1959) summation of both hysteretic and viscous damping coefficients in one of his expressions for the threshold speed of instability; which was presented for illustrative purposes only. However, this constitutive law is rather un-orthodox, because it combines the constitutive differential equation of viscous damping with a FR model of hysteretic damping.

Deriving bending moments from anelastic stress-strain relations does not account for the fact that hysteretic RID will be inoperative when stresses are time-invariant (synchronous circular precession) and a destabilising EOMs cross-coupling will be in effect regardless. Tondl (1963) had overcome this hurdle by multiplying the hysteretic damping force by the nondimensional term $\dot{\zeta}/|\dot{\zeta}|$ (2.18) thus insuring hysteretic RID is inoperative and does not affect the EOMs when there is no shaft flexing.

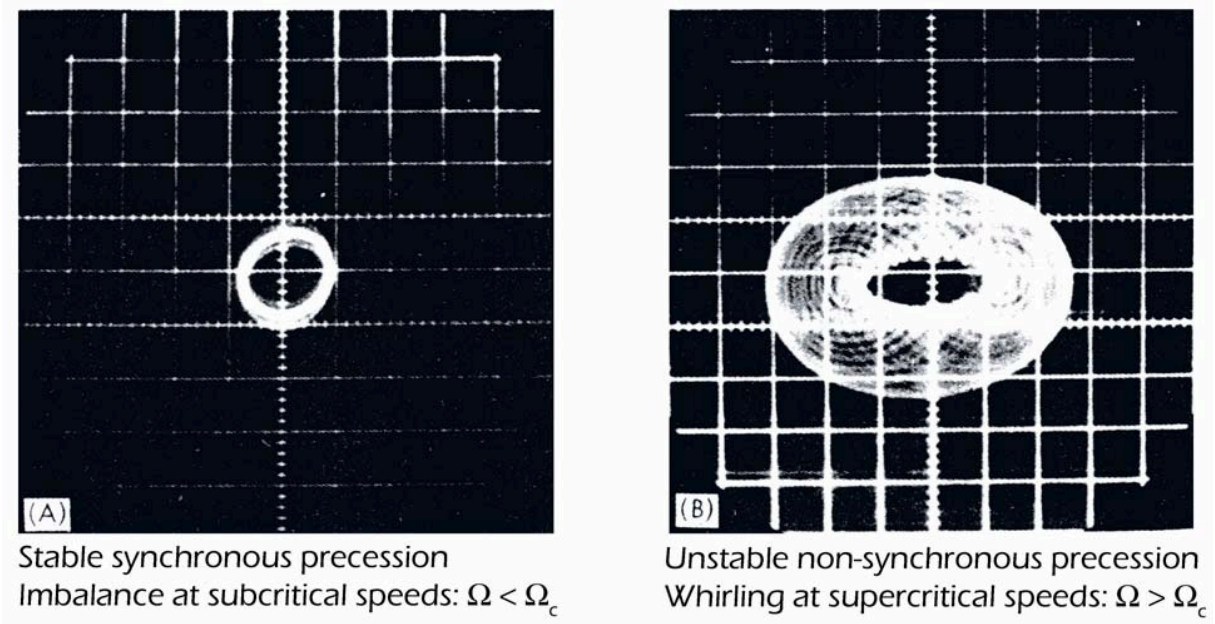


Figure 2.13.: Oscilloscope pictures of the stable and unstable (bounded self-induced whirling) motions below and above the threshold of instability respectively

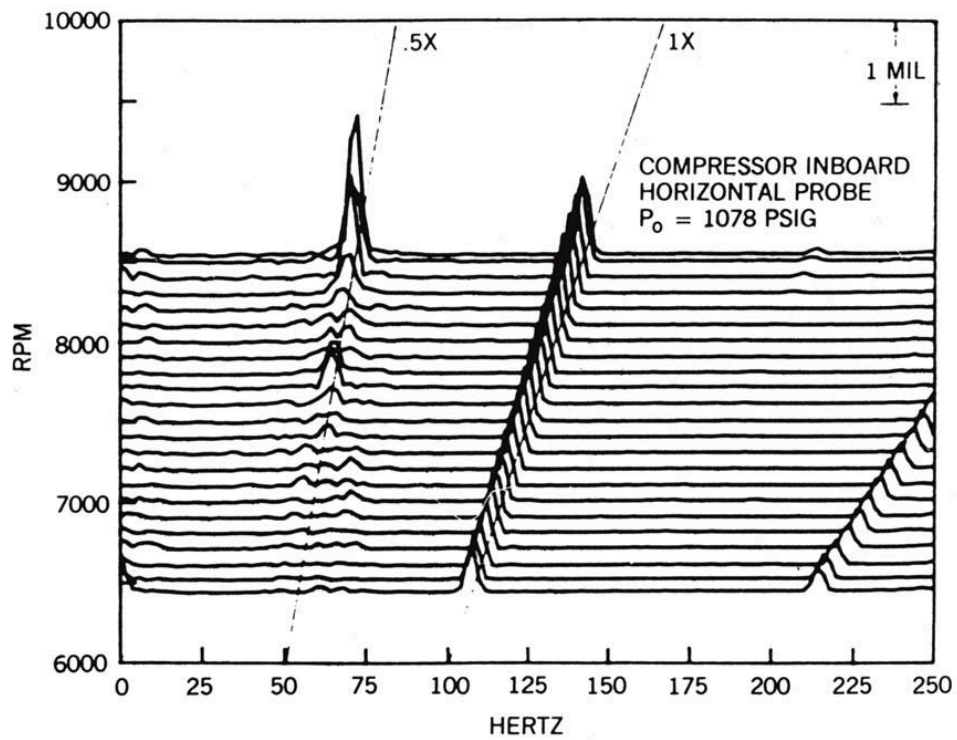
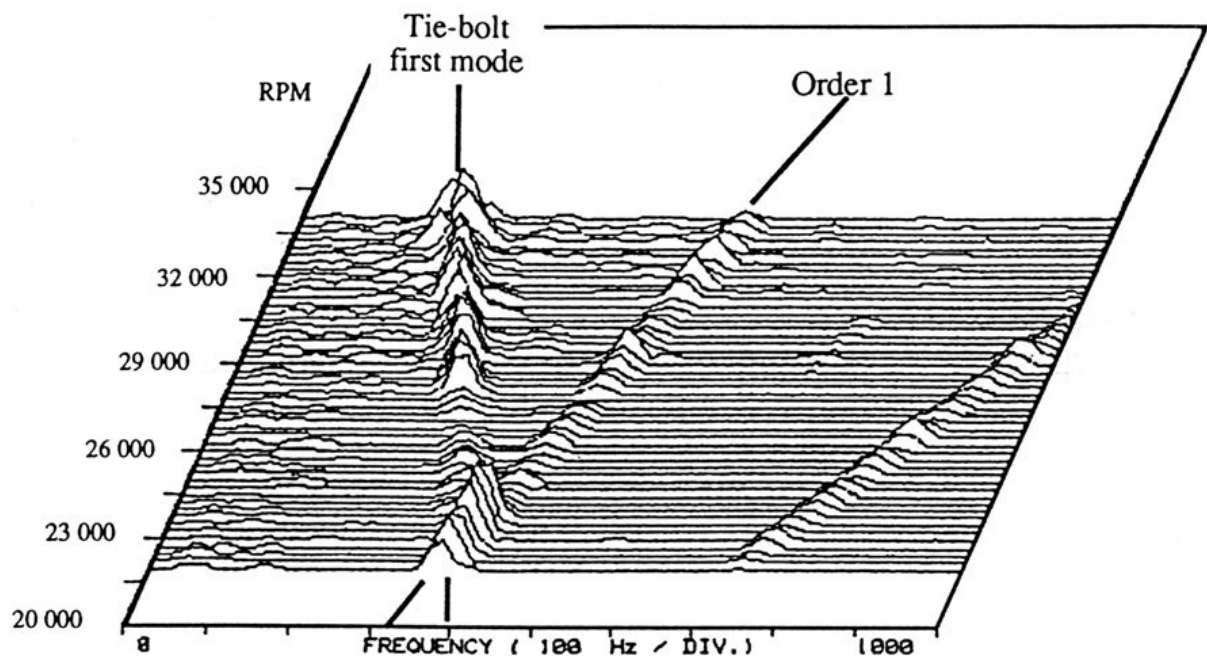


Figure 2.14.: A waterfall plot of a typical industrial rotordynamic instability



Waterfall plot taken off a strain gauge on the tie-bolt of TURBOMECA's engine during a run up. Whirling is at tie-bolt first bending frequency.

Figure 2.15.: Spline coupling RID-induces whirling of the MAKILA engine tie-bolt

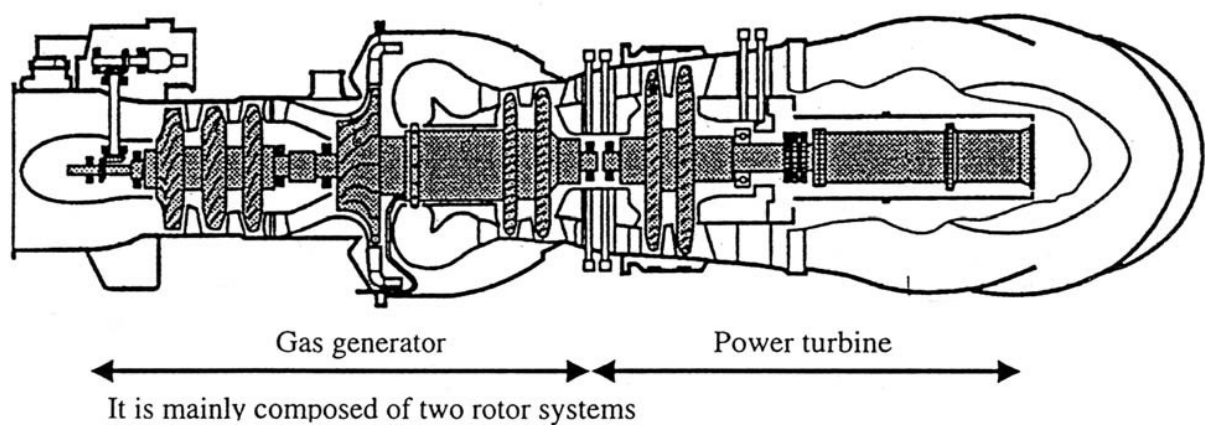


Figure 2.16.: The MAKILA engine main components

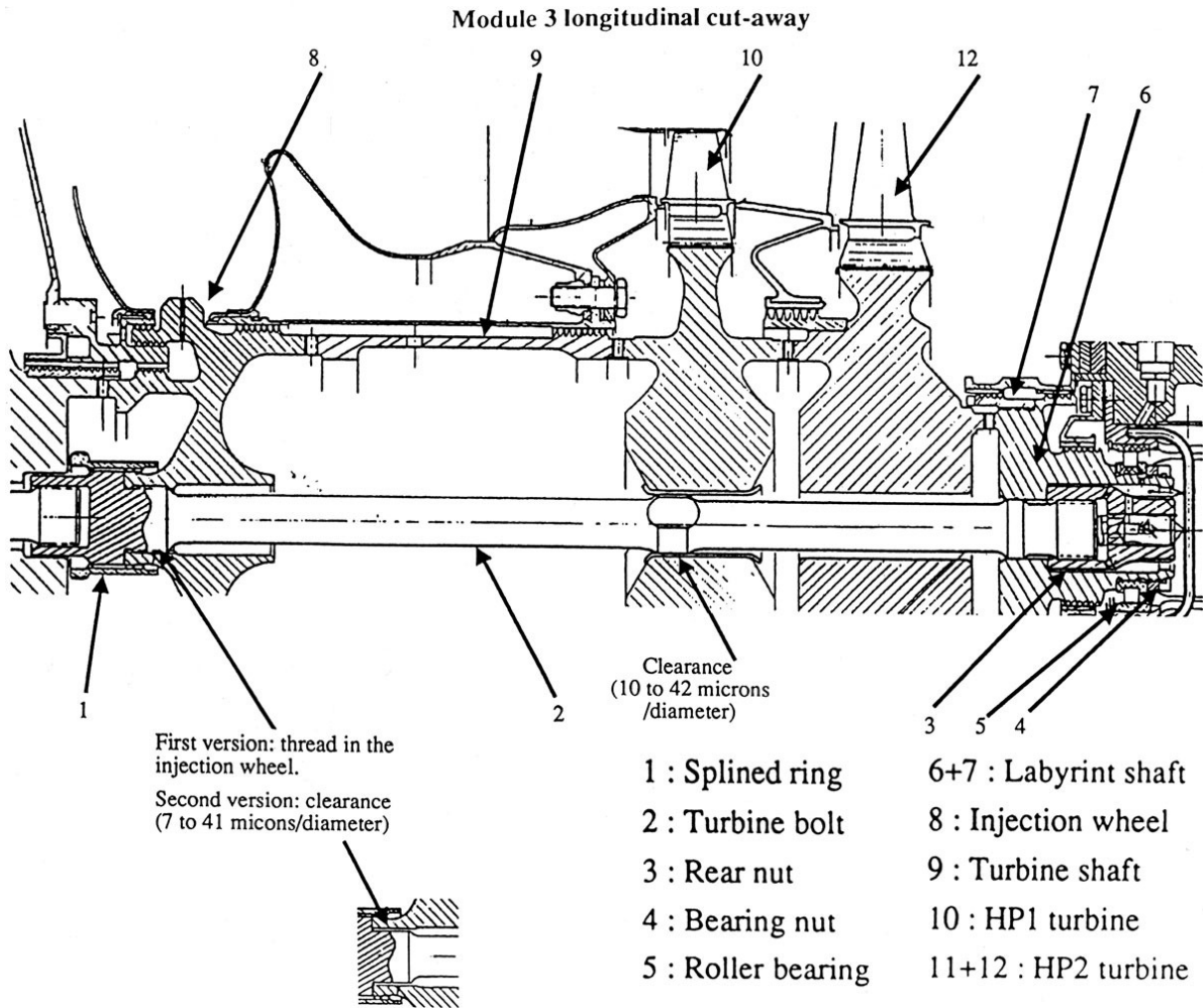


Figure 2.17.: Tie-bolt of the MAKILA engine at turbine section

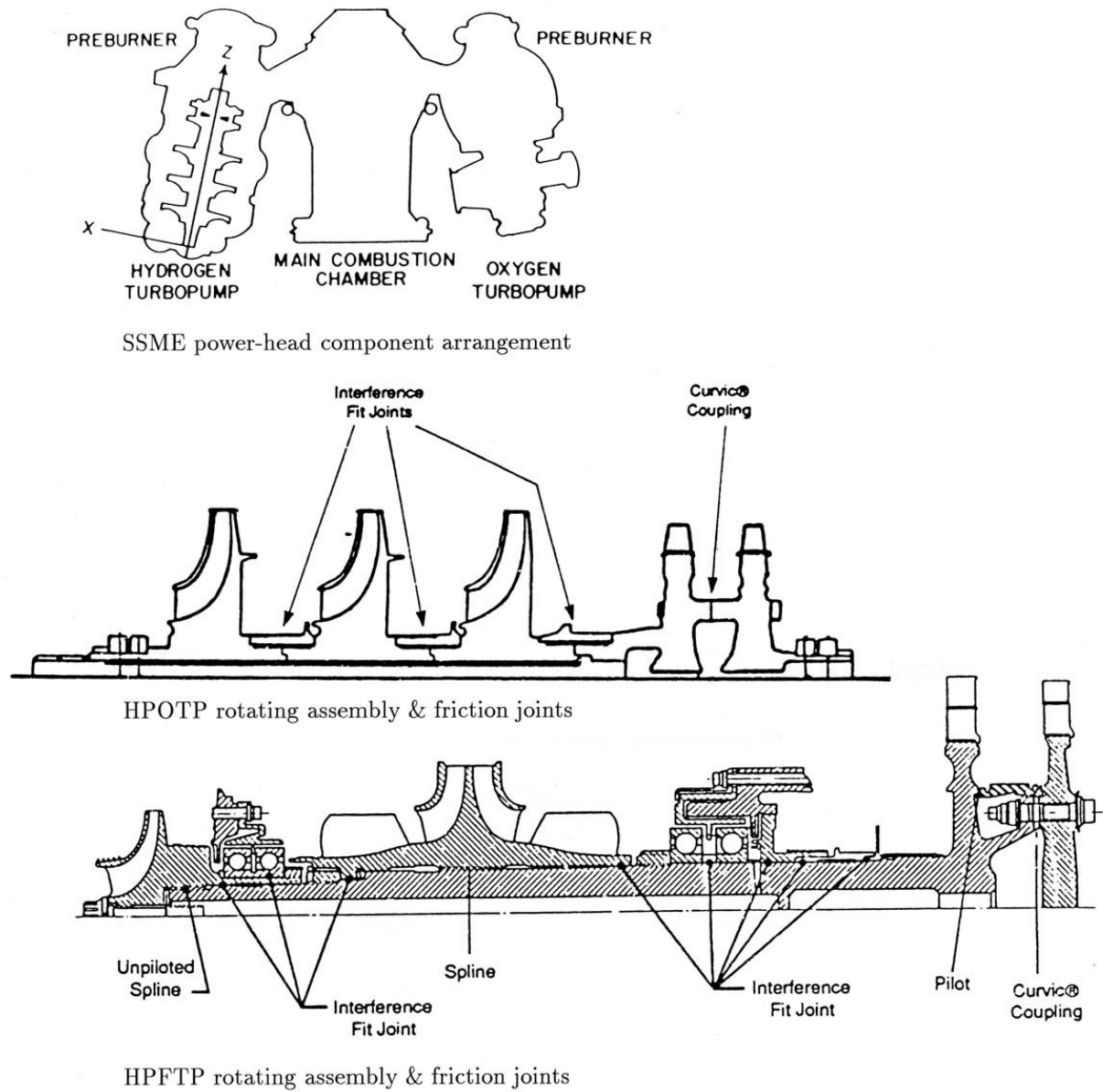
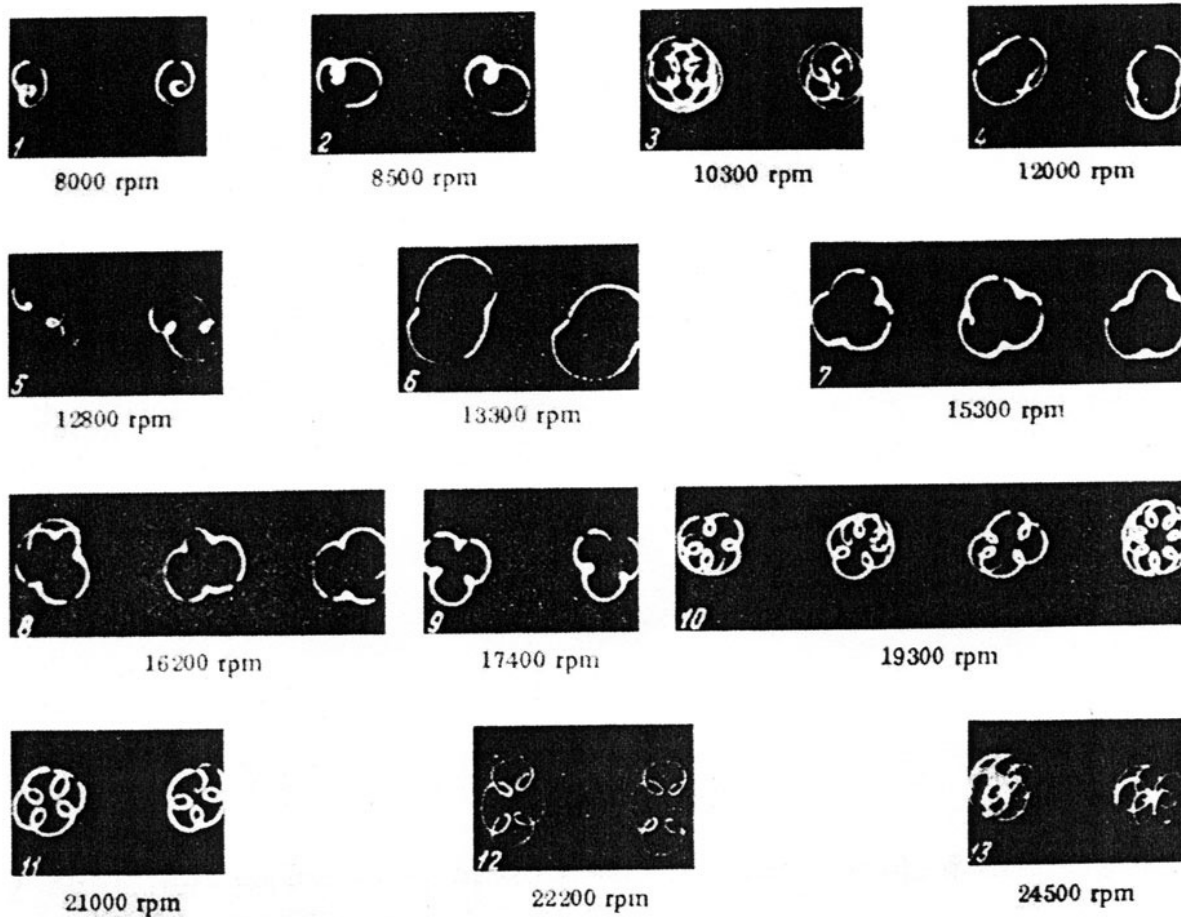
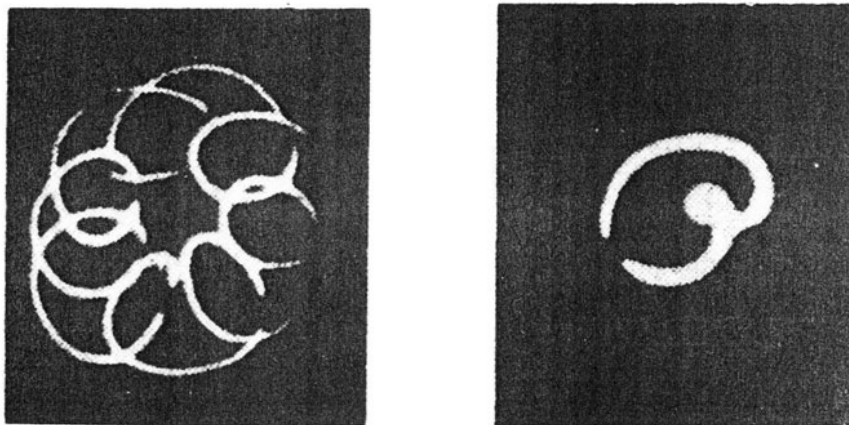


Figure 2.18.: Friction producing joints in the SSME turbines

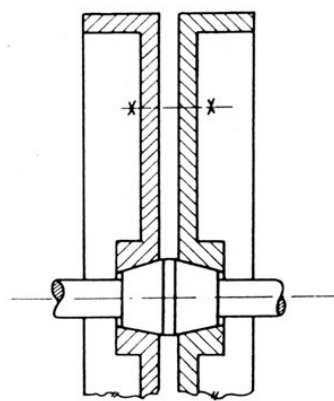


RID whirling at quasi-constant frequency over a wide range of speeds. Between 8000-8500 rpm the orbit has one stationary internal loop. At 12800 and 21000 rpm, the orbit has 2 and 4 internal loops respectively.

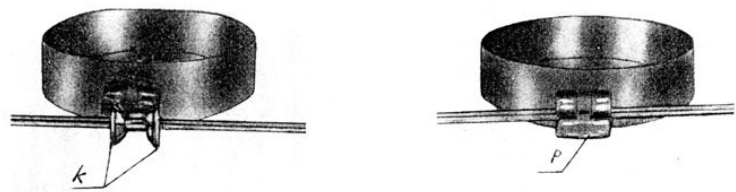


Abrupt jump of RID whirling frequency on increased speed:
From almost 1st FWD mode frequency to almost that of 2nd FWD mode

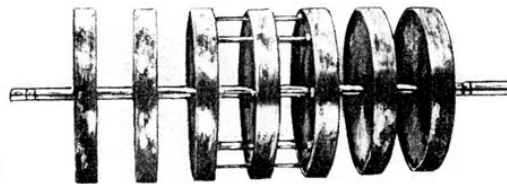
Figure 2.19.: Photographs of whirling rotor (textile spindle) orbits, above critical speed RID from a long shrink-fit. Speed: 4300 rpm; above instability threshold (Kushul, 1965)



Split disc on conical hub

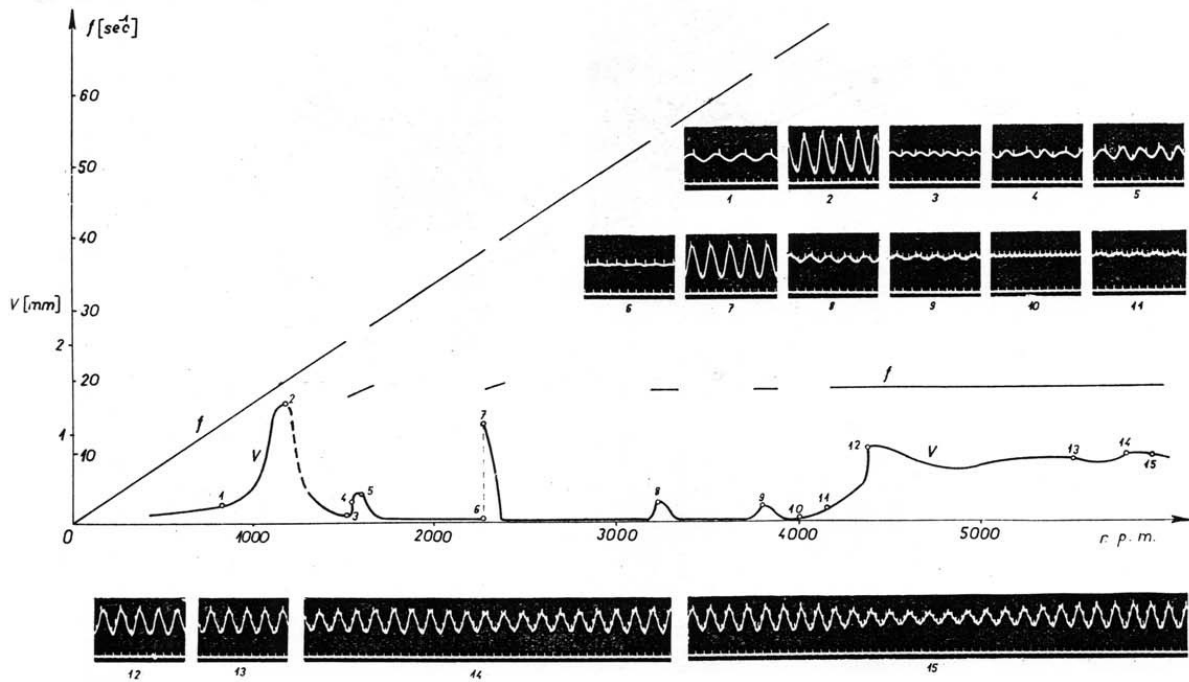


Sleeve on two small ring-like discs

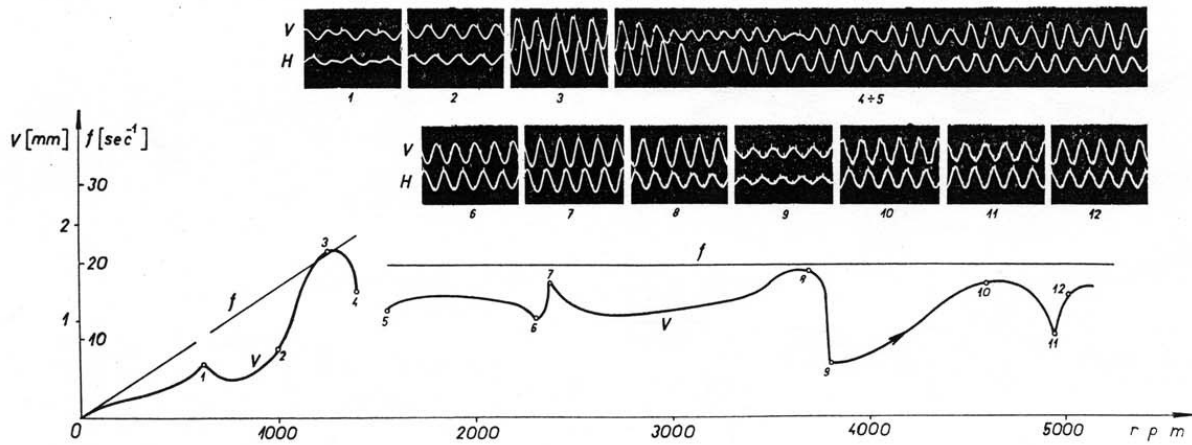


Seven-disc rotor with loose rods between central discs producing friction

Figure 2.20.: Tondl's experimental Rotors



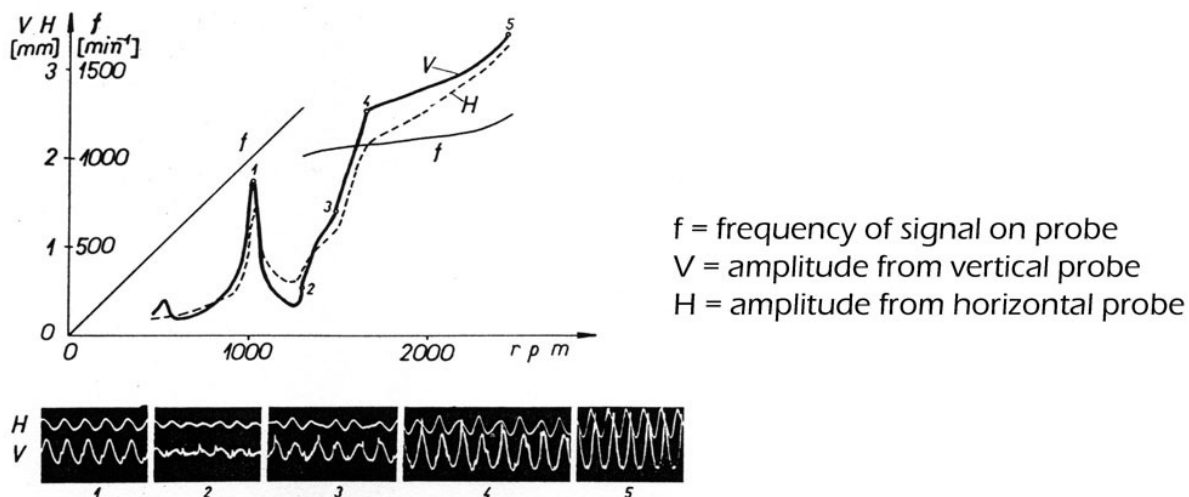
The sustained precession is set-up above 4000 rpm



The unfavourable effect of rapid acceleration after resonance: elevated amplitude of precession and lower speed for the set-up of sustained precession.

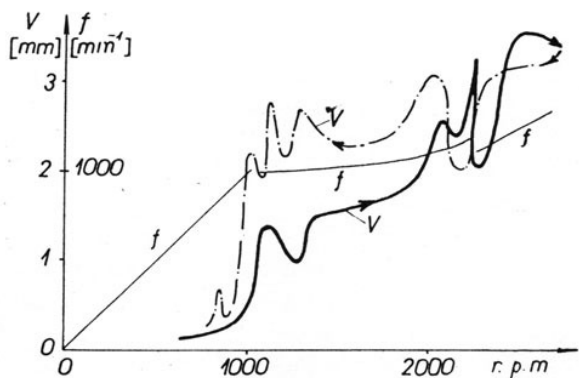
Figure 2.21.: Tondl, 1965: Friction RID whirling frequency's varying amplitude with rpm Rotor with central disc shrunk-on imperfectly. Measurements were not highly repeatable due to fabrication imperfection and wearing affecting friction forces. [V : signal in the vertical direction, H : signal in the horizontal direction, f : frequency of the signal. Notches on the signal pictured off the oscilloscope are from the speed-indicating marker on the rotating rotor]

2. Review of significant RID research



f = frequency of signal on probe
 V = amplitude from vertical probe
 H = amplitude from horizontal probe

Slow acceleration after critical speed. Increased whirling amplitude in both plane axis.



The unfavourable effects of acceleration and deceleration on whirling amplitude.
 The different whirling amplitude path whilst accelerating and decelerating.

Figure 2.22.: Tondl, 1965. Varying frequency and amplitude of friction RID precession when gyroscopes are effective—rotor with seven discs
 f : frequency of the signal from the vertical probe.

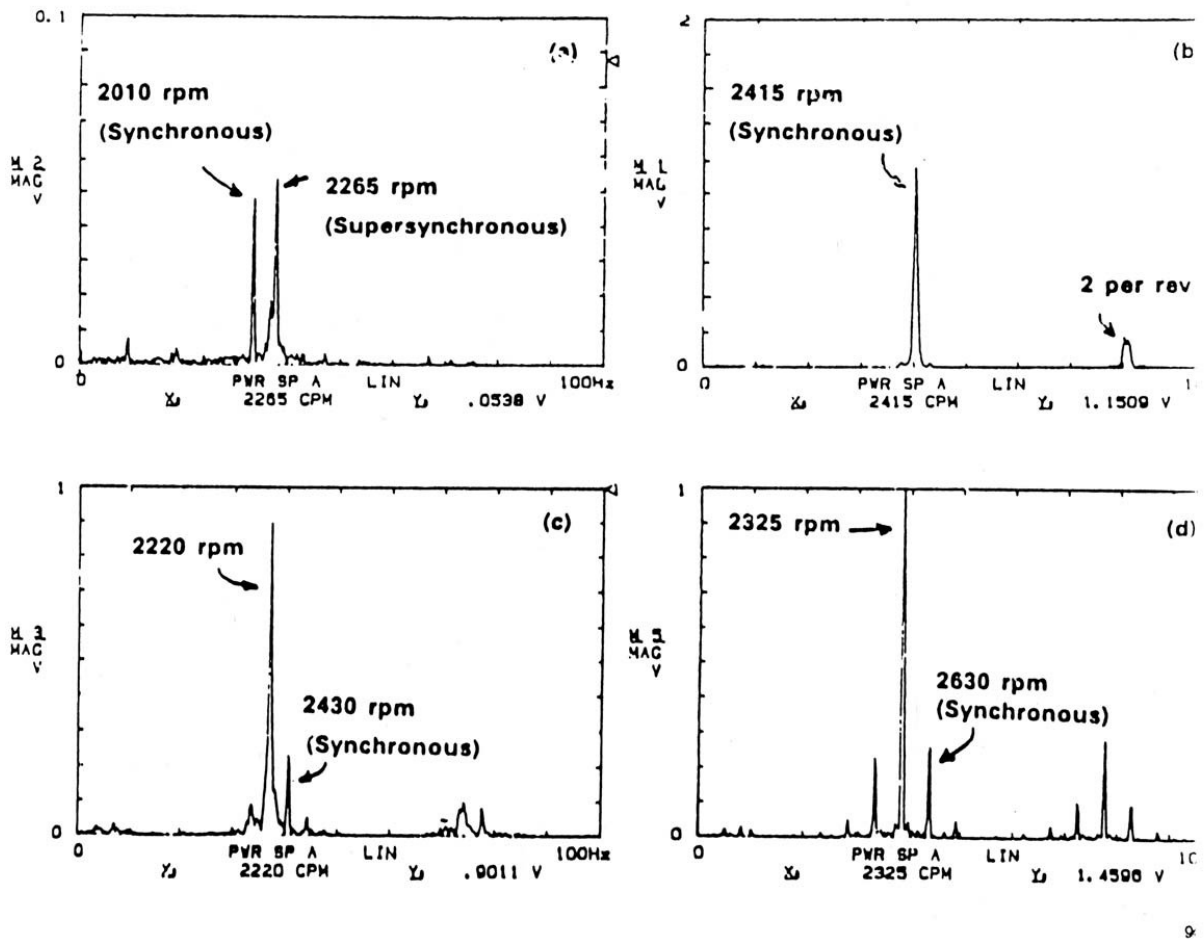


Figure 2.23.: MTI, 1990. FFT plots showing the sub and supercritical operation of rotor-dynamic test rig with axial spline
Critical speed 2200-2300. a) Sub-critical operation showing the supersynchronous excitation of the natural frequency. b) Super-critical operation with no subsynchronous component. c) Subsynchronous instability sets in after a small increase in speed. d) Change of the subsynchronous component frequency due to the spline coupling loose characteristics.

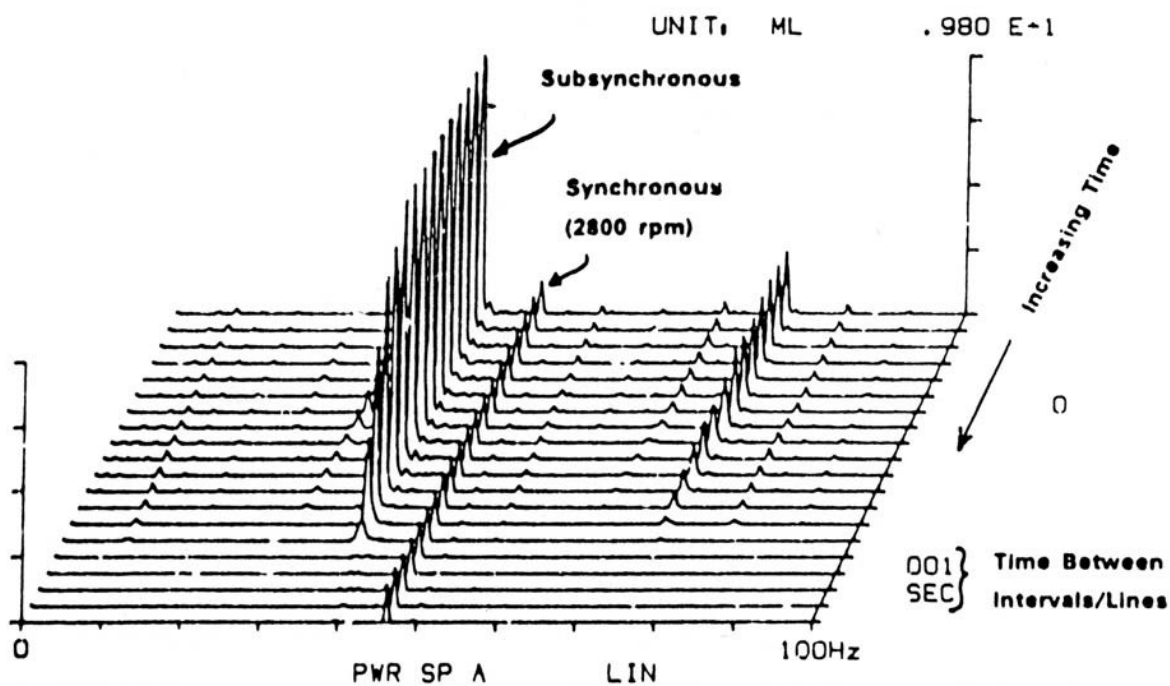
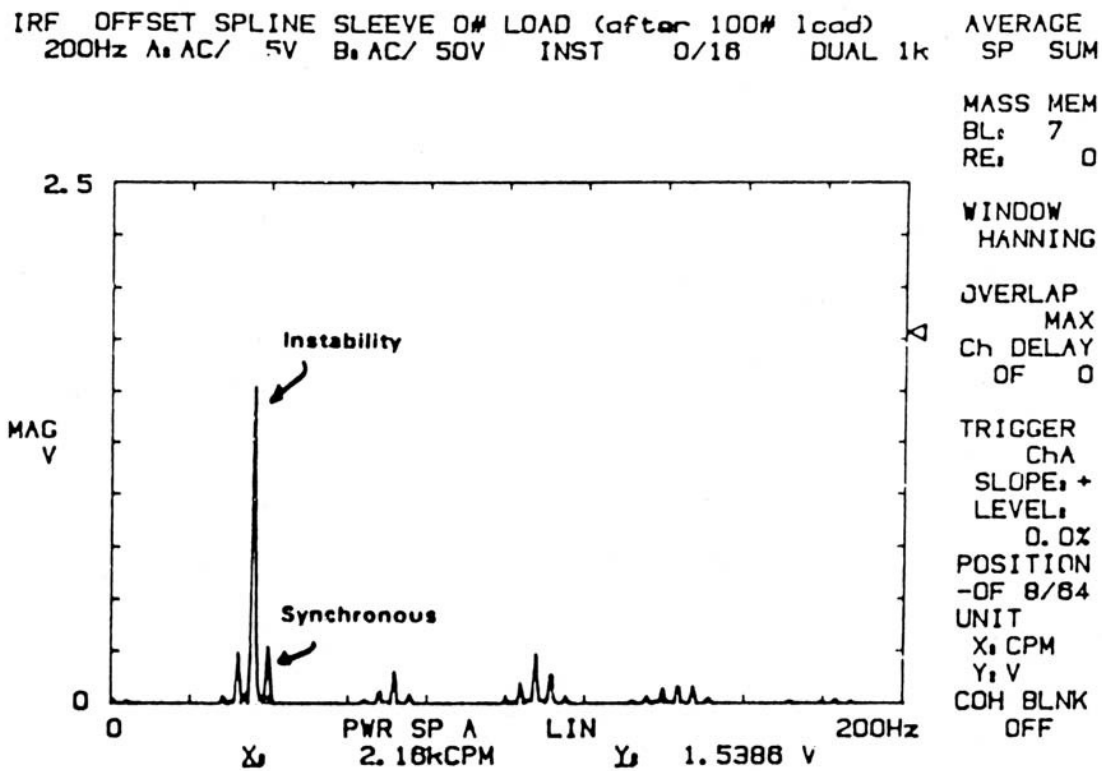


Figure 2.24.: MTI, 1990. Waterfall plot showing the varying amplitude of instability — loss of spline friction
 Above, FFT showing RID instability at the supercritical speed 2800 rpm.

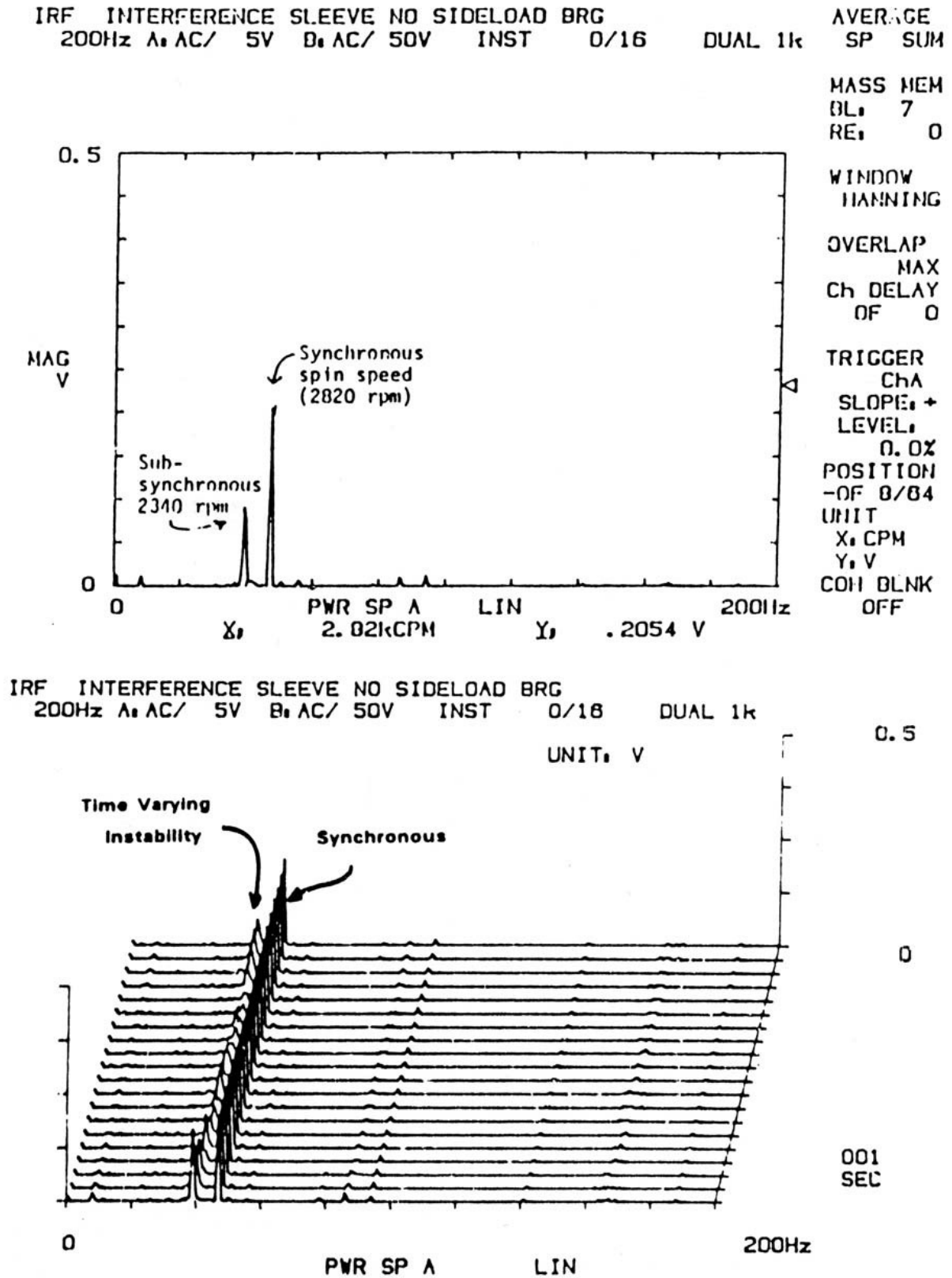


Figure 2.25.: MTI 1990. FFT & waterfall plot showing the time varying nature of the interference-fit-induced subsynchronous vibrations

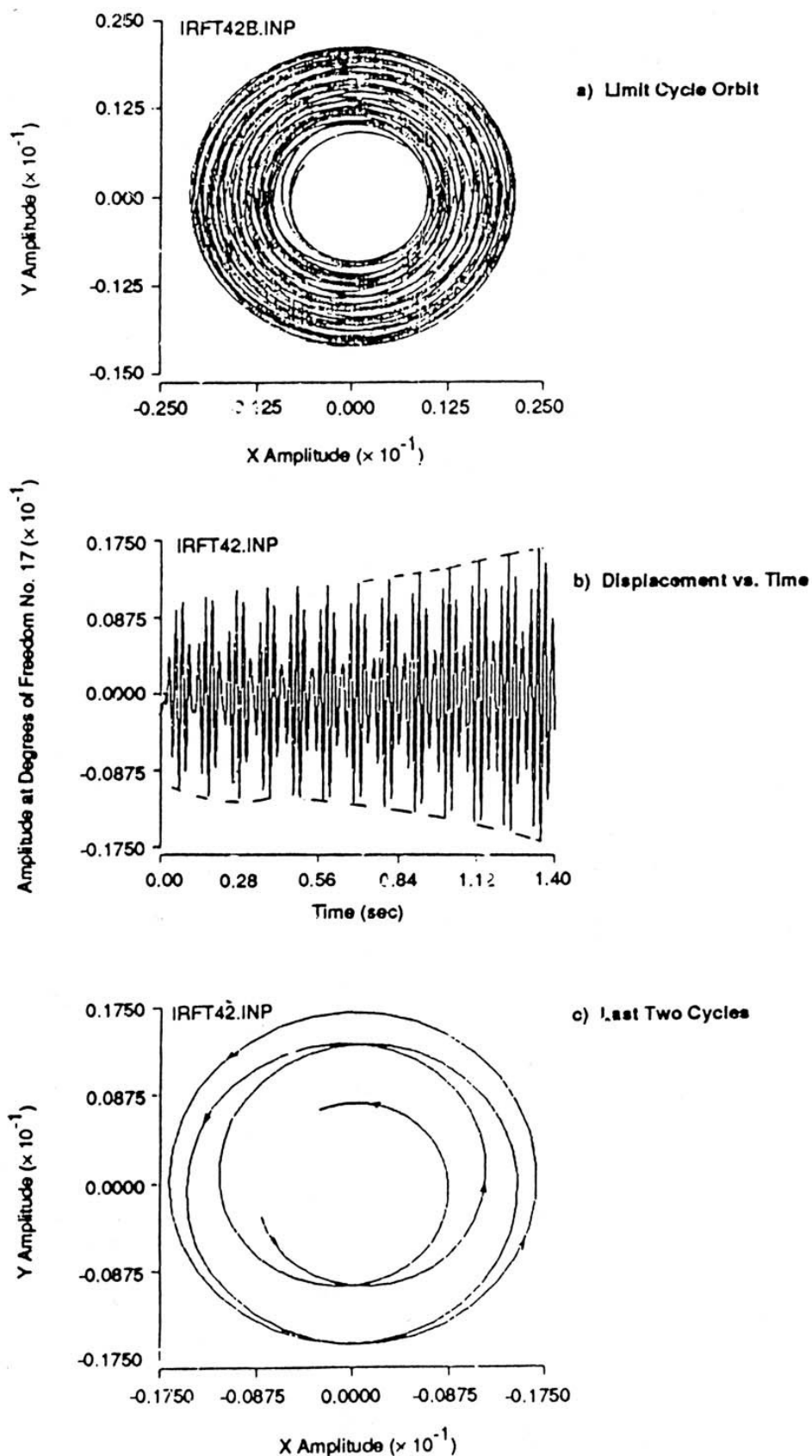


Figure 2.26.: MTI, 1990; Time transient analysis for predicting the motion of the rotor-dynamic test rig with axial spline coupling

A Coulomb friction model for RID is used. Rotor response settled into a limit cycle orbit alternating between an inner and an outer circle as it precessed

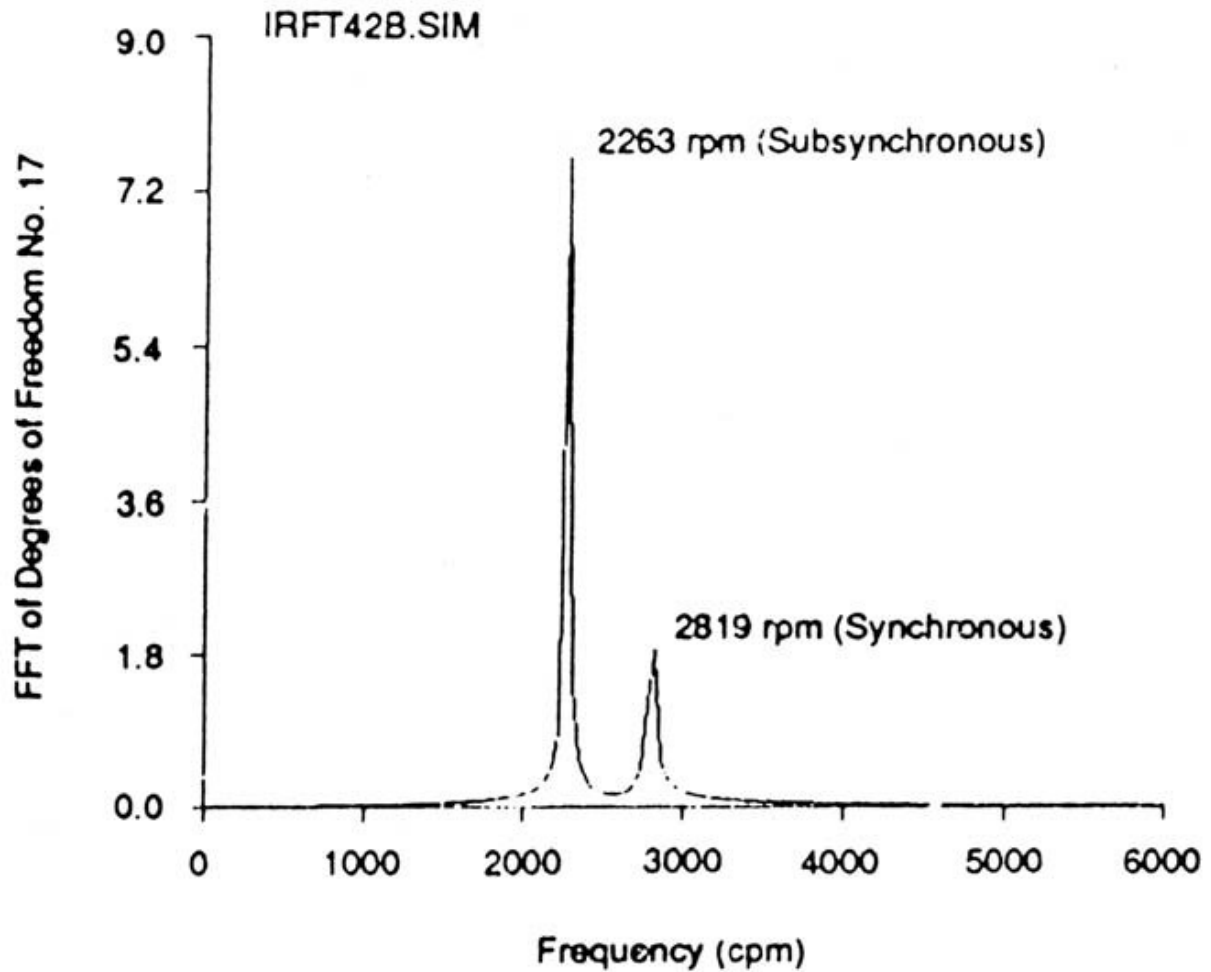


Figure 2.27.: MTI, 1990; Predicted FFT plot based on the time transient analysis of the rotordynamic test rig with the axial spline coupling

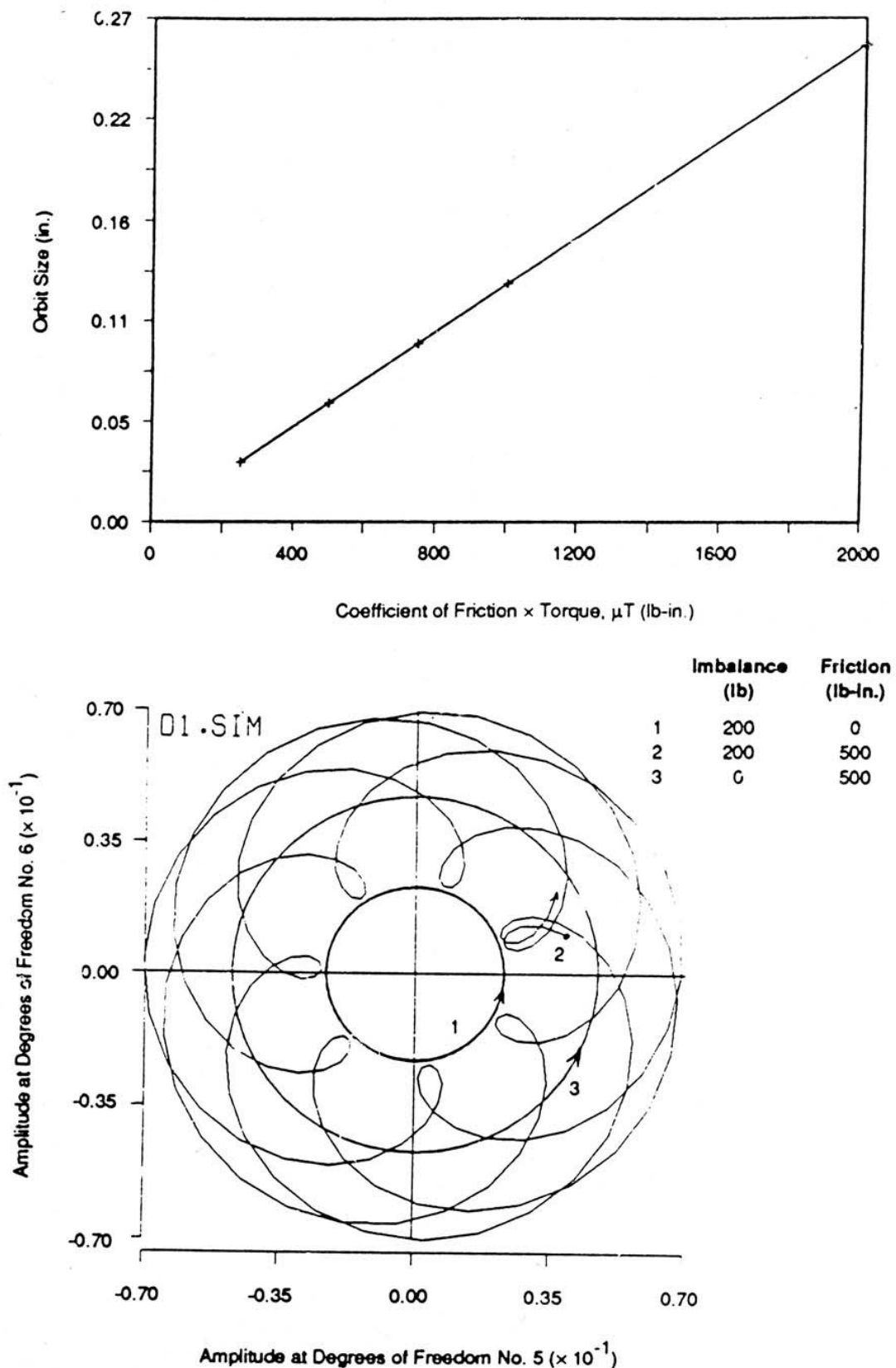


Figure 2.28.: MTI, 1990. The effect of imbalance and friction-torque product on the limit cycle orbits
Time marching predictions for the spline-coupling model.

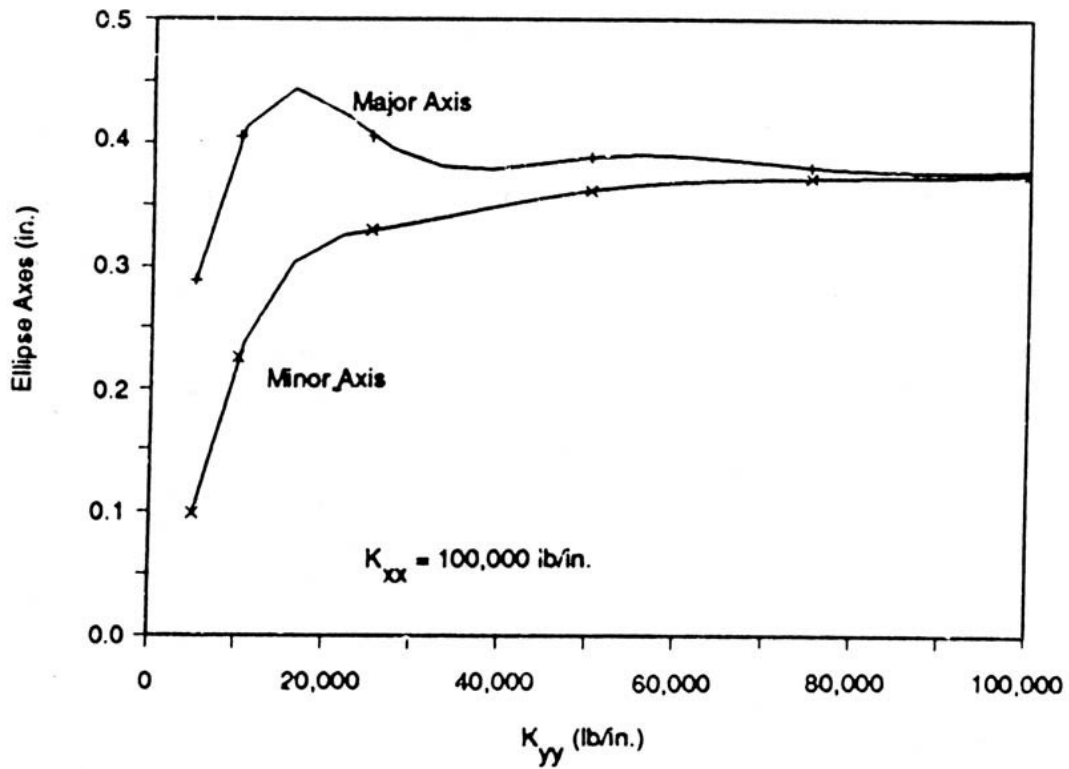
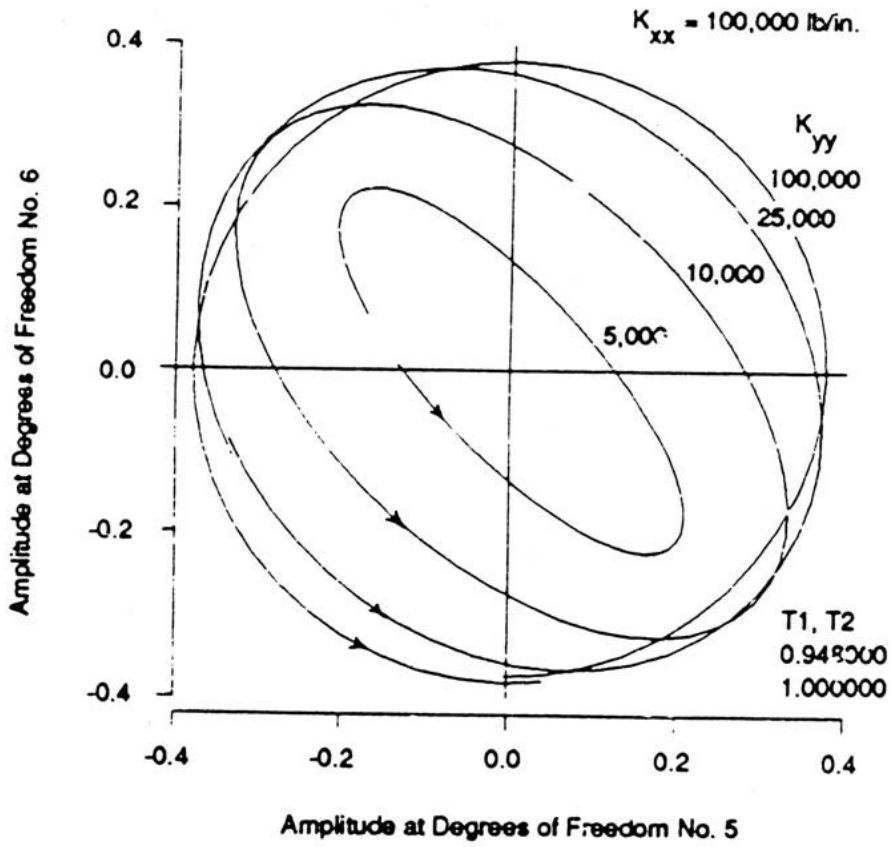


Figure 2.29.: MTI, 1990. The effect of bearing asymmetry on limit cycle orbits and ellipse sizes
Time marching predictions for the spline-coupling model.

3. RID systems modelling and characteristics

The foundation for linear and nonlinear (NL) analysis to follow is laid here. The overall NL system is separated $\mathcal{S}_{NL} \stackrel{s}{\supset} \{\mathcal{S}_L, \mathcal{S}_N\}$ into linear time-invariant (LTI) ‘ \mathcal{S}_L ’ and NL ‘ \mathcal{S}_N ’ (possibly time-varying) subsystems, which are setup in a feedback formulation (*fig. 3.5*), and whose characteristics will determine suitable analysis (*Chs. 4,5*).

Real and complex EOMs of the absolutely stable LTI/LTV gyroscopic subsystem are developed in the stationary and rotating frames, yielding State-Space and Transfer Function Matrices (TFM) representations, whose characteristics narrow down possible NL stability analysis. Closed-form analytical expressions of Eigen-results (§.3.1.3.2) are developed for comparison with RID-augmented systems, and are at the core of this work.

RID is introduced as a localised friction joint, which couples the linear rotor (*fig.3.1*) to the rotating frame ground (*fig.3.4*). Characteristics of various damping, including an assumed parabolic dry friction, models (rheological, FR, hysteresis) further limit the choice of NL analysis, and more importantly affect whirling behaviour significantly.

3.1. Linear rotordynamic characteristics

Practical spatial models of rotordynamic systems are invariably presented as a set of second-order ordinary differential equations that represent lumped-parameter models. These equations are assembled from the EOMs of the system’s components—shafts, discs, couplings, bearings, etc.—in a compatible manner with the analysis procedure to be implemented. The ‘Direct Stiffness Method’ (DSM) and the ‘Transfer Matrix Method’ (TMM) are the analysis procedures commonly used. The DSM is more widely adopted primarily due to the popularity of Finite Element Analysis (FEA).

3.1.1. EOMs of Linear Rotor-Bearing MDOF system

For transverse vibration analysis, a linear MDOF rotordynamic system \mathcal{S} can be represented in the stationary (Euclidean/inertial) frame of reference as:

$$\mathbf{M}\ddot{\mathbf{q}} + (\mathbf{G} + \mathbf{C})\dot{\mathbf{q}} + (\mathbf{K} + \mathbf{K}_{cc})\mathbf{q} = \mathbf{f} \quad (3.1a)$$

$$\mathbf{M}\ddot{\mathbf{q}} + \mathbf{C}_g\dot{\mathbf{q}} + \mathbf{K}_g\mathbf{q} = \mathbf{f} \quad (3.1b)$$

with \mathbf{C} , \mathbf{K} being generally indefinite and non-symmetric matrices. The cross-coupled (circulatory) \mathbf{K}_{cc} matrix derives from destabilising mechanisms such as RID. \mathbf{C}_g , \mathbf{K}_g are the stationary frame generalised damping and stiffness matrices. The \mathbf{q} vector comprises the translational and rotational DOFs of discretised stations, in which case \mathbf{f} comprises the corresponding external forces and moments. Small translational and rotational displacements can be related, whence the system's order can be halved.

3.1.1.1. 2DOF rotor in stationary xy -frame

This is a simple yet illustrative rotor-bearing LTI system with inertia and gyroscopic

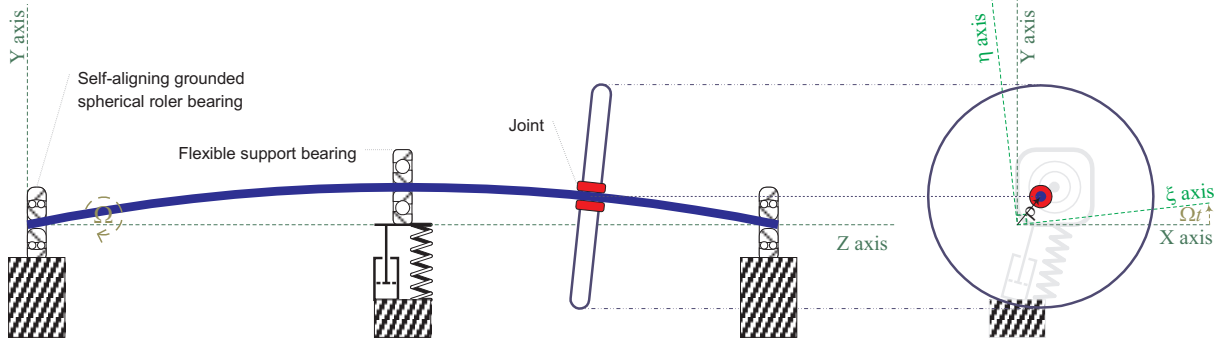


Figure 3.1.: Simple gyroscopic rotor on orthotropic bearings represented by 2 DOFs

effects from a disc as well as a symmetric flexible shaft, both comprising the rotor. This rotor is mounted on non-rigid bearings, which are possibly orthotropic and contribute stiffness and external linear viscous damping. This system can be modelled using an assumed 1st mode shape [96] as in (3.1) by:

$$\mathbf{q} = \begin{Bmatrix} x(t) \\ y(t) \end{Bmatrix}, \quad \mathbf{f} = \begin{Bmatrix} f_x(t) \\ f_y(t) \end{Bmatrix}; \quad \mathbf{I} = \begin{bmatrix} 1 & 0 \\ 0 & 1 \end{bmatrix}, \quad \mathbf{N} = \begin{bmatrix} 0 & -1 \\ 1 & 0 \end{bmatrix}, \quad \mathbf{M} = m\mathbf{I}, \quad \mathbf{G} = -\mathcal{G}\Omega\mathbf{N}$$

$$\text{orth. bearings:} \quad \mathbf{C} = \begin{bmatrix} c_x & 0 \\ 0 & c_y \end{bmatrix}, \quad \mathbf{K} = \begin{bmatrix} k_x & 0 \\ 0 & k_y \end{bmatrix} = \begin{bmatrix} k + \Delta k & 0 \\ 0 & k - \Delta k \end{bmatrix} \quad (3.2a)$$

$$\text{iso. bearings:} \quad \mathbf{K} = k\mathbf{I}, \quad \mathbf{C} = c\mathbf{I} \quad (3.2b)$$

External damping is said to be proportional when $\mathbf{C} = \alpha\mathbf{M} + \beta\mathbf{K}$. Thus far, $\mathbf{K}_{cc} \stackrel{\text{def}}{=} \mathbf{0}$ as the effect of RID or any other destabilising mechanism has not yet been considered.

3.1.1.2. EOMs of 2DOF rotor in rotating $\xi\eta$ -frame

As RID forces are initially augmented to rotating frame EOMs (§.3.2.2.1), the steps involved in shifting between $\xi\eta$ - and xy -frame EOMs are detailed due to their importance

Vector transformations between coordinate systems

$$\mathbf{T} = \begin{bmatrix} \cos \tau_\Omega & -\sin \tau_\Omega \\ \sin \tau_\Omega & \cos \tau_\Omega \end{bmatrix} \Rightarrow \dot{\mathbf{T}} = \Omega\mathbf{T}\mathfrak{N}, \ddot{\mathbf{T}} = -\Omega^2\mathbf{T}; \mathbf{T}^{-1} = \mathbf{T}^T, \dot{\mathbf{T}}^T = -\Omega\mathbf{T}^T\mathfrak{N}; \ddot{\mathbf{T}}^T = -\Omega^2\mathbf{T}^T \quad (3.3)$$

$$\mathbf{f} = \mathbf{T}\mathbf{f}_r = \mathbf{T} \begin{Bmatrix} f_\xi(t) \\ f_\eta(t) \end{Bmatrix} \quad \mathbf{q} = \mathbf{T}\mathbf{q}_r = \mathbf{T} \begin{Bmatrix} \xi(t) \\ \eta(t) \end{Bmatrix} \quad (3.4a)$$

$$\dot{\mathbf{q}} = \frac{d}{dt}(\mathbf{T}\mathbf{q}_r) = \mathbf{T}(\dot{\mathbf{q}}_r + \Omega\mathfrak{N}\mathbf{q}_r) \quad \ddot{\mathbf{q}} = \frac{d^2}{dt^2}(\mathbf{T}\mathbf{q}_r) = \mathbf{T}(\ddot{\mathbf{q}}_r + 2\Omega\mathfrak{N}\dot{\mathbf{q}}_r - \Omega^2\mathbf{q}_r) \quad (3.4b)$$

$$\mathbf{q}_r = \mathbf{T}^{-1}\mathbf{q} = \mathbf{T}^T \begin{Bmatrix} x(t) \\ y(t) \end{Bmatrix} \quad \dot{\mathbf{q}}_r = \dot{\mathbf{T}}^T\mathbf{q} + \mathbf{T}^T\dot{\mathbf{q}} = \mathbf{T}^T(\dot{\mathbf{q}} - \Omega\mathfrak{N}\mathbf{q}) \quad (3.4c)$$

System Matrices in the rotating frame The rotor system defined by (3.1, 3.2) is expressed in accordance with (3.3, 3.4) as

$$\mathbf{M}\mathbf{T}(\ddot{\mathbf{q}}_r + 2\Omega\mathfrak{N}\dot{\mathbf{q}}_r - \Omega^2\mathbf{q}_r) + (\mathbf{G} + \mathbf{C})\mathbf{T}(\dot{\mathbf{q}}_r + \Omega\mathfrak{N}\mathbf{q}_r) + \mathbf{K}\mathbf{T}\mathbf{q}_r = \mathbf{T}\mathbf{f}_r \quad (3.5)$$

To express the force vectors in the rotating frame we pre-multiply (3.2) or (3.5) by \mathbf{T}^T

$$\begin{aligned} \mathbf{T}^T\mathbf{M}\ddot{\mathbf{q}} + \mathbf{T}^T(\mathbf{G} + \mathbf{C})\dot{\mathbf{q}} + \mathbf{T}^T\mathbf{K}\mathbf{q} &= \mathbf{T}^T\mathbf{T}\mathbf{f}_r = \mathbf{f}_r \\ \mathbf{T}^T\mathbf{M}\mathbf{T}(\ddot{\mathbf{q}}_r + 2\Omega\mathfrak{N}\dot{\mathbf{q}}_r - \Omega^2\mathbf{q}_r) + \mathbf{T}^T(\mathbf{G} + \mathbf{C})\mathbf{T}(\dot{\mathbf{q}}_r + \Omega\mathfrak{N}\mathbf{q}_r) + \mathbf{T}^T\mathbf{K}\mathbf{T}\mathbf{q}_r &= \mathbf{f}_r \end{aligned} \quad (3.6)$$

The EOMs are then rearranged into rotating frame matrices and vectors:

$$\begin{aligned} \mathbf{M}_r\ddot{\mathbf{q}}_r + \mathbf{C}_r\dot{\mathbf{q}}_r + \mathbf{K}_r\mathbf{q}_r &= \mathbf{f}_r \quad (3.7) \\ \text{where } \begin{cases} \mathbf{M}_r = \mathbf{T}^T\mathbf{M}\mathbf{T} \\ \mathbf{C}_r = 2\Omega\mathbf{T}^T\mathbf{M}\mathfrak{N}\mathbf{T} + \mathbf{T}^T(\mathbf{G} + \mathbf{C})\mathbf{T} \\ \mathbf{K}_r = -\Omega^2\mathbf{T}^T\mathbf{M}\mathbf{T} + \Omega\mathbf{T}^T(\mathbf{G} + \mathbf{C})\mathfrak{N}\mathbf{T} + \mathbf{T}^T\mathbf{K}\mathbf{T} \end{cases} \end{aligned}$$

LTV matrices will emerge in the $\xi\eta$ -frame if any of the xy -frame matrices (3.1b) describes an anisotropic rotor e.g. (3.2a). According to (A.3), isotropy of the 2DOF rotor (3.2) requires $\mathbf{M}, \mathbf{C}_g, \mathbf{K}_g$ to have identical diagonal elements and skew-symmetric off-diagonal elements as in (3.2b). With orthotropic bearings $\mathbf{K} \neq \mathbf{K}_{\text{iso}} \therefore \Delta k \neq 0, \Rightarrow \mathbf{K}_r \stackrel{\text{def}}{=} \text{LTV}$ as in (3.9). In this case, proportional damping $\mathbf{C} \equiv \beta\mathbf{K} \Rightarrow \mathbf{C}_r \stackrel{\text{def}}{=} \text{LTV}$ as well.

The isotropic rotor (3.2) with (3.2b) yields (3.6) written as

$$m\mathbf{T}^T\mathbf{I}\mathbf{T}(\ddot{\mathbf{q}}_r + 2\Omega\mathfrak{N}\dot{\mathbf{q}}_r - \Omega^2\mathbf{q}_r) + c\mathbf{T}^T\mathbf{I}\mathbf{T}(\dot{\mathbf{q}}_r + \Omega\mathfrak{N}\mathbf{q}_r) - \mathcal{G}\Omega\mathbf{T}^T\mathfrak{N}\mathbf{T}(\dot{\mathbf{q}}_r + \Omega\mathfrak{N}\mathbf{q}_r) + k\mathbf{T}^T\mathbf{I}\mathbf{T}\mathbf{q}_r = \mathbf{f}_r$$

since $\mathbf{T}^T\mathbf{I}\mathbf{T} = \mathbf{I}$ and $\mathbf{T}^T\mathfrak{N}\mathbf{T} = \mathfrak{N}$, we have

$$m\mathbf{I}(\ddot{\mathbf{q}}_r + 2\Omega\mathfrak{N}\dot{\mathbf{q}}_r - \Omega^2\mathbf{q}_r) + (c\mathbf{I} - \mathcal{G}\Omega\mathfrak{N})(\dot{\mathbf{q}}_r + \Omega\mathfrak{N}\mathbf{q}_r) + k\mathbf{I}\mathbf{q}_r = \mathbf{f}_r$$

or on rearranging, keeping in mind that $\mathfrak{N}^2 = -\mathbf{I}$

$$m\mathbf{I}\ddot{\mathbf{q}}_r + \left(c\mathbf{I} + (2m - \mathcal{G})\Omega\mathfrak{N}\right)\dot{\mathbf{q}}_r + \left((k + (\mathcal{G} - m)\Omega^2)\mathbf{I} + c\Omega\mathfrak{N}\right)\mathbf{q}_r = \mathbf{f}_r \quad (3.8)$$

The anisotropic rotor (3.2, 3.2a) has $\Delta k \neq 0$. For simplicity, assume $\mathbf{C} = c\mathbf{I} \neq \beta\mathbf{K}$ hence, according to (3.7), the $\Delta k \in \mathbf{K}$ will affect only \mathbf{K}_r via:

$$\mathbf{T}^T\mathbf{K}\mathbf{T} = \mathbf{T}^T\left(k\mathbf{I} + \Delta k \begin{bmatrix} 1 & 0 \\ 0 & -1 \end{bmatrix}\right)\mathbf{T} = k\mathbf{I} + \Delta k \mathbf{T}^T \begin{bmatrix} 1 & 0 \\ 0 & -1 \end{bmatrix} \mathbf{T}$$

where, $\Delta k \mathbf{T}^T \begin{bmatrix} 1 & 0 \\ 0 & -1 \end{bmatrix} \mathbf{T} = \Delta k \begin{bmatrix} \cos 2\tau_\Omega & -\sin 2\tau_\Omega \\ -\sin 2\tau_\Omega & -\cos 2\tau_\Omega \end{bmatrix}$

leading to the LTV EOMs:

$$m\mathbf{I}\ddot{\mathbf{q}}_r + \left(c\mathbf{I} + (2m - \mathcal{G})\Omega\mathfrak{N}\right)\dot{\mathbf{q}}_r + \left((k + (\mathcal{G} - m)\Omega^2)\mathbf{I} + c\Omega\mathfrak{N} + \Delta k \begin{bmatrix} \cos 2\tau_\Omega & -\sin 2\tau_\Omega \\ -\sin 2\tau_\Omega & -\cos 2\tau_\Omega \end{bmatrix}\right)\mathbf{q}_r = \mathbf{f}_r \quad (3.9)$$

3.1.1.3. Complex EOMs of a 2DOF rotor

Complex EOM of the isotropic rotor version ($k_x = k_y = k$). Applying (A.4) to (3.2, 3.2b), the EOM in the stationary xy -frame is:

$$m\ddot{z} + (c - i\Omega\mathcal{G})\dot{z} + kz = f_z \quad (3.10)$$

The corresponding EOM in the rotating $\xi\eta$ -frame can be arrived at by applying the complex transformation (2.7) to (3.10), which is equivalent to applying (2.4,A.4) with $(\zeta, \mathbf{M}_r, \mathbf{C}_r, \mathbf{K}_r)$ in place of $(\mathbf{z}, \mathbf{M}, \mathbf{C}_g, \mathbf{K}_g)$ to (3.8), resulting in:

$$m\ddot{\zeta} + \left(c + i\Omega(2m - \mathcal{G})\right)\dot{\zeta} + \left(\left(k + (\mathcal{G} - m)\Omega^2\right) + i\Omega c\right)\zeta = f_{\zeta} \quad (3.11)$$

3.1.2. Linear system model representations

Although the RID problem is a nonlinear one, the special cases of linear (possibly time-varying LTV) RID systems are worthy of studying, because a linear system:

- Is always the first basis for system design and frequently for final analysis purposes.
- Affords analysis that is far more tractable yielding a unique formal solution, which is applicable for all initial conditions and inputs.
- Yields valuable insight into fundamentals of system behaviour, which are used for analogy to study effectively nonlinear systems.

A multivariable dynamic system \mathbf{S} can be represented by either state-space representations or by an input-output representation, e.g. transfer function matrix (TFM) $\mathbf{H}(s)$.

3.1.2.1. State-Space representations

A state-space representation consists of a set of first order differential equations, describing variables' evolution whose values at any given instant determine current state.

General dynamic systems representation State-space is suitable for representing *combinations* of $\mathbf{S} \stackrel{\text{def}}{=} \{\text{LTI, LTV, NL}\}$ that is described by a finite lumped-parameter model, which is setup as a set of ordinary differential equations. Modelling distributed-parameter infinite-dimensional systems described by partial differential equations is also possible, albeit with mathematical difficulties.

A general state-space model of l -dimensional lumped-parameter \mathbf{S} , which is possibly nonlinear and time-varying can be represented in the \mathbb{R}^l space as:

$$\dot{\mathbf{p}}_{l \times 1} = \mathbf{F}_{l \times 1}(\mathbf{p}, \mathbf{f}, t) \quad \textit{The State Equation} \quad (3.12)$$

where \mathbf{F} is generally nonlinear. To insure the mathematical validity of (3.12), certain restrictions maybe imposed on \mathbf{F} ; e.g. using idealised functions with peculiar features (e.g. discontinuities), and thereafter a careful examination of analysis is necessary to

ensure such features do not invalidate the solutions. Input-output descriptions/models especially of nonlinear elements may well be used in conjunction with state-space forms.

The linear time-varying version $\mathcal{S}(\mathbf{A}, \mathbf{B}, \mathbf{O}, \mathbf{D}, t)$ of (3.12) whose equations represent the states \mathbf{p} , inputs \mathbf{f} and outputs \mathbf{o} of \mathcal{S} is:

$$\dot{\mathbf{p}} = \mathbf{A}(t)\mathbf{p} + \mathbf{B}(t)\mathbf{f} \quad \text{LTV State equation} \quad (3.13a)$$

$$\mathbf{o} = \mathbf{O}(t)\mathbf{p} + \mathbf{D}(t)\mathbf{f} \quad \text{LTV Output equation} \quad (3.13b)$$

The time variable t indicates $\mathcal{S} \stackrel{\text{def}}{=} \text{LTV}$, where the relation of \mathcal{S} inputs (external forces) and outputs (responses) is time-dependent. Such model is representative of rotor-bearing systems with asymmetric rotor when represented in the xy -frame, or with orthotropic bearings when represented in the $\xi\eta$ -frame (3.9). The difficulty of solving for $\mathbf{A}(t)$ prevents much further progress, except in special cases, e.g. when $\mathbf{A}(t)$ is periodic.

The LTI subcategory $\mathcal{S}(\mathbf{A}, \mathbf{B}, \mathbf{O}, \mathbf{D})$ of (3.13a, 3.13b) is:

$$\dot{\mathbf{p}} = \mathbf{A}\mathbf{p} + \mathbf{B}\mathbf{f} \quad \text{LTI State equation}$$

$$\mathbf{o} = \mathbf{O}\mathbf{p} + \mathbf{D}\mathbf{f} \quad \text{LTI Output equation}$$

$\mathbf{A}_{l \times l}$ is known as the *dynamics (State) matrix* as it describes the system dynamics and controls the trajectories of the state vector $\mathbf{p}(t)$. The *input matrix* \mathbf{B} reflects the effect of forces (inputs) on the state variables $\in \mathbf{p}$ the state vector. The *output matrix* \mathbf{O} represents the relation (transformation) of \mathbf{p} to the *output vector* \mathbf{o} . The *transmission matrix* \mathbf{D} represents the direct effect of \mathbf{f} on \mathbf{o} , bypassing the \mathcal{S} dynamics in \mathbf{A} .

Linear rotordynamic system representation An n DOF LTI/LTV mechanical \mathcal{S} that is modelled as a set of second-order ordinary differential equations $\Rightarrow \mathbb{R}^l = \mathbb{R}^{2n}$. The state-space representation $\mathcal{S}(\mathbf{A}, \mathbf{B}, \mathbf{O}, \mathbf{D})$ is not unique and depends on the choice of \mathbf{p} . Intuitively, we can elect to set the displacements \mathbf{q} and velocities $\dot{\mathbf{q}}$ as candidates for \mathbf{p} in which case $\mathbf{p} \stackrel{\text{def}}{=} \text{a phase state vector}$. For our purposes, (3.13b) has $\mathbf{D} = \mathbf{0} = \mathbf{D}(t)$. A rotordynamic \mathcal{S} can be represented in state-space as:

$$\dot{\mathbf{p}} = \mathbf{A}\mathbf{p} + \mathbf{B}\mathbf{f} \quad (3.14a)$$

$$\mathbf{o} = \mathbf{O}\mathbf{p} \quad (3.14b)$$

where $\mathbf{p}_{2n \times 1}, \mathbf{f}_{n \times 1} \Rightarrow \mathbf{A}_{2n \times 2n}, \mathbf{B}_{2n \times n}$

3. RID systems modelling and characteristics

Setting $\mathbf{p} = \begin{Bmatrix} \mathbf{q} \\ \dot{\mathbf{q}} \end{Bmatrix}$ from (3.1) we have:

$$\mathbf{A} = \begin{bmatrix} \mathbf{0} & \mathbf{I} \\ -\mathbf{M}^{-1}\mathbf{K}_g & -\mathbf{M}^{-1}\mathbf{C}_g \end{bmatrix}_{2n \times 2n}, \quad \mathbf{B} = \begin{bmatrix} \mathbf{0} \\ \mathbf{M}^{-1} \end{bmatrix}_{2n \times n} \quad (3.15a)$$

\mathbf{B} in (3.15a) implies that an input (force f) is physically applicable to any coordinate (station). As imbalance is usually accounted for in the EOMs as an external force, it should contribute to \mathbf{f} of (3.14). The choice of \mathbf{O} depends on what is *measurable* and of interest from \mathbf{p} . If we are interested in \mathbf{q} or $\dot{\mathbf{q}}$ we can set $\mathbf{O} = \mathbf{O}^d$ or $\mathbf{O} = \mathbf{O}^v$ respectively, or even $\mathbf{O} = \mathbf{O}^{dv}$ if we want both $\mathbf{q}, \dot{\mathbf{q}}$:

$$\mathbf{O}^d = [\mathbf{I} \ \mathbf{0}]_{n \times 2n}, \quad \mathbf{O}^v = [\mathbf{0} \ \mathbf{I}]_{n \times 2n}, \quad \mathbf{O}^{dv} = \mathbf{I}_{2n \times 2n} \quad (3.15b)$$

$$\hookrightarrow \mathbf{o} = \mathbf{q}, \quad \hookrightarrow \mathbf{o} = \dot{\mathbf{q}}, \quad \hookrightarrow \mathbf{o} = \begin{Bmatrix} \mathbf{q} \\ \dot{\mathbf{q}} \end{Bmatrix} \quad (3.15c)$$

2DOF rotor-bearing \mathcal{S} representation in state-space:

Input and Output matrices used in both stationary and rotating frames are:

$$\mathbf{B} = \frac{1}{m} \begin{bmatrix} 0 & 0 \\ 0 & 0 \\ 1 & 0 \\ 0 & 1 \end{bmatrix}, \quad \mathbf{O}^d = \begin{bmatrix} 1 & 0 & 0 & 0 \\ 0 & 1 & 0 & 0 \end{bmatrix}, \quad \mathbf{O}^v = \begin{bmatrix} 0 & 0 & 1 & 0 \\ 0 & 0 & 0 & 1 \end{bmatrix}, \quad \mathbf{O}^{dv} = \begin{bmatrix} \mathbf{O}^d \\ \mathbf{O}^v \end{bmatrix} \quad (3.16)$$

State matrix in stationary frame for isotropic \mathcal{S} :

$$\mathbf{A} = \begin{bmatrix} 0 & 0 & 1 & 0 \\ 0 & 0 & 0 & 1 \\ -\frac{k}{m} & 0 & -\frac{c}{m} & -\frac{\Omega \mathcal{G}}{m} \\ 0 & -\frac{k}{m} & \frac{\Omega \mathcal{G}}{m} & -\frac{c}{m} \end{bmatrix} \quad (3.17)$$

State matrix in rotating frame for isotropic \mathcal{S}_r :

$$\mathbf{A}_r = -\frac{1}{m} \begin{bmatrix} 0 & 0 & -m & 0 \\ 0 & 0 & 0 & -m \\ k + \Omega^2(\mathcal{G} - m) & -\Omega c & c & \Omega(\mathcal{G} - 2m) \\ \Omega c & k + \Omega^2(\mathcal{G} - m) & -\Omega(\mathcal{G} - 2m) & c \end{bmatrix} \quad (3.18)$$

Complex formulations in state space, albeit unorthodox, are possible:

Input & Output matrices for the 2DOF \mathbf{S}_c :

$$\mathbf{B}_c = \begin{Bmatrix} 0 \\ \frac{1}{m} \end{Bmatrix}, \quad \mathbf{O}_c^d = \{1, 0\}, \quad \mathbf{O}_c^v = \{0, 1\}, \quad \mathbf{O}_c^{dv} = \mathbf{I}_{2 \times 2} \quad (3.19)$$

State matrix in stationary frame for 2DOF isotropic \mathbf{S}_c :

$$\mathbf{A}_c = \begin{bmatrix} 0 & 1 \\ -k/m & -(c - i\Omega\mathcal{G})/m \end{bmatrix} \quad (3.20)$$

State matrix in rotating frame for 2DOF isotropic \mathbf{S}_{rc} :

$$\mathbf{A}_{rc} = \begin{bmatrix} 0 & 1 \\ -(k + (\mathcal{G} - m)\Omega^2 + i\Omega c)/m & -(c + i\Omega(2m - \mathcal{G}))/m \end{bmatrix} \quad (3.21)$$

3.1.2.2. Transfer Function Matrices (TFMs) representations

We can derive TFMs $\mathbf{H}(s)$, e.g. the $n \times n$ *Receptance* $\mathbf{H}^d(s)$ and *Mobility* $\mathbf{H}^v(s)$ matrices, either from the EOMs directly or from the state-space representation of LTI $\mathbf{S}(\mathbf{A}, \mathbf{B}, \mathbf{O})$. Each of the $n \times n$ TFMs is made up of individual transfer functions (TFs) $H_{ij}(s) \in \mathbf{H}(s)$, with $i, j \in \{1 \dots n\}$. In vibration terminology, TFs of the form $H_{ii}(s)$ are referred to as *point* TFs since the input is applied to the same point where the output is measured/observed. On the other hand, $H_{ij}(s)$ are referred to as *transfer* TFs since the point of output is transferred from the point of input. As we are concerned here with 2×2 TFMs of a 2DOF rotordynamic \mathbf{S}_L , a transfer TF can only be established between two perpendicular directions (in quadrature). In order to avoid confusion of terms, the transfer TF $H_{ji}(s)$ e.g. $H_{yx}(s)$ will be referred to as a *quad* TF, as opposed to the point TF $H_{xx}(s)$.

TFMs construction from EOMs If we take the Laplace transform of the LTI (3.1) with *zero initial conditions*, we have:

$$(\mathbf{M}s^2 + \mathbf{C}_g s + \mathbf{K}_g) \mathbf{q}(s) = \mathbf{f}(s) \quad (3.22a)$$

$$\mathbf{S} \mathbf{q}(s) = \mathbf{f}(s) \quad (3.22b)$$

and with Laplace transform $\mathcal{L}(\dot{\mathbf{q}}) = s\mathbf{q}(s)$, we get:

$$s^{-1} \mathbf{S} s \mathbf{q}(s) = s \mathbf{V} \mathbf{q}(s) = \mathbf{f}(s) \quad (3.22c)$$

3. RID systems modelling and characteristics

We can construct $\mathbf{H}^d, \mathbf{H}^v$ from \mathcal{S}, \mathcal{V} respectively:

$$\mathbf{q}(s) = \mathbf{H}^d(s) \mathbf{f}(s) \quad \Rightarrow \quad \mathbf{H}^d(s) = \mathcal{S}^{-1} = \frac{\text{adj}[\mathcal{S}]}{|\mathcal{S}|} \quad (3.22d)$$

$$s\mathbf{q}(s) = \mathbf{H}^v(s) \mathbf{f}(s) \quad \Rightarrow \quad \mathbf{H}^v(s) = \mathcal{V}^{-1} = s\mathbf{H}^d(s) \quad (3.22e)$$

$$\begin{Bmatrix} \mathbf{q}(s) \\ s\mathbf{q}(s) \end{Bmatrix}_{2n \times 1} = \begin{bmatrix} \mathbf{H}^d(s) \\ s\mathbf{H}^d(s) \end{bmatrix}_{2n \times n} \mathbf{f}_{n \times 1}(s) \quad (3.22f)$$

TFMs construction from $\mathcal{S}(\mathbf{A}, \mathbf{B}, \mathbf{O})$ $\mathbf{H}(s)$ representing MIMO \mathcal{S}_L in (3.22) is:

$$\mathbf{H}(s) = \mathbf{O}[s\mathbf{I} - \mathbf{A}]^{-1}\mathbf{B} = \mathbf{O} \frac{\text{adj}[s\mathbf{I} - \mathbf{A}]}{|s\mathbf{I} - \mathbf{A}|} \mathbf{B} = \mathbf{O} \frac{\text{adj}[s\mathbf{I} - \mathbf{A}]}{D(s)} \mathbf{B} \quad (3.23)$$

$$\text{where } D(s) = s^{2n} + a_{2n-1}s^{2n-1} + \dots + a_1s + a_0 \quad \text{i.e. } a_{2n} = 1$$

Individual transfer functions $H_{ij} \in \mathbf{H}(s)$ can be derived directly from $\mathcal{S}(\mathbf{A}, \mathbf{B}, \mathbf{O})$ as:

$$H_{ij}(s) = \mathbf{O}_{i^{\text{th}} \text{ row}} \frac{\text{adj}[s\mathbf{I} - \mathbf{A}]}{D(s)} \mathbf{B}_{j^{\text{th}} \text{ col}} = \frac{N_{ij}(s)}{D(s)} \quad (3.24)$$

$$N_{ij}(s) = g_{ij}(s^u + b_{u-1}s^{u-1} + \dots + b_1s + b_0); \quad g_{ij} \stackrel{\text{def}}{=} \text{real gain} \in \langle -\infty, \infty \rangle, \quad 0 \leq u < 2n$$

By (3.24), the TF $H_{ij}(s)$ represents a SISO \mathcal{S}_L of order $n \geq 2$.

Example TFMs representing our 2DOF \mathcal{S} in both xy - and $\xi\eta$ -frames are presented. Firstly, the receptance (compliance) TFM representing \mathcal{S} with orthotropic bearings in the stationary frame (3.2a)—with $\mathbf{C} = c\mathbf{I}$ for simplicity—is derived from $\mathcal{S}(\mathbf{A}, \mathbf{B}, \mathbf{O})$ as:

$$\mathbf{H}_{\text{Orth}}^d(s) = \frac{1}{m^2 D(s)} \begin{bmatrix} s^2m + sc + k - \Delta k & -s\Omega\mathcal{G} \\ s\Omega\mathcal{G} & s^2m + sc + k + \Delta k \end{bmatrix} \quad (3.25a)$$

$$D(s) = (s^4m^2 + 2s^3mc + s^2(c^2 + \Omega^2\mathcal{G}^2 + 2mk) + 2skc + k^2 - \Delta k^2)/m^2 \quad (3.25b)$$

Isotropic rotor-bearing TFMs with $\Delta k = 0$ (3.2b) for receptance in both stationary and rotating frames, are derived from \mathcal{S} as in (3.22). The individual transfer functions $H_{11} = H_{22}; H_{12} = -H_{21}$ for both \mathbf{H}, \mathbf{H}_r as expected e.g. (3.26, 3.28).

In the stationary frame $\mathbf{H}^d(s)$ derives from \mathcal{S} that results from (3.22, 3.2):

$$\mathcal{S} = \mathcal{S}_{2 \times 2} = \begin{bmatrix} s^2m + sc + k & s\Omega\mathcal{G} \\ -s\Omega\mathcal{G} & s^2m + sc + k \end{bmatrix}$$

and since $\mathcal{S}_{11} = \mathcal{S}_{22}$, $\mathcal{S}_{21} = -\mathcal{S}_{12} \implies \text{adj}[\mathcal{S}_{2 \times 2}] \equiv \mathcal{S}^T$, we have:

$$\mathbf{H}^{d(s)} = \frac{1}{|\mathcal{S}|} \begin{bmatrix} s^2m + sc + k & -s\Omega\mathcal{G} \\ s\Omega\mathcal{G} & s^2m + sc + k \end{bmatrix} \quad (3.26a)$$

$$|\mathcal{S}| = s^4m^2 + 2s^3mc + s^2(c^2 + \Omega^2\mathcal{G}^2 + 2mk) + 2skc + k^2 \quad (3.26b)$$

The same $\mathbf{H}^{d(s)}$ in (3.26) can be derived from (3.23, 3.17) with \mathbf{B} , \mathbf{O}^d from (3.16)

In the rotating frame (3.22) is applied to (3.8), and $\mathbf{H}_r^{d(s)}$ is derived from \mathcal{S}_r

$$\mathcal{S}_r = \mathcal{S}_{r_{2 \times 2}} = \begin{bmatrix} s^2m + sc + k + \Omega^2(\mathcal{G} - m) & -s\Omega(2m - \mathcal{G}) - \Omega c \\ s\Omega(2m - \mathcal{G}) + \Omega c & s^2m + sc + k + \Omega^2(\mathcal{G} - m) \end{bmatrix} \quad (3.27)$$

and again $\text{adj}[\mathcal{S}_{r_{2 \times 2}}] \equiv \mathcal{S}_r^T$, leading to

$$\mathbf{H}_r^{d(s)} = \frac{1}{|\mathcal{S}_r|} \begin{bmatrix} s^2m + sc + k + \Omega^2(\mathcal{G} - m) & s\Omega(2m - \mathcal{G}) + \Omega c \\ -(s\Omega(2m - \mathcal{G}) + \Omega c) & s^2m + sc + k + \Omega^2(\mathcal{G} - m) \end{bmatrix} \quad (3.28a)$$

$$|\mathcal{S}_r| = s^4m^2 + 2s^3mc + s^2(c^2 + 2mk + \Omega^2(2m^2 - 2mg + \mathcal{G}^2)) + 2sc(k + \Omega^2m) + (k + \Omega^2(\mathcal{G} - m))^2 \quad (3.28b)$$

3.1.3. Modal analysis in stationary & rotating frames

3.1.3.1. Eigensolutions and modal directionality

The eigenvalue problem (3.29a) associated with the state matrix \mathbf{A} in (3.14, 3.21, 3.31), which is generally non-symmetric and indefinite, is a non-self-adjoint one. The eigenvalue problem and its adjoint are:

$$[\lambda_i \mathbf{I} - \mathbf{A}] \mathbf{r}_i = \mathbf{0} \quad \mathbf{A} \mathbf{r}_i = \lambda_i \mathbf{r}_i \quad (3.29a)$$

$$\mathbf{l}_i^T [\lambda_i \mathbf{I} - \mathbf{A}] = \mathbf{0} \quad \mathbf{A}^T \mathbf{l}_i^* = \lambda_i^* \mathbf{l}_i^* \quad (3.29b)$$

The eigensolutions of (3.29) are the eigenvalues λ_i and their corresponding (right) eigenvectors \mathbf{r}_i or left eigenvectors \mathbf{l}_i , where $i \in \{1 \dots \text{order of } \mathbf{A}\}$. The complex i^{th} eigensolution pair $(\lambda_i, \mathbf{r}_i)$ represents the i^{th} mode of lateral vibration, which is generally non-planar. Although not encountered herein, real eigensolutions are possible, especially in systems with hydrodynamic bearings.

The eigenvalues of \mathbf{S} (3.1) are the eigenvalues of \mathbf{A} describing it, which are the roots of its *characteristic polynomial* $|\lambda\mathbf{I} - \mathbf{A}|$ leading to the *characteristic equation*:

$$|\lambda\mathbf{I} - \mathbf{A}| = D(\lambda) = 0 \quad (3.30)$$

where the polynomial function $D(\lambda)$ is of the same order as \mathbf{A} . This is logical since the *free* response of a LTI \mathbf{S} (3.1, 3.2, 3.8) to initial conditions $\mathbf{p}(t_0)$ at $t = t_0$ is defined by setting $\mathbf{f} = \mathbf{0}$ in the state equation (3.14a) leading to:

$$\dot{\mathbf{p}} = \mathbf{A}\mathbf{p} \quad (3.31)$$

the solution of which is defined totally by \mathbf{A} and the initial conditions:

$$\begin{aligned} \mathbf{p}(t) &= e^{\mathbf{A}(t-t_0)}\mathbf{p}(t_0) \\ t_0 = 0 &\Rightarrow \mathbf{p}(t) = e^{\mathbf{A}t}\mathbf{p}(0) \end{aligned}$$

The eigenvalues are also the latent roots of the second-degree lambda-matrix $\mathbf{D}_2(\lambda)$ resulting from the latent equation:

$$|\mathbf{D}_2(\lambda)| \equiv |\lambda^2\mathbf{M} + \lambda\mathbf{C}_g + \mathbf{K}_g| = 0 \quad (3.32)$$

Eigenvectors and modal (latent) vectors: \mathbf{r}_i and $\hat{\mathbf{r}}_i$ are related by the construction of state matrix \mathbf{A} (3.15a) from system matrices (3.1), which results in:

$$\mathbf{r}_i = \begin{Bmatrix} \hat{\mathbf{r}}_i \\ \lambda_i \hat{\mathbf{r}}_i \end{Bmatrix} \quad \mathbf{D}_2(\lambda_i)\hat{\mathbf{r}}_i = [\lambda_i^2\mathbf{M} + \lambda_i\mathbf{C}_g + \mathbf{K}_g]\hat{\mathbf{r}}_i = \mathbf{0} \quad (3.33a)$$

$$\mathbf{l}_i^* = \begin{Bmatrix} \hat{\mathbf{l}}_i^* \\ \lambda_i^* \hat{\mathbf{l}}_i^* \end{Bmatrix} \quad \hat{\mathbf{l}}_i^T \mathbf{D}_2(\lambda_i) = \hat{\mathbf{l}}_i^T [\lambda_i^2\mathbf{M} + \lambda_i\mathbf{C}_g + \mathbf{K}_g] = \mathbf{0} \quad (3.33b)$$

Eigensolutions from real representation of a rotordynamic— $\mathbf{S}_L \in \mathbb{R}^{2n} \Rightarrow \mathbf{A}_{2n \times 2n} \Rightarrow (\lambda, \mathbf{r})_{i \in \{1 \dots 2n\}}$ —occur in n complex-conjugate pairs. Accordingly, (3.30-3.33) yield $2n$ eigen-solution pairs presented here as:

$$\mathbf{r}_i = \mathbf{r}_{i+n}^* \quad \mathbf{r}_{i,i+n} = \Re(\mathbf{r}_i) \pm \imath \Im(\mathbf{r}_i) \quad (3.34a)$$

$$\lambda_i = \lambda_{i+n}^* \quad \lambda_{i,i+n} = \Re(\lambda_i) \pm \imath \Im(\lambda_i) \quad (3.34b)$$

$$\text{where } \Re(\lambda_i) = -\frac{\gamma_i |\omega_i|}{\sqrt{1 - \gamma_i^2}} \quad \text{and } \Im(\lambda_i) = \omega_i; \quad i \in \{1, \dots, n\} \quad (3.34c)$$

In this modal model (3.34) that has been derived from the spatial model (3.1), the first n eigenvalues have (damped) modal frequencies $\omega_{i \in \{1 \dots n\}}$ that assume both positive (+ve) and negative (-ve) values (e.g. *fig. 4.2*). $\Re(\lambda_i) \stackrel{\text{def}}{=} \text{decay constant (rate)}$ and $\gamma_i \stackrel{\text{def}}{=} \text{modal damping factor}$ whose $\text{sgn}(\gamma_i)$ is opposite to $\text{sgn}(\Re(\lambda_i))$, both of which are independent of $\text{sgn}(\omega_i)$. For \mathbf{S}_L to be stable, $\Re(\lambda_i)$ has to be negative, which requires $\text{sgn}(\gamma_i)$ to be positive $\forall i \in \{1, \dots, 2n\}$, hence the use of $|\omega_i|$. Modal parameters, including the all important γ_i , can be equally derived from response models using as in *fig. 6.9*

Modal directionality Generally, each individual mode of lateral vibration represents a precession in the corresponding frame of reference, be it stationary or rotating. Modal directionality, as defined here, refers to the direction of such precession, which can be clockwise (CW \odot) or counterclockwise (CCW \ominus) with respect to the frame where the mode is derived. Modal directionality is expressed by the relation between the mode's eigensolution pair $(\lambda, \mathbf{r})_i$ defining it, e.g. (3.35). It is also possible to deduce modal directionality from response models (e.g. *figs. 4.8, 4.9, 6.7*) as presented in §4.1. It is worthy of noting that, in complex rotor models, not all modes have a unique direction.

Modes classified: FWD/BWD, CCW/CW In the stationary frame, modes are usually classified as forward (FWD) or backward (BWD), to reflect the co- or counter-rotating precessions respectively with the direction of rotation, which is taken as positive (+ve) in the \odot direction. The combination of:

- Lead/Lag structure of $\hat{\mathbf{r}}_{\mathbf{x}}$ to $\hat{\mathbf{r}}_{\mathbf{y}}$ in the modal vector $\hat{\mathbf{r}}_i = \begin{Bmatrix} \hat{\mathbf{r}}_{\mathbf{x}} \\ \hat{\mathbf{r}}_{\mathbf{y}} \end{Bmatrix}_i$
- Sign (+ve/-ve) of the corresponding modal frequency: $\text{sgn}(\omega_i)$, $i \in \{1, \dots, 2n\}$

from (3.33a) reveals the modal directionality, e.g. (3.35). The undamped ($\mathbf{C} = \mathbf{0}$) rotordynamic \mathbf{S}_L will have its modes classified in accordance with:

$$\begin{array}{ll} \text{FWD modes} & \text{BWD modes} \\ +\text{ve } \omega : & \hat{\mathbf{r}}_{\mathbf{x}} \text{ leads } \hat{\mathbf{r}}_{\mathbf{y}} \text{ by } \pi/2 & \hat{\mathbf{r}}_{\mathbf{x}} \text{ lags } \hat{\mathbf{r}}_{\mathbf{y}} \text{ by } \pi/2 & (3.35\text{a}) \end{array}$$

$$\begin{array}{ll} -\text{ve } \omega : & \hat{\mathbf{r}}_{\mathbf{x}} \text{ lags } \hat{\mathbf{r}}_{\mathbf{y}} \text{ by } \pi/2 & \hat{\mathbf{r}}_{\mathbf{x}} \text{ leads } \hat{\mathbf{r}}_{\mathbf{y}} \text{ by } \pi/2 & (3.35\text{b}) \end{array}$$

Clearly, (3.35a) and (3.35b) represent complex conjugate modes. The lead/lag angles of $\hat{\mathbf{r}}_{\mathbf{x}}$ to $\hat{\mathbf{r}}_{\mathbf{y}}$ in (3.35) of damped \mathbf{S}_L are generally close to but $\neq \pi/2$ due to the anisotropy introduced by $\mathbf{K} \neq \mathbf{K}_{\text{iso}}$ and/or non-proportional damping. Vector phasing of proportionally damped isotropic \mathbf{S}_L where $\mathbf{C} = \alpha \mathbf{M} + \beta \mathbf{K}_{\text{iso}}$ as defined in (A.3) follows (3.35), e.g (3.45). A similar classification to (3.35) can be applied to modes derived in the rotating frame. However, as the FWD and BWD terms lose their significance in the rotating frame, they are replaced by CCW \ominus and CW \odot modes respectively.

Rotational speed, eigenvalues and critical speed The eigenvalues $\lambda_{i \in \{1, \dots, 2n\}}$ associated with FWD and BWD modes are distinguished here as $\lambda_{f:i}$, $\lambda_{b:i}$ respectively. For compliance with the results of complex formulations e.g. (3.41) as well as convention:

$$\begin{array}{ll}
 \text{FWD modal freqs.} & \text{BWD modal freqs.} \\
 \lambda_{f:i} \Rightarrow \omega_{f:i} > 0, & \lambda_{b:i} \Rightarrow \omega_{b:i} < 0; \quad i \in \{1, \dots, n\} \\
 \lambda_{f:i+n} \equiv \lambda_{f:i}^* \Rightarrow \omega_{f:i+n} < 0, & \lambda_{b:i+n} \equiv \lambda_{b:i}^* \Rightarrow \omega_{b:i+n} > 0 \quad \leftarrow
 \end{array} \quad (3.36)$$

In general, increasing speed leads to increased absolute values of FWD modal frequencies and decreased absolute values of BWD modal frequencies (e.g. 3.41, 3.42 and *fig. 4.1*):

$$\Omega : [0 \triangleright \rangle \Rightarrow |\omega_{f:i}| \equiv |\omega_{f:i+n}| \nearrow \text{ and } |\omega_{b:i}| \equiv |\omega_{b:i+n}| \searrow$$

The critical speed $\Omega_c \stackrel{\text{def}}{=} \text{the rotational speed at which the first FWD modal frequency equals this rotational speed, i.e. at } \Omega_c, \omega_{f:1} = \Omega$. Therefore, at sub-critical speeds $\Omega < \Omega_c \Rightarrow \omega_{f:1} > \Omega$ and at super-critical speeds $\Omega > \Omega_c \Rightarrow \omega_{f:1} < \Omega$.

The modal solution Since the state matrix \mathbf{A} is non-symmetric with the $\mathbf{M}^{-1}\mathbf{K}_g$ block being a full matrix, using \mathbf{A} for free and forced response calculations can be rather taxing computationally for realistic FEA, due to the associated memory requirements, as well as being more prone to rounding-off errors. With \mathbf{A} being usually of a *simple structure*, it can be diagonalised by similarity transformations that preserve system properties, i.e. characteristic equation, eigensolutions and TFM. The right and left eigenvector matrices can be defined such that

$$\mathbf{A} = \mathbf{R}\mathbf{\Lambda}\mathbf{R}^{-1} \quad \mathbf{L}^T\mathbf{R} = \mathbf{I} \quad \mathbf{L}^T\mathbf{A}\mathbf{R} = \mathbf{\Lambda} \quad (3.37a)$$

$$\text{or } \mathbf{A}\mathbf{R} = \mathbf{R}\mathbf{\Lambda} \quad \mathbf{L}_i^T\mathbf{r}_j = \delta_{ij} \quad \mathbf{L}_i^T\mathbf{A}\mathbf{r}_j = \delta_{ij}\lambda_i \quad (3.37b)$$

stating that eigenvectors $\mathbf{r}_i, \mathbf{l}_i, i \in \{1, \dots, 2n\}$ are biorthonormal and $\mathbf{L}^T = \mathbf{R}^{-1}$, leading to:

$$[\lambda\mathbf{I} - \mathbf{A}]^{-1} = \mathbf{R}[\lambda\mathbf{I} - \mathbf{\Lambda}]^{-1}\mathbf{L}^T = \sum_{i=1}^{2n} \frac{\mathbf{r}_i\mathbf{l}_i^T}{\lambda - \lambda_i} \quad (3.38)$$

where $\mathbf{r}_i\mathbf{l}_i^T$ forms the i^{th} constituent (residue) matrix of \mathbf{A} .

The free and forced response of (3.14) can be obtained using the modal matrix \mathbf{R} (right

eigenvectors) in the similarity transformations¹:

$$\mathbf{p}(t) = \mathbf{R}\tilde{\mathbf{p}}(t)$$

$$\dot{\tilde{\mathbf{p}}} = \mathbf{R}^{-1}\mathbf{A}\mathbf{R}\tilde{\mathbf{p}} + \mathbf{R}^{-1}\mathbf{B}\mathbf{f} = \mathbf{\Lambda}\tilde{\mathbf{p}} + \tilde{\mathbf{B}}\mathbf{f} \quad (3.39a)$$

$$\mathbf{o} = \mathbf{O}\mathbf{R}\tilde{\mathbf{p}} = \tilde{\mathbf{O}}\tilde{\mathbf{p}} \quad (3.39b)$$

With $\mathbf{O} \equiv \mathbf{O}^d$ (3.15b), $\tilde{\mathbf{O}}_{n \times 2n}$ is simply a matrix of modal vectors $\hat{\mathbf{r}}_{v \in \{1 \dots 2n\}}$. If \mathbf{A} yields distinct $\lambda_s \therefore \mathbf{\Lambda} \stackrel{\text{def}}{=} \text{diag}\{\lambda_{v \in \{1 \dots 2n\}}\}$ and the resulting state equation (3.39) is modally uncoupled. Thus, the TFM of (3.23) can be expanded in modal partial fractions as:

$$\begin{aligned} \mathbf{H}(s) &= \tilde{\mathbf{O}}[s\mathbf{I} - \mathbf{\Lambda}]^{-1}\tilde{\mathbf{B}} = \sum_{v=1}^{2n} \frac{\tilde{\mathbf{o}}^{c_v} \tilde{\mathbf{b}}^{r_v}}{s - \lambda_v} = \sum_{v=1}^{2n} \frac{\mathbf{H}^v}{s - \lambda_v} = \sum_{v=1}^n \frac{\mathbf{H}^v}{s - \lambda_v} + \frac{\mathbf{H}^{v*}}{s - \lambda_v^*} \\ H_{ij}(s) &= \sum_{v=1}^{2n} \frac{\tilde{\mathbf{o}}_i^{c_v} \tilde{\mathbf{b}}_j^{r_v}}{s - \lambda_v} = \sum_{v=1}^{2n} \frac{H_{ij}^v}{s - \lambda_v} \quad \text{i.e.} \quad H_{ij}^v = \tilde{\mathbf{o}}_i^{c_v} \tilde{\mathbf{b}}_j^{r_v} = \tilde{\mathbf{O}}_{iv} \tilde{\mathbf{B}}_{vj} \end{aligned} \quad (3.40)$$

where $\mathbf{H}^v \equiv \lim_{s \rightarrow \lambda_v} (s - \lambda_v) \mathbf{H}(s)$ is the residue matrix for $\mathbf{H}(s)$ at the v^{th} mode. $\tilde{\mathbf{o}}^{c_v}$ is the v^{th} column of $\tilde{\mathbf{O}}$ and $\tilde{\mathbf{b}}^{r_v}$ is the v^{th} row of $\tilde{\mathbf{B}}$ with i^{th} and j^{th} elements being $\tilde{\mathbf{o}}_i^{c_v}$ and $\tilde{\mathbf{b}}_j^{r_v}$ respectively; which, in turn, are elements iv and vj of $\tilde{\mathbf{O}}$ and $\tilde{\mathbf{B}}$ respectively.

3.1.3.2. Modal analysis of 2DOF isotropic rotor

It is important and interesting to observe the relation between eigensolutions $\lambda_i, \hat{\mathbf{r}}_i$ in the stationary xy -frame and their corresponding $\lambda_{r:i}, \hat{\mathbf{r}}_{r:i}$ in the rotating $\xi\eta$ -frame, which is expressed formally in *p. 109*, as well as the resulting residue matrices $\mathbf{H}^v \equiv \mathbf{H}^{r:v}$.

Eigensolutions from complex formulation of the undamped rotor system An undamped rotor is one without the stabilising external damping or the destabilising RID. Although such a rotor is marginally stable and will not exhibit RID instability, its eigenvalues are presented here:

- For simplified illustration purposes
- Since its FWD modal frequency is used to determine Ω_{bn} the onset speed of instability, based on external/internal damping ratios in (4.22).

The complex 2×2 state matrices $\mathbf{A}_c, \mathbf{A}_{rc}$ (3.20, 3.21) yield the eigensolution pairs $(\lambda_c, \mathbf{r}_c)_i$ and $(\lambda_{rc}, \mathbf{r}_{rc})_{i \in \{1,2\}}$ respectively, which do not generally occur in complex-conjugate pairs as in the case of real formulations. Eigenvectors, e.g. $\mathbf{r}_{c:1,2} = \left\{ \begin{smallmatrix} \hat{r} \\ \lambda_r \end{smallmatrix} \right\}_{c:1,2}$, do not contribute to identifying the modal directionality since modal vectors reduce to $\hat{r}_{c:i}$ with no

¹Here v is used as a mode identifier to avoid conflict with subscript i used for $H_{ij} \in \mathbf{H}$

3. RID systems modelling and characteristics

lead/lag information of $\hat{r}_{x:i}$ to $\hat{r}_{y:i}$. As such, the i^{th} mode is represented as a rotating vector—of decaying magnitude for an externally damped rotor $\vec{Z}e^{(\lambda_{c:i})t} = \vec{Z}e^{\Re(\lambda_{c:i})t}e^{i(\omega_{c:i})t}$ where $\text{sgn}(\omega_{c:i})$ is the only representation of modal directionality.

In the stationary frame eigenvalues of the undamped rotor-bearing system are:

$$\lambda_{c:1,2} = i \left(\frac{\Omega\mathcal{G}}{2m} \mp \sqrt{\left(\frac{\Omega\mathcal{G}}{2m}\right)^2 + \frac{k}{m}} \right) = 0 + i\omega_{c:1,2} \quad (3.41)$$

As it stands, the square-root in (3.41) can be equally considered as +ve or -ve, however for the purposes of identifying modal directionality, as well as clarity and consistency, a square-root of positive real quantities is taken as positive throughout. Accordingly, ω_{c2} always has +ve value, while ω_{c1} always has -ve value. According to (3.36),

$$\begin{aligned} \therefore \quad & \Im(\lambda_{c1}) \equiv \omega_{c1} < 0 ; & \Im(\lambda_{c2}) \equiv \omega_{c2} > 0 \\ \therefore \quad & \lambda_{c1} \stackrel{\text{def}}{=} \lambda_b \Rightarrow \omega_{c1} \stackrel{\text{def}}{=} \omega_b ; & \lambda_{c2} \stackrel{\text{def}}{=} \lambda_f \Rightarrow \omega_{c2} \stackrel{\text{def}}{=} \omega_f \end{aligned}$$

with ω_f and ω_b being the FWD and BWD modal frequencies respectively. It is obvious from (3.41, 3.42) that both $\omega_{b,f}$ increase with increasing speed. In the case of ω_b , simple trigonometry dictates

$$0 > \omega_b = \frac{\Omega\mathcal{G}}{2m} - \sqrt{\left(\frac{\Omega\mathcal{G}}{2m}\right)^2 + \frac{k}{m}} > -\sqrt{\frac{k}{m}} \quad \forall \Omega > 0 \quad (3.42)$$

that ω_b increases from a -ve value to a lesser -ve value as Ω increases (*fig. 4.2*), hence its absolute value $|\omega_b|$ decreases with increased speed in agreement with (3.36).

In the rotating frame eigenvalues of the undamped rotor-bearing system are:

$$\lambda_{rc:1,2} = i \left(-\Omega + \frac{\Omega\mathcal{G}}{2m} \mp \sqrt{\left(\frac{\Omega\mathcal{G}}{2m}\right)^2 + \frac{k}{m}} \right) \quad (3.43a)$$

$$\equiv \lambda_{c:1,2} - i\Omega = \lambda_{b,f} - i\Omega = i(\omega_{b,f} - \Omega) \quad \because \Re(\lambda_{b,f}) = 0 \quad (3.43b)$$

Observe the relation (3.43b) between $\lambda_{c:i}$ (3.41) in xy -plane and their corresponding $\lambda_{rc:i}$ (3.43) in $\xi\eta$ -plane, which is exemplified in *figs. 4.2, 4.3*.

The Critical speed Ω_c of this undamped 2DOF rotor-bearing system is arrived at by setting $\omega_f = \Omega$ in (3.41) or $\omega_{r2} = 0$ in (3.43), which result in:

$$\Omega_c = \sqrt{\frac{k}{m - \mathcal{G}}} \quad (3.44)$$

Due to their significance, the FWD modal frequency of this undamped rotor system and its critical speed will be designated ω_{fu} and Ω_{cu} respectively.

Modal analysis with real representation of damped 2DOF rotor (3.2, 3.8) $\because \mathbf{A} \stackrel{\text{def}}{=} \text{real}$, its eigenvalues are those of the complex representation (e.g. 3.41, 3.43) and their complex conjugates:

$$\lambda_{1,2} = \lambda_{c:1,2}, \lambda_{3,4} = \lambda_{c:1,2}^*, \quad \lambda_{r:1,2} = \lambda_{rc:1,2}, \lambda_{r:3,4} = \lambda_{rc:1,2}^*$$

In the stationary frame the eigenvalues and modal vectors are:

$$\lambda_{1,2} = -\frac{c}{2m} + i\frac{\Omega\mathcal{G}}{2m} \mp i\sqrt{\left(\frac{\Omega\mathcal{G} + ic}{2m}\right)^2 + \frac{k}{m}} \quad \hat{\mathbf{r}}_{1,2} = \begin{Bmatrix} i\hat{r}_y \\ \hat{r}_y \end{Bmatrix}_{1,2} \quad (3.45a)$$

$$\lambda_{3,4} = -\frac{c}{2m} - i\frac{\Omega\mathcal{G}}{2m} \pm i\sqrt{\left(\frac{\Omega\mathcal{G} - ic}{2m}\right)^2 + \frac{k}{m}} \quad \hat{\mathbf{r}}_{3,4} = \begin{Bmatrix} \hat{r}_x \\ i\hat{r}_x \end{Bmatrix}_{3,4} \quad (3.45b)$$

In (3.45a), $\hat{r}_x = i\hat{r}_y \Rightarrow |\hat{r}_x| = |\hat{r}_y|$ representing a circular modal precession where x leads y by $\pi/2$ in the direction of rotation indicated by $\text{sgn}(\omega_{1,2})$. (3.45b) is a similar scenario with x lagging y . Together, $\omega_i \equiv \Im(\lambda_i)$ and $\hat{\mathbf{r}}_i$ elucidate the i^{th} mode's directionality, in accordance with (3.35) and agreement with (3.41). When the eigenvalues λ_i with the familiar and physically interpretable $\omega_i > 0$ (i.e. $\lambda_{2,3} \equiv \lambda_f, \lambda_b^*$) are plugged in (3.33a): $\lambda_2 \Rightarrow \hat{\mathbf{r}}_2 \equiv \odot$ a FWD mode, and $\lambda_3 \Rightarrow \hat{\mathbf{r}}_3 \equiv \ominus$ a BWD mode.

Although \mathbf{S} of (3.2, 3.2b) is defined with proportional damping $\mathbf{C} = \alpha\mathbf{M} + \beta\mathbf{K}$, the skew-symmetry introduced by \mathbf{G} renders \mathbf{C}_g not proportional to \mathbf{K} and/or \mathbf{M} , hence

$$\gamma_i \neq \frac{\beta\hat{\omega}_i}{2} + \frac{\alpha}{2\hat{\omega}_i} \quad \text{where} \quad \hat{\omega}_i = \frac{|\omega_i|}{\sqrt{1 - \gamma_i^2}} \quad \text{and} \quad \Re(\lambda_i) = -\gamma_i\hat{\omega}_i$$

Actually, the coexistence of isotropy and proportional viscous \mathbf{C} results in:

$$\frac{\Re(\lambda_f)}{|\Im(\lambda_f)|} = \frac{\Re(\lambda_b)}{|\Im(\lambda_b)|} = \frac{\Re(\lambda_i)}{|\Im(\lambda_i)|} = \frac{-\gamma_i}{\sqrt{1 - \gamma_i^2}}, \forall i \in 1 \dots 4 \quad \Rightarrow \quad \gamma_b \equiv \gamma_f \quad (3.46)$$

stating that the damping factor γ_i is identical for the four modes derived at constant Ω . Accordingly (3.34), the FWD modes decay faster than the BWD modes, e.g. *fig. 4.2*,

3. RID systems modelling and characteristics

$\because \forall \Omega \neq 0, |\omega_f| > |\omega_b| \Rightarrow \Re(\lambda_f) < \Re(\lambda_b)$. Usually, as $\Omega : [0 \triangleright)$, $\Re(\lambda_f) \searrow$ and $\Re(\lambda_b) \nearrow$, which is tempting to generalise as in p.241. However, the above is not sufficient to make such a generalisation without further examination, e.g.(A.5) since γ varies with Ω and with parameters (4.2), $\Omega : [0 \triangleright) \Rightarrow \gamma \searrow$, (fig 4.4).

In the rotating frame the eigenvalues and modal vectors are:

$$\lambda_{r:1,2} = -\frac{c}{2m} + \imath \left(\frac{\Omega \mathcal{G}}{2m} - \Omega \right) \mp \imath \sqrt{\left(\frac{\Omega \mathcal{G} + \imath c}{2m} \right)^2 + \frac{k}{m}} \quad \hat{\mathbf{r}}_{r:1,2} = \left\{ \begin{array}{l} \imath \hat{r}_\eta \\ \hat{r}_\eta \end{array} \right\}_{r:1,2} \quad (3.47a)$$

$$\lambda_{r:3,4} = -\frac{c}{2m} - \imath \left(\frac{\Omega \mathcal{G}}{2m} - \Omega \right) \pm \imath \sqrt{\left(\frac{\Omega \mathcal{G} - \imath c}{2m} \right)^2 + \frac{k}{m}} \quad \hat{\mathbf{r}}_{r:3,4} = \left\{ \begin{array}{l} \hat{r}_\xi \\ \imath \hat{r}_\xi \end{array} \right\}_{r:3,4} \quad (3.47b)$$

Relation of corresponding eigensolution pairs in xy - and $\xi\eta$ -frames

The relation of corresponding modal frequencies in xy - and $\xi\eta$ -frames $\omega_{ci} \Leftrightarrow \omega_{rc:i}$ expressed in (3.43b) is logical, according to (2.7), since an isolated undamped mode represented by a vector $\vec{Z}e^{\imath(\omega_{ci})t}$ that is rotating in the xy -frame is observed from the $\xi\eta$ -frame as $\vec{Z}e^{\imath(\omega_{ci}-\Omega)t} \equiv \vec{Z}e^{\imath(\omega_{rc:i})t}$. Consequently, at super-critical speeds $\Omega > \Omega_c$, both of the rotating frame modal frequencies $\omega_{rc:1,2} < 0 \because \omega_{c:1,2} < \Omega$ (fig. 4.3) resulting in \odot rotating vectors; i.e. both modes represent a CW \odot circular precession at their modal frequency in the $\xi\eta$ -frame.

This logical relation (3.43b) applies equally to eigenvalues of real representations:

$$\lambda_{r:1,2} \equiv \lambda_{b,f} - \imath\Omega = \Re(\lambda_{1,2}) + \imath(\omega_{1,2} - \Omega) \quad (3.48a)$$

which is obvious on comparing (3.45a) and (3.47a), and leads to:

$$\lambda_{r:3,4} \equiv \lambda_{r:1,2}^* = \Re(\lambda_{1,2}) - \imath(\omega_{1,2} - \Omega) \quad (3.48b)$$

Naturally, $\Re(\lambda_i) \equiv \Re(\lambda_{r:i})$ as the decay constant is unaffected by the coordinate transformation, which logically affects $\Im(\lambda_i) \Leftrightarrow \Im(\lambda_{r:i})$ the modal frequencies only—figs. 4.2, 4.3. In turn, this renders the damping factors $\gamma_{r:i \in 1 \dots 4}$ of modes in the $\xi\eta$ frame not necessarily equal (e.g. fig 4.4), which is contrary to the case (3.46) of the xy frame:

$$\gamma_{r:1} \neq \gamma_{r:2} \because \gamma_{r:i} = \gamma_i \frac{\hat{\omega}_i}{\hat{\omega}_{r:i}} \text{ hence } \gamma_{r:1} \approx \gamma \frac{|\omega_b|}{|\omega_b| + \Omega} \text{ and } \gamma_{r:2} \approx \gamma \frac{\omega_f}{|\omega_f - \Omega|} \quad (3.49)$$

Invariance of corresponding modal vectors and residue matrices By (3.45, 3.47), the rotating frame modal vectors $\hat{\mathbf{r}}_{\in \{r:1 \dots 4\}}$ have the same structure as their corresponding

stationary frame counterparts $\hat{\mathbf{r}}_{\in\{1\dots 4\}}$. Although corresponding modal vectors are structurally invariant under transformations from xy - to $\xi\eta$ -frames-of-reference, they can be scaled differently:

$$\begin{aligned}\hat{\mathbf{r}}_b &\stackrel{\text{def}}{=} \hat{\mathbf{r}}_1 \propto_b \hat{\mathbf{r}}_{r:1} \\ \hat{\mathbf{r}}_f &\stackrel{\text{def}}{=} \hat{\mathbf{r}}_2 \propto_f \hat{\mathbf{r}}_{r:2}\end{aligned}\tag{3.50}$$

in accordance with the modal matrix \mathbf{R} normalisation (3.37), hence generally, $\mathbf{R} \neq \propto \mathbf{R}_r$.

With the modal vector invariance (3.50), if we implement the same input and output matrices \mathbf{B}, \mathbf{O} for defining both $\mathcal{S}(\mathbf{A}, \mathbf{B}, \mathbf{O})$ and $\mathcal{S}_r(\mathbf{A}_r, \mathbf{B}, \mathbf{O})$, then the corresponding residue matrices are identical, in accordance with (3.40):

$$\mathbf{H}^v \equiv \mathbf{H}^{r:v} \text{ with } v \in \{1 \dots 4\}\tag{3.51}$$

3.1.4. Characteristics of rotordynamic TFM/FRM

Frequency response (FR) stability analysis methods are adopted and modified to suit the RID problem. It is necessary to examine the relevant TFM/FRM characteristics.

3.1.4.1. Properties of TFM and its individual TFs

It is imperative that all system modes be represented for *observation* in the specific transfer function (in the TFM) that is being analysed for system modes stability.

Controllability & Observability concepts in the time domain are associated with the ability to *control* the state variables $\in \mathbf{p}$, and *evaluate* them from the available output variables $\in \mathbf{o}$ of \mathcal{S} in (3.14). \mathcal{S} is *completely state controllable* if it is possible to construct an unbounded $\mathbf{f}(t)$ that will transfer any initial state $\mathbf{p}(t_0)$ to any final state $\mathbf{p}(t)$ in a finite time. Ranks of *state controllability* \mathbf{C}_{on} and *observability* \mathbf{O}_{bs} matrices

$$\mathbf{C}_{\text{on}} = [\mathbf{B} \ \mathbf{A}\mathbf{B} \ \mathbf{A}^2\mathbf{B} \ \dots \ \mathbf{A}^{2n-1}\mathbf{B}] \quad , \quad \mathbf{O}_{\text{bs}} = \begin{bmatrix} \mathbf{O} \\ \mathbf{O}\mathbf{A} \\ \vdots \\ \mathbf{O}\mathbf{A}^{2n-1} \end{bmatrix}\tag{3.52}$$

are standard checks for controllability of the LTI pair $(\mathbf{A}, \mathbf{B}) \subset \mathcal{S}(\mathbf{A}, \mathbf{B}, \mathbf{O})$ and observability of $(\mathbf{A}, \mathbf{O}) \subset \mathcal{S}(\mathbf{A}, \mathbf{B}, \mathbf{O})$: $\text{rank}(\mathbf{C}_{\text{on}}) = 2n \Rightarrow (\mathbf{A}, \mathbf{B}) \stackrel{\text{def}}{=} \text{controllable}$, and $\text{rank}(\mathbf{O}_{\text{bs}}) = 2n \Rightarrow (\mathbf{A}, \mathbf{O}) \stackrel{\text{def}}{=} \text{observable}$. As such, the systems \mathcal{S} defined by (3.22, 3.23, 3.26, 3.28) are completely controllable and observable. Actually, these systems will still be completely controllable and observable even if only one output is observed and only one

3. RID systems modelling and characteristics

input is controlled, *provided the EOMs are maintained coupled*; i.e. $\Omega\mathcal{G} \neq 0$ unlike (3.58). For instance, $H_{21}^d(s) \in \mathbf{H}^d(s)$ (3.26) is a TF representing a SISO \mathbf{S}_L (3.24), with $f_x(t)$ and $y(t)$ being the controlled input and observed output respectively, which is equivalent to the completely controllable and observable $\mathbf{S}_L(\mathbf{A}, \mathbf{B}, \mathbf{O})$ with $\mathbf{O} = [0100]$, $\mathbf{B} = \frac{1}{m}[0010]^T$ and \mathbf{A} of (3.17).

Individual transfer functions $H_{ij}(s) \in \mathbf{H}(s)$ are rational polynomial functions:

$$\begin{aligned} H_{ij}(s) &= \frac{\acute{b}_u s^u + \acute{b}_{u-1} s^{u-1} + \cdots + \acute{b}_1 s + \acute{b}_0}{\acute{a}_l s^l + \acute{a}_{l-1} s^{l-1} + \cdots + \acute{a}_1 s + \acute{a}_0} \\ &= \frac{1/\acute{a}_l}{1/\acute{a}_l} H_{ij}(s) \stackrel{\text{def}}{=} \frac{N_{ij}(s)}{D(s)} = \frac{\frac{1}{\acute{a}_l} (\acute{b}_u s^u + \acute{b}_{u-1} s^{u-1} + \cdots + \acute{b}_1 s + \acute{b}_0)}{D(s)} \\ &= \frac{g_{ij} (s^u + b_{u-1} s^{u-1} + \cdots + b_1 s + b_0)}{D(s)} \quad \therefore \quad g_{ij} = \frac{\acute{b}_u}{\acute{a}_l} \end{aligned} \quad (3.53)$$

An individual $H_{ij}(s)$ that represents a completely controllable and observable SISO \mathbf{S}_L is required to account for all the modes of \mathbf{A} and their respective eigenvalues that are given by the characteristic equation (3.29). Therefore the characteristic polynomial $D(s) = |s\mathbf{I} - \mathbf{A}|$ has to be presented intact with its highest order being $l = 2n$. This requires that $D(s)$ and $N_{ij}(s)$ be co-prime; i.e. no common factors. The difference in degrees of $D(s)$ and $N_{ij}(s)$ polynomials ($l - u$) is known as the *relative order*. All individual TFs $H_{ij} \in \mathbf{H}(s)$ (3.24, 3.53) are *strictly proper*, since always $u < l \therefore \mathbf{D} = \mathbf{0}$ (3.13b, 3.14).

Poles-Zeros-Gain representation If polynomials $D(s)$ and $N_{ij}(s)$ are co-prime, their respective roots are the full sets of poles $p_{1\dots l}$ and *finite* zeros $o_{1\dots u}$ of $H_{ij}(s)$ in (3.53), which can be represented as:

$$H_{ij}(s) = g_{ij} \frac{\prod_{q=1}^u (s - o_q)}{\prod_{v=1}^l (s - p_v)} \quad \text{for } u \neq 0 \quad (3.54)$$

Although the number of finite zeros is always less than that of poles in our strictly proper TFs $\therefore u < l$, the total number of zeros—including those at $s = \infty$ —is equal to number of poles.

Pole polynomial of $\mathbf{H}(s)$ Because the MIMO $\mathbf{S}(\mathbf{A}, \mathbf{B}, \mathbf{O})$ of (3.22, 3.23, 3.26, 3.28) are completely controllable and observable, the characteristic polynomial $D(s)$ of $H_{ij}(s)$ is also the *pole polynomial* of $\mathbf{H}(s)$, which is the common denominator polynomial $\forall H_{ij}(s) \in \mathbf{H}(s)$. In this case, poles of $\mathbf{H}(s)$ and eigenvalues of \mathbf{A} are identical: $D(s) = D(\lambda) \Rightarrow p_{v \in \{1\dots l=2n\}} \equiv \lambda_{v \in \{1\dots 2n\}}$ —compare *figs. 4.2-4.7*—and poles can be used instead of eigenvalues in partial-

fraction expansions (3.40) as:

$$\mathbf{H}(s) = \sum_{v=1}^n \frac{\mathbf{H}^v}{s - p_v} + \frac{\mathbf{H}^{v*}}{s - p_v^*} \quad \text{and} \quad H_{ij}(s) = \sum_{v=1}^n \frac{H_{ij}^v}{s - p_v} + \frac{H_{ij}^{v*}}{s - p_v^*} \quad (3.55)$$

Zeros of $\mathbf{H}(s)$ are transmission zeros, since the transmission of such ‘complex frequencies’ is blocked throughout \mathbf{S} ; a situation that does not occur in our rotors. However, different $H_{ij}(s)$ do have their specific finite zeros o_q , which usually differ in number and value for each $H_{ij}(s)$. Zeros of individual TFs are the result of all the modal partial-fraction terms in (3.55) cancelling out (summing to nil) at specific complex frequencies $s = o_{q \in \{1 \dots u\}}$. Due to the complex-conjugate nature of such terms, finite zeros occur as purely real, or in complex-conjugate pairs in-between two consecutive modal terms. *Almost always*, a mechanical \mathbf{S} will have point TFs that exhibit zeros in-between poles (e.g. *fig. 4.7*), and quad (transfer) TFs *without* zeros in-between poles, yet possibly with a zero at $s = 0$ if any [49].

xy-frame zeros and gains of $H_{11}^d(s) = H_{22}^d(s)$ and $H_{12}^d(s) = -H_{21}^d(s)$ in $\mathbf{H}^d(s)$ (3.26) are:

$$N_{11}^d(s) = \frac{s^2 m + sc + k}{m^2} \quad \Rightarrow \quad o_{1,2} = -\frac{c}{2m} \mp \sqrt{\frac{k}{m} - \left(\frac{c}{2m}\right)^2} \quad g_{11}^d = 1/m \quad (3.56a)$$

$$N_{21}^d(s) = \frac{s\Omega\mathcal{G}}{m^2} \quad \Rightarrow \quad o_1 = 0 \quad g_{21}^d = \Omega\mathcal{G}/m^2 \quad (3.56b)$$

which expresses that zeros are not speed-dependent in the xy -frame.

$\xi\eta$ -frame zeros and gains of $H_{r:ij}^d$ are a bit more interesting, with $N_{r:11}^d(s) = N_{r:22}^d(s)$ and $N_{r:12}^d(s) = -N_{r:21}^d(s)$

$$N_{r:11}^d(s) = \frac{s^2 m + sc + k + \Omega^2(\mathcal{G} - m)}{m^2} \quad \Rightarrow \quad o_{1,2} = \frac{-c \pm \sqrt{c^2 - 4m(k + \Omega^2(\mathcal{G} - m))}}{2m} \quad (3.57a)$$

$$N_{r:21}^d(s) = \frac{-(s\Omega(2m - \mathcal{G}) + \Omega c)}{m^2} \quad \Rightarrow \quad o_1 = \frac{-c}{2m - \mathcal{G}} \stackrel{\text{def}}{=} \text{‘purely real’} \quad (3.57b)$$

The gains are $g_{r:11}^d = \frac{1}{m}$ and $g_{r:21}^d = \frac{-\Omega(2m - \mathcal{G})}{m^2}$, the latter being -ve—usually $2m > \mathcal{G}$. By (3.57a), zeros $o_{1,2}$ of the $\xi\eta$ -frame point TFs will be complex for speeds upto Ω_c , afterwhich they assume real values of opposite signs (e.g. *figs.4.7*). With $c = 0$, (3.57a) yields complex $o_{1,2}$ for $\Omega < \Omega_c \equiv \sqrt{\frac{k}{m - \mathcal{G}}}$.

Incomplete controllability & observability Had $\mathbf{S}(\mathbf{A}, \mathbf{B}, \mathbf{O})$ not been completely controllable and observable, there would have been *pole-zero cancellations* $\forall \frac{N_{ij}(s)}{D(s)}$ and $\mathbf{H}(s)$ poles would have been just a subset of $\lambda_{v \in \{1 \dots 2n\}}$ of \mathbf{A} . This would have meant that certain

modes of $\mathbf{S}(\mathbf{A}, \mathbf{B}, \mathbf{O})$ would have not been excitable or observable from any \mathbf{S} input or output. Although this does not occur since our MIMO \mathbf{S}_L is controllable and observable, pole-zero cancellations may occur in certain $H_{ij(s)} = \frac{N_{ij(s)}}{D(s)}$ that do not represent a completely controllable and observable SISO \mathbf{S}_L . The modes cancelled out cannot be influenced or observed from this particular TF, although they can be influenced/observed from other TFs in the controllable and observable MIMO TFM. In rotordynamics, this will happen when the EOMs' coupling is lost, which is equivalent to $\Omega\mathcal{G} = 0$ in (3.2). An example would be the 2DOF rotor on orthotropic bearings, whose controllable and observable TFM representation (3.25) without gyroscopic coupling $\Omega\mathcal{G} = 0$ is:

$$\mathbf{H}_{\text{Orth}}^{d(s)} = \frac{1}{|\mathbf{S}|} \begin{bmatrix} s^2m + sc + k - \Delta k & 0 \\ 0 & s^2m + sc + k + \Delta k \end{bmatrix} \quad (3.58)$$

where $|\mathbf{S}| = s^4m^2 + 2s^3mc + s^2(c^2 + 2mk) + 2skc + k^2 - \Delta k^2$

$$\hookrightarrow \mathbf{H}^{d(s)} = \begin{bmatrix} 1/(s^2m + sc + k + \Delta k) & 0 \\ 0 & 1/(s^2m + sc + k - \Delta k) \end{bmatrix}$$

Minimum-/non-minimum-phase transfer functions Most stable physical systems have minimum-phase characteristics e.g. (3.56), with exceptions e.g. (3.57a) when $\Omega > \sqrt{\frac{k}{m-\mathcal{G}}}$. Such characteristics are used in conjunction with Nyquist-like criteria. They are also to be used here (§ 4.3) to examine \mathbf{S} for unstable poles and eigenvalues $\Re(p) > 0 \Rightarrow \Re(\lambda) > 0$.

Definition 3.1 A minimum-phase $H_{ij(s)}$ will have no poles or zeros in the right-half s -plane or on its ω -axis, excluding its origin ($s = 0$):

$$\Re(p, o) < 0, \forall \{p, o\} \neq 0$$

A non-minimum-phase transfer function will have at least one zero or pole in the right-half s -plane.

Positive Real (PR) and Strictly Positive Real (SPR) transfer functions are defined in terms of their Nyquist plot and their stability characteristics. These characteristics, if true, would allow for generating Lyapunov functions that are interpretable physically.

Theorem 3.1 (PR/SPR transfer functions) If

$$\Re(H(s)) \geq 0 \quad \forall \Re(s) \geq 0 \Rightarrow H(s) \stackrel{\text{def}}{=} \text{PR}$$

$$\Re(H(s - \epsilon)) \geq 0 \quad \forall \Re(s) \geq 0, \text{ any } \epsilon > 0 \Rightarrow H(s) \stackrel{\text{def}}{=} \text{SPR}$$

Theorem (3.1) implies simple *necessary conditions* for asserting if $H(s) \stackrel{\text{def}}{=} \text{SPR}$:

1. $H(s)$ is strictly stable
2. The Nyquist plot of $H(j\omega)$ lies entirely in the right-half complex H -plane
3. $H(s)$ has a relative order $l - u = 0, 1$.
4. $H(s)$ is strictly minimum-phase: zeros & poles strictly in left-half s -plane

The basic difference is that unlike SPR, PR will tolerate poles on $\Im(s), j\omega$ axis. The concept of PR/SPR $H(s)$ can be extended to $\mathbf{H}(s)$ so as to handle MIMO systems:

Definition 3.2 A square TFM $\mathbf{H}(s) \stackrel{\text{def}}{=} \text{PR}$ if:

- $H_{ij} \in \mathbf{H}(s)$ are analytic $\forall \Re(s) > 0$
- $\mathbf{H} + \mathbf{H}^{*T} \equiv \text{PSD} \forall \Re(s) > 0$
- $\mathbf{H}(s) \stackrel{\text{def}}{=} \text{SPR}$ if $\mathbf{H}(s - \epsilon) \stackrel{\text{def}}{=} \text{PR}$ for any $\epsilon > 0$

On examining $H_{ij} \in \mathbf{H}(s)$ of (3.28, 3.26) we find that all H_{ij} are *not* PR/SPR. Although all H_{ij} satisfy condition 1—no destabilising mechanisms considered yet—they fail to satisfy conditions 2,3 and sometimes 4. With definition (3.2) we conclude that the TFMs $\mathbf{H}(s)$ of (3.28, 3.26) are *not* PR/SPR.

3.1.4.2. Frequency response matrix and its FRFs

The frequency response matrix (FRM) $\mathbf{H}(j\omega)$ and its individual FRFs $H_{ij}(j\omega)$ are obtained simply by substituting s in $\mathbf{H}(s)$ with $j\omega$. Each FRF $H_{ij}(j\omega) = \frac{\bar{q}_i(j\omega)}{f_j(j\omega)} \stackrel{\text{def}}{=} \text{complex ratio}$ of steady-state output to input sinusoids. The more formal description of an FRF is *conformal mapping* (part of) the imaginary $j\omega$ -axis of the s -plane (*fig. 4.7*) onto the complex H -plane via $H_{ij}(s) : s = j\omega \xrightarrow[\omega_a \triangleright \omega_b]{H(s)} H(j\omega)$, which is widely known as a polar (or Nyquist) plot, e.g *figs. 4.8, 4.9*. On the magnitude plot $|H_{ij}(j\omega)|$, $\Im(p_{1,\dots,i})$ and $\Im(o_{1,\dots,u})$ are frequencies, around which an FRF exhibits resonances and anti-resonances ($|H_{ij}(j\omega)| \gtrsim 0$) respectively; i.e. are very close, but generally not identical, to frequencies of resonances and anti-resonances, provided \mathbf{S} is not excessively damped.

Normality of the FRM $\mathbf{H}(j\omega)$ is defined in terms of $\mathbf{H}^{*T} = (\mathbf{H}^*(j\omega))^T$ its *associate matrix*, which is the conjugate transposed of $\mathbf{H}(j\omega)$. $\mathbf{H}(j\omega)$ is *normal* If:

$$\mathbf{H}(j\omega)\mathbf{H}^{*T}(j\omega) = \mathbf{H}^{*T}(j\omega)\mathbf{H}(j\omega) \quad (3.59)$$

The TFMs in the stationary (3.26) and rotating (3.28) frames and their FRMs have been examined for condition (3.59) which was satisfied, hence the FRMs are normal.

Diagonal dominance (DD) of $\mathbf{H}(i\omega)$ is defined terms of its relative magnitudes $|H_{ij}|$.

$$\begin{aligned}
 |H_{ii}| &> \sum_{j=1}^n |H_{ij}| && \forall i \in \{1, \dots, n\} j \neq i \Rightarrow \text{Row dominance} \\
 |H_{ii}| &> \sum_{j=1}^n |H_{ji}| && \forall i \in \{1, \dots, n\} j \neq i \Rightarrow \text{Column dominance} \\
 |H_{ii}| &> \sum_{j=1}^n (|H_{ij}| + |H_{ji}|)/2 && \forall i \in \{1, \dots, n\} j \neq i \Rightarrow \text{Mean dominance}
 \end{aligned}$$

Equation (3.56) shows that $H_{11}, H_{22} \in \mathbf{H}(s)$ of (3.26) will exhibit anti-resonances around $\omega = \Im(o_{1,2})$ where both $|H_{11}|, |H_{22}| \gtrsim 0$ i.e. *very close to zero*. On the other hand, each of $H_{12}, H_{21} \in \mathbf{H}(s)$ has a single real o_1 at the origin of the s -plane. This argument suggests that around $\omega = \Im(o_{1,2}), |H_{11}| < |H_{12}| \Rightarrow \mathbf{H} \neq \text{DD}$. On examining the FRMs of (3.26, 3.28) in *figs. 4.8, 4.9*, it is found that $\forall \omega > 0$ between the two poles with $\Im(p) > 0, \mathbf{H}(i\omega), \mathbf{H}_r(i\omega) \neq \text{DD}$; of course the same goes for the complex conjugate of the frequency range. However, both $\mathbf{H}, \mathbf{H}_r \stackrel{\text{def}}{=} \text{DD}$ outside these ranges.

3.2. RID characteristics and modelling

Rotor joints are a prominent source² of localised stiffness and damping nonlinearities, and are the prime source of RID in industrial rotors (non-composite nor viscoelastic) where material damping is virtually negligible [180]. However, rotor couplings are modelled regularly as linear elastic components possibly with inertia [47]. For simplistic stability analysis of relatively large systems, RID from such couplings is modelled as linear viscous elements that are stacked parallel to the elastic elements (2.40). Occasionally, ideal linear hysteretic RID is used in the same manner, which may be a rather misleading.

Linear modelling is arguably justified by the small vibration amplitudes that rotors are designed to endure. Some couplings however, e.g. splines especially un-piloted ones, exhibit obvious nonlinear behaviour even at low vibration amplitudes, in which case a nonlinear joint model is necessary if the dynamic predictions are to be relied upon. Indeed, RID-induced precession, which can be predicted only by analysing a nonlinear model, is observed mainly in rotors with interference-fits and/or spline couplings. Both such joints result in nonlinear stiffness and damping, yet spline couplings exhibit nonlinear characteristics that are pronounced strongly, which sometimes under certain disturbances leads to unbounded precession.

Modelling RID properly for further analysis entails two important tasks:

²Other sources of nonlinearity are the various rotor-stator interactions

1. Use of a representative friction joint model
2. Introducing this model appropriately in the rotordynamic system

Both of which are presented hereafter.

3.2.1. Models of general nonlinear joints with friction damping

Damping here defines the energy dissipated under cyclic loading that results in a hysteresis loop (external force-displacement), with ΔE being the area inside it:

$$\Delta E = \oint f_x dx \quad (3.60)$$

representing the total energy absorbed per cycle. It is relatively straightforward to acquire experimentally hysteresis loops of structural joints and materials, which are found to be symmetric about their centre points. However, except for the simplest cases, rheological (differential) models (equations) of form (3.61) are virtually unavailable to regenerate hysteresis loops, in which case hybrid models (3.69-3.72) need be relied upon.

Rotor joints' physical characteristics (inertia, stiffness and damping) have a considerable effect on the dynamic behaviour and accordingly, an accurate mathematical model is rather important for reliable predictions. Although such joints usually have nonlinear stiffness and damping characteristics, they are modelled regularly as linear elastic components with isotropic translational or rotational stiffness coefficients k, \widehat{k} (2.39) between the two rotor stations at the ends of rotor segments that are coupled. One reason is that nonlinear joint models are difficult to obtain let alone generalise under various conditions. This is particularly the case when nonlinear friction is involved since friction forces and the energy hence dissipated depend on numerous factors which cannot all be modelled simultaneously in a dynamic model. Some rheological rotor joint models in the form of (3.61b) have been derived from the joint's geometry and surface conditions with Coulomb friction at the interface, e.g (2.43), and implemented in a time domain analysis. These are rather simplified, hardly reliable and are at best representative qualitatively. Another issue to bear in mind whilst modelling joints is that some important friction characteristics vary significantly during operation as well as with time and repeated usage e.g. temperature, lubrication and surface-finish.

3.2.1.1. Fundamentals of modelling general nonlinear friction joints

A friction joint generally describes any connection of two structural members, where two surfaces are pressed together by a normal force N applied through clamping or interference mechanisms. With this definition, the clamped edge of a panel, the root of a turbine blade,

rotor couplings and fits are joints with friction at their contact surface, which is referred to as the interface. Damping, as defined in (3.60), results from the interfaces' relative tangential motion.

The route to arriving at a friction joint's model Since a friction joint is largely characterised by its hysteresis loop, its model is expected to predict and regenerate this loop as accurately as possible. Two factors have a marked influence on a joint's damping characteristics, namely: 1) The clamping force N , which may range from loose as in an un-piloted spline coupling to very tight as in a Curvic coupling, and 2) Interfaces' finish/treatment, identifying the many parameters of which can prove to be a seriously elusive goal. Generally, joint models fall in two categories: Rheological and Hybrid.

A general joint rheological model is an input-output model relating 'restoring' force \mathcal{F} to displacement and/or velocity and possibly inertia as in:

$$\mathcal{F}_{\text{lin}} = m\ddot{x} + c\dot{x} + kx \quad (3.61a)$$

$$\mathcal{F}_{\text{SVNL}}(\dot{x}) = m\ddot{x} + c_{\text{NL}}(\dot{x})\dot{x} + kx \quad (3.61b)$$

$$\mathcal{F}_{\text{MVNL}}(\dot{x}, x, t) = m\ddot{x} + c_{\text{NL}}(x, \dot{x})\dot{x} + k_{\text{NL}}(x, \dot{x})x \quad (3.61c)$$

All equations of (3.61) are intended to describe an autonomous system with time-invariant coefficients. While (3.61a) is the usual linear EOM, the rest have nonlinear damping $c_{\text{NL}}(x, \dot{x})$ and stiffness $k_{\text{NL}}(x, \dot{x})$ coefficients, which are functions of displacement and/or velocity. (3.61 b) expresses a single valued nonlinearity (SVNL) \mathcal{F} that is uniquely defined against \dot{x} as in (*fig.3.2*). (3.61 c) expresses the more general \mathcal{F} as a nonlinear function of both displacement and velocity, and accordingly is not single valued with either on its own. This is reflected in \mathcal{F} being a function of t that is not explicit in the model, which denotes a nonlinearity with memory, i.e. $\mathcal{F}_{\text{MVNL}}$ is a multi-valued nonlinearity (MVNL) depending on current state (x, \dot{x}) as well as state history. Such rheological models are at best difficult to derive for a nonlinear joint with any degree of complexity, geometric or physical, particularly when friction is involved.

Implementing hybrid techniques to model a general nonlinear joint is another popular approach that utilises both analytical and experimental data, which have been developed to produce fairly accurate models, particularly for hysteresis loops. The joint model and its coefficients are validated by correlating to experimental results. For analysis purposes, these techniques serve best when the joint model is derived separately as a substructure that is subsequently coupled to a target substructures to form the overall (mechanical) structure. Since understanding the nature and configuration of a joint is

essential to derive a suitable dynamic model, the most effective path to defining such a model [100, 131, 151] probably is:

1. *Study joint's dynamic characteristics.* Typically, this is carried out through a set of static as well as dynamic tests to define a restoring force-response relationship. External force is chosen appropriately leading to responses that are as representative as possible of operating conditions, so as to characterise the nonlinear joint. Harmonic excitation is favoured for characterising a nonlinear joint due to its precision and controllability of variables e.g. frequency, response or excitation amplitudes.
2. *Develop an accurate general mathematical model.* This is the challenge and the resulting model is restricted to test parameters e.g. type of excitation, frequency range, amplitudes of force and response, etc.
3. *Identify parameters of proposed model.* For many-parameter models, this usually involves an iterative model updating process. For simpler models and joints e.g. cubic stiffness, curve-fitting the force-response relation does the trick.

Friction joints models can take the familiar but difficult to derive rheological:

$$\mathcal{F}(\dot{x}, x, t) = c_{\text{NL}}(x, \dot{x})\dot{x} + k_{\text{NL}}(x, \dot{x})x \quad (3.61d)$$

which is thus restricted to simple friction elements (3.68) and hence unrepresentative, but may be used for preliminary qualitative investigations. Alternatively, the more widely implemented hybrid techniques are used, where an analytical rule (*p.118*) is applied to a load-deformation relation $\mathcal{L}(x)$ resulting in $\mathcal{F}_{\text{MVNL}}(x, t)/x$, which depends on the deformation history $x[t_0 : t]$. Under sinusoidal deformation, a friction $\mathcal{F}_{\text{MVNL}}(x, t)$ yields a symmetric double-valued nonlinearity (DVNL) model $\mathcal{F}_{\text{DVNL}}(\text{sgn}(\dot{x}), x)$ (3.69—3.72). The $\mathcal{F}_{\text{DVNL}}(\text{sgn}(\dot{x}), x)$ models are validated against experimentally-acquired hysteresis loops, and have been found to be in good to excellent agreement if allowances are made for minor experimental inconsistencies. Different hysteresis loops can be conducted at various experiment temperatures, albeit with difficulty, should heat-dependency of friction need be characterised.

Modes of joint's interfacial slip: Macro, Macro-Micro and Micro-Micro With friction resulting from interfaces' relative deformation/motion, it is important to identify or classify types of such relative motion/slip before discussing further the means of modelling a friction joint and friction elements involved.

Macroslip (sliding) occurs when both joint's interfaces are totally sliding against each other. Accordingly, macroslip is not encountered in Curvic and flanged rotor couplings, is rarely noticeable in shrink/interference fits enduring large amplitudes, but is commonplace with spline couplings. Even then, macroslip might not occur from the outset, as slip may occur over some parts of the interface before the two components slide fully against each other, which is referred to as *microslip*.

Microslip phenomena have the unifying feature of a gradually decreasing joint's stiffness (slope $\frac{d\mathcal{L}(x)}{dx}$ of loading curve) with deformation on account of partial slip (*fig.3.3*). Microslip can be categorised into two distinct mechanisms, namely: Macro-microslip and micro-microslip. *Macro-microslip* is noticeably effective at large flexible interfaces, and refers to microslip caused by joint components elasticity/deformation or by varying surface pressure due to concentrated loads or waviness. *Micro-microslip* is caused by the effects of uneven asperities on interfaces, is significant even at very small areas and is the most prevalent mechanism in stiff joint components enduring small amplitudes.

Hysteresis and Masing's rule An analytical hysteresis loop is derived promptly from a rheological model with dissipative velocity coefficients as in viscous and Coulomb damping (3.68) as well as the flawed linear hysteretic damping FRF model (3.64). However, in the usual absence of rheological models, some hypothesis (e.g. *Th.3.2*) can be applied to the skeleton (initial loading) curve $\mathcal{L}(x)$ so as to achieve $\mathcal{F}_{\text{DVNL}}(x)$ comprising two distinct nonlinear functions and defining the analytical hysteresis loop (*fig.3.3*).

Theorem 3.2 (Masing's rule) *If a joint consists of linear components and dry friction elements only, its properties are fully defined by the force-deformation relation of the initial loading, i.e. further unloading and reloading relationships can be obtained directly from the initial loading curve.*

Publications concerning Masing's rule existed in the 60's [70], but to the author's knowledge, its proof was published in English as late as 1992 [151]. To date [121] Masing's rule [66, 152, 153] and its extensions [14, 29, 32, 119] yield analytical results that are in good agreement with experimental results [5, 35, 74, 110, 120, 141, 142, 144, 186, 192].

A Masing-type joint described by (*Th.3.2*), can simplify the $\mathcal{F}_{\text{MVNL}}(x,t)/x$ analysis significantly, regardless of the loading/unloading pattern endured. The properties of a Masing's joint, are fully defined by $\mathcal{L}(x)$, which is usually identified experimentally.

If an interface is subjected to an initial load \mathcal{F} and the deformation x follows the path (curve) $\mathcal{L}(x)$ to the *initial* point $A(x_i, \mathcal{F}_i)$, then an *unloading* path $\mathcal{N}_u(x)$ to point

$B(x_u, \mathcal{F}_u)$ can be expressed by:

$$\begin{aligned} \mathcal{N}_u &= \mathcal{F}_i - 2\mathcal{L}\left(\frac{x_i - x_u}{2}\right) & \text{for } x_u \geq -x_i \\ \mathcal{N}_u &= -\mathcal{L}(-x_u) & \text{for } x_u < -x_i \end{aligned}$$

Similarly, a *reloading* path from point $B(x_u, \mathcal{F}_u)$ to some point $C(x_r, \mathcal{F}_r)$ is:

$$\begin{aligned} \mathcal{N}_r &= \mathcal{F}_u + 2\mathcal{L}\left(\frac{x_r - x_u}{2}\right) & \text{for } |x_r| \leq \max(|x_u|, |x_i|) \\ \mathcal{N}_r &= \mathcal{L}(x_r) & \text{for } |x_r| > \max(|x_u|, |x_i|) \end{aligned}$$

Regenerating hysteresis loops using Masing's rule is fairly straightforward when assuming sinusoidal deformation $x(t) = \bar{X} \cos \tau$. The resulting model is a symmetric $\mathcal{F}_{\text{DVNL}}(x, \text{sgn} \dot{x})$ defining the hysteresis loop, and comprising the unloading ($\mathcal{N}_u(x)$ when $\text{sgn}(\dot{x}) \leq 0$) and reloading ($\mathcal{N}_r(x)$ when $\text{sgn}(\dot{x}) > 0$) curves:

$$\begin{aligned} \mathcal{N}_u &= \bar{\mathcal{F}} - 2\mathcal{L}\left(\frac{\bar{X}(1 - \cos \tau)}{2}\right) \\ \mathcal{N}_r &= -\bar{\mathcal{F}} + 2\mathcal{L}\left(\frac{\bar{X}(1 + \cos \tau)}{2}\right) \end{aligned}$$

which can be constructed using $\mathcal{L}(x)$ and vice versa. *Energy dissipated* ΔE by a Masing's joint is a function of peak amplitude \bar{X} , and is obtainable directly from $\mathcal{L}(x)$ [151].

Masing's rule applies to the macro- and microslip models (3.69—3.72) presented in this thesis and is used to generate the analytical hysteresis loops (*fig.3.3*). Although Masing's is the more popular method for modelling hysteresis, there are more recent hysteresis models [4] derived from $\mathcal{L}(x)$ using interesting rules other than Masing's.

3.2.1.2. Friction elements models and characteristics

Dry friction is arguably [177] the main energy dissipative mechanism, particularly at joints such as hubs shrunk-on shafts, flanged and Curvic couplings, as well as spline couplings that may be only initially lubricated or might have a dry lubricant. Generally however, joints exhibit nonlinear anelasticity, i.e. with stiffness as well as damping characteristics. Many joints with energy-dissipating characteristics that are encountered frequently have been studied, identified and modelled if with undetermined coefficients. Such nonlinear anelasticity models are an analytical approximation of experimentally acquired hysteresis curves. Alternatively, there are the usual explicit rheological equations that are input-independent, such as those for the ideal viscous and coulomb dampers. Some of these models will be used in conjunction with analysis to be developed hereafter.

Approaches to obtain model parameters: Prediction Vs. Identification In order to arrive at a joint's model, some parameters for the friction elements exemplified (§.3.2.1.2) need be defined. There are two approaches to adopt, depending on the element used, namely: Identification and prediction. *The Identification approach* involves identifying experimentally some intermediate parameters for the joint model, primarily the initial loading curve $\mathcal{L}(x)$ and/or the joint's hysteresis loop. *The prediction approach* predicts joint properties from the basic parameters, namely: Normal pressure and friction coefficient (2.43) from surface condition, e.g. roughness, flatness and hardness.

From a design point of view, the prediction approach is the more desirable, since the aforementioned design parameters can be used directly to predict analytically the joint's force-deformation relation. Indeed, if this can be done accurately, analysing a dynamic system with friction joint should not be very problematic and the joint's friction characteristics and damping capacity may be optimised. Unfortunately, the prediction approach is often not realistic on account of joint's complexity. Other than normal pressure and surface condition, joint properties are believed to be determined by contact duration and interface contamination, as well as many other unknown factors, which are not adequately represented by basic parameters [16, 84]. Accordingly, although attractive for design purposes, the prediction approach is currently less than satisfactory should a joint model of decent accuracy and reliability be sought.

Linear damping models are convenient as they can be used in conjunction with a standard linear eigen-analysis for most dynamic systems that may be adequately modelled as linear, which includes a handsome percentage of industrial turbines. The two popular linear damping models; namely viscous and hysteretic, have shortcomings when considering the rotor's stability or lack thereof as discussed below. Serious caution ought be considered when implementing the hysteretic model.

Linear viscous damping initially employed by Rayleigh [150], is a simple and convenient model for linear analysis, with a realisable constitutive law, and thus has proper TFs (and FRFs $H(\omega)$) as well as impulse response functions $\bar{h}(t)$:

$$\mathcal{F}_{\text{visc}} = c\dot{x} \quad (3.62a)$$

$$H_{\text{visc}}^v(\omega) = 1/c \quad H_{\text{visc}}^d(\omega) = 1/\omega c \quad (3.62b)$$

$$\bar{h}^v(t) = \frac{1}{c}\delta(t) \quad \bar{h}^d(t) = \frac{1}{c}u(t) \quad (3.62c)$$

The drawback of this linear model is that the force and energy dissipated per cycle of sinusoidal motion are linearly frequency-dependent. Although analytically sound, it will be shown that using linear viscous RID is not really representative of joint RID and is not

very well-suited to such analysis, since RID instability occurs only above critical speeds, which implies rather high frequencies that exaggerate the effect of viscous RID.

Ideal hysteretic damping: A flawed model [37]. Studying flutter, Theodorsen and Garrick [176] introduced a linear structural friction/damping model with frequency-independent energy dissipation per cycle. Myklestad [125] introduced the popular and widely-used concept of complex stiffness K damping (3.63), which for many years along with FRF (3.64) were the only known means of representing hysteretic damper's, and both were *unorthodoxly* mixed with differential operators in EOMs of the form:

$$m\ddot{x} + Kx = f_x(t), \quad \text{where } K = k(1 + \nu\kappa) \quad \text{and} \quad \kappa = \frac{d}{k} \quad (3.63)$$

Bishop and Johnson [23] emphasised that hysteretic damping representations of form (3.63) *are viable only for single-frequency steady-state sinusoidal motion*. Although *there is no differential or rheological equation to relate the physical parameters of hysteretic damping* and the determination of an impulse function is not straightforward [37], its behaviour is defined properly by the less-popular FRFs:

$$H_{\text{hyst}}^v(\omega) = \frac{\omega \operatorname{sgn}(\omega)}{d}, \quad H_{\text{hyst}}^d(\omega) = \frac{\operatorname{sgn}(\omega)}{\nu d} \quad (3.64)$$

which when applied properly to EOMs like (3.63) yield the frequency response relations:

$$\begin{aligned} (K - m\omega^2)\vec{X} &= \vec{f}_x & \text{for +ve } \omega \\ (K^* - m\omega^2)\vec{X} &= \vec{f}_x & \text{for -ve } \omega \text{ where } K^* = k(1 - \nu\kappa) \end{aligned} \quad (3.65)$$

Although a negative frequency (-ve ω) is not a popular recurrence in FRF analysis, it is rather significant in rotordynamics (*p.103*) as exemplified in (§.3.1.3.2). *The careful implementation of complex stiffness K and its complex conjugate K^* in conjunction with +ve and -ve ω respectively for rotordynamic eigenvalues (fig.4.19) and complex system frequency response analysis (fig.5.4) is of paramount importance.*

Several attempts were made to study the transient motion of EOMs such as (3.63) by obtaining impulse response functions for systems with hysteretic damping:

$$\bar{h}^d(t) = -\frac{1}{\pi dt} \quad \bar{h}^v(t) = -\frac{1}{\pi dt^2} \quad (3.66)$$

These lead to some early confusions and the fact that: The ideal *hysteretic damper* (as well as its modified Band-limited hysteretic damper) model *violates the requirement of causality*; i.e. the system responds before it is excited. If this flaw is set aside, the impulse response function (3.66) may be used, utilising convolution integrals, to establish the

relation between physical force and motion variables as in:

$$m\ddot{x} + \int_{-\infty}^{\infty} -\frac{d}{\pi t}(\theta)x(t-\theta)d\theta + kx = f_x(t) \quad (3.67)$$

Alternatively, to avoid the anomalous non-causal behaviour of transient response, Jones [75] levied the restrictive assumption of constant complex modulus' parameters. Allowing such parameters to vary with frequency; i.e. a complex modulus with frequency-dependent parameters resolves the issue of non-causality.

The main problem with modelling RID as ideal hysteretic damping stems from using the complex stiffness model as in (3.63) whilst not accounting for $\text{sgn}(\omega)$ as in (3.64). Not accounting for $\text{sgn}(\omega)$ *is erroneous and may yield misleading results in both:*

- Stability analysis based on assessing eigenvalues with negative modal frequencies
- Frequency response of complex rotor representation, which may in-turn lead to erroneous conclusions in a FR-based stability analysis

both of which will be elaborated and exemplified along with the necessary remedies in §.4.2.3. However, it is unfortunate that several aero-engine manufacturers model rotors with hysteretic RID (based on [200]) in such a manner that leads to erroneous conclusions, which are not compliant with actual RID behaviour.

SVNL Dry Friction elements are expressed rheologically and plotted against relative velocity v , thus having purely dissipative characteristics. As such, these elements are not realistic on their own, and results of analysis using them are more satisfying qualitatively than quantitatively.

Idealised Coulomb friction is most well known yet overly simplified relay-type force/velocity model. Most other friction models are based on, or are closely related to this model. Its direct use leads to the simplest joint model—the *point contact dry friction* element; since the friction force is independent of the area and shape of the interface and is also independent of the pressure at the interface. In other words, the joint can be considered as contacting at one point only. An implication of the dry friction law is that before sliding is initiated, the deformation of the joint is zero.

Coulomb's dry friction law requires the tangential friction force \mathcal{F}_{col} be largely independent of relative velocity, while proportional to the normal clamping force N via a friction coefficient μ reflecting material properties and surface finish. Without slippage,

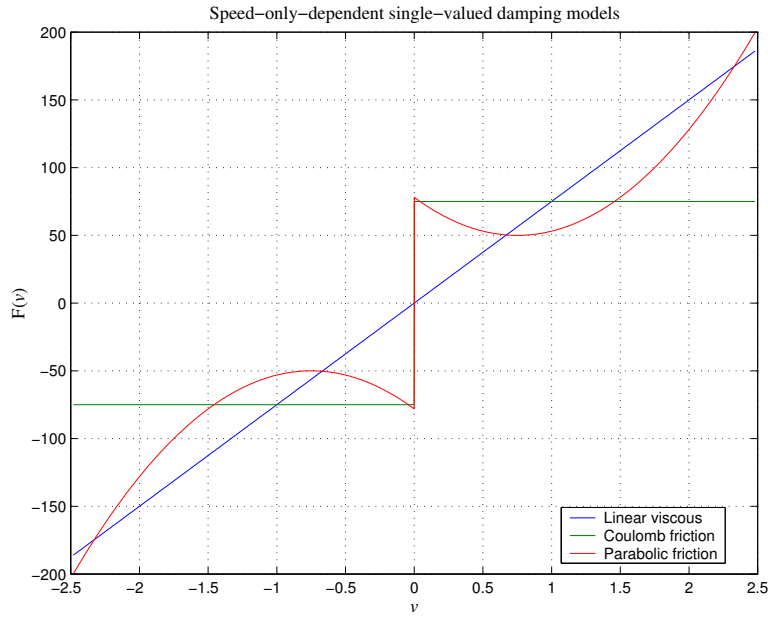


Figure 3.2.: Speed-dependent Single-valued Damping Models

the internal joint force is equivalent to the externally applied force (*fig.3.2*).

$$\begin{aligned} \mathcal{F}_{\text{col}} &= \text{sgn}(v)\mu N & \text{for } |v| > 0 \\ &= f_x & \text{for } v = 0 \end{aligned} \quad (3.68)$$

Coulomb's friction was used (2.43) to model friction in rotor joints, with the assumption that all coupling teeth have slipped, which is obviously unrealistic.

An arguably more realistic SVNL dry friction law might assume the \mathcal{F}_{rdf} shape depicted in (*fig.3.2*) according to Tondl. There is disagreement between several researchers (some are discussed in [109]) as to whether \mathcal{F}_{rdf} is greater prior to relative slippage, let alone having a minimum, after which it picks up. However, not only do old-school authors such as Tondl, Dementberg and Atherton [9] support such a function, it actually offers an explanation (§.5.3.2.2) as to why RID-induced precession at one speed may be bounded for minor disturbances yet unstable for more significant disturbances. For later numerical exemplifications, a parabolic function is assumed for \mathcal{F}_{rdf} in *fig.3.2*.

Macro-microslip joint models based on Coulomb friction and joint elasticity are usually possible in closed form on account of this element's simplicity, with the basic assumption: Coulomb's friction law is held at infinitesimally small areas and under infinitesimally small deformations, which is generally unrealistic. Generally, such joints have very simple geometry, with the assumptions of uniform stress distribution over the interfaces and uniform surface conditions in place. Interestingly however, some available

joint models feature multiple slipped areas with bi-directional shear stress, which may not be totally balanced by external forces and moments.

Since Coulomb friction does not account for the effect of asperities and their elasticity, it is unrealistic to implement in deriving a joint model particularly at low amplitudes. Although it might be viable to model asperities' rub by the dry friction law, it cannot account for asperities' deformation at low amplitudes before breaking-up, especially if their relative motion is small compared to their size.

Piecewise-linear Macro-microslip models/assemblies were originally introduced to model the yielding behaviour of continuous and composite materials [73, 190]. They are based on various physical configurations of individual bilinear elements (3.69), which can be connected in any parallel-series combination to yield different $\mathcal{L}(x)$, and to which Masing's rule is always applicable.

The Bi-linear element is an extension of Coulomb's friction law, stacking a linear spring in series with Coulomb's friction element. Friction occurs at displacements greater than critical X_{cr} , *dictating an abrupt transition from elastic deformation to macroslip*:

$$\begin{aligned}\mathcal{L}_{Bi}(x) &= kx & \text{for } x < X_{cr} \\ &= kX_{cr} & \text{for } x \geq X_{cr}\end{aligned}\tag{3.69}$$

Unlike dry friction elements at zero deformation, $\mathcal{F}_{Bi}(x, t)$ is determined under any state.

Features of bilinear element-based microslip joint models The bilinear element may be adopted as a simplistic means of accounting for the effect of interfaces' asperities. It reflects Menq et al [114] suggestion of linear asperities' stiffness before slipping as well as identical properties (a substantial idealisation) thus approximating the contact interface in a small area by a linear spring until the contact is broken. Although joints based on the bilinear element are more realistic than those based on Coulomb friction, they are more difficult to derive in closed form, which are in turn limited to simple joint configurations, pressure distributions and surface conditions. However, macro-microslip joint models may be suited for flexible joint components with large interfaces.

Micro-microslip elements start off deformation in microslip mode and converge with increased amplitude to macroslip-like characteristic. Accordingly, unlike the Bilinear element, energy is dissipated under any deformation however minuscule without the energy-conserving linear elasticity capability. Two important and physically meaningful micro-microslip models are presented. These are suited to model stiff friction joints enduring

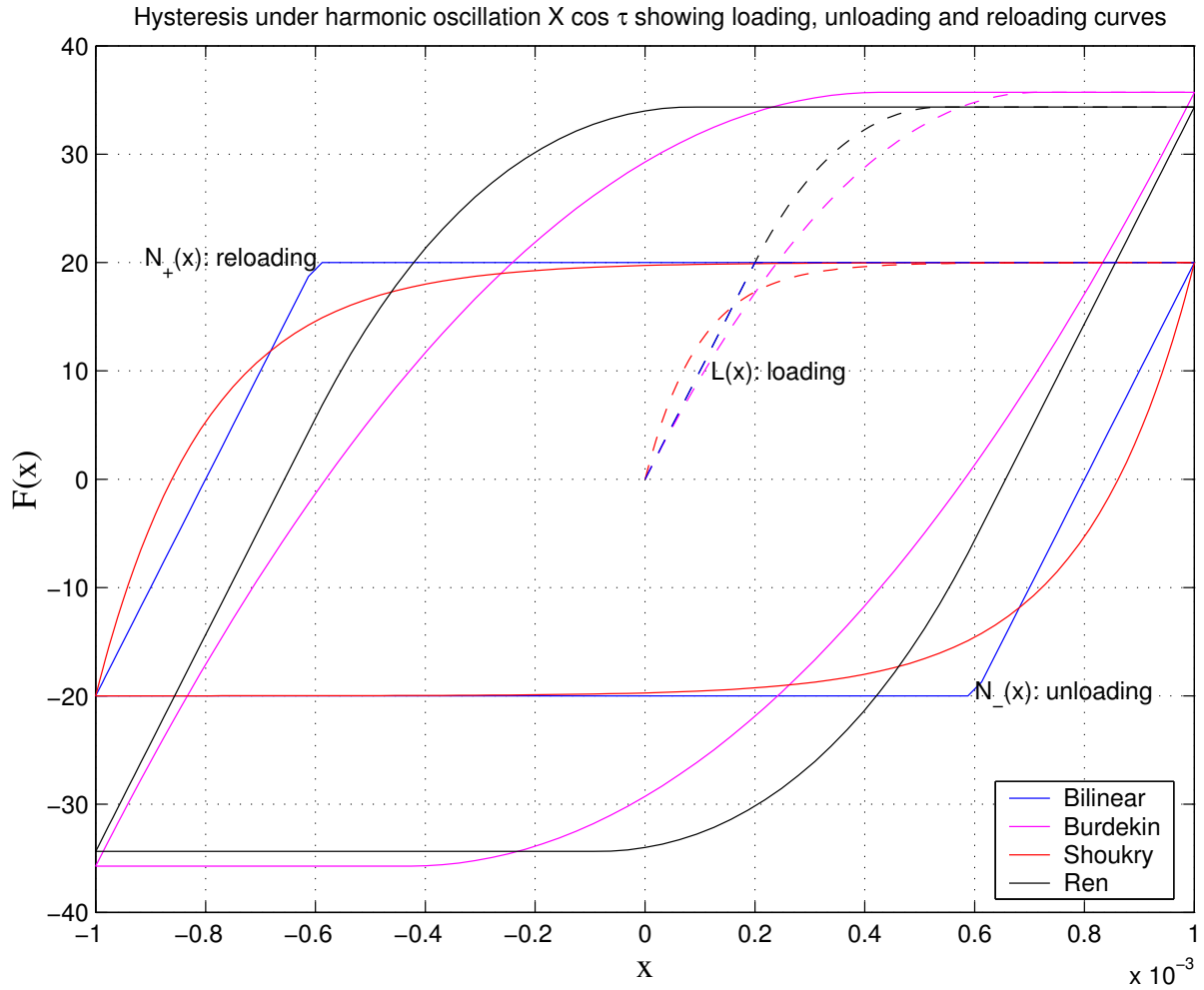


Figure 3.3.: Hysteresis loops of Macro-microslip and Micro-microslip joint models

small vibration amplitudes, when different asperities' shapes have the imposing influence on energy dissipation characteristics.

Burdekin's element model was the first proposed [28] microslip element in 1978. Each asperity is represented as a prismatic rod with the same stiffness and each rod is modelled as a bilinear element. After assuming a linear height distribution of rods, the initial loading relation is supposed to follow:

$$\mathcal{L}_{\text{Brd}}(x) = kx - bx^2 \quad \text{for } 0 < x < \frac{k}{2b} \quad (3.70a)$$

$$= \frac{k^2}{4b} \quad \text{for } x \geq \frac{k}{2b} \quad (3.70b)$$

where k and b are parameters determined by the apparent contact area, normal and shear stiffness of the asperities, normal displacement, friction coefficient and a constant relating the number of contacts to the normal displacement of the surfaces. The parameters of

Burdekin's model are derived from $\mathcal{L}_{\text{Brd}}(x)$, which is *identified experimentally*.

Shoukry's element model [167] was developed using Mindlin's spherical contact element [115], thus microslip may occur at each asperity. Assuming exponential peak height distribution of the spherical contact element, the force-deformation relation is:

$$\mathcal{L}_{\text{sh}}(x) = \mu N (1 - e^{-\frac{\Delta x}{\bar{\sigma}}}) \quad (3.71)$$

where $\bar{\sigma}$ is the standard deviation of peak height distribution, and $\Delta = \frac{2(1-\nu)}{\mu(2-\nu)}$ with ν being Poisson's ratio. It is not necessary to identify experimentally this model, as it can be *predicted from physical parameters*, e.g surface finish and normal pressure.

Multi-slip mode elements are more versatile on account of their ability to model all deformation/slip modes, as well as other features discussed below.

Combined elements model is Sanliturk's simple approach to include macro- and microslip characteristics in one model, using an empirical weighting factor β :

$$\mathcal{L}_{\text{Hyb}}(x) = (e^{-\beta \frac{x}{X_{\text{cr}}}}) \mathcal{L}_{\text{sh}}(x) + (1 - e^{-\beta \frac{x}{X_{\text{cr}}}}) \mathcal{L}_{\text{Bi}}(x) \quad (3.72)$$

Where X_{cr} , $\mathcal{L}_{\text{Bi}}(x)$ and $\mathcal{L}_{\text{sh}}(x)$ are defined in eqs. (3.69, 3.71) respectively.

Ren's element model [151] uses a small area of the interface as the basic element, which is unlike Burdekin's and Shoukry's models (3.70, 3.71) that assume an element for each single asperity. Each of these small areas is modelled by a bilinear element, all of which are of identical stiffness, and may comprise several asperities or represent only a part of an asperity. The concept of a stiffness-area (**s**-area) is introduced, with domain $\mathbf{s} \in [0, 1]$ representing the slipped **s**-area as a proportion of the total initial stiffness contributed from an interface area, whose $\mathbf{s} \stackrel{\text{def}}{=} 1$. With $\mathbf{s} \in [0, 1]$ and deformation x being reciprocal functions $\mathbf{s} \stackrel{\text{def}}{=} \mathbf{s}(x) \Leftrightarrow x \stackrel{\text{def}}{=} x(\mathbf{s})$, the problem is definable in the **s**-domain and the resulting model (3.73) can represent any Masing's type joint. Ren's generalised element may represent joints experiencing: *a*) pure stiffness when $x \leq x(\mathbf{0})$, *b*) Micro-slip when $x(\mathbf{0}) < x < x(\mathbf{1})$ only partial interfacial slip occurs, or *c*) Macro-slip when $x \geq x(\mathbf{1})$ the

whole interface is sliding and Coulomb's friction law applies.

$$\mathcal{L}_{\text{Ren}}(x) = kx \quad \text{for } 0 < x \leq X_{\text{sl}} \quad (3.73a)$$

$$= k \frac{x - X_{\text{sl}} + x(b - \ln x + \ln X_{\text{sl}})}{b} \quad \text{for } X_{\text{sl}} < x \leq X_{\text{sl}}e^b \quad (3.73b)$$

$$= k \frac{X_{\text{sl}}(e^b - 1)}{b} \quad \text{for } x \geq X_{\text{sl}}e^b \quad (3.73c)$$

where X_{sl} is the slip limit—maximum linear elastic deformation without friction—and b represents the level of difference between asperities, which reflects differences in individual bilinear elements' X_{cr} in (3.69). Naturally, different hysteresis loops result according to choice of parameters, particularly varying b :

- With $b \simeq 0$, the resulting hysteresis loop is (virtually) that of the bilinear element described by (3.69), which reflects (3.73a,c).
- With gradual increase of b , the hysteresis loop is a mixture of macro- and microslip
- With substantial increase in b , the hysteresis loop describes primarily microslip

3.2.2. RID Modelling: Concept, assumptions and EOMs

In the following modelling approach, a rotor joint is assumed to be localised at a single rotor station (point). As interest is in stability of lateral vibration, only lateral forces are considered with axial forces ignored. Since small angular displacements are related to and accounted for by lateral displacements (§.3.1.1), the rotor joint is thus modelled by its lateral restoring force resulting from its stiffness and friction characteristics, while joint's inertia is ignored. As with other friction joint models (§.3.2.1), the RID joint model can be rheological or hybrid. While, to the authors knowledge, hybrid models have not been implemented in studying RID instability, simple rheological models have been used, where (a joint with) RID is modelled by:

- A simple restoring force model with assumed coefficients representing the overall effect of RID from joint and/or shaft, e.g. linear viscous (3.77) or nonlinear Coulomb friction for an illustrative sort of analysis
- A *predicted* joint model (as discussed on p.119) derived from joint's design and interface parameters: Configuration, normal pressure and assumed friction coefficient. Again a simple rheological damping model is assumed, i.e. a joint with linear viscous (2.40) and/or Coulomb damping (2.42) characteristics at interfaces

The following modelling approach does not preclude the use of hybrid models (3.69—3.72), some of which are to be implemented so as to explain some of the more interesting features that may be physically observed during an RID instability.

3.2.2.1. Augmenting RID to linear rotordynamic EOMs in rotating frame

RID is effective only on rotor (shaft) flexing, to which the system's behaviour resulting from RID is related. For linear viscous RID, it is advantageous to consider rotor's flexing in the rotating frame of reference so as to isolate it from the overall system's vibration, which might not cause rotor flexing e.g synchronous precession of isotropic Jeffcott rotor. However, *it is essential to use rotating frame EOMs for other RID models:*

- FR models (linear hysteretic or DFs of NL RID) assuming single-sinusoidal input.
- A hybrid model that requires a single dimension loading history.
- A rheological nonlinear model that is not easily transferred to the stationary frame.

Previous RID modelling method Researchers had modelled RID as a force \mathcal{F}_ζ augmented to the complex $\xi\eta$ -frame EOM of Jeffcott rotor (2.9) to result in (2.10), which are (3.11) and (3.76) with $\mathcal{G} = 0$ respectively, for qualitative illustrations. \mathcal{F}_ζ is supposed to be the restoring force corresponding to the RID-induced moments at a shaft cross-section or coupling—see §2.4.5. Generally, $\mathcal{F}_\zeta \stackrel{\text{def}}{=} c_i(\zeta, \dot{\zeta})\dot{\zeta}$ is nonlinear depending on shaft flexing amplitude and its rate, which is equivalent to (3.61d). To simplify analysis, stiffness was not expressed and $\mathcal{F}_\zeta \stackrel{\text{def}}{=} c_i(\dot{\zeta})\dot{\zeta}$ had a purely dissipative nature. Polar coordinates $\rho e^{i\phi} = \sqrt{(\xi^2 + \eta^2)} e^{i\phi} = \zeta$ were used [41, 177] to expand (2.10) for RID models other than linear viscous, arguing that $\mathcal{F}_\zeta(\zeta, \dot{\zeta})$ is not necessarily opposite in direction to $\dot{\zeta}$. Partial derivatives of ρ, ϕ yielded two *geometrically nonlinear* EOMs (2.20). Lyapunov linearisation (5.2) was used thereafter to assess *local* absolute stability. Although (3.76) linear viscous coefficients can be transferred with ease to the stationary frame (3.84), this is a luxury not afforded by nonlinear models, yet an argument addressing this issue is presented in the following section.

RID joint physical representation and analytical modelling In this thesis, RID is modelled in a similar fashion to (2.10). Two orthogonal directions ξ, η are used so as to satisfy Tondl's aforementioned argument as well as accommodate the constant deflection due to imbalance, which can be different in the ξ, η directions. Polar coordinates ρ, ϕ are not used due to the unnecessary geometric nonlinearity they introduce to EOMs.

Physical representation A RID-introducing joint such as that in *fig.3.1* is represented by two elements as illustrated in *fig.3.4*, which:

- Are in the orthogonal directions ξ, η , between the shaft and rotating frame ground
- Are generally nonlinear with displacement and velocity in the widest sense, but may also be linear viscous elements represented by simple dashpots
- On displacement, each results in a (nonlinear) restoring force output $\mathcal{F}_\xi, \mathcal{F}_\eta$ that is an element of the internal (nonlinear) force vector \mathcal{F}

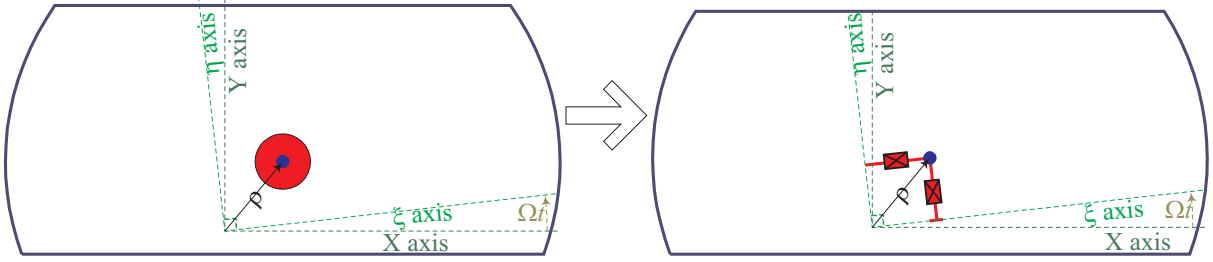


Figure 3.4.: RID joint representation and modelling for 2DOF rotor

\mathcal{F} is introduced to the otherwise linear system in the rotating frame (e.g. 3.6) as:

$$\mathbf{M}_r \ddot{\mathbf{q}}_r + \mathbf{C}_r \dot{\mathbf{q}}_r + \mathbf{K}_r \mathbf{q}_r + \mathcal{F} = \mathbf{f}_r \quad (3.74)$$

Most generally, all elements in \mathcal{F} are functions of all state variables in state vector \mathbf{p}_r

$$\mathcal{F} \stackrel{\text{def}}{=} \mathcal{F}(\mathbf{p}_r) \stackrel{\text{def}}{=} \mathcal{F}(\mathbf{q}_r, \dot{\mathbf{q}}_r), \quad \text{which for 2DOF is } \mathcal{F} \stackrel{\text{def}}{=} \left\{ \begin{array}{l} \mathcal{F}_\xi(\mathbf{q}_r, \dot{\mathbf{q}}_r) \\ \mathcal{F}_\eta(\mathbf{q}_r, \dot{\mathbf{q}}_r) \end{array} \right\}$$

Modelling assumptions for RID-induced \mathcal{F} and box \mathcal{N} of nonlinearities \mathcal{N} The MIMO system of (3.74) may be viewed as a linear system with a multivariable (multi-dimensional) nonlinearity \mathcal{N} having $2n$ inputs $p_{r \in \{1 \dots 2n\}}$ and n outputs $\mathcal{F}_{i \in \{1 \dots n\}}$, each of which is a function of all inputs. A useful visualisation for forthcoming analysis is considering $\mathcal{F}_{n \times 1}$ to be the output of a box $\mathcal{N}_{2n \times n}$ (set) of \mathcal{N} when subjected to an input $\mathbf{p}_{r 2n \times 1}$. With the definition of a phase state vector (3.15), \mathcal{N} can be an n -square set of MVNL $\mathcal{N}_{ij} \in \mathcal{N}_{n \times n}$ with rate memory. In the most general sense, all $\mathcal{N}_{ij} \stackrel{\text{def}}{=} \mathcal{N}_{ij}(\mathbf{p}_r)$ are functions of all inputs. A less general scenario is considering each output to be the sum of separate nonlinear functions of each input, as in: $\mathcal{F}_i = \sum_{j=1}^n \mathcal{N}_{ij}(q_j)$, which is the least necessary for hard nonlinearities to avoid discontinuity of output \mathcal{F}_i during continuous whirling. The simplest scenario exists when there is no cross-coupling in \mathcal{N} so that: $\mathcal{F}_i = \mathcal{N}_{ii}(q_i)$, which is assumed hereafter for RID in accordance with the following arguments. This is

a fair assumption for linear RID, but results in a discontinuous \mathcal{F}_i for the hard NL RID models used, which is an issue that can be overlooked in lieu of simplified analysis that are approximate in the first place.

In general (3.74), \mathcal{F} results from internal restoring forces due to (nonlinear) elements, each of which is characterised by \mathcal{N}_{ij} and is connected between the single coordinates q_{r_i} and q_{r_j} . Hence, the input to \mathcal{N}_{ij} is seen to be the *inter-coordinate relative displacements* $q_{r_{ij}} = q_{r_i} - q_{r_j}$ and/or their velocities. As in (2.10) a joint with RID is seen to connect the rotor to the ground of the $\xi\eta$ -frame, so $q_{r_{ij}} = q_{r_i} - 0 = q_{r_i}$. It can be viewed as a spatial nonlinear coupling between the LTI rotor subsystem \mathbf{S}_L and the ground via the nonlinear joint model \mathcal{N} whose input is merely the coordinates' displacements and velocities. Accordingly, the RID force vector \mathcal{F} and \mathcal{N} box for the 2DOF rotor of (3.74):

$$\mathcal{F} = \begin{Bmatrix} \mathcal{N}(\xi, \dot{\xi}) \\ \mathcal{N}(\eta, \dot{\eta}) \end{Bmatrix}, \quad \text{and} \quad \mathcal{N} = \begin{pmatrix} \mathcal{N}(\xi, \dot{\xi}) & 0 \\ 0 & \mathcal{N}(\eta, \dot{\eta}) \end{pmatrix} \quad (3.75)$$

3.2.2.2. EOMs for 2DOF rotor with RID models

EOMs with simple single-valued RID models, e.g. linear viscous (3.62) and nonlinear Coulomb RID (3.68) models are presented here in accordance with §.3.2.2.1 and in formats necessary for further analysis. Gyroscopic effects may actually simplify analysis.

Complex representation \mathcal{F}_ζ of RID force vector \mathcal{F} in the rotating $\xi\eta$ -frame Generally, complex EOMs representations are beneficial in reducing problem size and used in frequency response and eigen analysis (§.4.1, 4.2). Other than avoiding the aforementioned discontinuous $\mathcal{F}_i = \mathcal{N}_{ii}(q_i)$ pitfall (3.75) with real system representation, complex representation is essential for further graphical (nonlinear) analysis (§.5.3.2.1). The aim is to arrive at and justify the complex EOM with complex RID representation \mathcal{F}_ζ :

$$m\ddot{\zeta} + \left(c + (2m - \mathcal{G})\Omega\iota\right)\dot{\zeta} + \left((k + (\mathcal{G} - m)\Omega^2) + c\Omega\iota\right)\zeta + \mathcal{F}_\zeta = f_\zeta \quad (3.76)$$

from expanding (3.74), with the 2DOF $\xi\eta$ -frame EOMs being:

$$m\mathbf{I}\ddot{\mathbf{q}}_{\mathbf{r}} + \left(c\mathbf{I} + (2m - \mathcal{G})\Omega\mathbf{N}\right)\dot{\mathbf{q}}_{\mathbf{r}} + \left((k + (\mathcal{G} - m)\Omega^2)\mathbf{I} + c\Omega\mathbf{N}\right)\mathbf{q}_{\mathbf{r}} + \mathcal{F} = \mathbf{f}_{\mathbf{r}}$$

In the case of nonlinear RID however, complex representation (3.76) is only arguably viable based on operational assumptions for models other than Coulomb's.

Linear RID force vectors For the straightforward case of linear viscous RID:

$$\mathcal{N} = c_i \dot{q}_r \quad \therefore \quad \mathcal{F} = \mathcal{F}_{\text{visc}} = \begin{Bmatrix} c_i \dot{\xi} \\ c_i \dot{\eta} \end{Bmatrix} = \begin{bmatrix} c_i & 0 \\ 0 & c_i \end{bmatrix} \begin{Bmatrix} \dot{\xi} \\ \dot{\eta} \end{Bmatrix} = c_i \mathbf{I} \dot{\mathbf{q}}_r \quad (3.77)$$

In which case $\mathcal{F}_{\text{visc}}$ is augmented to the 2 EOMs as:

$$m \mathbf{I} \ddot{\mathbf{q}}_r + \left((c + c_i) \mathbf{I} + (2m - \mathcal{G}) \Omega \mathbf{N} \right) \dot{\mathbf{q}}_r + \left((k + (\mathcal{G} - m) \Omega^2) \mathbf{I} + c \Omega \mathbf{N} \right) \mathbf{q}_r = \mathbf{f}_r \quad (3.78)$$

which can in turn be written in complex format, with $(1, \iota)$ representing (\mathbf{I}, \mathbf{N}) , as:

$$m \ddot{\zeta} + \left((c + c_i) + \iota (2m - \mathcal{G}) \Omega \right) \dot{\zeta} + \left((k + (\mathcal{G} - m) \Omega^2) + \iota c \Omega \right) \zeta = f_\zeta \quad (3.79)$$

Similarly, *hysteretic RID* can be augmented *whilst including the all important* $\text{sgn}(\omega)$:

$$m \ddot{\zeta} + \left((c + \iota d \text{sgn}(\omega)) + \iota (2m - \mathcal{G}) \Omega \right) \dot{\zeta} + \left((k + (\mathcal{G} - m) \Omega^2) + \iota c \Omega \right) \zeta = f_\zeta \quad (3.80)$$

where ω may be either positive or negative, but only representing either of:

- Frequency of response to excitation, with both being *circular* rotating vectors
- Modal frequency when $f_\zeta = 0$

Although $\text{sgn}(\omega)$ renders (3.80) nonlinear, Eigen-analysis may be applied once for each of -ve and +ve $\text{sgn}(\omega)$, depending on the mode of interest.

Argument for using a complex representation of a general nonlinear \mathcal{F} As discussed in §.3.1.1.3, A.1, the condition for representing the general nonlinear \mathcal{F} by its complex form \mathcal{F}_ζ in the complex EOM of isotropic 2DOF rotor (3.76) is: $\mathcal{F} \stackrel{\text{def}}{=} \left\{ \frac{\mathcal{F}(\tau)}{\mathcal{F}(\tau \mp \pi/2)} \right\}$ with \mp representing CCW and CW precessions respectively. This is a very viable assumptions to make on account of gyroscopic coupling whilst rotating and common $\mathcal{N} \equiv \mathcal{N}_\xi \equiv \mathcal{N}_\eta$, since displacement and/or velocity input to \mathcal{N} in the case of:

- Sustained asynchronous precession from 1) Bidirectional forcing resulting in circular rotating vector, or 2) Limit cycle due to nonlinearity. In both cases inputs are identical with $\pi/2$ lead or lag depending on rotating vector directionality and reflected by $\text{sgn}(\omega_e)$ in (figs.4.12, 4.13) or the precessing mode respectively
- Unidirectional forcing: Inputs are very similar, especially around resonances with $\pi/2$ lead or lag on account of gyroscopic coupling (figs.4.8, 4.9)

3. RID systems modelling and characteristics

- Any disturbance: Inputs are comparable with $\pi/2$ lead or lag depending on modal contributions. This is perhaps a gray area, but is of no concern here as interest lies primarily in the first item.

Accordingly, (3.76) is used with confidence for the FR graphical analysis in §.5.3.2.1.

Representing \mathcal{F} in the stationary frame and analysing the system in the xy -frame can prove very useful, especially in the case of rotor on orthotropic bearings so as to avoid the hassle of handling EOMs with time-varying matrices in the rotating frame.

Express system in stationary frame the $\xi\eta$ -frame EOMs (3.74) are expanded:

$$\begin{aligned} \mathbf{T}^T \mathbf{M} \mathbf{T} (\ddot{\mathbf{q}}_r + 2\Omega \mathbf{N} \dot{\mathbf{q}}_r - \Omega^2 \mathbf{q}_r) + \mathbf{T}^T (\mathbf{G} + \mathbf{C}) \mathbf{T} (\dot{\mathbf{q}}_r + \Omega \mathbf{N} \mathbf{q}_r) + \mathbf{T}^T \mathbf{K} \mathbf{T} \mathbf{q}_r + \mathcal{F} &= \mathbf{f}_r \\ \text{Or equally} \quad \mathbf{T}^T \mathbf{M} \ddot{\mathbf{q}} + \mathbf{T}^T (\mathbf{G} + \mathbf{C}) \dot{\mathbf{q}} + \mathbf{T}^T \mathbf{K} \mathbf{q} + \mathcal{F} &= \mathbf{f}_r \end{aligned} \quad (3.81)$$

Then, pre-multiplying (3.81) by \mathbf{T} transfers the EOMs back to the stationary frame as:

$$\mathbf{M} \ddot{\mathbf{q}} + (\mathbf{G} + \mathbf{C}) \dot{\mathbf{q}} + \mathbf{K} \mathbf{q} + \mathbf{T} \mathcal{F} = \mathbf{T} \mathbf{f}_r = \mathbf{f} \quad (3.82)$$

Expressing \mathcal{F} in terms of $(\mathbf{q}, \dot{\mathbf{q}})$ should be rather convenient, if not very straight forward, when considering EOMs in the stationary frame. According to (3.3,3.4) the non-linear force vector becomes a function of xy -frame displacements and velocities as:

$$\mathcal{F}(\mathbf{q}_r, \dot{\mathbf{q}}_r) = \mathcal{F}(\mathbf{T}^T (\dot{\mathbf{q}} - \Omega \mathbf{N} \mathbf{q}), \mathbf{T}^T \mathbf{q}) \quad (3.83)$$

In the case of linear viscous RID where $\mathcal{F} = c_i \mathbf{I} \dot{\mathbf{q}}_r$ and according to (3.82, 3.83) the EOMs are:

$$\begin{aligned} \mathbf{T} \mathcal{F} &= c_i \mathbf{T} \mathbf{I} \dot{\mathbf{q}}_r = c_i \mathbf{T} \mathbf{I} \mathbf{T}^T (\dot{\mathbf{q}} - \Omega \mathbf{N} \mathbf{q}) = c_i \mathbf{I} (\dot{\mathbf{q}} - \Omega \mathbf{N} \mathbf{q}) \\ &= \begin{bmatrix} c_i & 0 \\ 0 & c_i \end{bmatrix} \begin{Bmatrix} \dot{x} \\ \dot{y} \end{Bmatrix} + \Omega \begin{bmatrix} 0 & c_i \\ -c_i & 0 \end{bmatrix} \begin{Bmatrix} x \\ y \end{Bmatrix} \end{aligned} \quad (3.84)$$

By (3.84), linear viscous RID introduces to the xy -frame EOMs:

1. The symmetric matrix $c_i \mathbf{I}$, which enhances stability as it adds to the stabilising $c\mathbf{I} = \mathbf{C}$ matrix in the overall \mathbf{C}_g (3.1).
2. The speed-dependant skew-symmetric matrix $\mathbf{K}_{cc} = c_i \Omega \mathbf{N}$ (3.1), which has a destabilising effect [33] that increases with speed.

In the case of Coulomb RID (3.68)

$$\mathbf{T}\mathcal{F} = \mu\mathbf{N}\mathbf{T} \operatorname{sgn}(\dot{\mathbf{q}}_r) = \mu\mathbf{N}\mathbf{T} \operatorname{sgn}(\mathbf{T}^T(\dot{\mathbf{q}} - \Omega\mathbf{R}\mathbf{q})) \quad (3.85)$$

3.2.2.3. Feedback formulation of RID problem

Feedback formulations are used to separate $\mathbf{S}_{NL} \stackrel{s}{\supset} \{\mathbf{S}_L, \mathbf{S}_N\}$ for analysis requiring considering each subsystem separately. It promotes the more efficient DFM (§.5.3) over the HBM on account of reduced system order. Also, such setups have been studied extensively in the rich NL control engineering (§.A.2.3), which facilitates further adaptations.

System setup considering (3.81), \mathcal{F} is moved to the righthand-side, resulting in:

$$\mathbf{M}_r\ddot{\mathbf{q}}_r + \mathbf{C}_r\dot{\mathbf{q}}_r + \mathbf{K}_r\mathbf{q}_r = \mathbf{f}_r - \mathcal{F} \quad (3.86)$$

The LTI lefthand-side of (3.86) part is represented by its TFM $\mathbf{H}_r(s)$, whose input then becomes $\mathbf{f}_r - \mathcal{F}$. This setup is suited for a nonlinear closed loop system representation with $\mathcal{F}(\dot{\mathbf{q}}_r, \mathbf{q}_r)$ in the feedback loop, and $\mathbf{H}_r(s)$ in the feed-forward path. Furthermore, with complex representations of this setup, graphical stability and response predictions of SISO systems with minimum-phase TFs can be applied as demonstrated in §.5.3.2.

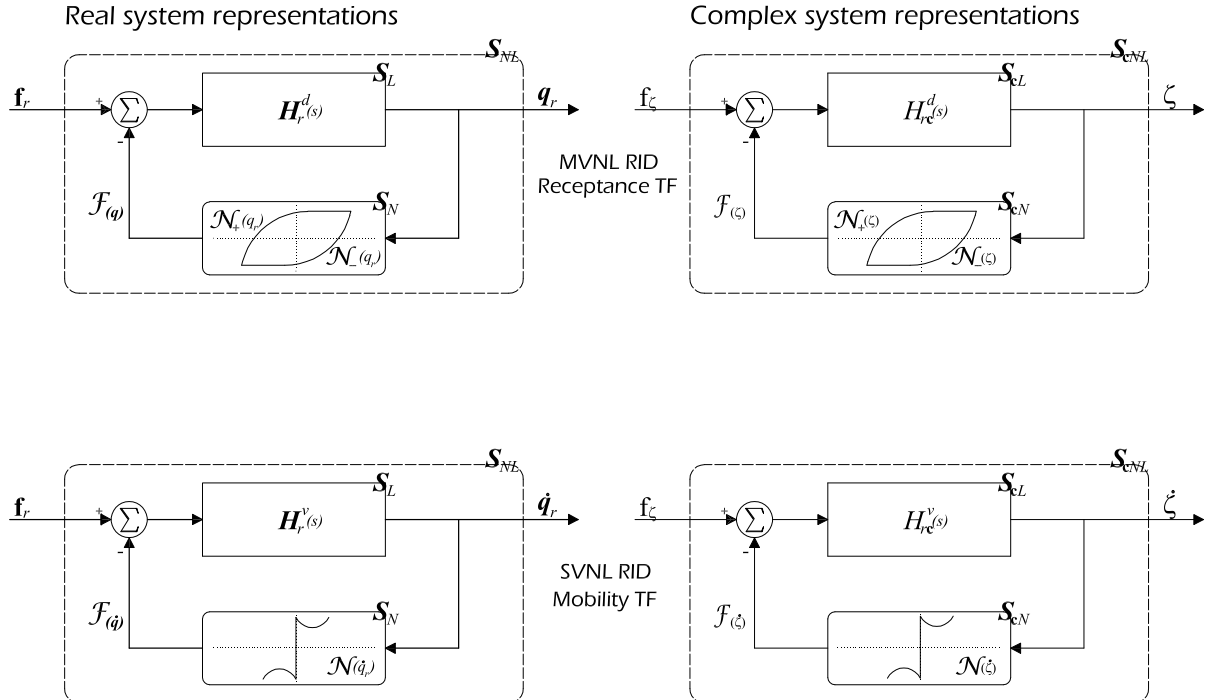


Figure 3.5.: RID feedback setup in rotating frame

State matrices from state and output equations including feedback RID are identical to those from EOMs. From the feedback setup (3.86) according to (3.15,3.18)

$$\dot{\mathbf{p}}_r = \mathbf{A}_r \mathbf{p}_r + \mathbf{B}(\mathbf{f}_r - \mathcal{F})$$

With linear viscous RID in the feedback loop and excluding external forces leads to:

$$\begin{aligned} \dot{\mathbf{p}}_r &= \mathbf{A}_r \mathbf{p}_r - \mathbf{B}(c_i \mathbf{I} \mathbf{O}^v \mathbf{p}_r) \\ &= (\mathbf{A}_r - c_i \mathbf{B} \mathbf{O}^v) \mathbf{p}_r = \check{\mathbf{A}}_r \mathbf{p}_r \end{aligned}$$

The overall system state matrix $\check{\mathbf{A}}_r$ is identical to that derived from EOMs (3.78) as:

$$\check{\mathbf{A}}_r = -\frac{1}{m} \begin{bmatrix} 0 & 0 & -m & 0 \\ 0 & 0 & 0 & -m \\ k + \Omega^2(\mathcal{G} - m) & -\Omega c & c + c_i & \Omega(\mathcal{G} - 2m) \\ \Omega c & k + \Omega^2(\mathcal{G} - m) & -\Omega(\mathcal{G} - 2m) & c + c_i \end{bmatrix} \quad (3.87)$$

Similarly, the overall TFM of the MIMO feedback system is given by:

$$\mathbf{G}(s) = [\mathbf{I} + \mathbf{H}(s)\mathbf{B}(s)]^{-1} \mathbf{H}(s) \quad (3.88)$$

Complex formulations in state space are possible, albeit unorthodox, yielding the characteristic equation:

$$m\lambda^2 + \underbrace{(c + c_i + i(2m - \mathcal{G})\Omega)}_{c_r} \lambda + \underbrace{k + (\mathcal{G} - m)\Omega^2 + i c \Omega}_{k_r} = 0 \quad (3.89)$$

3.3. Concluding remarks

The Infrastructure, necessary for linear and nonlinear analysis developed and implemented in chapters to follow, was laid here. System characteristics and the physically localised nature of RID encouraged separating the overall NL system $\mathbf{S}_{NL} \stackrel{S}{\supset} \{\mathbf{S}_L, \mathbf{S}_N\}$ into LTI ‘ \mathbf{S}_L ’ and NL ‘ \mathbf{S}_N ’ subsystems, whose characteristics will narrow down suitable NL analysis to the approximate DFM. Rotating frame \mathbf{S}_L and \mathbf{S}_N subsystems are setup in a feedback formulation (*fig. 3.5*) to make use of Nyquist like criteria (*Ch.4*) and facilitate further adaptations from the rich NL control engineering (§.A.2.3, *fig.A.2*).

Linear Rotordynamic system As RID is initially augmented to rotating frame EOMs (§.3.2.2.1), their relation to those of the stationary frame are detailed to emphasise the physically comprehensible effects on FWD/BWD modes and FRFs, and postulate on

the precession-quenching effect (*p.193*) of incommensurate 2Ω -frequency from support anisotropy (3.9). Complex EOMs of the stable gyroscopic subsystem are stated in both frames, as they better represent modal frequencies signs, and are used in conjunction with the adapted Nyquist criterion (*Ch.4*).

Eigen-results closed-form expressions (§.3.1.3.2) are developed in both frames for comparison with RID-augmented systems, and their relation (3.48) used to: 1) Conclude on the stability of FWD/BWD modes from those analysed in the rotating frame, which is essential for complex stiffness RID; 2) Arrive at the critical speed expression (3.44), necessary to elucidate the impossibility of subcritical RID instability; and 3) Emphasise modal vectors' (3.50), and corresponding residue matrices (3.51) invariance, which reflect on frequency-shifted FRFs and their peculiarities (§.3.1.2.3). Modal directionality was classified (*p.103*) to aid in identifying FWD/BWD mode-dominated FRF portions.

Frequency response NL stability methods are to be adopted/modified for the RID problem, so it was necessary to examine the relevant \mathbf{S}_L TFM/FRM characteristics. Although FRMs in both stationary and rotating frames satisfied the Normality condition, they failed the Diagonal Dominance (away from resonances) and Positive Real conditions. While individual TFs in the stationary frame were fairly standard, with speed-invariant zeros hence anti-resonances, the rotating frame point TFs exhibited an interesting zeros pattern. Both zeros $o_{1,2}$ will be complex for speeds up to Ω_c , after which they assume real values of opposite signs (e.g. *figs.4.7*), which renders the TF of non-minimum-phase at supercritical speeds. However, for the adapted Nyquist criterion (*Ch.4*) the complex rotating frame TF satisfies the minimum-phase requirements. All TFs developed represent completely observable and controllable systems, provided gyroscopic coupling is maintained, which is necessary (§4.3) to investigate unstable poles.

RID is modelled as a localised friction joint that couples the linear rotor (*fig.3.1*) to the rotating frame ground (*fig.3.4*) by two elements in the orthogonal ξ, η directions, resulting in internal (nonlinear) restoring force output $\mathcal{F}_\xi, \mathcal{F}_\eta \in \mathcal{F}$.

Linear viscous and (flawed) hysteretic damping models are arguably justified by the small vibration amplitudes that rotors are designed to endure, and are viable for tight joints, e.g. Curvic Couplings. The main problem with hysteretic RID stems from using its complex stiffness (3.63) whilst not accounting for $\text{sgn}(\omega)$ (3.64), which yields misleading results in assessing modal stability with negative frequencies, and FR-based stability analysis of complex rotor representation. This FR model (3.64) can be augmented to

3. RID systems modelling and characteristics

rheological EOMs *whilst including the all important* $\text{sgn}(\omega)$ but does not transfer to the stationary frame with ease, and has to be analysed in the rotating frame.

NL damping models are more representative of different RID joints, but have hard characteristics that further limit suitable NL analysis. SVNL models include the simple Coulomb and a *proposed* parabolic friction elements (*fig.3.2*) which offers an explanation (§.5.3.2.2) as to why spline coupling RID-induced whirling at one speed may be bounded for minor disturbances yet jumps (*fig.5.5*) to unbounded with significant disturbances (*p.203*). MVNL models are various Macro- and Micro-microslip Masing's elements, which are more representative of interference and flanged couplings. Naturally, representing \mathcal{F} in the stationary frame is rather favourable for physical appreciation as well as to avoid possible LTV terms. However, with the exception of Coulomb damping, this process proved to be rather intractable.

4. Analysis of linear RID system

In this chapter, the eigen-analysis, frequency response and modal stability analysis of the 2DOF LTI RID system are elaborated and exemplified numerically. Conditions for the existence of RID instability are arrived at using the Routh-Hurwitz criterion, and elucidate the stabilising gyroscopic effect. The effect of linear RID on BWD and FWD modes and their stability is derived and compared to the rotor-without-RID case. The flawed hysteretic RID model is implemented appropriately in the rotating frame whilst accounting for $\text{sgn } \omega$, and yields representative results in the stationary frame. The experimentally-observed unusual CCW Nyquist plot possibility is explained thoroughly as the result of unstable poles in the right-half- s -plane. This explanation is the fundamental basis of the experimentally-applicable stability test (EAST) for a possibly-unstable general dynamic system, which is presented lastly.

4.1. Modal analysis and frequency response of stable rotor without RID

This section sets-off by validating and exemplifying the analytical derivations and findings of *CH.3* for asymptotically stable rotor-bearing system without RID. The validated results are then further probed into for later comparison with the effects of introducing linear RID to the LTI rotordynamic system \mathbf{S}_L (§.4.2).

Numerical examples from several textbooks [49, 96, 97] were utilised to verify the eigen-solver [1] results and thereafter, the analytical derivations of *CH.3*. A verification example, using a simple xy -frame spatial model (3.2, 4.1) from [96] for a single-disc rotor that is mounted on orthotropic bearings, is presented (*fig. 4.1*) for illustration purposes. The numerical values borrowed:

$$\begin{aligned} m &= 14.29 & \mathcal{G} &= 2.871 & \text{in Kg} \\ k_x &= 1.570e6 & k_y &= 1.195e6 & \text{in N/m} = \text{Kg/s}^2 \end{aligned} \tag{4.1}$$

were derived by Rayleigh-Ritz method with the displacement function being the first mode shape of a simply-supported beam representing the rotor's symmetric shaft. The full set of modal frequencies $\Im(\lambda_i)_{i \in \{1 \dots 4\}}$ are plotted against increasing rotational speed

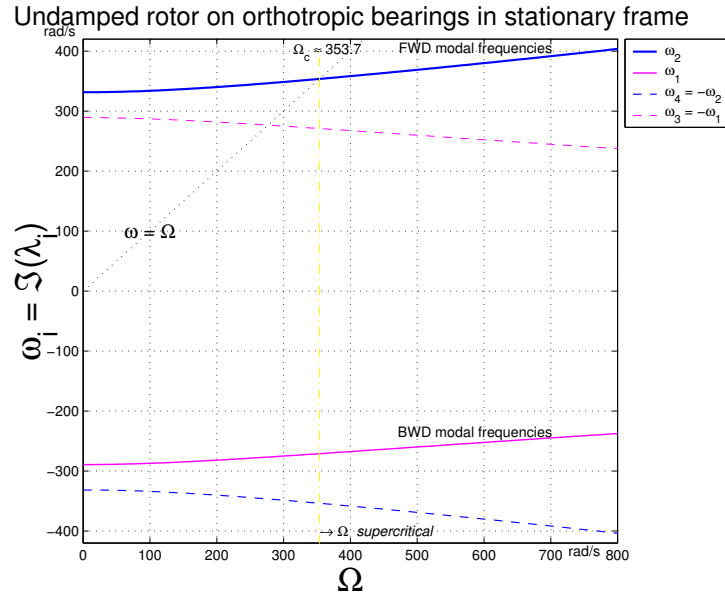


Figure 4.1.: Modal frequencies $\omega_i = \Im(\lambda)_{i \in \{1...4\}}$ of anisotropic rotor (3.2, 4.1) $\mathbf{C} = \mathbf{0}$

$\Omega : [0 \triangleright 800 \gtrsim_{(\Omega \equiv 2\omega_f)}]$ to well above the critical speed $\Omega_c \simeq 353.7$ rad/s, at which $\omega_{f_u} \equiv \Omega$ (fig. 4.1) and after which $\omega_f \equiv \omega_2 = -\omega_4 < \Omega_{\text{super-critical}}$.

Numerical results of the initial validation phase, i.e. Eigenvalues (e.g. figs. 4.1, 4.2) and FRFs (e.g. figs. 4.8, 4.9) of stable \mathbf{S}_L , are in excellent agreement with those of [96] as well as the eigenvalue expressions in §3.1.3.2, which validates the:

- State-space and FRM models set-up in §3.1.2
- Analytical eigenvalue expressions derived in §3.1.3.2
- Eigensolver [1] used throughout

The numerical values borrowed from [96] for the isotropic rotor of (3.2) are:

$$m = 14.29 \text{ Kg}; \quad \mathcal{G} = 2.871 \text{ Kg}; \quad c = 75 \text{ Ns/m} \quad k = 1.195e6 \text{ N/m} \quad (4.2)$$

4.1.1. Analytical modal analysis

4.1.1.1. Eigenvalues

Eigenvalues in the stationary xy -frame The expression for eigenvalues $\lambda_{b,f}$ (3.45) is restated here (4.3) in a rearranged form primarily to examine conveniently the changes to $\Re(\lambda_{b,f})$ with speed Ω , which are to be compared to those of the same system when

augmented with RID (4.12).

$$\lambda_{b,f} = \frac{-c + i\left(\Omega\mathcal{G} \mp \sqrt{(\Omega\mathcal{G} + ic)^2 + 4mk}\right)}{2m} \quad (4.3)$$

The expression under the square-root in (4.3) is complex $\forall \Omega \neq 0$, and of the form:

$$\sqrt{(\Omega\mathcal{G} + ic)^2 + 4mk} = \sqrt{a + ib} \quad (4.4a)$$

$$\text{where } a = 4mk + (\Omega\mathcal{G})^2 - c^2 > 0 \quad \text{and} \quad b = 2\Omega\mathcal{G}c > 0 \quad (4.4b)$$

The square-root of a complex expression/quantity, e.g. (4.4) results in another complex expression, whose real and imaginary parts are expressed by (A.5) the formula for square-roots of complex quantities. By the foregoing (4.3,4.4), real parts of eigenvalues $\Re(\lambda_{b,f})$ have two contributors:

- The quantity $-\frac{c}{2m}$ is common and contributes equally to both $\Re(\lambda_b)$ and $\Re(\lambda_f)$
- The imaginary quantity $i\Im\left(\sqrt{(\Omega\mathcal{G} + ic)^2 + 4mk}\right)$ multiplied by $(\frac{i}{2m})$, contributes to both $\Re(\lambda_b)$ and $\Re(\lambda_f)$, yet in an opposite sense in accordance with (4.3)

Since $b = 2\Omega\mathcal{G}c$ is +ve (4.4b), formula (A.5a) applies to $\sqrt{(\Omega\mathcal{G} + ic)^2 + 4mk}$, i.e.

$$\begin{aligned} \sqrt{a + ib} &= \sqrt{\frac{a + \sqrt{a^2 + b^2}}{2}} + i\sqrt{\frac{-a + \sqrt{a^2 + b^2}}{2}} \quad \text{for } b > 0 \\ &= \Re\left(\sqrt{(\Omega\mathcal{G} + ic)^2 + 4mk}\right) + i\Im\left(\sqrt{(\Omega\mathcal{G} + ic)^2 + 4mk}\right) \end{aligned}$$

with the resulting imaginary quantity ($\times \frac{i}{2m}$):

- Adds to $-\frac{c}{2m}$ in the case of λ_b , hence increasing $\Re(\lambda_b)$ —less negative.
- Subtracts from $-\frac{c}{2m}$ in the case of λ_f , hence decreasing $\Re(\lambda_f)$ —more negative

Since $b \stackrel{\text{def}}{=} 2\Omega\mathcal{G}c$ increases with increased speed, then $\Re(\lambda_b)$ increases while $\Re(\lambda_f)$ decreases with increased speed as demonstrated in *fig. 4.2*.

Numerical examples of eigenvalues' variation with speed *Fig. 4.2* presents the eigenvalues $\lambda_{1,2} \equiv \lambda_{b,f}$ that were calculated for \mathbf{S}_L represented in the stationary xy -frame (3.2), while *fig. 4.3* presents the eigenvalues $\lambda_{r:1,2}$ calculated for \mathbf{S}_{rL} in the rotating $\xi\eta$ -frame (3.8), with rotordynamic coefficients (4.2). In (*figs. 4.2, 4.3*), $\lambda_{1,2}, \lambda_{r:1,2}$ are separated into real and imaginary parts $\Re(\lambda), \Im(\lambda)$ that are presented on the same graph (*figs. 4.2,*

4. Analysis of linear RID system

4.3) with two ordinates, one for each part, against the abscissa Ω . The modal frequency $\omega = \Im(\lambda)$ ordinate represents increasing ω , while the decay rate ordinate represents decreasing $\Re(\lambda) \Rightarrow$ increasing $|\Re(\lambda)|$ for stable \mathbf{S}_L .

Coefficients (4.2) result in an undamped system's $\Omega_{cu} = \sqrt{\frac{k}{m-g}} \approx 323.5 \text{ rad/s}$, which by inspection, is virtually identical to this damped system's Ω_c that is indicated on plots with $\Omega : [\Omega_1 \triangleright \Omega_2]$ because of its strong significance to all analysis that follow. Observing and comparing both figures (figs. 4.2, 4.3) shows:

- As $\Omega : [0 \triangleright 800]$ rad/s,
 - FWD mode: The +ve $\omega_2 \equiv \omega_f \nearrow$ and $\Re(\lambda_f) \searrow \Leftrightarrow |\Re(\lambda_f)| \nearrow$;
 - BWD mode: The -ve $\omega_1 \equiv \omega_b \nearrow \Rightarrow |\omega_b| \searrow$ and $\Re(\lambda_b) \nearrow \Leftrightarrow |\Re(\lambda_b)| \searrow$
- $\omega_{r:1,2} \equiv \omega_{1,2} - \Omega$, while $\Re(\lambda_{r:1,2}) \equiv \Re(\lambda_{1,2})$
- $\omega_{r:1}$ is always -ve, while $\omega_{r:2}$ is $\begin{cases} +ve \text{ for } \Omega < \Omega_c \\ -ve \text{ for } \Omega > \Omega_c \end{cases}$

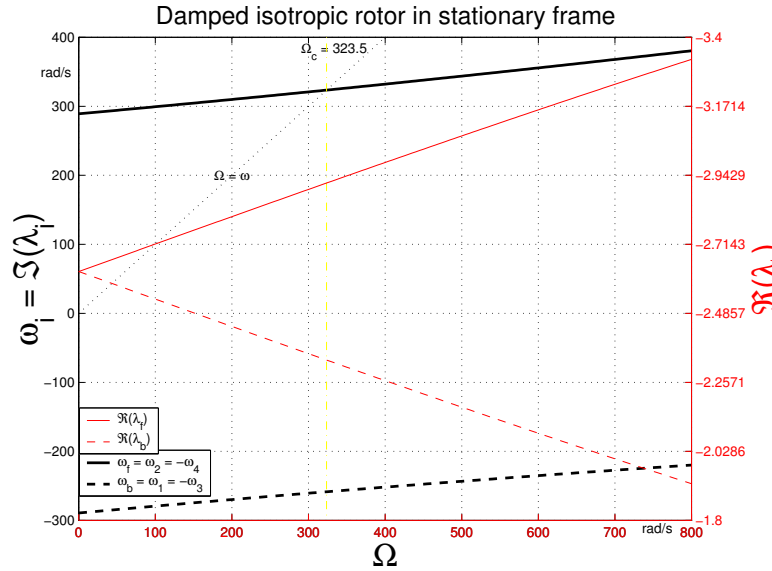


Figure 4.2.: Eigenvalues $\lambda_{b,f}$ (3.45) of isotropic rotor (3.2, 3.10) with parameters (4.2)

4.1.1.2. Modal damping factors

Modal damping is important for our stability analysis purposes as it is readily identifiable (§.6.2, fig.6.9) from response models, obtained experimentally or analytically, using off-the-shelf commercial software. Although $\text{sgn}(\Re(\lambda))$ assesses \mathbf{S}_L stability, damping factors $\gamma_{1,2}$ in stationary and $\gamma_{r:1,2}$ in rotating frames that were derived from the modal models (3.45, 3.47) are presented (fig. 4.4) for illustration and later-on comparisons with those derived from response models. As derived (3.46), fig. 4.4 shows that $\gamma_b \equiv \gamma_f$ but $\gamma_{r:1} \neq \gamma_{r:2}$

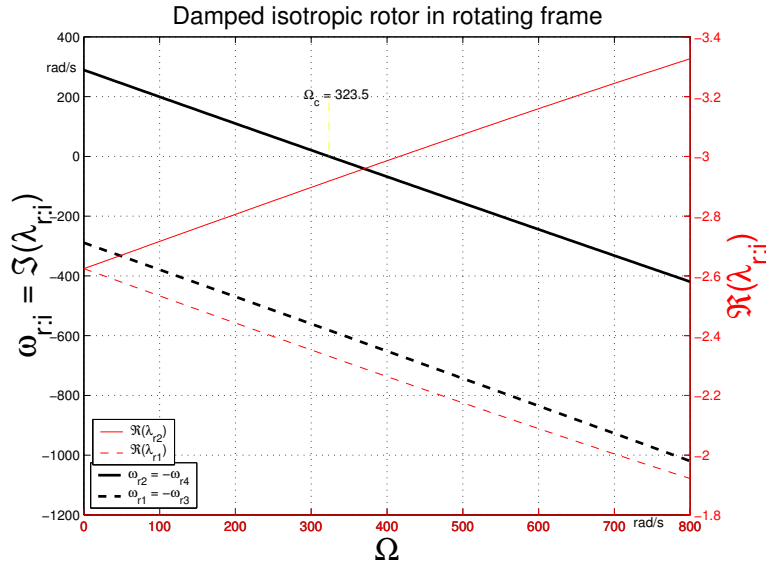


Figure 4.3.: Eigenvalues $\lambda_{r:1,2}$ (3.47) of isotropic rotor (3.8, 3.11) with parameters (4.2)

in the rotating $\xi\eta$ -frame. Unlike $\gamma_{b,f}$, $\gamma_{r:i \in \{1 \dots 4\}}$ are plotted on a logarithmic scale so as to accommodate their significant value variations.

It is interesting to observe the damping factors $\gamma_{r:2,4}$ of $\lambda_{r:2,4}$ rotating frame modes—resulting from FWD modes with $\lambda_f, \lambda_f^* = \lambda_{2,4}$ in xy -frame—around Ω_c . At the critical speed $\Omega_c, \because \omega_f = \Omega \therefore \omega_{r:2} = \omega_f - \Omega_c = 0 = \omega_{r:4} \Rightarrow \hat{\omega}_{r:2,4} = 0$, when the eigensolution is a non-oscillatory exponential decay with $\Im(\lambda_{r:2,4}) = 0$ and $\Re(\lambda_{r:2,4}) \equiv \Re(\lambda_{2,4}) \neq 0$; in which case: Neither $\Re(\lambda)_{r:2,4} = -(\gamma\hat{\omega})_{r:2,4}$ nor (3.34c) apply and damping factors $\gamma_{r:2,4}$ are *not defined*. As $\Omega \rightarrow \Omega_c$ from either end, $\hat{\omega}_{r:2,4} \rightarrow 0$ and $\gamma_{r:2,4} \rightarrow 1$ so as to compensate for the sustained $\Re(\lambda_{r:2,4}) \neq 0$ while $\hat{\omega}_{r:2,4} \neq 0$. As $\gamma_{r:2,4} \rightarrow 1$ around Ω_c , modes with $\lambda_{r:2,4}$ are almost critically damped and will exhibit very few oscillations albeit at $\omega_{r:2,4} \simeq 0$.

4.1.2. Frequency response of analytical rotordynamic models

FRF polar plots are used (§.4.3, 5.3.2) to examine stability. EAST (§.4.3) in particular, assesses modal stability based on examining the effect of unstable poles $\Re(p) > 0$ on the FRF phase angle swept $\Delta \angle H_{ij}(i\omega)$ on sweeping the range $\omega : [\omega_{e:1} < \Im(\lambda) < \omega_{e:2}]$. However, the effect of individual left- or right-half s -plane poles and zeros on $\Delta \angle H_{ij}(i\omega)$ can differ markedly, depending on: The ratio $|\frac{\Re}{\Im}|$ of each pole and zero, the frequency range $[\omega_{e:1}, \omega_{e:2}]$, as well as how well-separated poles are from each other (fig. 4.5). Accordingly, a thorough understanding of FRF polar plots' general behaviour is necessary.

4. Analysis of linear RID system

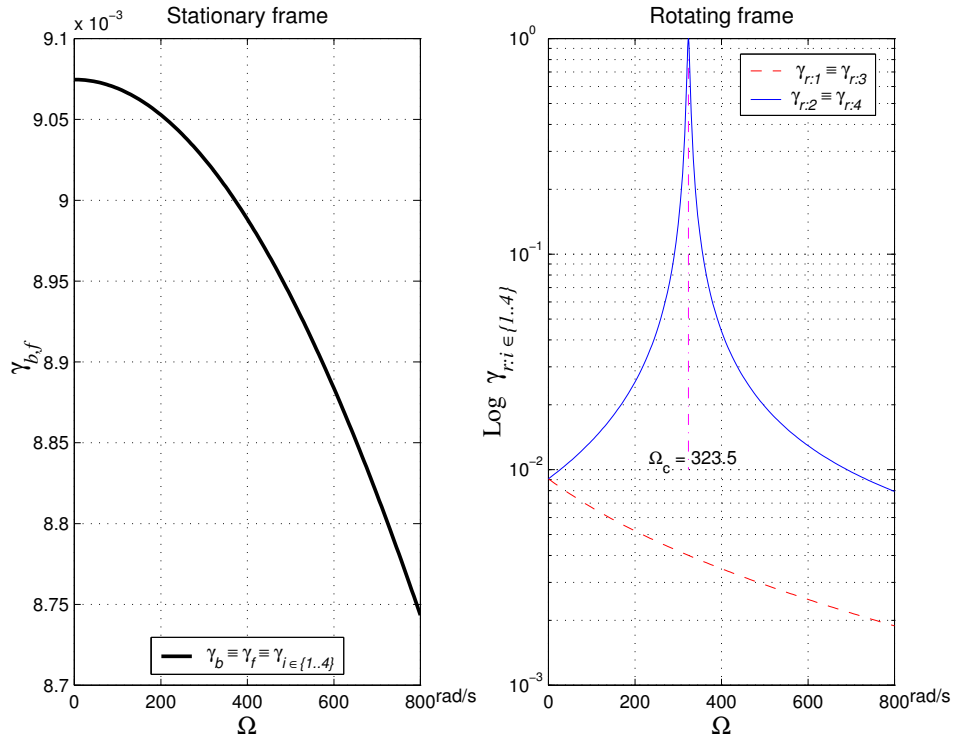


Figure 4.4.: Damping factors $\gamma_{1,2}, \gamma_{r,1,2}$ vs. Ω for stable rotor: parameters (4.2)

4.1.2.1. FRF characteristics of system with well-separated modes

A system with well-separated modes is one whose every mode is clearly identifiable from its FRF; i.e. every mode that is represented by a partial fraction (PF) in the FRF expansion (4.7) emulates a SDOF with a clear resonance on the magnitude plot and a quasi-circle on the polar plot, which are easily separable from those of other modes, e.g. *figs. 4.6, 4.9*. Rotors with RID that are of interest to this research would largely fall in this category on account of moderate external damping and well-separated modal frequencies, as will be elaborated hereafter. Also, the reliable implementation of EAST (§.4.3) requires a rotordynamic system with well-separated modes.

General FRF relation to poles, zeros, gains and frequency range According to the pole-zero-gain representation (3.54) of individual TFs, the corresponding FRFs' $|H_{ij}(i\omega)|$

and $\angle H_{ij}(i\omega)$ can be represented as:

$$\begin{aligned}
 H_{ij}(i\omega) &= g_{ij} \frac{\prod_{q=1}^u (i\omega - o_q)}{\prod_{v=1}^l (i\omega - p_v)}, & \text{with } u < l = 2n \\
 \therefore |H_{ij}(i\omega)| &= |g_{ij}| \frac{\prod_{q=1}^u |i\omega - o_q|}{\prod_{v=1}^l |i\omega - p_v|} \\
 \angle H_{ij}(i\omega) &= \angle(g_{ij}) + \sum_{q=1}^u \angle(\overrightarrow{i\omega - o_q}) - \sum_{v=1}^l \angle(\overrightarrow{i\omega - p_v}); & \angle(g_{ij}) = \begin{cases} 0 \forall +ve \operatorname{sgn}(g_{ij}) \\ -\pi \forall -ve \operatorname{sgn}(g_{ij}) \end{cases}
 \end{aligned} \tag{4.5}$$

Angles in a complex plane are measured in the CCW direction: $\Delta\angle(\cdot) \stackrel{\text{def}}{=} +ve$ in \odot .

The differences $(i\omega - p_v)$ and $(i\omega - o_q)$ represent complex pole and zero vectors $\overrightarrow{i\omega - p_v}$, $\overrightarrow{i\omega - o_q}$ respectively in the s -plane, from the pole $p_{v \in \{1 \dots l\}}$ or zero $o_{q \in \{1 \dots u\}}$ to some (excitation) frequency $i\omega_e$ on the imaginary axis (*fig. 4.5*). A pole or zero vector, e.g. $(i\omega - p)$ has a length $|(i\omega - p)|$ and angle $\angle(i\omega - p)$, which at $\omega = \Im(p)$ are $\Re(p)$ ‘shortest’ and 0 respectively. On sweeping a frequency range $\omega_e : [\omega_{e:1} \triangleright \omega_{e:2}]$ a pole (or zero) vector will sweep:

$$\Delta\angle(i\omega_e - p) \Big|_{\omega_e: [\omega_{e:1} \triangleright \omega_{e:2}]} = \angle(i\omega_{e:2} - p) - \angle(i\omega_{e:1} - p) = \tan^{-1}\left(\frac{\omega_{e:2} - \Im(p)}{-\Re(p)}\right) - \tan^{-1}\left(\frac{\omega_{e:1} - \Im(p)}{-\Re(p)}\right)$$

According to (4.5), all pole/zero vectors contribute to $\angle H_{ij}(i\omega)$; with $\angle(i\omega - o)$ adding to, and $\angle(i\omega - p)$ subtracting from the overall sum that results in $\angle H_{ij}(i\omega)$.

Angle swept by left-half s -plane pole/zero vectors Vectors of *enclosed*¹ poles or zeros will sweep a net angle of π radians as the $i\omega$ -axis is traversed from $-i\infty$ to $i\infty$:

$$\Delta\angle(i\omega_e - p) \Big|_{\omega_e: \langle -\infty \triangleright \infty \rangle} = \angle(i\infty - p) - \angle(-i\infty - p) = \pi \quad \text{if } \Re(p) < 0 \tag{4.6a}$$

Angle swept by right-half s -plane pole/zero vectors Vectors of such poles or zeros sweep a net angle of $-\pi$ radians as the $i\omega$ -axis is traversed from $-i\infty$ to $i\infty$:

$$\Delta\angle(i\omega_e - p) \Big|_{\omega_e: \langle -\infty \triangleright \infty \rangle} = \angle(i\infty - p) - \angle(-i\infty - p) = -\pi \quad \text{if } \Re(p) > 0 \tag{4.6b}$$

Impact of well-separated modes on FRFs An FRF with clearly identifiable and well-separated modes requires that consecutive eigenvalues have real parts that are substantially lower than the difference of their frequencies. A moderately-damped system whose

¹see *concept.A.1, p.241*

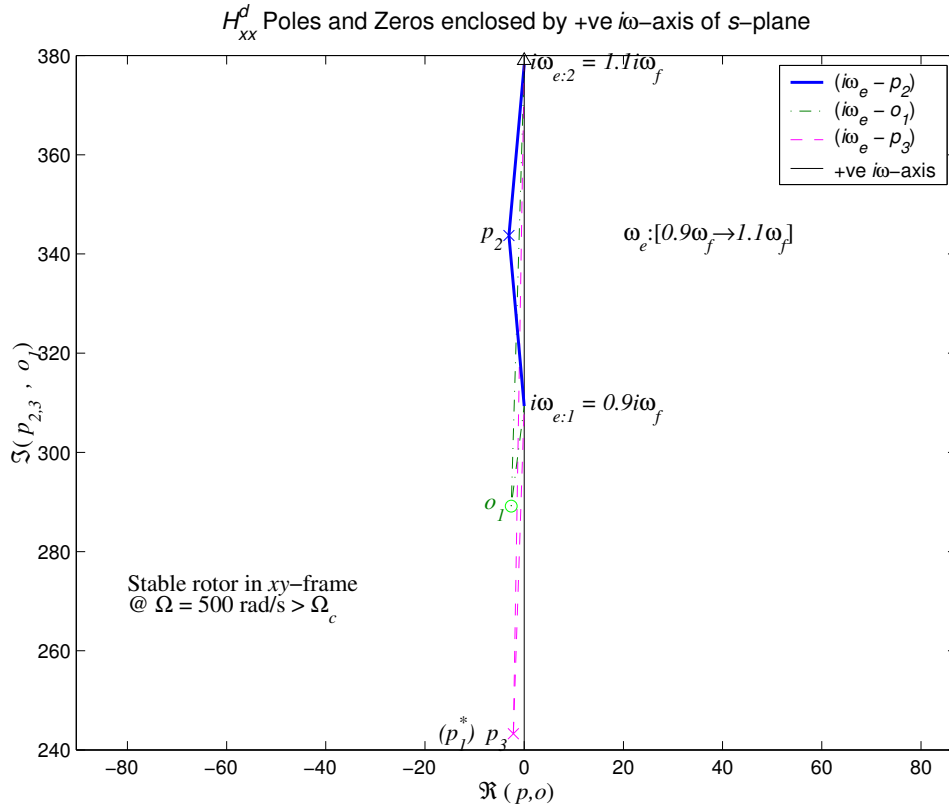


Figure 4.5.: Example $\Delta\angle(i\omega_e - p)$, $\Delta\angle(i\omega_e - o)$ contributing to $\Delta\angle H_{ij}(i\omega)$
 $\omega: [\omega_{e:1} \triangleright \omega_{e:2}]$

resonant frequencies are separated by 10% or more of their frequency is generally considered to be one with well-separated modes. Interest in analysing stability of RID systems implies that they fall in such a category because:

- Stability analysis is concerned with moderately- to lightly-damped modes, and evidently, rotordynamic systems that exhibit RID instability are not supplemented by overly heavy external damping. Consequently, the xy -frame S_L has parameters leading to modes with: $\Im(\lambda) \gg \Re(\lambda)$, which is reflected in TFs' poles with $\Im(p_v) \gg \Re(p_v)$ as well as zeros $\Im(o_q) \gg \Re(o_q)$ —see (3.57).
- RID instability may occur only at $\Omega > \Omega_{cu}$, which usually implies well-separated modal frequencies and hence well-separated poles and zeros.

FRF in frequency vicinities of moderately-damped, well-separated modes Parameters (4.2) at $\Omega = 500_{\text{rad/s}} > \Omega_c$ result in well-separated poles and zeros with the ratios: $|\frac{\Im}{\Re}(p)| \equiv |\frac{\Im}{\Re}(\lambda)| \simeq 112$ and $|\frac{\Im}{\Re}(o)| \simeq 110 \forall \Omega$ (fig. 4.5). Here onwards, a relatively limited frequency range in the neighbourhood of a zero or pole frequency $\omega_e : [\omega_{e:1} \triangleright \Im(o_p) \triangleright \omega_{e:2}]$ is denoted as $\Delta\omega_{o_q}$ or $\Delta\omega_{p_v}$ in the vicinities of the q^{th} zero and v^{th} pole respectively.

Accordingly, on sweeping $\Delta\omega_{p_v}$ or $\Delta\omega_{o_q}$ the relevant pole or zero vector will exhibit the following, which is demonstrated for $(i\omega_e - p_2)$ with $\Delta\omega_{p_2} \stackrel{\text{def}}{=} \omega_e : [0.9\omega_f \triangleright 1.1\omega_f]$:

- A substantial angle sweep $\Delta\angle(i\omega_e - p_2) \lesssim \pi_{\text{rad.}}$, e.g.:

$$\Delta\angle(i\omega_e - p_2) = \tan^{-1}\left(\frac{0.1\omega_f}{-\Re(p_2)}\right) - \tan^{-1}\left(\frac{-0.1\omega_f}{-\Re(p_2)}\right) \simeq 0.943\pi \quad ;$$

$\omega_e: [0.9\omega_f \triangleright 1.1\omega_f]$

- A significant variation in length, which is very short at $\omega_e = \Im(p_2)$

Meanwhile, the other pole/zero vectors sweep a negligible angle, and vary in length smoothly and monotonically; e.g. $\Delta|i\omega_e - p_3| \lesssim (\omega_{e:2} - \omega_{e:1})$, see *fig. 4.5*.

According to the foregoing and (4.5), each pole/zero vector of a system with well-separated modes has a marked influence on the FRF's:

- Magnitude $|H_{ij}(i\omega)|$ in the immediate vicinity of pole/zero frequency $\omega \simeq \Im(o_p)$. Because pole/zero vectors are *very short* at $\omega = \Im(o_p)$: $\prod_{q=1}^u |i\omega - o_q|$ diminishes and so does $|H_{ij}(i\omega)| \gtrsim 0$ at $\omega \simeq \Im(o_q)$; $\prod_{v=1}^l (i\omega - p_v)$ diminishes, and so $|H_{ij}(i\omega)|$ peaks at $\omega \simeq \Im(p_v)$. Although, the v^{th} resonance and q^{th} anti-resonance frequencies are very close to $\Im(p_v)$ and $\Im(o_q)$ respectively, they are generally not exactly equal due to the other pole and zero vectors' influence, albeit minimal.
- Phase angle swept $\Delta\angle H_{ij}(i\omega)$ on sweeping $\Delta\omega_{p_v}$ or $\Delta\omega_{o_q}$. A zero vector will *add* $\Delta\angle H_{ij}(i\omega) \lesssim \pi$, while a pole vector will *subtract* $\Delta\angle H_{ij}(i\omega) \lesssim \pi$ from $\angle H_{ij}(i\omega)$.

Partial fractions emulate a SDOF in modal frequency vicinities The foregoing is the rational reasoning behind stating that: Within a small frequency range $\Delta\omega_{p_v}$ in the vicinity of the v^{th} modal frequency ω_v , an individual FRF $H_{ij}(i\omega)$ is dominated by the v^{th} mode; thus behaving as a SDOF, which is represented by approximating the partial-fraction expansion (3.40) as:

$$H_{ij}(i\omega) = \sum_{v=1}^{2n} \frac{H_{ij}^v}{i\omega - p_v} \approx \frac{H_{ij}^v}{i\omega - p_v} + E_{ij}^v \quad \text{where } H_{ij}^v = \tilde{\mathbf{o}}_i^{\mathbf{c}v} \tilde{\mathbf{b}}_j^{\mathbf{r}v} = \tilde{\mathbf{O}}_{iv} \tilde{\mathbf{B}}_{vj} \quad (4.7a)$$

$$\mathbf{H}(i\omega) = \sum_{v=1}^{2n} \frac{\mathbf{H}^v}{i\omega - p_v} \approx \frac{\mathbf{H}^v}{i\omega - p_v} + \mathbf{E}^v \quad \text{where } \mathbf{H}^v = \tilde{\mathbf{o}}^{\mathbf{c}v} \tilde{\mathbf{b}}^{\mathbf{r}v} \quad , \forall \omega \in \Delta\omega_{p_v} \quad (4.7b)$$

The constant elements E_{ij}^v of matrix \mathbf{E}^v approximate the contributions of $2n - 1$ modes, other than the v^{th} mode, to $H_{ij}(i\omega)$ over frequency range $\Delta\omega_{p_v}$. Observing the FR contributions $\frac{H_{xx}^v}{i\omega - p_v}$, of the four modal partial fractions (PF) $v_{\in 1 \dots 2n=4}$, to their receptance

4. Analysis of linear RID system

$|H_{xx}^d(i\omega)|$ over the +ve ω -axis (fig. 4.6) validates such approximation and justifies its use later on. The four residue matrices of receptance for parameters (4.2) at $\Omega = 500_{\text{rad/s}} > \Omega_e$, with corresponding matrices in xy - and $\xi\eta$ -frame being identical, are:

$$\begin{aligned} \mathbf{H}^b \stackrel{\text{def}}{=} \mathbf{H}^1 \equiv \mathbf{H}^{r:1} &= \begin{bmatrix} 9.12 + i5960.76 & -5960.76 + i9.12 \\ 5960.76 - i9.12 & 9.12 + i5960.76 \end{bmatrix} 10^{-8} = \mathbf{H}^{3*} \equiv \mathbf{H}^{r:3*} \\ \mathbf{H}^f \stackrel{\text{def}}{=} \mathbf{H}^2 \equiv \mathbf{H}^{r:2} &= \begin{bmatrix} -9.12 - i5960.76 & 5960.76 - i9.12 \\ -5960.76 + i9.12 & -9.12 - i5960.76 \end{bmatrix} 10^{-8} = \mathbf{H}^{4*} \equiv \mathbf{H}^{r:4*} \end{aligned} \quad (4.8)$$

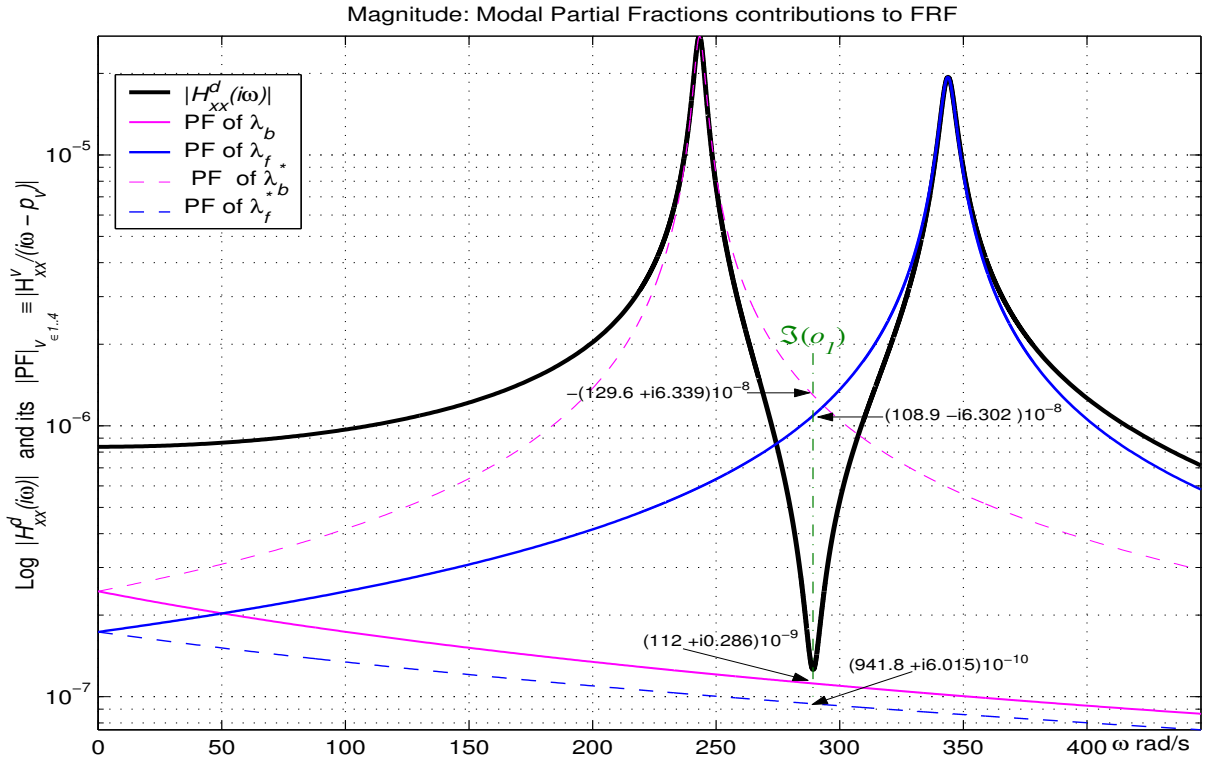


Figure 4.6.: Modal contributions to point receptance in xy -frame at $\Omega = 500_{\text{rad/s}}$

In fig. 4.6, attention is drawn to the anti-resonance frequency that is virtually equal to $\Im(o_1)$ the zero frequency, in accordance with the PFs summing-up to nil at the complex frequency o_1 (3.55)-p.111. At frequencies away from a +ve modal frequency $\omega_v > 0$: $\angle \frac{H_{ii}^v}{i\omega - p_v} \approx 0 \forall \omega_e < \omega_v$ and $\angle \frac{H_{ii}^v}{i\omega - p_v} \approx \pi \forall \omega_e > \omega_v$. Similarly, for $\omega_v < 0$: $\angle \frac{H_{ii}^v}{i\omega - p_v} \approx \pi \forall \omega_e < \omega_v$ and $\angle \frac{H_{ii}^v}{i\omega - p_v} \approx 0 \forall \omega_e > \omega_v$. Accordingly, $\Im(o_1)$ lies in-between the two consecutive poles' frequencies $-\omega_b, \omega_f$, whose PFs' FR intersect $\left| \frac{H_{xx}^3}{i\omega_{\text{int}} - p_3} \right| = \left| \frac{H_{xx}^2}{i\omega_{\text{int}} - p_2} \right|$ at a frequency ω_{int} fairly close to $\Im(o_1)$. This is because at the anti-resonance frequency, PFs of λ_b^* and λ_f have FRs that are almost π_{rad} out-of-phase yet with comparable magnitudes, which are about one order higher than those of λ_b and λ_f^* PFs. This scenario is typical of most moderately damped mechanical systems, rotating or stationary, and is elaborated here

for comparison with the atypical scenario of point FRFs in the $\xi\eta$ -frame.

4.1.2.2. Example pole-zero maps and FRF plots

It is important to have a firm grasp of the relation between poles/zeros and FRFs' phasing as this shall be used for identifying instability. A commentary on both *point* and *quad* receptance FRFs as a consequence of their TFs' poles, zeros and gain is presented here for stationary-frame $H_{xx}^d(i\omega)$, $H_{yx}^d(i\omega)$ and rotating-frame $H_{\xi\xi}^d(i\omega)$, $H_{\eta\xi}^d(i\omega)$. First, pole-zero maps are presented (*fig. 4.7*) for point TFs $H_{xx}^d(s)$, $H_{\eta\xi}^d(s)$ on s -planes with unequally-scaled real and imaginary axis for compactness reasons. As each TF in a TFM of this rotor represents a completely controllable and observable $\mathbf{S}_L(\mathbf{A}, \mathbf{B}, \mathbf{O})$, the poles of quad TFs $H_{yx}^d(s)$, $H_{\eta\xi}^d(s)$ are identical to those of point TFs. Zeros and gains of all TFs considered, including $H_{yx}^d(s)$, $H_{\eta\xi}^d(s)$, are given by (3.56b, 3.57b).

FRF plots are presented in log-magnitude and polar plot formats (*figs. 4.8, 4.9*). Point FRFs are in solid while quad FRFs are in dashed lines. The frequency range $\Delta\omega_e \stackrel{\text{def}}{=} \omega_e : [\omega_{e:1} \triangleright \omega_{e:2}]$ swept is part of the s -plane +ve ω -axis, which is selected in each case to include the vicinities $\Delta\omega_{p_{\downarrow}}, \Delta\omega_{o_{\downarrow}} \forall (p, o)$ of point TFs that are in the upper-half s -plane, except for those at $s = 0$. Start frequencies ($\omega_{e:1}$) are chosen to be not far from $\Im(p_b)$ so as to make $H_{(\omega_{e:1})}$ visible/unmasked on the polar plot. These poles' and zero's frequencies are shown on magnitude plots so as to indicate approximately the frequencies of resonances and anti-resonances. $\Delta\omega_e$ is split into two segments $[\omega_{e:1} \triangleright \Im(o)]$ and $[\Im(o) \triangleright \omega_{e:2}]$ that are connected at the point TF's zero-frequency. The corresponding FRF mappings $H_{ij}(\omega)_{[\omega_{e:1}, \Im(o)]}$ and $H_{ij}(\omega)_{[\Im(o), \omega_{e:2}]}$ are distinguished by different line weights. This is to identify the part of FRF that is influenced by the FWD mode from that influenced by the BWD mode, especially on the polar plots. Also, the first FRF point $H_{(\omega_{e:1})}$ is marked by 'o' on the polar plots so that the direction of phase angle swept $\Delta\angle H_{(\omega)}_{[\omega_{e:1} \triangleright \Im(o) \triangleright \omega_{e:2}]}$ can be established.

At sub-critical speeds: $\Omega < \Omega_c$ (*fig. 4.8*)

In the stationary xy -frame: Both $H_{xx}(s)$ and $H_{yx}(s)$ have the two poles $p_3(\equiv p_1^*)$ and p_2 in the upper-left-quarter s -plane, which correspond to the BWD mode with $\lambda_3(\equiv \lambda_b^*)$ and the FWD mode with λ_2 respectively (3.45). $H_{xx}^d(s)$ has a complex zero o in between p_3 and p_2 (3.56), while $H_{yx}^d(s)$ does not, which is characteristic of point and quad TFs [49] respectively. However, $H_{yx}^d(s)$ does have a zero at the origin $s = 0$. Accordingly, both $H_{xx}(i\omega)$ and $H_{yx}(i\omega)$ exhibit resonances around $\omega_3(\equiv -\omega_b)$ and $\omega_2(\equiv \omega_f)$. Meanwhile, around $\omega = \Im(o)$, $H_{xx}^d(i\omega)$ has an anti-resonance, while $H_{yx}^d(i\omega)$ exhibits a minimum. By (4.5), at $\omega = 0$, $|H_{xx}^d(i0)| > 0$ but $\angle H_{xx}^d(i0) = 0$ as the angles of complex-conjugate pole/zero vectors cancel out. On the other hand, $|H_{yx}^d(i0)| = 0$ due to the zero at $s = 0$; a static force

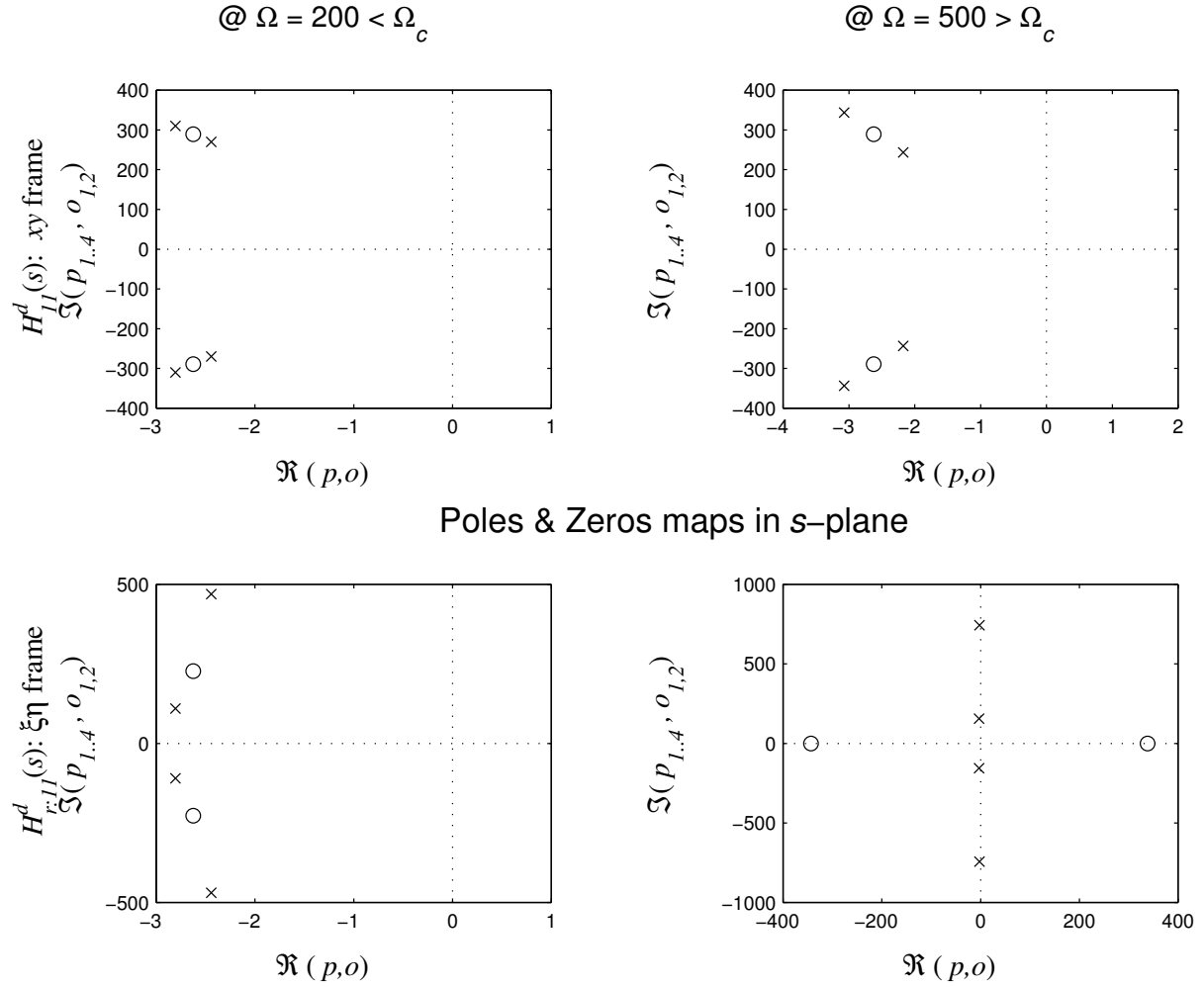
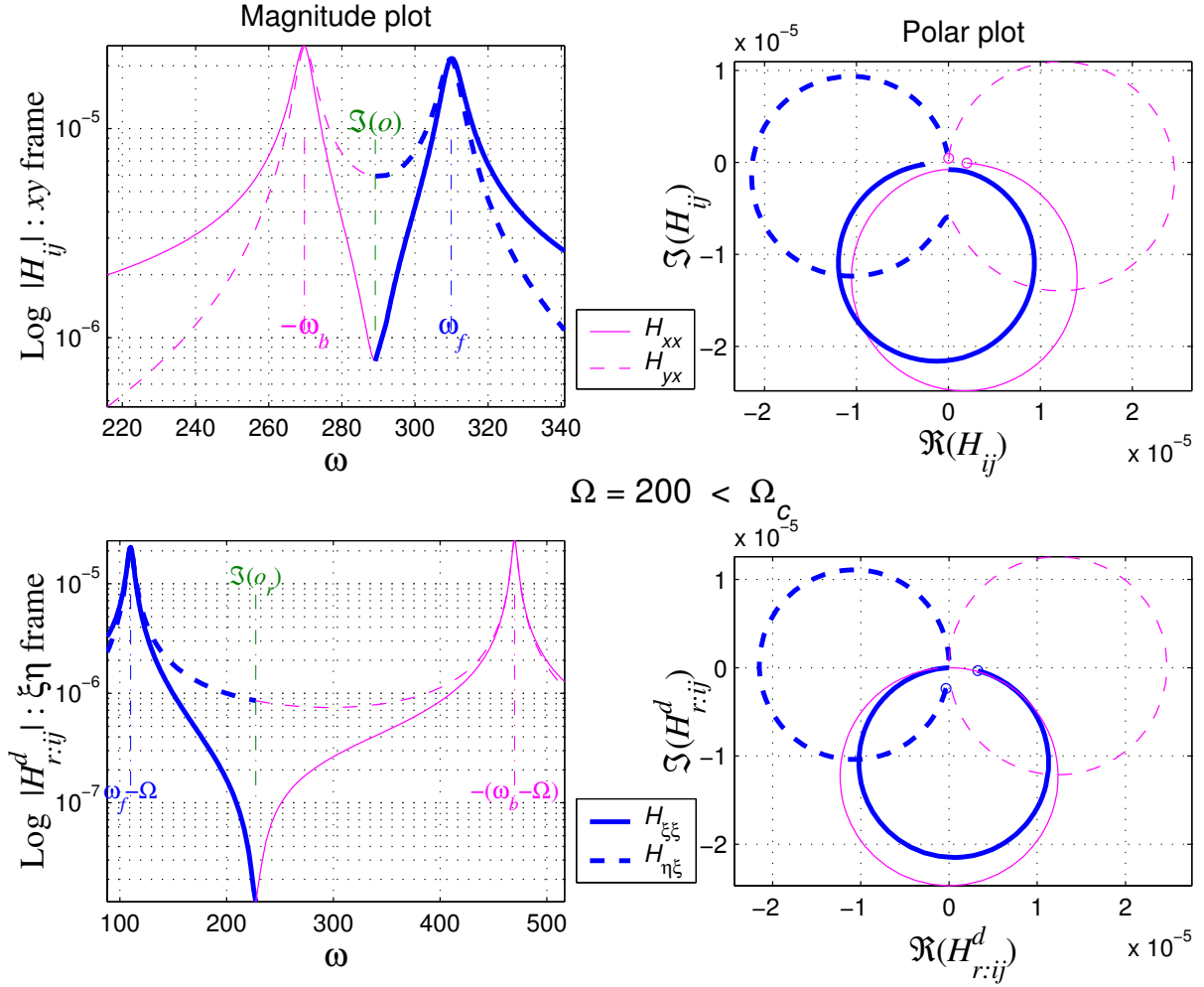


Figure 4.7.: Point TF Pole-Zero maps at sub/supercritical speeds in xy - and $\xi\eta$ -frames
 $H_{\xi\xi}^d(s)$ poles at $\Omega > \Omega_c$ are complex, but seem to be almost on $i\omega$ -axis due to their comparatively very small real parts and the scaling used to accommodate the purely real zeros (3.57a) of comparative magnitude (but opposite signs) with poles imaginary parts.

f_x does not cause a response (deflection) in the perpendicular direction y . Meanwhile, $\angle H_{yx}^d(i\omega) = \pi/2$ for $\omega \gtrsim 0$ due to the corresponding zero vector $\angle(i\omega - 0) = \pi/2$. This situation does not change much as ω increases up-to $\omega_{e:1} \approx 200_{\text{rad/s}}$ as demonstrated (fig. 4.8) with $\angle H_{xx}^d(i\omega_{e:1}) \lesssim 0$, $\angle H_{yx}^d(i\omega_{e:1}) \lesssim \pi/2$ and $|H_{yx}^d(i\omega_{e:1})| \gtrsim 0$.

As frequency range $\omega : [\omega_{e:1} \triangleright \Im(p_3) \triangleright \Im(o) \triangleright \Im(p_2) \triangleright \omega_{e:2}]$ is swept, the following FRF phase variations occur:

- Point FRF $H_{xx}^d(i\omega)$: On traversing $\Delta\omega_{p_3}$, the pole vector $(\overrightarrow{i\omega_e - p_3})$ sweeps an angle $\Delta\angle(i\omega_e - p_3) \lesssim \pi$ which subtracts from $\angle H_{xx}^d(i0) = 0$ leading to a phase angle swept $\Delta\angle H_{xx}^d(i\omega) \approx -\pi$ and leaving $\angle H_{xx}^d(i\omega) \approx -\pi$. Onto traversing $\Delta\omega_{o}$, the zero vector sweeps $\Delta\angle(i\omega_e - o) \lesssim \pi$, hence adding $\Delta\angle H_{xx}^d(i\omega) \approx \pi$ which annuls the phase introduced by $(\overrightarrow{i\omega_e - p_3})$ and leaves $\angle H_{xx}^d(i\omega) \approx 0$. Notice that at $\omega_e = \Im(o)$,


 Figure 4.8.: FRFs in stationary (1st row) and rotating (2nd row) at $\Omega < \Omega_c \Rightarrow \Omega < \omega_f$

$\angle H_{xx}^d(i\Im(o)) = -\pi/2$. By the time $\omega_{e:2}$ is reached, the other pole vector ($\overline{i\omega_e - p_2}$) had swept another $\Delta\angle(i\omega_e - p_2) \lesssim \pi$ leaving $\angle H_{xx}^d(i\omega_{e:2}) \approx -\pi$; i.e. the overall change in phase angle $\Delta\angle H_{xx}^d(i\omega) \gtrsim -\pi$.

$\omega: [\omega_{e:1} \triangleright \omega_{e:2}]$

- Quad FRF $H_{yx}^d(i\omega)$: The first pole vector sweeps $\Delta\angle(i\omega_e - p_3) \lesssim \pi$, which subtracts from $\angle H_{yx}^d(i\omega_{e:2}) \approx \pi/2$, leaving $\angle H_{yx}^d(i\omega) \approx -\pi/2$. Then ($\overline{i\omega_e - p_2}$) sweeps another $\Delta\angle(i\omega_e - p_2) \lesssim \pi$, leaving $\angle H_{yx}^d(i\omega_{e:2}) \approx -3\pi/2$. The overall change in phase angle $\Delta\angle H_{yx}^d(i\omega) \lesssim -2\pi$.

$\omega: [\omega_{e:1} \triangleright \omega_{e:2}]$

In the rotating $\xi\eta$ -frame: Both $H_{\xi\xi}(s)$ and $H_{\eta\xi}(s)$ in $\mathbf{H}_r^d(s)$ have $p_{r:2} \equiv (\lambda_f - i200)$ corresponding to the CCW mode (3.47a), and $p_{r:3} \equiv (\lambda_b - i200)^*$ corresponding to the CW mode (3.47b), in the upper-left-quarter s -plane. $H_{\xi\xi}^d(s)$ has a complex zero o_r in between $p_{r:2}$ and $p_{r:3}$, while $H_{\eta\xi}^d(s)$ has a -ve real zero and -ve gain $g_{\eta\xi}^d$ (3.57). Both $H_{\xi\xi}(i\omega)$ and $H_{\eta\xi}(i\omega)$ exhibit resonances around $\omega_e = (\omega_f - 200)$ and $\omega_e = -(\omega_b - 200)$. Although $H_{\xi\xi}^d(i\omega)$ has

4. Analysis of linear RID system

an anti-resonance around $\omega_e = \Im(o_r)$, $H_{yx}^d(\omega)$ does not exhibit its minimum thereabouts. Like $H_{xx}^d(i\omega)$, $|H_{\xi\xi}^d(i\omega)| > 0$ and $\angle H_{\xi\xi}^d(i\omega) = 0$. Unlike $H_{yx}^d(i\omega)$ however, $|H_{\eta\xi}^d(i\omega)| > 0$ and $\angle H_{\eta\xi}^d(i\omega) = -\pi$ due to the -ve zero and -ve $g_{\eta\xi}^d$ respectively. As ω increases up-to $\omega_{e:1} \approx 90_{\text{rad/s}}$, this situation does not change much *except for* $\angle H_{\eta\xi}^d(\omega_{e:1}) \approx -\frac{\pi}{2}$ (fig. 4.8) due to the angle swept by the real zero's vector $\Delta\angle\left(\overrightarrow{i\omega + \frac{c}{2m-g}}\right) \underset{\omega:[0 \triangleright \omega_{e:1}]}{\lesssim} \frac{\pi}{2} \Rightarrow \Delta\angle H_{\eta\xi}^d(\omega) \underset{\omega:[0 \triangleright \omega_{e:1}]}{\lesssim} \frac{\pi}{2}$.

As $\omega : [\omega_{e:1} \triangleright \Im(p_{r:2}) \triangleright \Im(o_r) \triangleright \Im(p_{r:3}) \triangleright \omega_{e:2}]$, these phase variations occur :

- $H_{\xi\xi}^d(\omega)$: Like $\angle H_{xx}^d(\omega)$, $\angle H_{\xi\xi}^d(\omega)$ traces out two quasi circles in \circlearrowleft direction, representing two semi-SDOFs, leaving $\angle H_{\xi\xi}^d(\omega_{e:2}) \approx -\pi$ and $\Delta\angle H_{\xi\xi}^d(\omega) \underset{\omega:[\omega_{e:1} \triangleright \omega_{e:2}]}{\gtrsim} -\pi$ overall change, which reflects the two poles and zero in-between ($p_{r:2}, o_r, p_{r:3}$).
- Starting at $\angle H_{\eta\xi}^d(\omega_{e:1}) \underset{\omega:[\omega_{e:1} \triangleright \omega_{e:2}]}{\lesssim} -\frac{\pi}{2}$, $\angle H_{\eta\xi}^d(\omega)$ traces out two quasi circles, with an overall change $\Delta\angle H_{\eta\xi}^d(\omega) \underset{\omega:[\omega_{e:1} \triangleright \omega_{e:2}]}{\approx} -2\pi$ and leaving $\angle H_{\xi\xi}^d(\omega_{e:2}) \approx -\frac{\pi}{2}$, which reflects the two poles ($p_{r:2}, p_{r:3}$) *without* a zero in-between.

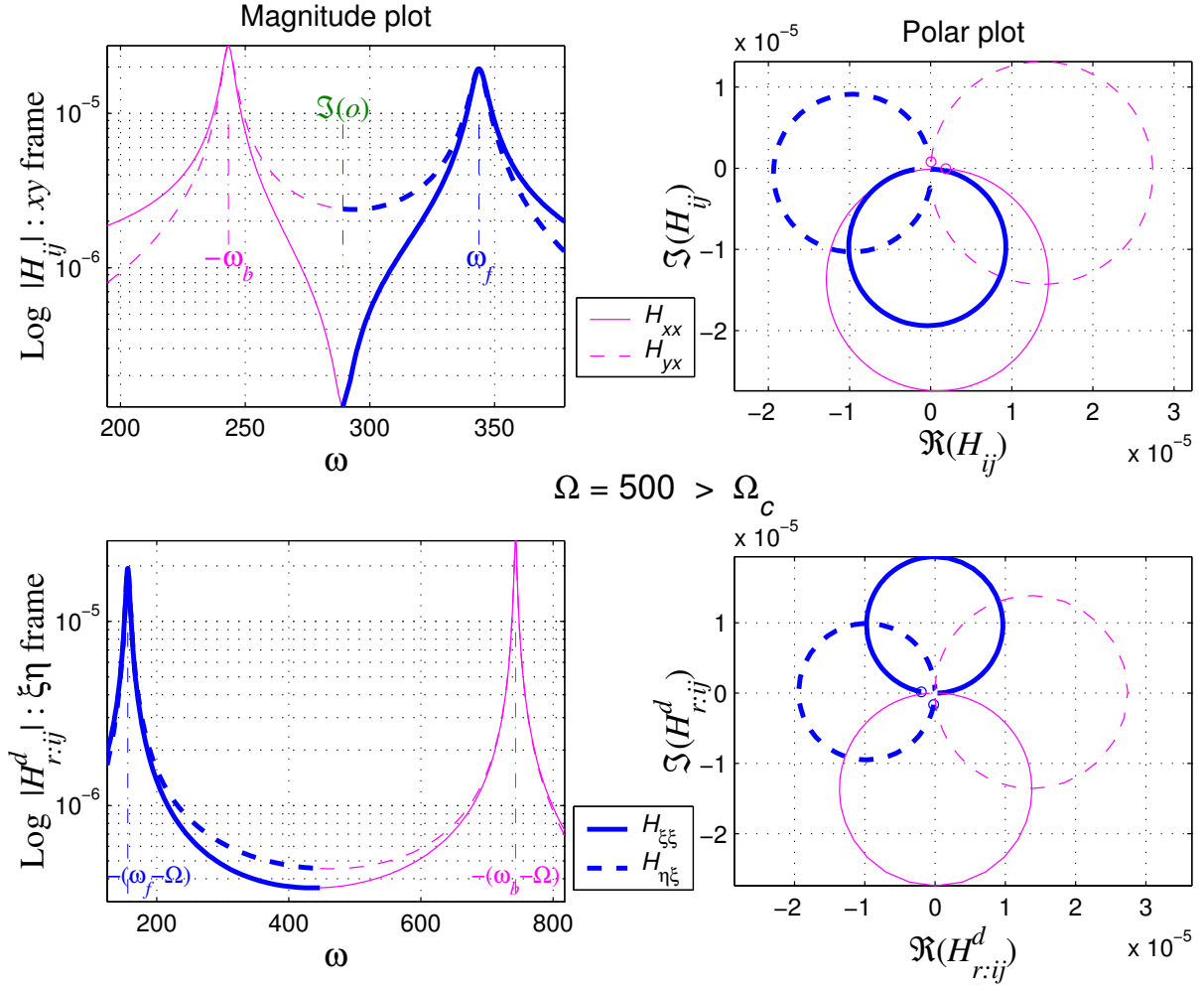
Observe that any phase change $\Delta\angle H(\omega)$ is in the \circlearrowleft direction as long as ω is swept in the increasing direction, i.e. $\Delta\omega \stackrel{\text{def}}{=} +\text{ve}$.

At super-critical speeds $\Omega > \Omega_c$ (fig. 4.9)

In the stationary xy -frame: At $\Omega = 500_{\text{rad/s}} > \Omega_c$, $H_{xx}^d(s)$ and $H_{yx}^d(s)$ have pole-zero maps (fig. 4.7) that are similar in layout to those at $\Omega = 200_{\text{rad/s}} < \Omega_c$. Naturally, the upper-half s -plane poles are further separated to reflect the better separated BWD and FWD modes with λ_b^*, λ_f , hence the stronger claim that $H(\omega)$ behaves like a quasi-SDOF as $\Delta\omega_p$ is traversed (4.7). Therefore, at $\Omega = 500_{\text{rad/s}}$, $H_{xx}^d(\omega)$ and $H_{yx}^d(\omega)$ have very similar phase $\angle H(\omega)$ and magnitude $|H(\omega)|$ characteristics to those at $\Omega = 200_{\text{rad/s}}$, albeit with different (more separated) resonant frequencies.

In the rotating $\xi\eta$ -frame: Point FRFs, at supercritical speeds, are perhaps the most interesting, due to the significant change in layout of point TF $H_{\xi\xi}(s)$ pole-zero map. In the upper-left-quarter s -plane:

- $H_{\xi\xi}(s)$ (and $H_{\eta\xi}(s)$) now has $p_{r:4} \equiv (\lambda_f - i500)^* \equiv p_{r:2}^*$ and $p_{r:3} \equiv (\lambda_b - i500)^*$ consecutively, both corresponding to CW modes (3.47b). $p_{r:2}$ that was significant at $\Omega < \Omega_c$ moved below the \Re -axis, since at $\Omega > \Omega_c$, $\Im(p_{r:2}) \equiv \Im(\lambda_f - i500) < 0$ and, unlike its complex-conjugate $p_{r:4}$, does not have a significant effect on $H(\omega)$.
 $\Delta\omega_e$


 Figure 4.9.: FRFs in stationary (1st row) and rotating (2nd row) at $\Omega > \Omega_c \Rightarrow \Omega > \omega_f$

- $H_{\xi\xi}^d(s)$ does not have complex zeros in-between consecutive poles at $\Omega > \Omega_c$, which is *atypical* of point TFs; instead, two real zeros of opposite sign $o_2 \equiv \Re(o_2) \equiv -o_1$ (3.57a).

Accordingly, both $H_{\xi\xi}(\omega)$ and $H_{\eta\xi}(\omega)$ exhibit resonances around $\omega_e = -(\omega_f - 500)$ and $\omega_e = -(\omega_b - 500)$ consecutively, while neither exhibits an anti-resonance. At $\omega = 0$, $|H_{\eta\xi}^d(\omega)| > 0$ and $\angle H_{\eta\xi}^d(\omega) = -\pi$, as for sub-critical speeds, due to the -ve $g_{\eta\xi}^d$. On the other hand, unlike the sub-critical case, $\angle H_{\xi\xi}^d(\omega) = -\pi$ because of the +ve real zero vector $\angle(\overrightarrow{i0 - o_1}) = -\pi$. As ω increases up-to $\omega_{e:1} \approx 120 \text{ rad/s}$, $\angle H_{\xi\xi}^d(\omega_{e:1}) \approx -\pi$ does not change much $\because \Delta \angle(\overrightarrow{i\omega - o_1}) = -\Delta \angle(\overrightarrow{i\omega - o_2})$, and $\angle H_{\eta\xi}^d(\omega_{e:1}) \approx -\frac{\pi}{2}$ as in the $\Omega < \Omega_c$ case. On sweeping the frequency range $\Delta\omega_e = [\omega_{e:1} \triangleright \Im(p_{r:4}) \triangleright \Im(p_{r:3}) \triangleright \omega_{e:2}]$, both $\angle H_{\xi\xi}^d(\omega)$ and $\angle H_{\eta\xi}^d(\omega)$ trace out two quasi circles in \cup direction, each representing two semi-SDOFs with overall changes: $\Delta \angle H_{\xi\xi}^d(\omega) \approx -2\pi \approx \Delta \angle H_{\eta\xi}^d(\omega)$, and leaving $\angle H_{\xi\xi}^d(\omega_{e:2}) \approx -\pi$ and

4. Analysis of linear RID system

$\angle H_{\eta\xi}^d(i\omega_{e:2}) \approx -\frac{\pi}{2}$, which reflects the two poles $(p_{r:4}, p_{r:3})$ without complex zeros in-between.

4.1.2.3. Peculiarities of point FRF in the rotating frame

Minimum or non-minimum? That is the question All TFs encountered thus far are minimum-phase TFs, with the exception of $H_{\xi\xi}^d(s) \forall \Omega > \Omega_c$ due to its +ve real zero $o_{r:1}$. However, $\forall \Omega < \Omega_c$, $H_{\xi\xi}^d(s)$ is strictly minimum-phase since all its poles and zeros are in the left-half s -plane. This is an intriguing situation, not only because stable physical systems generally have minimum-phase TFs, but mainly because this particular TF shifts characteristics from minimum-phase to apparent non-minimum-phase as Ω exceeds Ω_c . It is interesting to understand the cause of this behaviour and its implications on FRFs.

Point TFs almost always have complex-conjugate zeros in-between their complex-conjugate poles and, although in a noticeably different layout that affects its FRF markedly (fig.4.10), $H_{\xi\xi}^d(s)$ is no exception at $\Omega = 200 \text{ rad/s} < \Omega_c$. On the +ve frequency axis, $\omega_{r:3}$

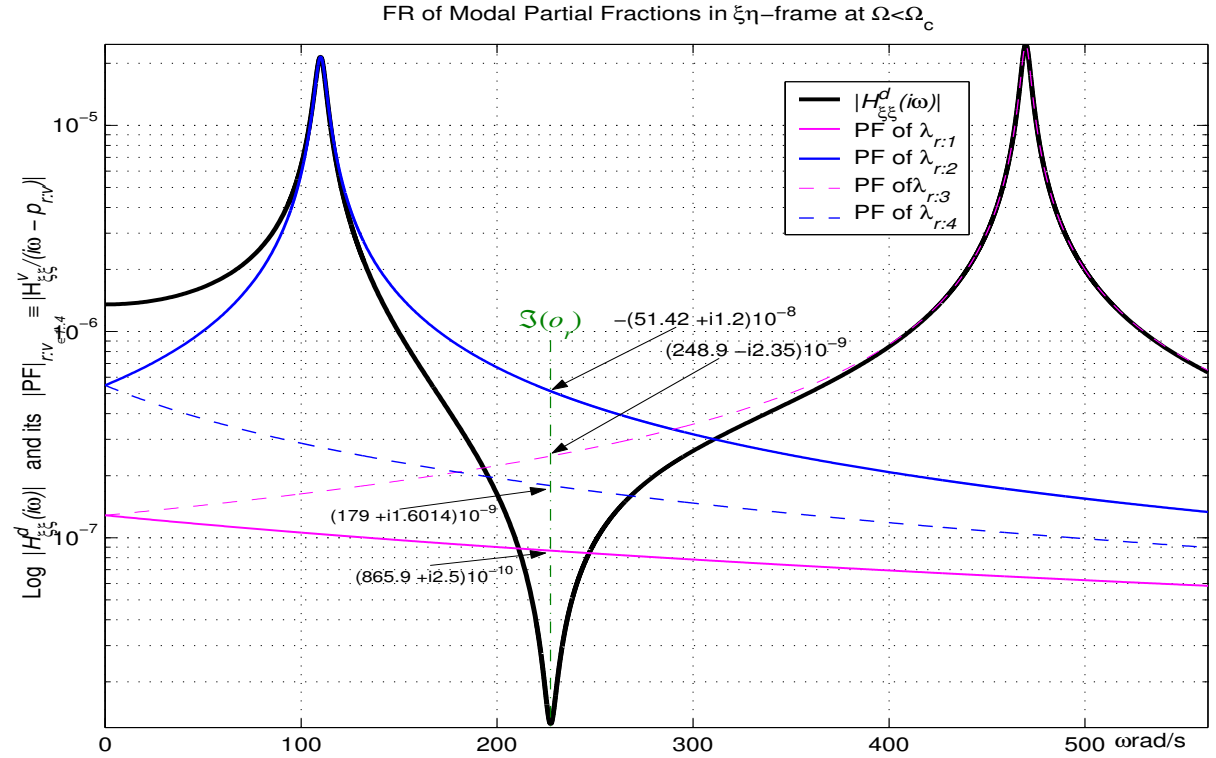


Figure 4.10.: Partial Fractions of point FRF in $\xi\eta$ -frame at sub-critical speed

and $\omega_{r:2}$ have switched the relative location of their corresponding stationary-frame modal frequencies ω_3 and ω_2 , hence $\omega_{r:3} > \omega_{r:2}$ whilst their modal fractions terms maintain the same residues H_{xx}^3 and H_{xx}^2 of their corresponding xy -frame λ_f and λ_b^* respectively. As a result, the $\xi\eta$ -frame FRF scenario differs from that in the xy -frame in two interesting respects:

- The complex zero $o_{r:1}$ that is reflected on $H_{\xi\xi}^d(i\omega)$ as an anti-resonance in-between the two consecutive resonances, occurs when $\angle \frac{H^3}{i\omega - p_{r:3}} \approx 0$ and $\angle \frac{H^2}{i\omega - p_{r:2}} \approx \pi$.
- The frequency of anti-resonance is far from ω_{int} —where the two dominant PFs have $\left| \frac{H^2}{i\omega_{\text{int}} - p_{r:2}} \right| = \left| \frac{H^3}{i\omega_{\text{int}} - p_{r:3}} \right|$ with virtually opposite phases—as the other PFs of $\lambda_{r:1,4}$ are of comparable magnitude.

At $\Omega > \Omega_c$ Things are different (*fig.4.11*) for $H_{\xi\xi}^d(i\omega)$ as $\omega_{r:2}$ and $\omega_{r:4}$ switch places, being -ve and +ve respectively, whilst maintaining the same xy -frame residues H_{xx}^2, H_{xx}^4 (4.8). Consequently, PFs of $\lambda_{r:3,4}$ are the magnitude dominant ones in-between resonances on

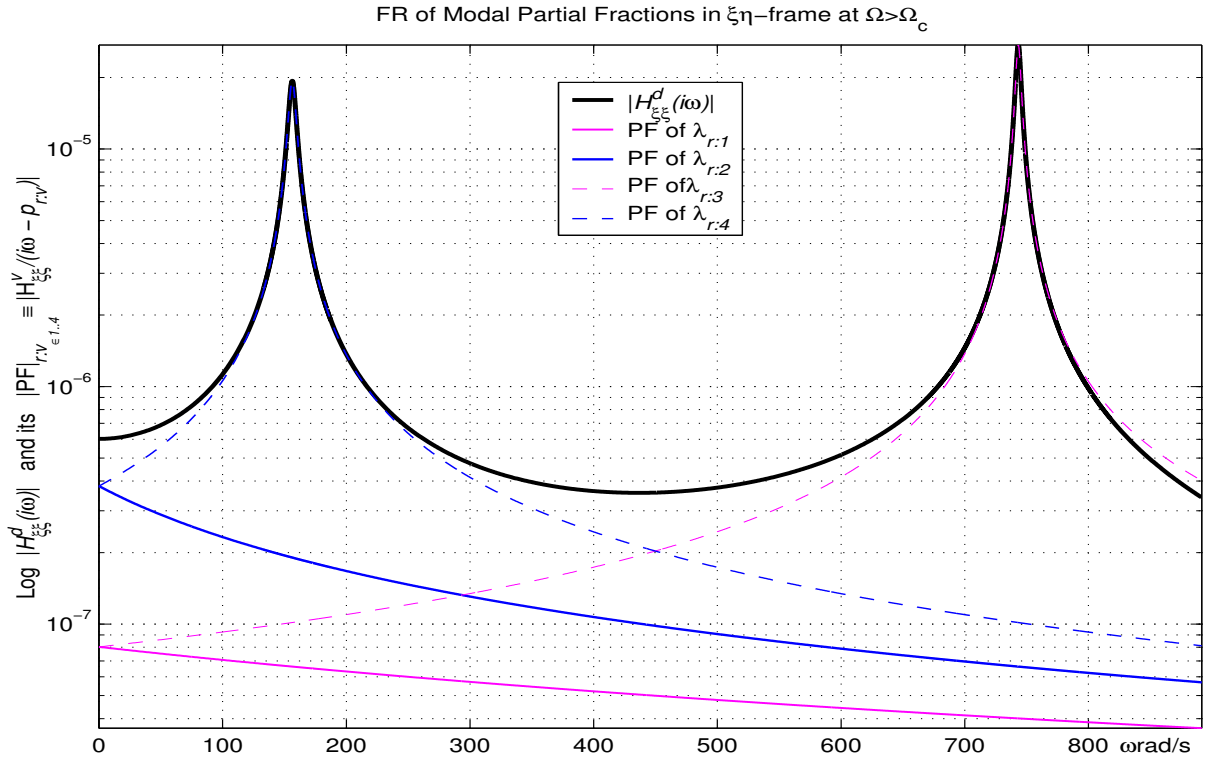


Figure 4.11.: Partial Fractions of point FRF in $\xi\eta$ -frame at supercritical speed

the +ve frequency range. They intersect at ω_{int} where $\left| \frac{H^4}{i\omega_{\text{int}} - p_{r:4}} \right| = \left| \frac{H^3}{i\omega_{\text{int}} - p_{r:3}} \right|$, yet with virtually same phases of approximately 0 and hence add-up as opposed to cancel-out, resulting in no anti-resonance thereabouts.

4.1.2.4. Identification of modal directionality from polar plots

In order to examine the differing effects of RID on FWD and BWD modes' stability using polar plots, it is necessary to identify the dominant mode and its directionality within a frequency range, which is not explicitly expressed in a polar plot. This is a simple task for polar plots of analytical models (*figs.4.8,4.9*), since FRF portions are

4. Analysis of linear RID system

marked clearly to reflect dominant modes over specific frequency ranges, based on modal analysis results (3.45, 3.47) (figs.4.2,4.3). However, this luxury is not always afforded with experimentally-acquired FRFs. Fortunately, ‘examining the relative *point-quad* polar plots phasing $\angle H_{xx}^d(\omega) - \angle H_{yx}^d(\omega)$ [$\angle H_{\xi\xi}^d(\omega) - \angle H_{\eta\xi}^d(\omega)$] around resonances’ $\Delta\omega_{p_v}$ (figs.4.8,4.9) can establish modal directionality, albeit with some provisos.

Argument Relative phasing of quasi-circles reflects the construction of a modal vector and its entries relative phasing, which along with +ve $\text{sgn}(\omega)$, determines the directionality of the dominant mode in question. Examining the polar plots (figs.4.8,4.9) with a general topological perspective, it is fair to accept that the (FRF points of) quasi-circles of $H_{xx}^d(\omega)$ lags [leads] that of $H_{yx}^d(\omega)$ by approximately $\frac{\pi}{2}$ in the vicinity $\Delta\omega_{p_3}$ [$\Delta\omega_{p_2}$] where the BWD [FWD] mode is dominant. Thereabouts, approximation (4.7): $H_{ij}(\omega) \approx \frac{H_{ij}^v}{i\omega - p_v} + E_{ij}^v$ where $H_{ij}^v = \tilde{\mathbf{o}}_i^{\mathbf{c}^v} \tilde{\mathbf{b}}_j^{\mathbf{r}^v} = \tilde{\mathbf{O}}_{iv} \tilde{\mathbf{B}}_{vj}$ is most valid, particularly for resonance points. With the excitation coordinate fixed $j \stackrel{\text{def}}{=} x$ [$j \stackrel{\text{def}}{=} \xi$] for $H_{xx}^d(\omega)$ and $H_{yx}^d(\omega)$ [$H_{\xi\xi}^d(\omega)$ and $H_{\eta\xi}^d(\omega)$], their relative phasing reflects directly the relative phasing of $\tilde{\mathbf{O}}_{xv}$ to $\tilde{\mathbf{O}}_{yv}$, which are the elements of the v^{th} modal vector $\hat{\mathbf{r}}_v \stackrel{\text{def}}{=} \tilde{\mathbf{o}}^{\mathbf{c}^v}$ by (3.39, 3.40). Before concluding on this argument, two issues have to be verified:

- The relative magnitude of each E_{ij}^v to its $\frac{H_{ij}^v}{i\omega - p_v}$ has to be negligible.
- The relative magnitude and phase of \mathbf{E}^v elements E_{xx}^v and E_{yx}^v is comparable.

both of which are true, particularly for resonance points.

Important physical significance The $\pi/2$ relative phasing of *point-quad* FRFs $\angle H_{xx}^d(\omega) - \angle H_{yx}^d(\omega)$ reflects the perpendicular x - and y -directions (figs.4.8, 4.9). This is on account of phase angles $\angle \vec{X}, \angle \vec{Y}$ difference of their corresponding responses in the x - and y -directions to a single force \vec{f}_x .

4.1.2.5. FRFs of complex system representations

The force and response solutions of complex rotor representation are vectors with relative phase lead/lag that are rotating in the complex plane at ω_e , and which represent the real forces and responses in perpendicular directions, as portrayed in §.3.1.1.3. TFs for xy - and $\xi\eta$ -frames are derived from (3.10, 3.11) or (3.20, 3.21), with rotating frame TFs:

$$H_c^d(s) = \frac{1}{ms^2 + (c + i(2m - \mathcal{G})\Omega)s + (k + (\mathcal{G} - m)\Omega^2 + ic\Omega)} \quad (4.9)$$

$$H_c^v(s) = sH_c^d(s)$$

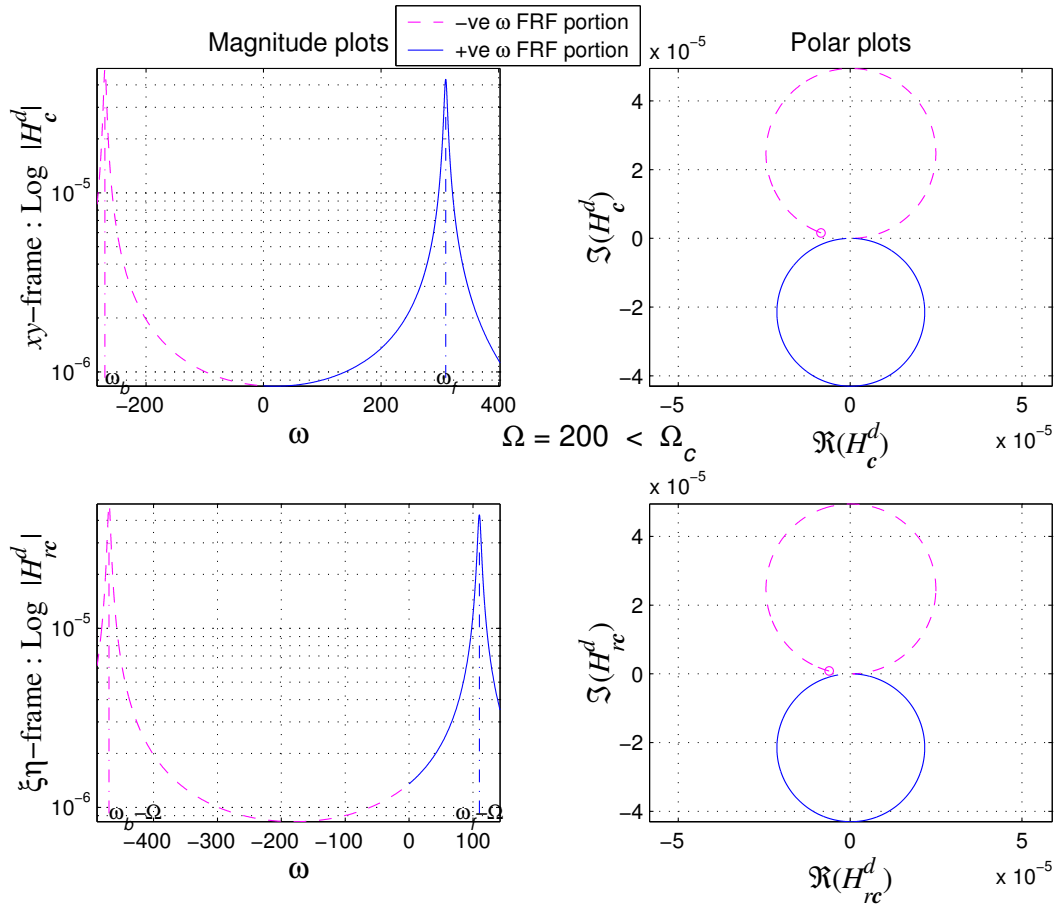


Figure 4.12.: FRFs of complex representations at $\Omega < \Omega_c$ in xy - and $\xi\eta$ -frames

Relations between FRFs of real and complex representations can be derived from §.3.1.1.3, and are reflected on comparing (figs. 4.12, 4.13) with (figs. 4.8, 4.9) respectively.

TFs/FRFs characteristics of complex 2DOF isotropic rotor TFs have no zeros. Their poles are the two eigenvalues with +ve and -ve modal frequencies. FRF frequency range extends from a -ve $\omega_{e:1}$ to a +ve $\omega_{e:2}$ so as to cover vicinities $\Delta\omega_{p_b}$ and $\Delta\omega_{p_f}$. It is perhaps peculiar to find stationary frame FRF minima at $\omega_e \approx 50 > 0$ (figs. 4.12, 4.13).

Vector phase Lead or lag? its up to ω_e because $\text{sgn}(\omega_e)$ may be +ve or -ve. A +ve $\angle H_c^d(\omega)$ with -ve $\omega_e \stackrel{\text{def}}{=} \text{lag}$, i.e. response lags force. Had $\text{sgn}(\omega_e)$ been +ve, a +ve $\angle H_c^d(\omega)$ indicates response leads force, which is a symptom of an unstable system.

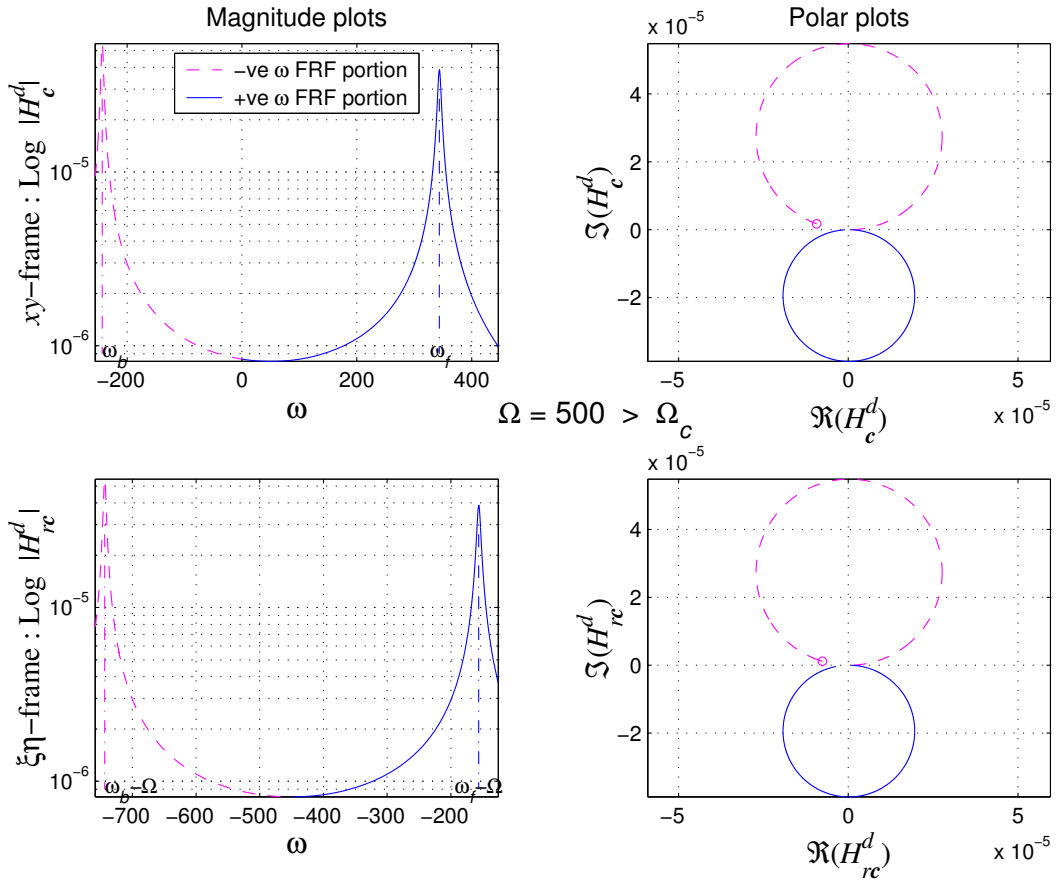


Figure 4.13.: FRFs of complex representations at $\Omega > \Omega_c$ in xy - and $\xi\eta$ -frames

4.2. Linear-RID-augmented system: Modal analysis and frequency response

LTI rotordynamic systems that are augmented with linear RID models in accordance with §3.2.2.1 are analysed here. Linear RID models are viable and can be justified for rotor joints, which do not endure substantial vibration amplitudes nor exhibit significant relative slippage at the desired operating speeds. Examples of such joints are Curvic couplings and tightly-bolted flanged-couplings, but certainly not spline couplings especially when un-piloted.

4.2.1. Effect of linear viscous RID on stability characteristics

Introducing or augmenting linear viscous RID to the asymptotically stable rotor system of (3.2, 3.8) as described in §3.2.2.1 introduces/adds new force vectors (3.82-3.84) to (3.2)

in the xy -frame, which results in overall EOMs:

$$\mathbf{M}\ddot{\mathbf{q}} + (\mathbf{C} + \mathbf{C}_i + \mathbf{G})\dot{\mathbf{q}} + (\mathbf{K} + \mathbf{K}_{cc})\mathbf{q} = \mathbf{f} \quad (4.10a)$$

$$m\mathbf{I}\ddot{\mathbf{q}} + ((c + c_i)\mathbf{I} - \mathcal{G}\Omega\mathbf{N})\dot{\mathbf{q}} + (k\mathbf{I} - c_i\Omega\mathbf{N})\mathbf{q} = \mathbf{f} \quad (4.10b)$$

The complex formulation of which is:

$$m\ddot{z} + (c + c_i - \imath\Omega\mathcal{G})\dot{z} + (k - \imath\Omega c_i)z = f_z \quad (4.10c)$$

representing a 2DOF LTI rotor with destabilising RID. Comparing EOMs (4.10) of this potentially unstable system with (3.2) those of the otherwise asymptotically stable system, shows that RID introduces two coefficient matrices \mathbf{C}_i and \mathbf{K}_{cc} , each affecting stability in a contrary manner to that of the other:

1. Stability enhancing \mathbf{C}_i : RID coefficient c_i adds to the stabilising external damping coefficient c , hence enhancing overall stability.
2. Stability challenging \mathbf{K}_{cc} : This speed-dependant skew-symmetric stiffness matrix (3.84) will be shown to enhance the stability of BWD mode and challenge that of FWD mode, possibly destabilising it at some speed Ω_{cn} ; with such effects on stability being progressive with speed. The opposite effect on FWD and BWD modes' stability is due to the sign compliance $\mathbf{K}_{cc} \propto \mathbf{G}$ of RID-introduced skew-symmetric stiffness and gyroscopic matrices as reflected by their complex format $-\imath\Omega c_i$ and $-\imath\Omega\mathcal{G}$ in (4.10c).

4.2.1.1. RID effect on stability of BWD and FWD modes

EOMs (4.10) result in the real state matrix:

$$\tilde{\mathbf{A}} = -\frac{1}{m} \begin{bmatrix} 0 & 0 & 1 & 0 \\ 0 & 0 & 0 & 1 \\ k & \Omega c_i & c + c_i & \Omega\mathcal{G} \\ -\Omega c_i & k & -\Omega\mathcal{G} & c + c_i \end{bmatrix} \quad (4.11)$$

and its complex version $\check{\mathbf{A}}_c$, whose BWD and FWD modes' eigenvalues are:

$$\lambda_{b,f} = \frac{-(c + c_i) + \imath(\Omega\mathcal{G} \mp \sqrt{(\Omega\mathcal{G} + \imath(c + c_i))^2 + 4m(k - \imath\Omega c_i)})}{2m} \quad (4.12)$$

The relation of EOM (4.10c) and eigenvalues (4.12) is examined and compared to (3.10, 4.3) that of rotor without RID, in order to identify the terms introduced by RID and their

4. Analysis of linear RID system

effects on modal stability:

1. Stabilising element: RID coefficient c_i is added to external damping coefficient c wherever it exists, which reflects the effect of RID matrix \mathbf{C}_i in (4.10), thus enhancing the stability of both FWD and BWD modes at any specific speed when compared to those of rotor without RID.
2. Destabilising element: Stiffness coefficients in (4.10c), including $-\imath\Omega c_i$ that represents the destabilising skew-symmetric \mathbf{K}_{cc} , are carried-over unaltered to the square-root in $\lambda_{b,f}$ (4.12) expression. The -ve imaginary quantity $4m(-\imath\Omega c_i)$ introduced in (4.12) can *and usually will* alter the sign of imaginary quantity under square-root, thus reversing its original contributions to $\Re(\lambda_{b,f})$ as explained below.

As with (4.3), the square-root in (4.12) is of a complex quantity $\forall \Omega \neq 0$:

$$\sqrt{(\Omega\mathcal{G} + \imath(c + c_i))^2 + 4m(k - \imath\Omega c_i)} = \sqrt{a + \imath b} \quad (4.13a)$$

$$\text{where } a = 4mk + (\Omega\mathcal{G})^2 - (c + c_i)^2 \quad , \quad b = 2\Omega(\mathcal{G}(c + c_i) - 2mc_i) \quad (4.13b)$$

Accordingly, the square root of (4.13a) results in both a real quantity as well as an imaginary one, with the latter (multiplied by $\frac{\imath}{2m}$) contributing to $\Re(\lambda_{b,f})$ in a manner that depends on $\text{sgn}(b)$ being +ve or -ve.

Negative imaginary quantity under square root (4.13) This scenario requires:

$$\frac{2m}{\mathcal{G}} - 1 > \frac{c}{c_i} \quad \text{i.e.} \quad c_i > \left(\frac{\mathcal{G}}{2m - \mathcal{G}}\right)c \Rightarrow b = 2\Omega(\mathcal{G}(c + c_i) - 2mc_i) < 0 \quad (4.14)$$

which is true whenever RID c_i is not negligible compared to external damping c . For example, using parameters (4.2), inequality (4.14) requires that $c_i \gtrsim 0.112c$ for (4.13) to have a -ve b , which is reasonably realistic and makes an interesting case to examine. However, this is unlike the case of rotor without RID (4.4), and formula (A.5b):

$$\sqrt{a + \imath b} = \sqrt{\frac{a + \sqrt{a^2 + b^2}}{2}} - \imath \sqrt{\frac{-a + \sqrt{a^2 + b^2}}{2}} \quad \text{for } b < 0$$

applies to square root of (4.13a) whose resulting imaginary quantity ($\times \frac{\imath}{2m}$):

- Adds to $-\frac{(c+c_i)}{2m}$ in the case of λ_f , thus contributing positively increasing $\Re(\lambda_f)$
- Subtracts from $-\frac{(c+c_i)}{2m}$ in the case of λ_b , thus contributing negatively to $\Re(\lambda_b)$

The above being exactly the opposite of what happens in the case of the rotor without RID (4.3, 4.4). Furthermore, since b of (4.13, 4.14) is speed-dependant, $\Re(\lambda_b)$ decreases (more

negative), while $\Re(\lambda_f)$ increases with increased speed (fig. 4.14). Although a negative imaginary quantity under square root (4.13) is *most likely* to cause an unstable FWD mode at some Ω_{on} , it is not guaranteed—just like $\Re(\lambda_b)$ of rotor without RID (4.3, 4.4) does not become +ve $\forall \Omega$. As will be demonstrated (4.20), one condition for RID-instability is $c_i > \left(\frac{\mathcal{G}}{m-\mathcal{G}}\right)c$, which dictates a higher c_i than that required by (4.14).

Positive imaginary quantity under square root (4.13) This scenario dictates negligible RID when compared to external damping of an average rotor with gyroscopic effects, or no RID in a rotor without gyroscopic effects. The system is hence always asymptotically stable.

4.2.1.2. Conditions for the existence of RID instability

Examining the eigenvalues of rotor with RID as in §4.2.1.1 indicated that a relation between the ratio c_i/c of internal to external damping and the rotor's invariant parameters: m, \mathcal{G}, k has to be satisfied for RID instability to possibly exist. Provided such relation is satisfied, RID instability will exist only after a specific onset speed of instability Ω_{on} —the main concern—due to the speed-progressive destabilising nature of \mathbf{K}_{cc} . Although it is possible to identify the conditions for the existence of RID instability, namely:

- Relation of ratio c_i/c to rotor's invariant parameters m, \mathcal{G}, k , which is the essential requirement for RID instability to be possible
- Onset speed of instability Ω_{on} , after which RID instability will set in

by examining $\Re(\lambda_f)$, this exercise can prove to be unduly tedious if not intractable. Conversely, such conditions are identified below in a fairly straightforward manner using one of the Routh-Hurwitz criteria.

Which Routh-Hurwitz criterion to use? As the system defined by (4.10) is of small order, conditions for stability/instability can be arrived at with some degree of easiness using one of the Routh-Hurwitz criteria. With all system variables $m, \mathcal{G}, c, c_i, k$ set as unknown, an expression for Ω_{on} and its relation to ω_{f_u} (FWD modal frequency of the undamped rotor) can be derived. With the objective of this exercise being to maximise clarity and straightforward applicability, the question stated above becomes a valid concern. It will be shown that using the Routh-Hurwitz criteria for equations with complex coefficients to identify Ω_{on} and its relation to ω_{f_u} , based on the relation of c_i/c to rotor's m, \mathcal{G}, k , is the best-suited way forward.

The Routh-Hurwitz criteria for characteristic equations of real systems are necessary and sufficient conditions, which if satisfied insure the characteristic equation has roots with only negative real parts, i.e. stable eigenvalues in the left-half s -plane. The Hurwitz criterion, which involves checking the sign of $2n$ Hurwitz determinants that are set-up using the coefficients of characteristic equation (4.15) for system (4.10):

$$\begin{aligned} \check{D}(\lambda) = \lambda^4 + \frac{2m(c+c_i)}{m^2}\lambda^3 + \frac{(c+c_i)^2 + (\Omega\mathcal{G})^2 + 2mk}{m^2}\lambda^2 \\ + 2\frac{k(c+c_i) + \Omega^2gc_i}{m^2}\lambda + \frac{(\Omega c_i)^2 + k^2}{m^2} = 0 \end{aligned} \quad (4.15)$$

is perhaps the more familiar to mechanical engineers. Even though (4.15) has $2n = 4$, the Hurwitz criterion can be more than a handful here. On the other hand, the Routh array $\mathbf{Ra}_{(2n+1) \times 1}$ for (4.15) does simplify matters by merely checking for sign consistency of its 5 elements:

$$\begin{array}{ll} +ve & Ra_1 & m^2 : \lambda^4 \\ +ve & Ra_2 & 2m(c+c_i) : \lambda^3 \\ ? & Ra_3 & mk + (\omega\mathcal{G})^2 + (c+c_i)^2 - \omega^2mg\frac{c_i}{(c+c_i)} : \lambda^2 \\ ? & Ra_4 & 2((\omega\mathcal{G})^2 + (c+c_i)^2)\frac{\omega^2gc_i(c+c_i) + k(c+c_i)^2 - \omega^2mc_i^2}{(c+c_i)Ra_3} : \lambda^1 \\ +ve & Ra_5 & (\Omega c_i)^2 + k^2 : \lambda^0 \end{array}$$

Routh array elements $Ra_{1,2,5}$ are always positive, while $Ra_{3,4}$ may be positive or negative as well as being interdependent, and thus form the criteria for instability, albeit less than instantaneously obvious.

The Routh-Hurwitz criterion for equations with complex coefficients is not as popular with engineers as its counterparts for real systems, yet it will yield a more obvious set of stability criteria that is straightforward to arrive at. This criterion provides a necessary and sufficient condition for a complex equation to only have *roots with positive imaginary parts*, i.e. in the right-half s -plane. In order to utilise this criterion in identifying stability conditions for system (4.10), we need to consider a modified complex characteristic equation (4.16), whose roots' positive imaginary parts represent negative real parts of the original complex equation's roots, as in:

$$\Im(\check{\lambda}_{1,2}) \stackrel{\text{def}}{=} -\Re(\lambda_{\mathbf{c}:1,2})$$

This involves assuming a solution for (4.10c) of the form:

$$z = \vec{Z}_1 e^{i\lambda_1 t} + \vec{Z}_2 e^{i\lambda_2 t}$$

i.e. $\lambda \stackrel{\text{def}}{=} i\lambda$, which results in the modified characteristic equation:

$$\begin{aligned} m\lambda^2 - (i(c + c_i) + \Omega\mathcal{G})\lambda + i\Omega c_i - k &= 0 \\ (\dot{a}_0 + i\dot{b}_0)\lambda^n + (\dot{a}_1 + i\dot{b}_1)\lambda^{(n-1)} + (\dot{a}_n + i\dot{b}_n) &= 0 \quad \leftrightarrow \quad n = 2 \end{aligned} \quad (4.16)$$

Accordingly, conditions that satisfy the Routh-Hurwitz criterion for complex equations when applied to (4.16) are the conditions necessary for the stability of system (4.10).

When applied to (4.16), the Routh-Hurwitz criterion for complex equations requires:

$$(-1)^1 \begin{vmatrix} a_0 & a_1 \\ b_0 & b_1 \end{vmatrix} > 0 \Rightarrow m(c + c_i) > 0 \quad \checkmark \quad (4.17a)$$

$$(-1)^2 \begin{vmatrix} a_0 & a_1 & a_2 & 0 \\ b_0 & b_1 & b_2 & 0 \\ 0 & a_0 & a_1 & a_2 \\ 0 & b_0 & b_1 & b_2 \end{vmatrix} > 0 \Rightarrow m(k(c + c_i)^2 + \Omega^2 g c_i (c + c_i) - m\Omega^2 c_i^2) > 0 \quad ? \quad (4.17b)$$

With condition (4.17a) always satisfied, satisfying condition (4.17b) becomes the criterion for system (4.10) to have eigenvalues in the left-half s -plane.

Conditions for instability Stability condition (4.17b) is conveniently rearranged as:

$$\frac{k(1 + c/c_i)^2}{m - \mathcal{G}(1 + c/c_i)} > \Omega^2 \quad (4.18)$$

Since condition (4.18) is *necessary* for the absolute stability of the LTI system (4.10), its violation: $\frac{k(1+c/c_i)^2}{m-\mathcal{G}(1+c/c_i)} \leq \Omega^2$ results in either:

1. An unstable system (4.10) with $\Re(\lambda_f) > 0$ when $\frac{k(1+c/c_i)^2}{m-\mathcal{G}(1+c/c_i)} < \Omega^2$.
2. A marginally stable system (4.10) with $\Re(\lambda_f) = 0$ when the operating speed:

$$\Omega = \sqrt{\frac{k(1 + c/c_i)^2}{m - \mathcal{G}(1 + c/c_i)}} = \Omega_{\text{bn}} \quad (4.19)$$

Accordingly, the system parameters necessary for (4.10) to be unstable can be identified. In essence, violating condition (4.18) requires two simultaneous conditions:

4. Analysis of linear RID system

1. The fundamental condition of a positive denominator for the left-hand-side of (4.18), since its right-hand-side as well as the numerator are positive, requires:

$$m - \mathcal{G}(1 + c/c_i) > 0 \quad \Rightarrow \quad \frac{c_i}{c} > \frac{\mathcal{G}}{m - \mathcal{G}} \quad (4.20)$$

without which, RID instability cannot take place in system (4.10).

2. An operating speed that is equal to or higher than the onset speed of instability Ω_{on} , which is in turn higher than Ω_{c_u} (3.44) the critical speed of the undamped system, except for the unusual situation of no external damping when $\Omega_{\text{on}} = \Omega_{c_u}$:

$$\Omega \geq (1 + c/c_i) \sqrt{\frac{k}{m - \mathcal{G}(1 + c/c_i)}} \geq \sqrt{\frac{k}{m - \mathcal{G}}} \quad (4.21)$$

i.e. $\Omega \geq \Omega_{\text{on}} \geq \Omega_{c_u}$

Onset speed relation to FWD modal frequency based on RID ratio The onset speed of instability Ω_{on} as expressed by (4.19), which is derived from stability condition (4.17b) can be related to ω_{f_u} the FWD modal frequency of the corresponding undamped system that is derived in (3.41) by the simple and convenient relation:

$$\frac{\Omega_{\text{on}}}{\omega_{f_u}} = (1 + c/c_i) \quad (4.22)$$

Eq.(4.22) states that RID-instability can not set in at speeds lower than the frequency ω_{f_u} , which increases with speed due to gyroscopic effects as well as dictates that RID-instability can not set in at sub-critical speeds; see (*figs.4.14, 4.15*).

Gyroscopic effects favour stability is a fact that is obvious from the instability condition (4.20), the requirement (4.14) of a negative quantity under square-root (4.13) in eigenvalues (4.12) for the RID-instability to be possible, as well as being an intuitive notion considering the gyroscopic stabilising effect on a spin-top for instance. For the unrealistic case of a rotor that is void of gyroscopic effects $\mathcal{G} = 0$, (4.20) dictates this rotor will inevitably become unstable at some Ω_{on} regardless of how minuscule the RID coefficient is. On the other hand, the existence of gyroscopic effects $\mathcal{G} \neq 0$ may refute the possibility of RID-instability altogether if RID ratio to external damping is small.

4.2.1.3. Numerical examples of modal analysis for rotor with RID

This section illustrates numerically (*figs.4.14, 4.15*) the findings of previous sections regarding the effect of RID on stability characteristics. The numerical values used for rotor

coefficients are given by (4.2), whilst varying the ratio of external/internal damping coefficients as in: $\frac{c}{c_i} = 75(\frac{1}{0}, \frac{1}{1}, \frac{1}{2}, \frac{0}{1}, \frac{0}{2})$. Baring the first $\frac{c}{c_i} = \frac{75}{0}$ ratio, which is that of the asymptotically stable rotor taken as reference, all other $\frac{c}{c_i}$ ratios in conjunction with (4.2) satisfy requirement (4.14) that is necessary for a negative quantity under square-root (4.13) of eigenvalues (4.12) as well as the instability condition (4.20), which in turn signifies that RID-instability is possible at some Ω_{on} .

Respectively, (fig.4.14) and (fig.4.15) are the decay parts of eigenvalues $\Re(\lambda_{b,f})$ and damping factors $\gamma_{b,f}$ corresponding to (4.2), with the aforementioned various c/c_i ratios, plotted against operating speed Ω . Each onset speed Ω_{on} corresponding to a specific c/c_i ratio, at which $\Re(\lambda_f) \equiv 0$ and $\gamma_f \equiv 0$, is indicated along with its ratio to the relevant ω_{f_u} on each plot. Although FWD modal frequencies of the undamped rotor ω_{f_u} are not presented in full against Ω , they can be checked by the fairly close approximation of $\Im(\lambda_f)$ against Ω presented in fig.4.2 for (4.2).

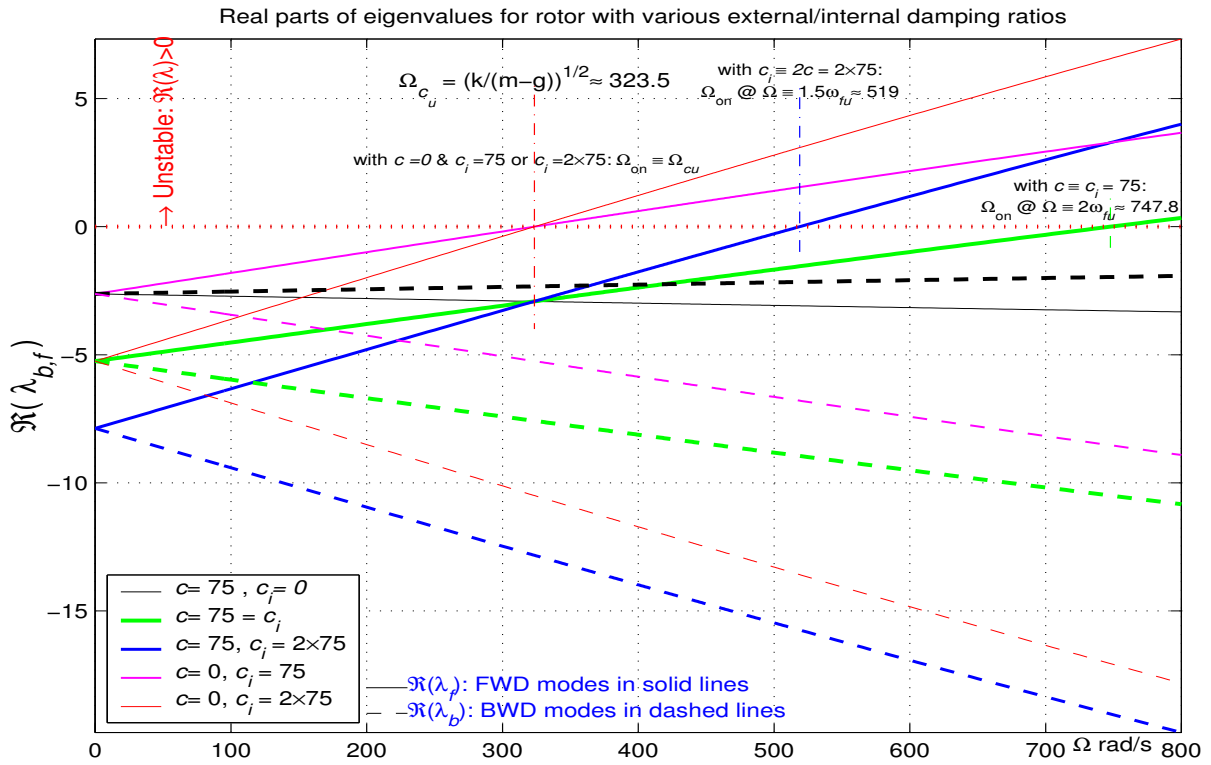


Figure 4.14.: $\Re(\lambda_{b,f})$: Effect of various viscous external/internal damping $c_i \cup c$

Effect of significant RID on FWD and BWD modes With the basic RID-instability condition (4.20) satisfied, §4.2.1.1 shows that RID contributes to $\Re(\lambda_{b,f})$ and whence $\gamma_{b,f}$ in two ways. Part of this contribution is not speed-dependent affecting both BWD and FWD modes equally, while the other part is speed-progressive challenging the stability of FWD modes while enhancing that of BWD modes.

4. Analysis of linear RID system

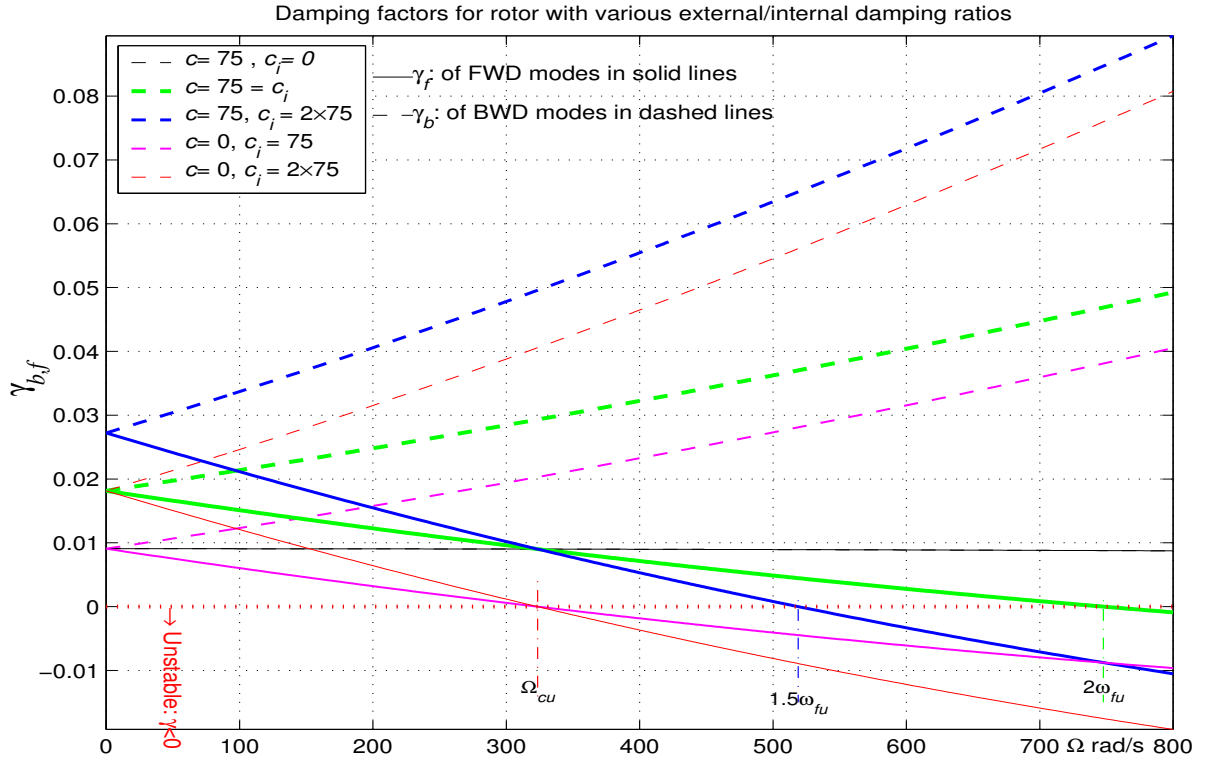


Figure 4.15.: Damping factor $\gamma_{b,f}$ variation with Ω for rotors $c \cup c_i = 0, c = c_i, c_i \cup c = 0$

Stationary rotor $\Omega = 0 \Rightarrow -i\Omega c_i = 0$: In this case the speed-dependant contribution of RID to $\Re(\lambda_{b,f})$ is nil, while c_i adds to c wherever it exists in (4.12) and affects $\Re(\lambda_{b,f})$ as well as $\gamma_{b,f}$. Accordingly at $\Omega = 0$:

- For any specific c/c_i ratio, $\Re(\lambda_f) \equiv \Re(\lambda_b)$ and $\gamma_f \equiv \gamma_b$
- All $\frac{c}{c_i}$ ratios that lead to the same $c + c_i$, e.g. $(\frac{75}{0}$ and $\frac{0}{75})$ or $(\frac{75}{75}$ and $\frac{0}{2 \times 75})$, have the same $\Re(\lambda)$ and γ
- $\Re(\lambda)$ and γ resulting from $\frac{c}{c_i} = \frac{75}{2 \times 75}$ is triple that resulting from $\frac{c}{c_i} = \frac{75}{0}$ or $\frac{0}{75}$, which in turn is half that resulting from $\frac{c}{c_i} = \frac{75}{75}$ or $\frac{0}{2 \times 75}$.

Rotating rotor $\Omega \neq 0 \Rightarrow -i\Omega c_i \neq 0$: The speed-dependant contribution of RID to $\Re(\lambda_{b,f})$ sets in decreasing $\Re(\lambda_b)$ thus increasing γ_b for BWD modes, while increasing $\Re(\lambda_f)$ thus decreasing γ_f for FWD modes, which results in a non-uniform damping factor $\gamma_b \neq \gamma_f$ at any one speed. With RID effect $(-i\Omega c_i)$ being speed-progressive, so are the trends of $\Re(\lambda_{b,f})$ and $\gamma_{b,f}$ with increased speed until RID-instability sets in at some Ω_{on} , the value of which depends on $\frac{c}{c_i}$ ratio. The $\Re(\lambda_{b,f})$ and $\gamma_{b,f}$ trends for this RID-augmented rotor represent a total reversal compared to those of the reference rotor without RID, which is also illustrated in (figs.4.14, 4.15).

The effect of different c/c_i external damping to RID ratios on onset speed Both equations (4.19, 4.22) show that Ω_{on} the onset speed of RID-instability depends on the ratio $\frac{c}{c_i}$. In accordance with (4.22), (figs.4.14, 4.15) show that:

- RID-instability cannot set in at sub-critical speeds
- The ratio $\frac{c}{c_i}$ dictates Ω_{on} the onset speed's relation to ω_{f_u} modal frequency of corresponding undamped rotor; e.g. $\frac{c}{c_i} = \frac{1}{2} \Rightarrow \Omega_{\text{on}} \equiv 1.5\omega_{f_u}$
- In the hypothetical case of $c = 0$ nil external damping: $\Omega_{\text{on}} \equiv \omega_{f_u} \equiv \Omega_{c_u}$, regardless of RID magnitude. Accordingly, both $c_i = \left\{ \begin{matrix} 75 \\ 2 \times 75 \end{matrix} \right.$ result in $\Omega_{\text{on}} \equiv \Omega_{c_u}$ when $c = 0$

Tempting but untrue It is perhaps tempting to investigate whether the simultaneous RID stabilising and destabilising elements annul each other at Ω_{c_u} , with the stabilising element overwhelming the destabilising one $\forall \Omega < \Omega_{c_u}$ and vice-versa $\forall \Omega > \Omega_{c_u}$, when the FWD mode would only be stable on account of external damping counter-acting the destabilising element of RID. Such initiative might be taken up in view of:

- The discussions of §4.2.1.1 on p.157 concerning the two contradicting yet simultaneous roles of RID, namely: speed-independent stabilising and speed-progressive destabilising roles
- figs.4.14, 4.15 which show that any RID value results in $\Omega_{\text{on}} \equiv \Omega_{c_u}$ when $c = 0$, as well as give the *false impression* that damping ratios $\frac{c}{c_i} = \frac{1}{0}, \frac{1}{1}$ result in identical $\Re(\lambda_f), \gamma_f$ at $\Omega = \Omega_{c_u}$.

Investigating this possibility, both numerically and analytically revealed it to be untrue, albeit tempting to conclude at.

4.2.2. Effect of linear viscous RID on analytical forced response

This section examines and illustrates analytically the (static load and sinusoidal) forced response characteristics of RID-augmented rotor model, which can be unstable. FRF polar plots in the frequency vicinity of an unstable eigenvalue are particularly interesting, informative and can be used to identify unstable modes as detailed in §4.3. Although a FRF cannot be actually/experimentally acquired, as well as being undefined, for an unstable physical system, it is possible to define FRFs for an unstable *subsystem* that is part of an overall stable system (§4.3).

4.2.2.1. FRF polar plots of unstable system with well-separated modes

An unstable dynamic system will have eigenvalue/s with positive real parts, i.e. in the right-half s -plane, representing unstable mode/s. If any unstable mode is observable (represented) in a system's TF, this TF will have right-half s -plane poles that are identical to the eigenvalues of observable unstable modes. According to §.4.1.2.1, FRF polar plots are directly related to poles' and zeros' locations on the s -plane, which influences polar plots (*fig.4.17*) heavily in the case of a system with well-separated modes. A right-half s -plane pole p_{rhsp} , in its frequency vicinity $\Delta\omega_{p_{\text{rhsp}}}$, will have an unmistakable effect on the polar plot of a system with well-separated modes; namely, the polar plot traces a CCW quasi-circle as $\Delta\omega_{p_{\text{rhsp}}}$ is traversed, e.g. *figs.4.17, 4.18*.

Interpretation of CCW polar plots for unstable systems in frequency vicinity $\Delta\omega_{p_{\text{rhsp}}}$:

According to (4.6b), a right-half s -plane pole vector will sweep $\Delta\angle(\omega_e - p_{\text{rhsp}}) = -\pi$ as $\omega_e: \langle -\infty \triangleright \infty \rangle$ the whole of ω -axis is swept, thus adding π to $\angle G(\omega)$ in the process (4.5). As discussed in §.4.1.2.1 for a system with well-separated modes, the FRF polar plot will be heavily influenced by p_{rhsp} in its frequency vicinity $\Delta\omega_{p_{\text{rhsp}}}$ and the effect of $\Delta\angle(\omega_e - p_{\text{rhsp}}) \approx -\pi$ is very obvious on $\Delta\angle G(\omega) \approx \pi$, which translates into a CCW \odot quasi-circle polar plot. If modes are not well-separated, poles will be close in frequency and a CCW quasi circle may be masked, especially if these two poles are on opposite sides of the s -plane, e.g. in the case of a Jeffcott rotor without gyroscopic effects. Luckily, most rotors have well-separated modes, at least the first few ones, and the CCW polar plot characteristic can be used to identify unstable modes as explained in §4.3.

Polar plot characteristics of unstable RID-augmented rotor As is the case with virtually every rotor, our viscous RID-augmented 2DOF rotor (4.10) has totally observable TFs, be they the result of complex (4.23) or real (4.25) representations, which dictates that system's eigenvalues are identical to their corresponding TF poles. Accordingly, if system (4.10) has an unstable FWD mode, then *any* of its TFs will have a corresponding pole $p_f \stackrel{\text{def}}{=} p_{\text{rhsp}}$ (*fig.4.16*), which will result in a quasi-circle on the polar plot that is traversed in the CCW \odot direction (*figs.4.17,4.18*) as the frequency vicinity $\Delta\omega_{p_{\text{rhsp}}}$ of the unstable FWD mode is traversed.

In the following, receptance FRFs of rotor (4.10) are presented using coefficients (4.2) and $\Omega = 500_{\text{rad/s}} > \Omega_{c_u}$, whilst varying external/internal damping: $\frac{c}{c_i} = 75(\frac{1}{0}, \frac{1}{1}, \frac{1}{2}, \frac{0}{1}, \frac{0}{2})$. Ratios $\frac{c}{c_i} = 75(\frac{0}{1}, \frac{0}{2})$ result in unstable FWD modes, i.e. p_f is in the right-half s -plane with $\Re(p_f) > 0$, while the other $\frac{c}{c_i}$ ratios result in an asymptotically stable system with p_f in the left-half s -plane.

4.2.2.2. Forced response of complex rotor representation

The xy -frame receptance TF and FRF of complex rotor (4.10c) representation are:

$$\begin{aligned} G_{\mathbf{c}}^d(s) &= \frac{1}{ms^2 + (c + c_i - i\Omega\mathcal{G})s + (k - i\Omega c_i)} \\ G_{\mathbf{c}}^d(i\omega) &= \frac{1}{-m\omega^2 + (c + c_i - i\Omega\mathcal{G})i\omega + (k - i\Omega c_i)} \end{aligned} \quad (4.23)$$

FRF polar plot behaviour According to §.4.1.2.1, polar plots (*fig.4.17*) will depend heavily on the s -plane location of pole pairs $p_{b,f}$ (*fig.4.16*) corresponding to the various $\frac{c}{c_i}$ ratios. Since complex TF (4.23) is completely controllable and observable, each pair $p_{b,f}$ is identical to the corresponding system's eigenvalues $\lambda_{b,f}$. Accordingly (*figs.4.14,4.16*):

- Mode separation: A specific pole pair $p_{b,f}$ corresponding to one damping ratio $\frac{c}{c_i}$ will have very well-separated p_b and p_f with no zeros in between.
- Modal frequencies: External/internal damping ratios $\frac{c}{c_i} = 75(\frac{1}{0}, \frac{1}{1}, \frac{1}{2}, \frac{0}{1}, \frac{0}{2})$ result in $\Im(p_b)$ and $\Im(p_f)$ that are virtually invariant for these $\frac{c}{c_i}$ ratios.
- Decay rates: Damping ratios $\frac{c}{c_i}$ have a marked effect on stability and hence damping rates that are identical to pole real parts $\Re(p_{b,f})$ —check (*fig.4.14*). Since RID is stabilising to BWD modes, save the reference rotor without RID, they are not moderately-damped $\frac{\Im(p_b)}{\Re(p_b)} \not\geq 25$ anymore and are heavily-damped with $\frac{c}{c_i} = 75(\frac{1}{2}, \frac{0}{2})$ when $\frac{\Im(p_b)}{\Re(p_b)} < 15$.

In view of poles' layout (*fig.4.16*), the excitation frequency range chosen for receptance FRF starts from the -ve $1.1\Im(p_b)$ up to the +ve $1.3\Im(p_f)$, $\Delta\omega_e \stackrel{\text{def}}{=} \omega_e : [1.1\omega_b \triangleright 1.3\omega_f]$.

Polar plot in BWD modes' frequency vicinity $\Delta\omega_{p_b}$ All BWD modes' poles p_b lie in the lower-left-quarter s -plane, and their vectors sweep $\Delta\angle(i\omega_e - p_b) \approx \pi$ as the -ve frequency vicinity $\Delta\omega_{p_b}$ is traversed. Accordingly, the FRF sweeps $\Delta\angle G(i\omega) \approx -\pi$ a quasi-circle in the CW \odot direction, the completeness and size of which depends on the magnitude $|\Re(p_b)|$. The BWD mode of reference rotor without RID is moderately-damped with least $|\Re(p_b)|$, in which case the FRF sweeps $\Delta\angle G(i\omega) \simeq -\pi$ the largest quasi-circle that is most complete in this group. However, as $|\Re(p_b)|$ increases, the corresponding quasi-circles get smaller and less complete; a situation that is obvious in the case of most damped BWD mode resulting from $\frac{c}{c_i} = 75(\frac{1}{2})$.

Polar plot in FWD modes' frequency vicinity $\Delta\omega_{p_f}$ FWD modes' poles p_f are either in the upper-left-quarter s -plane representing asymptotically stable FWD modes, or in the

4. Analysis of linear RID system

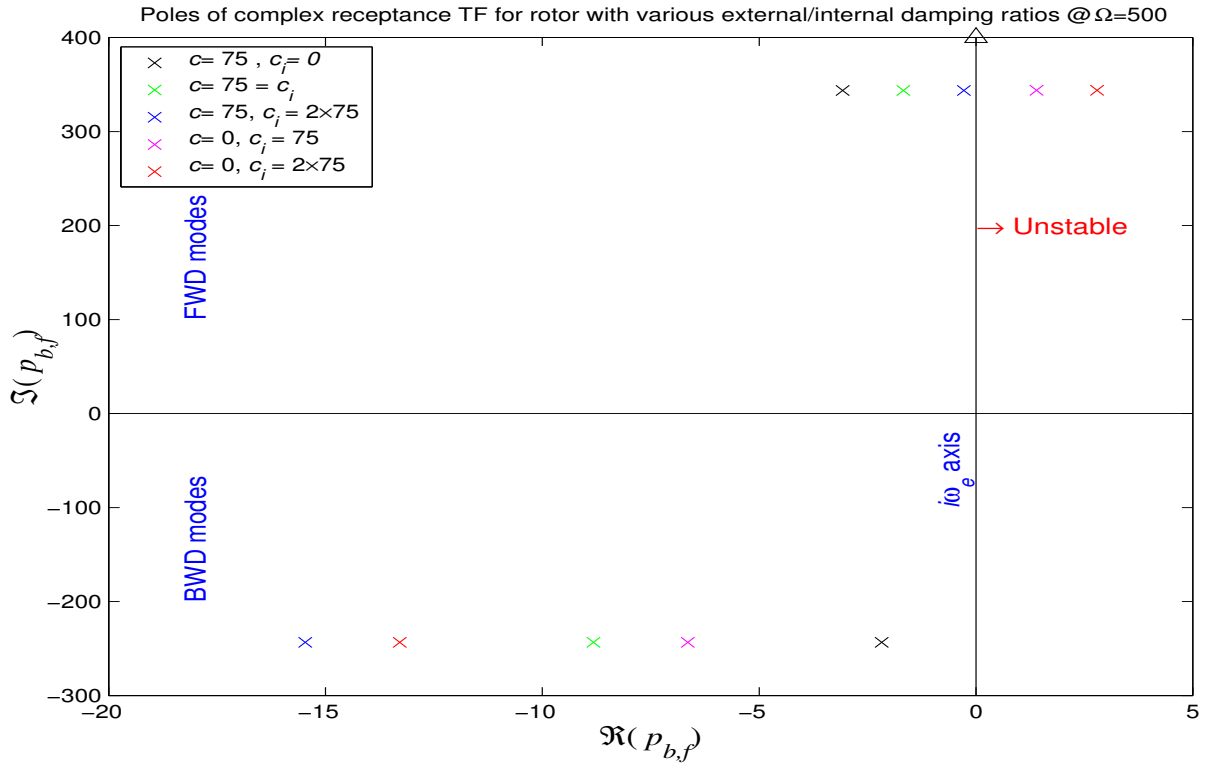


Figure 4.16.: s -plane with stable and unstable poles based on $\frac{\text{internal}}{\text{external}}$ damping ratio

upper-right-quarter s -plane representing unstable FWD modes, depending on the ratio $\frac{c}{c_i}$. All p_f presented have $\Im(p_f) \gg |\Re(p_f)|$ i.e. $\frac{\Im(p_f)}{|\Re(p_f)|} \geq 112$, which leads to the FRF sweeping quasi-circle in the CW \odot or CCW \ominus direction depending on FWD mode stability. As the frequency vicinity $\Delta\omega_{p_f}$ is traversed, a stable left-half s -plane pole vector will sweep $\Delta\angle(i\omega_e - p_f) \simeq \pi$ and the FRF sweeps $\Delta\angle G(i\omega) \simeq -\pi$ a quasi-circle in the CW \odot direction, while an unstable right-half s -plane pole vector will sweep $\Delta\angle(i\omega_e - p_f) \simeq -\pi$ and the FRF sweeps $\Delta\angle G(i\omega) \simeq \pi$ a quasi-circle in the CCW \ominus direction.

Response to static force Unlike $H_e^d(s)$, the TF of reference rotor without RID case, $G_c^d(s)$ results in a +ve phase shift of the static response to the static load/force:

$$\vec{Z}e^{i0} = \frac{k + i\Omega c_i}{k^2 + (\Omega c_i)^2} \vec{f}_ze^{i0} \quad (4.24)$$

This phase shift is solely due the RID-introduced term $-i\Omega c_i$ in $(k - i\Omega c_i)$ of (4.23), which is similar to that due to gyroscopic effects yet is operative even under static ($i\omega = 0$) forcing. The phase shift is always positive, i.e. in the direction of rotation that is CCW \ominus , due to the sign compliance of gyroscopic- and RID-introduced terms.

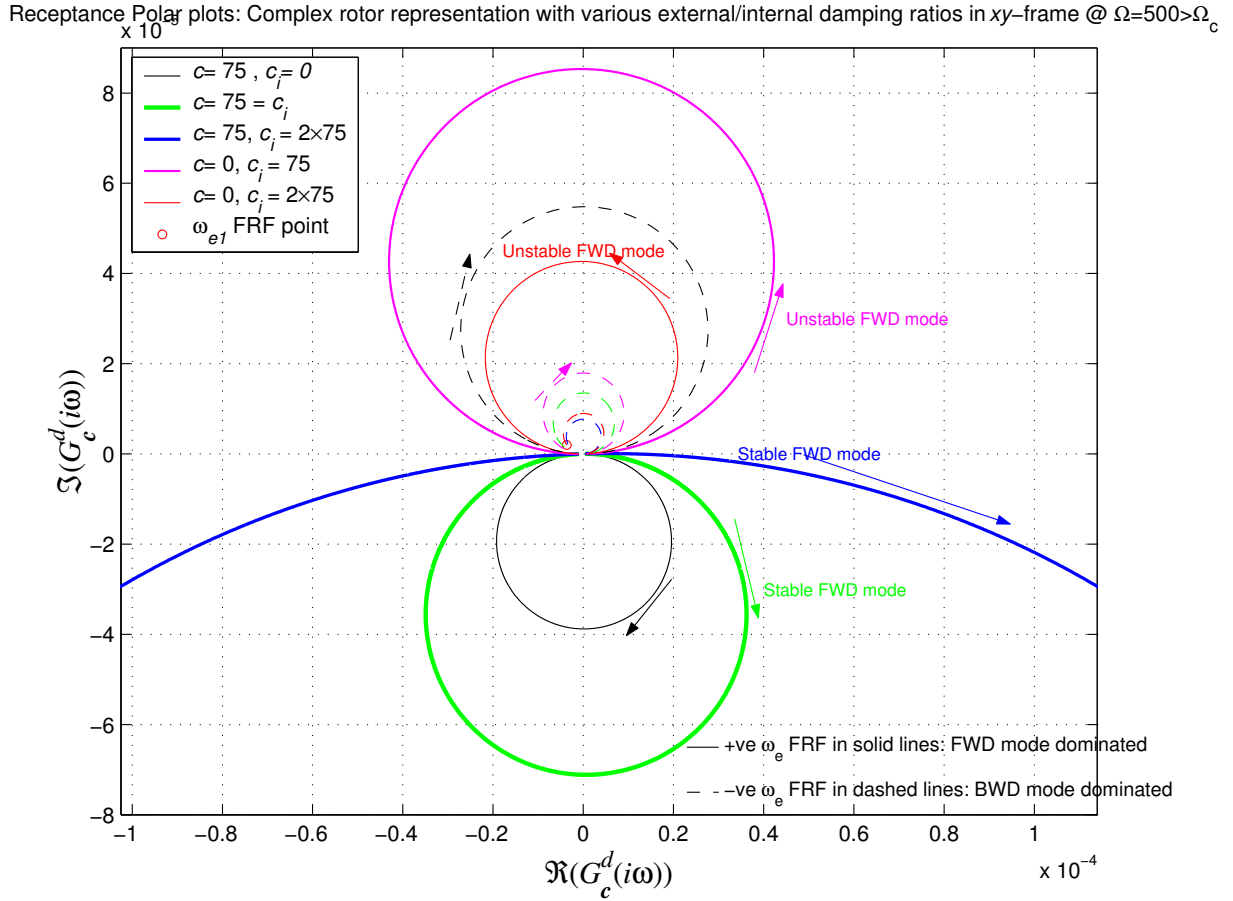


Figure 4.17.: Polar plots of stable/unstable (complex) rotor, based on $\frac{\text{internal}}{\text{external}}$ damping

4.2.2.3. Forced response of real rotor representation

The xy -frame receptance TFM of real rotor representation (4.10b) is:

$$\mathbf{G}^d(s) = \frac{1}{|\check{\mathcal{S}}|} \begin{bmatrix} s^2m + s(c + c_i) + k & -\Omega(sg + c_i) \\ \Omega(sg + c_i) & s^2m + s(c + c_i) + k \end{bmatrix} \quad (4.25)$$

$$|\check{\mathcal{S}}| = s^4m^2 + 2s^3m(c + c_i) + s^2((c + c_i)^2 + \Omega^2\mathcal{G}^2 + 2mk) + 2s(\Omega^2c_i\mathcal{G} + k(c + c_i)) + k^2 + (\Omega c_i)^2$$

Point and quad FRFs' polar plots $G_{xx}^d(i\omega), G_{yx}^d(i\omega)$ are presented here for comparison with experimental results, since those are the ones normally obtained without manipulation from a sine sweep modal test. FRFs $G_{xx}^d(i\omega), G_{yx}^d(i\omega)$ of two RID-augmented rotors, the first having stable FWD modes and the second with unstable FWD modes, are presented (fig.4.18) for comparison. These two rotors, which have identical coefficients except for damping coefficients: $\frac{c}{c_i} = 75(\frac{1}{1}, \frac{0}{1})$, are selected because of:

- Comparable $|\Re(p_f)|$ real parts of FWD modes' poles, albeit in opposite half-sides

4. Analysis of linear RID system

of the s -plane (*fig.4.16*), which dictates similar FRF magnitude plots but markedly differing polar plots in the FWD mode frequency vicinity $\Delta\omega_{p_f}$. Also, although $|\Re(p_f)| \ll |\Im(p_f)|$, $\Re(p_f)$ in both rotors is not infinitesimal so the FWD mode-dominated polar plot portions are not enormous and are easily presentable.

- BWD modes, although more damped than the reference rotor without RID, still have $|\Re(p_b)| \ll |\Im(p_b)|$, so BWD mode-dominated FRF portions are not overly diminished and are thus readily identifiable in both cases, which does not apply for coefficients $\frac{c}{c_i} = 75(\frac{1}{2}, \frac{0}{2})$.

Receptance pole-zero maps' layout of both RID-augmented rotors are similar to those of the reference rotor (*figs.4.5, 4.7*), with very well-separated modes, as well as poles and zeros. However, there are two obvious exceptions that are due to RID:

- Right-half s -plane poles representing unstable FWD modes of $\frac{c}{c_i} = 75(\frac{0}{1})$ rotor.
- Quad TF $G_{yx}^d(s)$ has a *non-zero* zero $o = -\frac{c_i}{g}, \forall \Omega \neq 0$, as opposed to $H_{yx}^d(s)$ in (3.26) that has a zero o at $s = 0$ (3.56b). Consequently, a static force in one direction will cause a static deflection in the quad direction, as explained hereafter.

The *positive* frequency range $\Delta\omega_e \stackrel{\text{def}}{=} \omega_e : [-0.9\omega_b \triangleright 1.1\omega_f]$ is selected to examine $G_{xx}^d(\omega), G_{yx}^d(\omega)$ behaviour (*fig.4.18*) in the frequency vicinities of p_b^*, p_f —as well as the left-upper-quarter s -plane $G_{xx}^d(s)$ zero o_1 in between them. Pole-zero maps' layouts emphasise that both modes, BWD and FWD, will dominate the FRF within their frequency vicinities (see §.4.1.2.1). Accordingly, $\Delta\omega_e$ is split into two ranges $[\omega_{e:1} \triangleright \Im(o)]$ and $[\Im(o) \triangleright \omega_{e:2}]$ so as to distinguish the corresponding mappings $G_{ij}^d(\omega)_{[\omega_{e:1}, \Im(o)]}$ and $G_{ij}^d(\omega)_{[\Im(o), \omega_{e:2}]}$ by different line weights, which in turn identifies FRF portions that are influenced by BWD and FWD modes respectively. Meanwhile, the relative phasing of $G_{xx}^d(\omega)$ to $G_{yx}^d(\omega)$ FRFs expresses modal directionality as elaborated on (*p.153*), and thus reveals the dominant mode, be it BWD or FWD, over a specific frequency range. Also, the first FRF point $G(\omega_{e:1})$ is marked by 'o' on both magnitude and polar plots so that the direction of phase angle swept $\Delta\angle G(\omega)_{[\omega_{e:1} \triangleright \Im(o) \triangleright \omega_{e:2}]}$ is evident. Observing *fig.4.18*, although FRF magnitude plots of both rotors are virtually identical, polar plots are markedly different depending on the location of p_f be it in the left or right-upper-quarter s -plane:

BWD-mode-dominated FRF portions where $\angle \frac{G_{xx}^d(\omega)}{G_{yx}^d(\omega)} \approx -\frac{\pi}{2}$ These are four quasi-circles representing polar plots of $G_{xx}^d(\omega)_{[\omega_{e:1} \triangleright \Im(o)]}$ and $G_{yx}^d(\omega)_{[\omega_{e:1} \triangleright \Im(o)]}$ for each of the two rotors, which are traversed in the CW \odot direction since both rotors have BWD mode poles p_b^* in the left-upper-quarter s -plane.

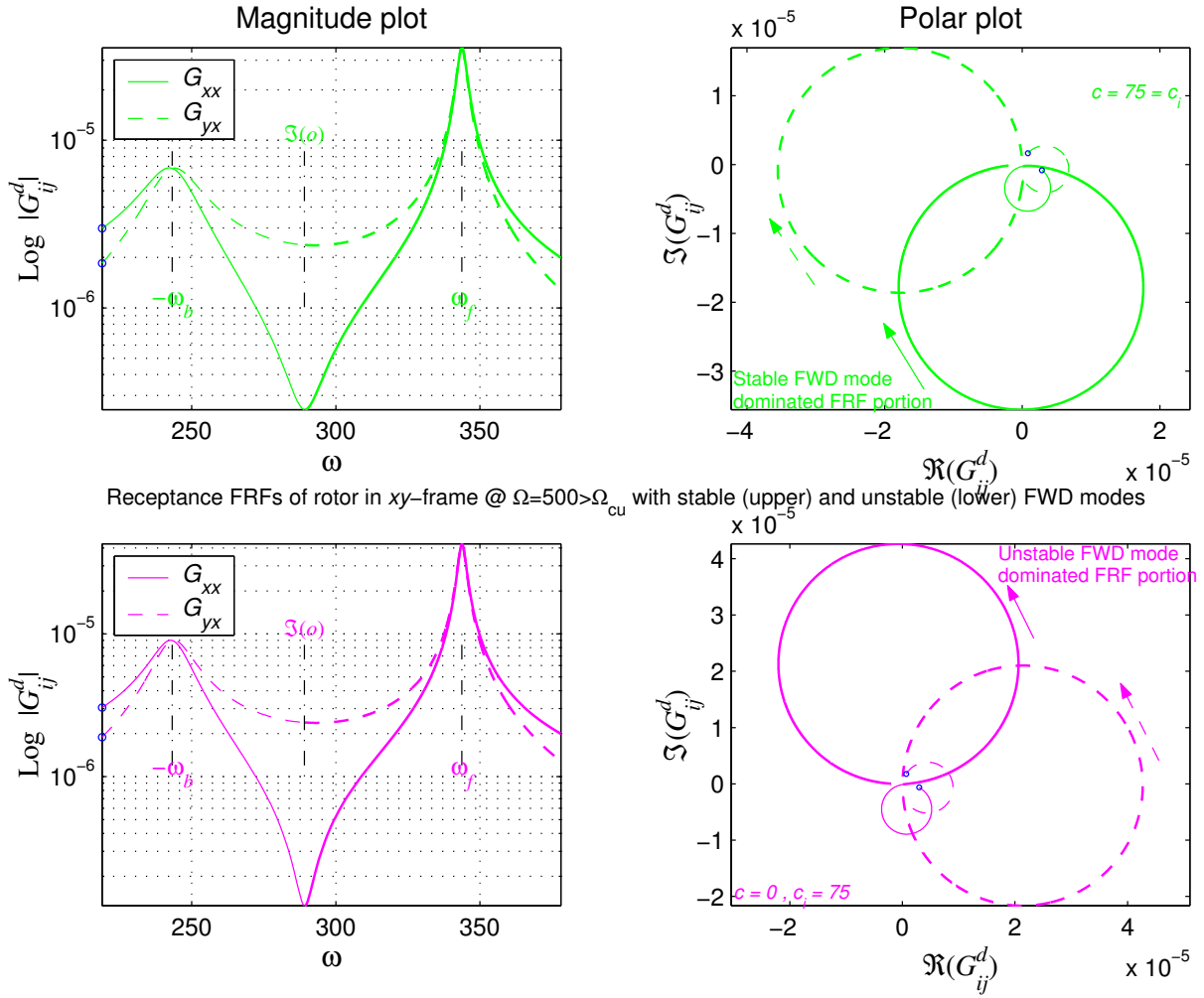


Figure 4.18.: FRFs of rotor with stable/unstable FWD modes, based on $\frac{\text{internal}}{\text{external}}$ damping

FWD-mode-dominated FRF portions where $\angle \frac{G_{xx}^d(\omega)}{G_{yx}^d(\omega)} \approx \frac{\pi}{2}$ The stable rotor has its FWD mode pole p_f in the left-upper-quarter s -plane, so the two FRF portions $G_{ij}(\omega)_{[\Im(\omega), \omega_{e:2}]}$ are quasi-circles traversed in the CW \odot direction as expected/usual. Meanwhile the two mappings $G_{ij}(\omega)_{[\Im(\omega), \omega_{e:2}]}$ for rotor with unstable FWD mode are quasi-circles traversed in the CCW \ominus direction on account of p_f being in the right-upper-quarter s -plane.

Quad response to static force: $\vec{f}_i e^{i0} \Rightarrow \vec{q}_j e^{i0}$ (4.25) represents the cross-coupling effect of RID, even to a static load e.g. gravity, provided the rotor is rotating. This is in agreement with typical literature [86, 177] examples of viscous RID (2.14) and logic of co-rotating RID follower force for a shaft with viscous stress (§.2.4.2, fig.2.3). Unlike rotor without RID, a static force f_x will cause static deflections in the y - as well as the x -direction, with such deflections mimicking the direction of rotation as expressed by (4.24). Equally, a gravity force (in -ve y -direction) will cause static deflections in the +ve x - and

-ve y -direction.

4.2.3. Appropriate use of ideal Hysteretic RID model

Some authors attempted to study the effect of a hysteretic RID model on stability using linear eigen-analysis in the stationary frame of reference based on [200]. They reached the unrealistic conclusion that a hysteretic RID model would have a destabilising effect from the outset ($\Omega \geq 0$) and would cause instability in the absence of stabilising external damping, which is generally unrepresentative of realistic operation.

Hysteretic RID is modelled here as per §3.2.2.1. Its complex notation (3.63) is augmented cautiously to the rotor's EOMs, which may possibly include linear viscous RID, in the rotating $\xi\eta$ -frame of reference as:

$$m\mathbf{I}\ddot{\mathbf{q}}_{\mathbf{r}} + \left((c + c_i)\mathbf{I} + (2m - \mathcal{G})\Omega\mathfrak{N} \right) \dot{\mathbf{q}}_{\mathbf{r}} + \left((k + (\mathcal{G} - m)\Omega^2 + \imath d)\mathbf{I} + c\Omega\mathfrak{N} \right) \mathbf{q}_{\mathbf{r}} = \mathbf{f}_{\mathbf{r}} \quad (4.26a)$$

Or in Complex format as:

$$m\ddot{\zeta} + \left((c + c_i) + (2m - \mathcal{G})\Omega\imath \right) \dot{\zeta} + \left(k + (\mathcal{G} - m)\Omega^2 + \imath(c\Omega + d) \right) \zeta = f_{\zeta}, \quad \kappa = \frac{d}{k} \quad (4.26b)$$

Two important points to state about (4.26):

- These can be used to analyse the system only under the assumption of single-frequency steady state vibration, which may be forced response *or individual modes*
- For conciseness purposes, the complex notation of hysteretic RID does not account for the all important $\text{sgn}(\omega)$ as in (3.64), which is necessary when considering modes and FRF-portions with negative frequencies, particularly when analysing a complex rotor model (4.26b).

The effect of hysteretic RID on modal stability is examined and elaborated using eigen-values (§4.2.3.1), while points are noted on frequency response analysis (§4.2.3.3) which is at the heart of stability analysis when used in conjunction with §.4.2.2.1 or §.5.3.2.1. Since hysteretic RID is only properly modelled via a FR model:

- The truly proper means of assessing stability is via FR techniques such as the adapted Nyquist criterion presented in §.5.3.2.1 for hysteretic damping (*fig.5.4*).
- No attempt is made here to study the system in the stationary xy -frame, since transferring a FRF as in (3.63) is different from transferring a time-domain coefficient as in $c_i\dot{\zeta}$, which is a good topic for further research. Rather, the stability of modes derived in xy -frame is inferred from those derived in $\xi\eta$ -frame, in accordance with logical relations (3.43, 3.48).

The results thus achieved are more representative of actual operating conditions, albeit with an abrupt change around Ω_c when frame-transferred FWD modal frequency ($\omega_{r:2} = \omega_f - \Omega$) changes sign, which is to be expected on account of $\text{sgn } \omega$ in the hysteretic damping model (3.64).

4.2.3.1. Eigenvalues-based stability analysis

Although it is common practice to use a complex notation representing hysteretic damping in stable systems as a more representative damping model as well as for the sake of a more straightforward analysis, it is well known that such analysis is less than rigorous. For systems represented in first order state-space form, the real parts of resulting eigenvalues from (3.30) with positive modal frequencies $\Re(\lambda) \forall \lambda$ with $\Im(\lambda) > 0$ are considered, while for those resulting from second-order representations as in (3.32), i.e. $\lambda^2 = \omega^2(1 + \nu\kappa)$, κ is always considered to be positive implying a stable system.

Effect of complex stiffness on eigenvalues Since EOMs (4.26a) are complex, their corresponding eigenvalues $\lambda_{r:i \in \{1...4\}}$ do not generally occur in complex-conjugate pairs and are not the complex-conjugates of $\lambda_{rc:1,2}$ corresponding to (4.26b). This applies equally to modal frequencies as well as decay constants, and is due to the non-complex-conjugate contributions of νd to initially complex-conjugate eigenvalues since $\text{sgn}(\omega)$ in (3.64) is not accounted for when considering eigenvalues with negative modal frequencies, i.e. $\forall \lambda$ with $\Im(\lambda) < 0$. This situation may cause confusion and lead to conflicting and erroneous results when assessing modal stability based on eigenvalues, and is hence expanded upon and exemplified hereafter.

Different contributions of complex stiffness to λ and λ^* As shown in (3.47), viscous damping, be it internal or external, contributes to both $\Re(\lambda)$ and $\Im(\lambda)$ in a complex-conjugate manner for complex conjugate eigenvalues. Accordingly, should (4.26a) be considered with $d = 0$, i.e. linear viscous damping is the only dissipation mechanism, complex conjugate eigenvalues would be:

$$\lambda = \sigma_{\text{vis}} + \omega_{\text{vis}} \quad \text{and} \quad \lambda^* = \sigma_{\text{vis}} - \omega_{\text{vis}}$$

Similarly, complex stiffness contributes to both $\Re(\lambda)$ and $\Im(\lambda)$, but in a non-complex-conjugate manner for complex conjugate eigenvalues due to lack of $\text{sgn}(\omega)$. Accordingly, should (4.26a) be considered with hysteretic damping as the only dissipation mechanism, i.e. $c = 0 = c_i$, eigenvalues with complex conjugate modal frequencies would be:

$$\lambda^{+\omega} = \sigma_{\text{hys}} + \omega_{\text{hys}} \quad \text{and} \quad \lambda^{-\omega} = -\sigma_{\text{hys}} - \omega_{\text{hys}}$$

4. Analysis of linear RID system

Simply stated, if the complex stiffness results in a stable (unstable) eigenvalue with positive frequency, it will result in a corresponding eigenvalue with negative frequency, which *appears* to be unstable (stable). This is synonymous with eigenvalues of a system with stabilising positive viscous damping coefficient e.g. $c\dot{x}$, when compared to those of the same system with destabilising negative viscous damping coefficient e.g. $-c\dot{x}$.

With both dissipation mechanisms operative, EOMs (4.26a) yield eigenvalues that are not complex conjugates. While the modal frequencies may be made out as approximate complex conjugates, i.e. $\omega_{r:i} \approx -\omega_{r:i+n}$, the decay constants are certainly not $\Re(\lambda_{r:i}) \neq \Re(\lambda_{r:i+n})$, considering that:

$$\Re(\lambda_{r:i}) = \sigma_{\text{hys}}^i + \sigma_{\text{vis}}^i \quad \text{and} \quad \Re(\lambda_{r:i+n}) = \sigma_{\text{hys}}^{i+n} + \sigma_{\text{vis}}^{i+n} \approx -\sigma_{\text{hys}}^i + \sigma_{\text{vis}}^i$$

which may be used to identify the different contributions of viscous and hysteretic damping mechanisms as:

$$\sigma_{\text{hys}}^i = \sigma_{\text{hys}}^{i+n} \approx \frac{\Re(\lambda_{r:i}) - \Re(\lambda_{r:i+n})}{2} \quad \text{and} \quad \sigma_{\text{vis}}^i = \sigma_{\text{vis}}^{i+n} \approx \frac{\Re(\lambda_{r:i}) + \Re(\lambda_{r:i+n})}{2}$$

Accordingly, when using a complex stiffness in an eigen-analysis, one should only consider eigenvalues with positive modal frequencies when assessing stability. This in turn requires analysing real representation of rotor systems so as to account for all precession modes being present with positive modal frequencies.

Using complex stiffness with complex rotor representation Should it be interesting to analyse a rotor's complex representation, possibly to identify readily eigenvalues corresponding to FWD and BWD modes in the stationary frame $\lambda_{\text{rc}:1,2} \Leftrightarrow \lambda_{b,f}$, some remedy is necessary so as to handle the problem of assigning $id \text{sgn}(\omega)$. Attempting to include hysteretic damping as $id \text{sgn}(\omega)$ in EOMs (4.26b) renders the system nonlinear; a situation that will upset most eigen-solvers. The simple solution is to analyse (4.26b) with id for λ_{rc} having positive ω and $-id$ for λ_{rc} having negative ω . As both λ_{rc} of (4.26b) will have negative modal frequencies ω for speeds $\Omega > \Omega_c$, using id is only necessary at speeds $\Omega < \Omega_c$ and only for $\lambda_{\text{rc}:2}$, which will then have positive ω . Failure to abide by the foregoing may lead to confusion and the erroneous conclusion that BWD modes (as transferred to $\xi\eta$ -frame) may be unstable, which is untrue.

4.2.3.2. Effect of hysteretic RID on modal stability characteristics

Analysing the eigenvalues *with positive modal frequencies* of system from (4.26a) as in §.4.2.1.1 reveals that hysteretic RID affects the stability of FWD and BWD modes—as inferred from their corresponding modes in the rotating frame—in the following manner:

- Enhances the stability of BWD modes at all speeds, as does viscous RID
- Enhances the stability of FWD modes at sub-critical speeds $\Omega < \Omega_c$, but challenges it at super-critical speeds $\Omega > \Omega_c$, as does viscous RID
- Unlike viscous RID, the effect of Hysteretic RID is speed-independent so, in the absence of other speed-dependent dissipation mechanisms, $\Re(\lambda)$ varies only very slightly with speed on account of square-root in (4.13), except around Ω_c .
- $\Re(\lambda_{r:2})$, reflecting FWD mode stability, changes abruptly around Ω_c as $\text{sgn}(\omega_{r:2})$ changes over from positive to negative

Should external viscous damping exist in EOMs (4.26) $c_e \neq 0$, FWD modes may not become unstable at all for comparably small value $\kappa = \frac{d}{k}$, which is a viable thesis. However, due to the speed-progressive nature of external damping contribution to $\Re(\lambda)$ (figs. 4.2, 4.3), FWD modes may become stable at higher speeds after being initially unstable, which is perhaps unusual. The foregoing states that if FWD modes are to be unstable on account of hysteretic RID alone, then they will become unstable right after Ω_c , which is not a common scenario case. Accordingly, introducing a small viscous RID coefficient c_i may solve the situation amicably by introducing a speed-progressive destabilising effect. The above is demonstrated in fig.4.19 for the isotropic rotor of (4.26) with coefficients (4.2) and variants of hysteretic and viscous RID coefficients. The first set of damping coefficients in fig.4.19 is perhaps the more representative of actual operating conditions when FWD modes become gradually less stable with increased speed until RID instability onset speed is reached.

4.2.3.3. Hysteretic RID model in FRF with negative frequency: $\omega_e < 0$

FRFs of complex rotor representations are required for the FR stability analysis in §.4.2.2.2, 5.3.2.1, 5.3.2.2. These FRFs will have a negative frequency range so as to account for all modes' vicinities. In such case:

- The hysteretic RID model must account for $\text{sgn}(\omega)$ as in (3.64) or,
- Any complex stiffness, be it hysteretic damping K or a describing function $\mathbb{k}(X)$ (A.21) must be replaced by its complex conjugate K^* , $\mathbb{k}^*(X)$ as in (3.65), when used in conjunction with a -ve ω .

It is easy to appreciate the necessity for the complex conjugates K^* , $\mathbb{k}^*(\bar{\zeta})$ with a complex rotor representation, where a -ve ω has a physical meaning, i.e. CW precession: With a cyclic input $\zeta(t) = \Re(\bar{\zeta}e^{\omega t})$ into the complex stiffnesses (K, \mathbb{k}), their imaginary part ($d, \Im(\mathbb{k})$) causes their outputs ($f_{\text{hyst}}(t), \mathcal{F}_\zeta^1(t)$) to lead $\zeta(t)$ by a phase angle ψ in the CCW

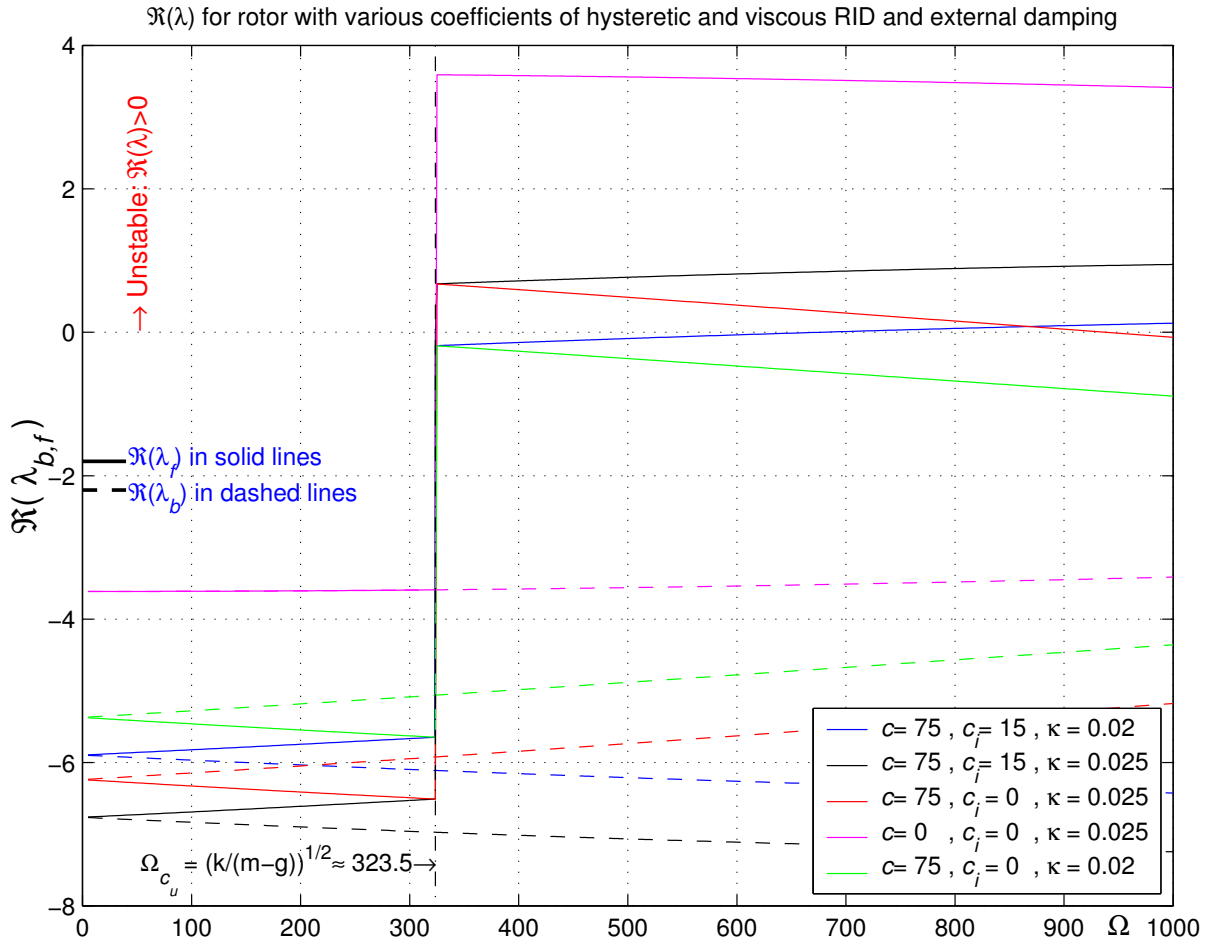


Figure 4.19.: Effect of hysteretic RID on modal stability

direction of rotation. In other words: steady-state response lags force by ψ . In the CW precession scenario, steady-state response should also lag force by ψ , which is reflected by the -ve imaginary parts ($-d, -\Im(\mathbb{k})$) in $K^*, \mathbb{k}^*(\bar{\zeta})$ to account for the (-ve) CW precession. Failure to account for $\omega_e < 0$ will reverse the effect of hysteretic RID on modal damping and stability. In the limit, if hysteretic RID is the prominent dissipative mechanism, it may give a conclusion about stability that is just the opposite of reality.

4.3. Experimentally-Applicable Stability Test: EAST

EAST is an *experimental* technique developed to assess safely and conclusively the stability (and its margins) of a *target* dynamic system, e.g. an industrial turbine or turbo-engine, which may become unstable when operated under various steady or transient conditions. This is accomplished by analysing experimentally-acquired FRFs of the target system whilst operational, but included as a subsystem in an overall-stable system.

Although proper dynamic systems' design ought to be within proven safety parameters

and accordingly avoid most instabilities, there are many situations, e.g. reengineering or new turbine design, where designers might have not accounted for unforeseeable operational conditions or might want to test the limits and/or fine-tune parameters of their design. In such situations, the proof of the pudding is always in the eating, i.e. performance and stability of a prototype during actual operation whilst varying operational parameters and conditions. Should the prototype dynamic system being tested be prone to instability, the results may range from undesirable to catastrophic.

There may be dynamic systems, e.g. some electronic circuits, where instability during prototype-testing does not constitute major loss, might not warrant serious safety precautions and only entails redesign procedures. However, other dynamic systems—such as rotordynamic ones, e.g. oxygen and fuel turbines/compressors on the space shuttle—instability even in a prototype test is not only very costly but also extremely dangerous, generally life-threatening and probably catastrophic. In such situations, safe testing/operation is introduced by implementing EAST during prototype experimentation, which in turn provides a definitive stability appraisal on the off chance of *analytical* models/design being inaccurate. Subsequently, EAST may be instrumental in re-design phases and system parameter fine-tuning, possibly to adjust the levels of stabilising external damping so as to reach an optimum modal stability margin. EAST was developed on the tails of the author’s experimental findings detailed in §.6.2.2.2.

4.3.1. EAST overview

Analytically, East concludes on target system stability by assessing the stability of system modes (modal stability) utilising FRF characteristics. EAST is based on examining the ClockWise (CW/CCW) direction in which the polar plot of an *experimentally-acquired* FRF $G(\omega)$ is traversed. In accordance with §.4.1.2.1 and §.4.2.2.1, if the polar plot is traversed in a CW [CCW] direction as the frequency range $\Delta\omega_{p_v}$ in the vicinity of the v^{th} mode is swept increasingly, this v^{th} mode in question is stable [unstable].

Generally, EAST is applicable to any dynamic system be it linear or quasi-linearised nonlinear, where the suspected unstable modes can be excited and observed. In so doing, the analyst using EAST needs to fulfil two essential elements to achieve the above goals:

- Acquire an experimental FRF of a potentially unstable dynamic system. If the target system is indeed unstable, careful intervention is necessary to render such exercise achievable.
- Analyse the FRFs to assess polar plot directionality and extract modal values, especially damping. Confidence in modal analysis yielding unmistakable conclusions should be ensured.

both of which are elaborated upon hereafter.

4.3.2. Concept of EAST

Acquiring a FRF of the target system dictates it be excited by some pre-determined and quantified input (force). Since attempting to excite an unstable system will result in instability that may be destructive, careful intervention is necessary to make a modal test feasible, yet without altering the target system dynamics, especially modal damping, or mask any of its modes. The idea is to acquire a FRF of the possibly unstable target system represented by TF $G(s)$ whilst incorporated as a subsystem in an overall stable system \mathcal{S}_{oa} with TF $G_{oa}(s)$ that has *added external damping*, which is sufficient to insure overall stability (e.g. *fig.4.20*).

There are two significant issues to consider in realising the concept above, namely: The manner in which the target system is incorporated in an overall stable system, and the excitation method.

4.3.2.1. Target system setup as a subsystem of an overall stable system

The objective here is to be able to acquire a FRF of the target system (e.g. $G_{xy}^d(\omega)$ of TF $G(s)$) from $\frac{\text{output}}{\text{input}} \left(\frac{x}{f_y} \right)$, without the rest of \mathcal{S}_{oa} influencing the stand-alone $G(s)$. This can be achieved by stacking a damper (energy dissipator) array *in parallel* with excitation (input) coordinate y on the target system (*fig.4.21*), thus matching its vibration (output), whilst splitting the overall input to \mathcal{S}_{oa} with TF $H_{oa}(s)$, i.e. force (input) f_{oa} is split as:

- f_d into the damper array and
- f_y into $G(s)$

Should the target system with $G(s)$ have an unstable mode, its $G(\omega)$ will exhibit a CCW polar plot in the frequency vicinity of the corresponding right-half s -plane pole. However, $H_{oa}(\omega)$ will exhibit a CW polar plot in the same frequency vicinity on account of the damper array, which stabilises the overall system, which is exemplified in §.4.3.4.

4.3.2.2. Excitation

In order to acquire the necessary FRFs of the target and overall systems, the latter needs to be excited by means appropriate to the target system. For a linear target system, most excitation methods (impulse, step, sine-sweep) are viable, only the data postprocessing differs, using FFT or FRA methods. However, should the target system be nonlinear, some form of quasi-linearisation is necessary. Response quasi-linearisation—controlling/maintaining response amplitude constant in each cycle at different excitation

frequencies—requires sinusoidal excitation, which like the other signals can be achieved using a wave generator.

4.3.2.3. Precautions on Damping estimates from a modal test

In the process of acquiring a FRF of mechanical systems, damping that is not inherent to the target or overall systems may be unintentionally introduced to both. Caution must be exercised here since this might yield erroneous results, as explained below.

Attachments' damping is introduced to the target system from the material layer used to attach force gauges, accelerometers, etc. This sort of damping is seen in the modal test as inherent to the target system and may erroneously *overestimate* modal damping values deduced thus possibly disguising an unstable mode as a stable one. Efforts to minimise or eliminate attachments' damping introduced to the target system should be exercised. One way of eliminating attachments' damping is to eliminate attachments by using non-contact excitation and response measurement, e.g. electromagnetic exciters and laser doppler or proximity probes.

Shaker external damping is introduced to the overall S_{oa} but not the target system if an electrodynamic (or hydraulic, etc.) shaker is used to excite the overall system as seen in *fig.4.20*. Through their dynamics, shakers introduced this external damping, which compliments the intentionally introduced external damping hence enhancing the overall S_{oa} stability. **Caution** is drawn to this issue of shaker-introduced damping. Although most electrodynamic shakers have heavily-damped dynamics due to the common use of a spider construction, some new-design shakers do not have this spider construction and subsequently have relatively minimal if not negligible damping. *It is thus unwise to rely solely on shaker-derived damping to stabilise S_{oa} .*

4.3.3. Ideal Use: System modes

Generally, EAST is applicable to any dynamic system be it linear or quasi-linearised, where the suspected unstable mode can be excited and observed. Ideally however, for EAST to be undoubtedly conclusive, the target system needs to be totally observable with well-separated modes; and if nonlinear should not be heavily so. Modal analysis of this ideal system's FRFs would:

- Avoid the possibility of an unstable mode being not represented in the TF due to pole-zero cancellations (§.3.1.4) hence such unstable mode won't be identifiable from the FRF.

4. Analysis of linear RID system

- Avoid poles with similar frequencies but in different halves of the s -plane, i.e. one stable and one unstable pole, annulling each others effect on the FRF as frequency is swept. An example of such situation is a forward mode unstable rotor without gyroscopic effects, i.e. Jeffcott rotor when $\Im(\lambda_b) \equiv \Im(\lambda_f)$ but $\Re(\lambda_b) \stackrel{\text{def}}{=} -\text{ve}$ while $\Re(\lambda_f) \stackrel{\text{def}}{=} +\text{ve}$.
- Readily identify the polar plot directionality (CW/CCW) in the vicinity of the mode in question as the limited frequency range is swept.
- Estimate properly modal values, especially damping that reflects on stability.

4.3.4. Analytical background and application of EAST

4.3.4.1. EAST exemplified using SDOF

EAST, which is applicable to a general MDOF target system with well-separated modes that is totally observable, is exemplified here using a *hypothetical* SDOF (fig.4.20) with damping that could be stabilising or destabilising. The target SDOF has the EOM:

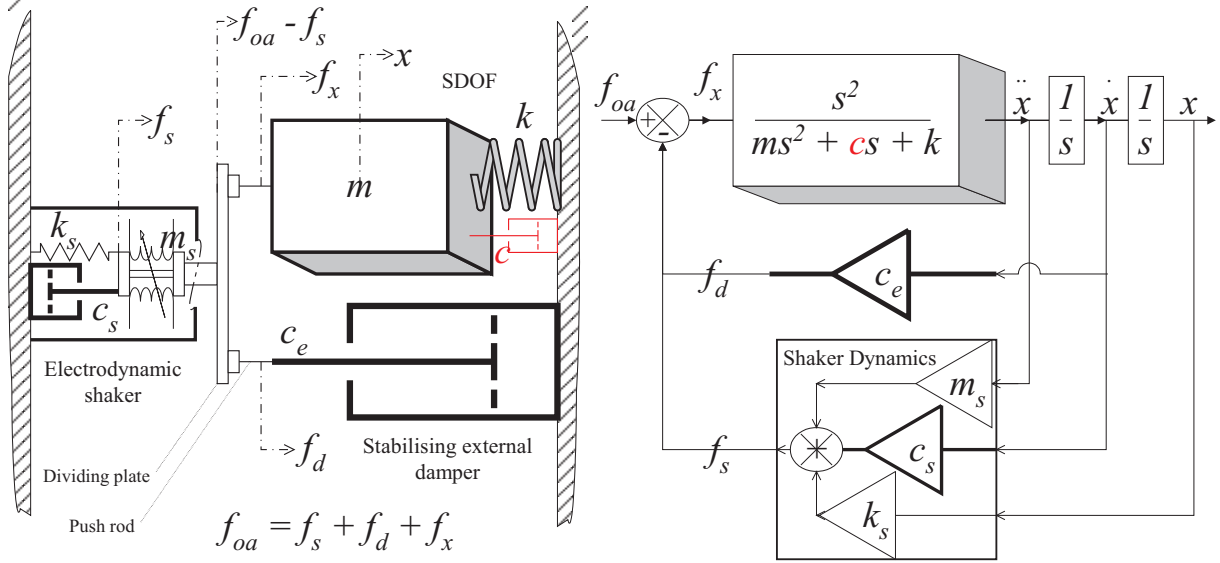


Figure 4.20.: EAST illustration using a SDOF with possible hypothetical -ve damping

$$m\ddot{x} + c\dot{x} + kx = f_x \quad \text{where } c \stackrel{\text{def}}{=} \begin{cases} +\text{ve} \Rightarrow \text{stable system} \\ -\text{ve} \Rightarrow \text{unstable system} \end{cases} \quad (4.27)$$

Fig.4.20 represents system (4.27) with a SISO TF having force f_x as input and acceleration \ddot{x} as output that is integrated sequentially, so as to allow for the overall system \mathbf{S}_{oa} dynamics to be represented. \mathbf{S}_{oa} , which comprises the SDOF, the heavy external damper

with c_e and the shaker, has the EOM:

$$f_{oa} = \begin{matrix} f_x \\ +f_d \\ +f_s \end{matrix} = \begin{matrix} m\ddot{x} + c\dot{x} + kx \\ +c_e\dot{x} \\ +m_s\ddot{x} + c_s\dot{x} + k_sx \end{matrix} \quad (4.28)$$

Stabilising damping in \mathcal{S}_{oa} derives not only from the heavy external damper c_e , but also from the electrodynamic shaker c_s . The stability of \mathcal{S}_{oa} is determined by whether the overall damping $c_{oa} = c + c_s + c_e$ is positive or negative. Obviously if the target system is stable with $c \stackrel{\text{def}}{=} +ve$, then \mathcal{S}_{oa} is definitely stable since c_e and c_s are both positive. However, should c be negative, then the stability of \mathcal{S}_{oa} depends on whether $c < c_s + c_e$ or not. Since it shouldn't be difficult to design a stable \mathcal{S}_{oa} with c_e that overwhelms a negative c , experimental FRFs e.g. $G_{xx}^d(\omega) = \frac{\bar{X}(\omega)}{\bar{f}_x(\omega)}$ and $H_i^d(\omega) = \frac{\bar{X}(\omega)}{\bar{f}_i(\omega)}$ may be obtained using:

- Output x using a sensor on the SDOF
- Practically-measurable inputs e.g. $f_i = f_{oa} - f_s$ or f_x using force gauges on the dividing plate and SDOF respectively

The Target system's stability may then be assessed from the polar plot of its FRF $G(\omega)$ in accordance with §.4.2.2.1.

4.3.4.2. EAST applied to a general rotor with RID

Validity The application of EAST to rotors that are susceptible to RID instability under design-operating conditions should be valid for most realistic rotors since these generally satisfy the criteria stated at the beginning of §.4.3. This is because such rotors are essentially not heavily-damped with well-separated modes, which are totally identifiable from any FRF that is acquired properly. An exception would be when a BWD and FWD mode have the same or similar frequency at a specific speed; a situation that is simple to identify from FE analysis and is easily remediable by applying EAST at a higher operating speed.

Application EAST can be applied to a general rotor with RID from a coupling for instance as shown in (fig.4.21). Overall input force f_{oa} to the overall system \mathcal{S}_{oa} is split at the dividing plate as f_d into the stabilising external damper array and f_y into the target system at excitation coordinate y . Response can be measured at another convenient coordinate x . Naturally, inputs and outputs have to be located appropriately away from the nodes of all FWD modes and possibly at some anti-nodes. In the block diagram, the target system is represented by its mobility TF so as to model external damping as a

4. Analysis of linear RID system

simple gain of c_e after accounting for the relation between \dot{x} and \dot{y} , which would derive primarily from the rotor's dominant mode shape ψ at the excitation frequency.

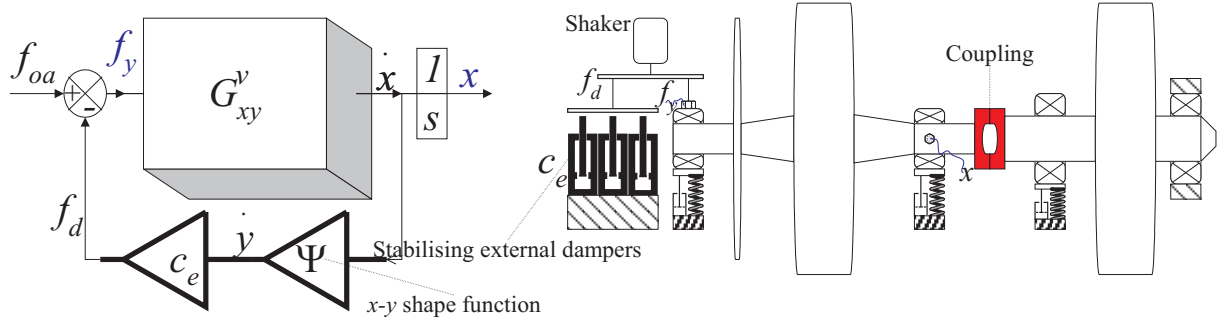


Figure 4.21.: A proposed experimental setup for EAST on a general rotor configuration

Example: EAST applied to 2DOF isotropic rotor with RID The stabilising external damper with coefficient c_e is stacked in parallel to excitation coordinate x on the target rotor (*fig.3.1*) to form the overall stable system \mathbf{S}_{oa} . The target rotor described by EOMs (4.10) has the state matrix $\check{\mathbf{A}}$ given by (4.11), while that of \mathbf{S}_{oa} is:

$$\check{\mathbf{A}}_{oa} = -\frac{1}{m} \begin{bmatrix} 0 & 0 & 1 & 0 \\ 0 & 0 & 0 & 1 \\ k & \Omega c_i & c + c_i + c_e & \Omega \mathcal{G} \\ -\Omega c_i & k & -\Omega \mathcal{G} & c + c_i \end{bmatrix} \quad (4.29)$$

Numerical values in (4.2) with $c = c_i = 75$, $c_e = 150$ Ns/m and $\Omega = 800$ rad/s are used in this example, which results in a target rotor with unstable FWD modes but a stable overall system \mathbf{S}_{oa} .

Overall force input f_{oa} that is applied parallel to the x coordinate is split as f_x into the target rotor with TFM $\mathbf{G}(s)$ and f_d into the damper array. The resulting receptance FRFs (*fig.4.22*) are obtainable experimentally since \mathbf{S}_{oa} has TFM $\mathbf{H}_{oa}(s)$ with all poles in the left-half s -plane, thus $H_{xx}^d(\omega) = \frac{\vec{X}(\omega)}{f_{oa}(\omega)}$ for example traces a polar plot with CW quasi-circles around the frequency vicinities of both BWD and FWD modes (§.4.1.2.1). However, $\mathbf{G}(s)$ has poles of FWD modes in the right-half s -plane, so $G_{xx}^d(\omega) = \frac{\vec{X}(\omega)}{f_x(\omega)}$ for example traces a CCW quasi-circle around the frequency vicinity of the FWD mode (§.4.2.2.1).

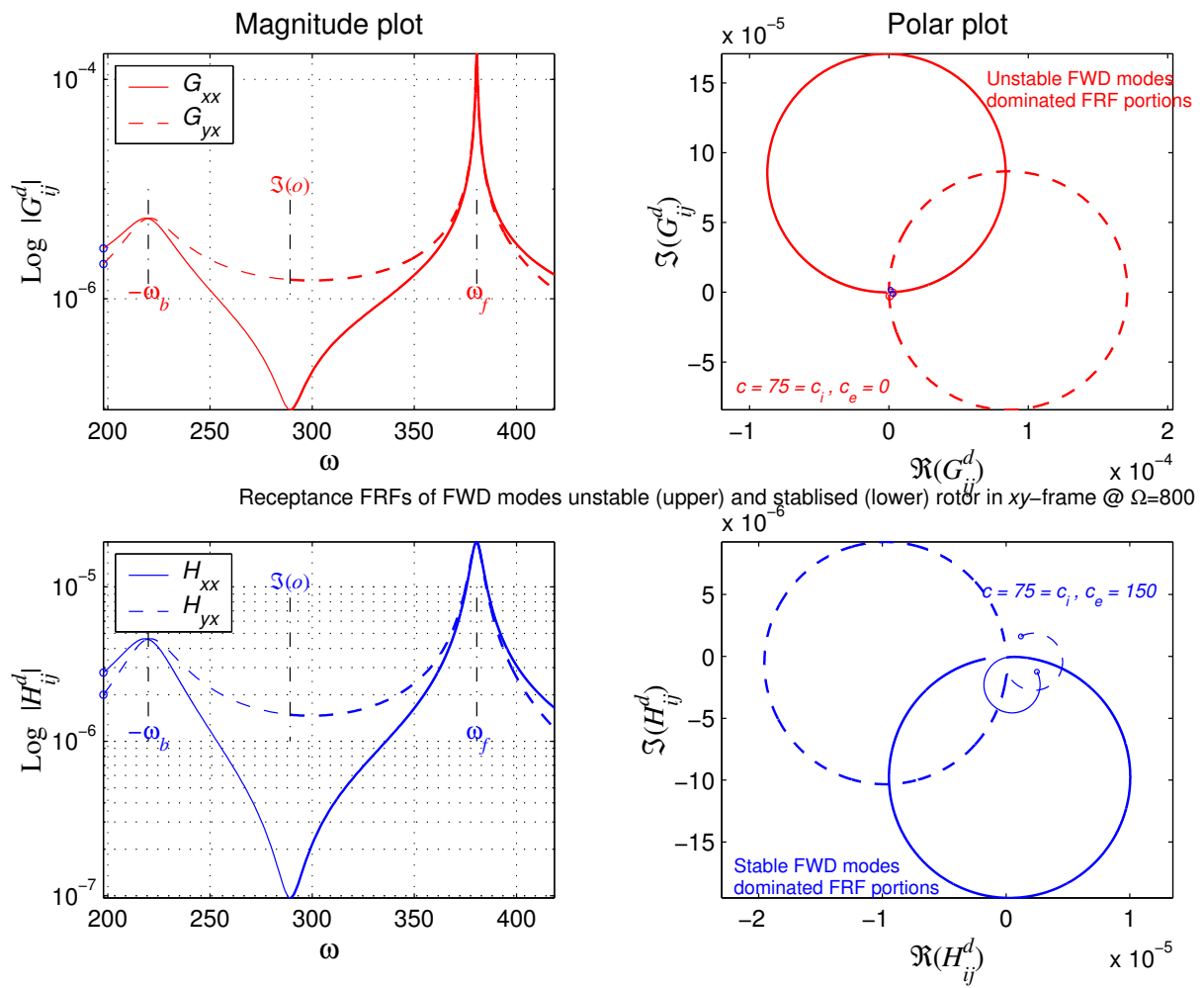


Figure 4.22.: FRFs of RID-unstable rotor derived from EAST

5. Nonlinear analysis: Stability, Limit Cycles and Forced Response

In this chapter, nonlinear (NL) analysis techniques that are suitable for handling the NL RID problem are identified, modified and implemented. It will be seen that quasilinearisation is arguably the only way forward for NL RID analysis. Furthermore, graphical prediction tools are needed in conjunction with quasilinearisation for initial guesses, as well as predicting NL behavioural patterns, e.g. varying precession boundedness.

5.1. Aspects of nonlinear behaviour

Although linear systems are favoured for ease of design and powerful analysis, they are idealisations justified by Lyapunov's linearisation method (5.2). However, not all systems can be linearised comfortably, such as those with friction RID. Some significant differences between linear and nonlinear RID systems' behaviour are set out below.

5.1.1. Stability Concepts

5.1.1.1. Local and global stability aspects

These are important to keep in mind, when considering significant deviations from the nominal operating condition, when NL systems' stability properties are substantially more complicated than those of linear(ised) ones. With linear systems, there is no distinction between local and global stability: A stable [unstable] linear system at a nominal point is stable [unstable] at any point. However, NL system's stability in the neighbourhood of an equilibrium point does not necessarily imply any global property. There may be many equilibria, some stable and others not, in which case there will be only a limited region of convergence (domain of attraction) around any equilibrium point which is locally asymptotically stable.

5.1.1.2. Limit cycles or Precession

These are periodic oscillations generated *within* the system, which constitute a sort of dynamic, rather than static, equilibrium and have no true counterpart in linear systems. There may be several dynamic equilibria, some are *locally* stable (bounded) and others not (unbounded). Possibilities extend from simple periodic LCs to limit sets and on to the quasi-stochastic behaviour, despite the system's deterministic nature. Chaos is particularly prevalent in discrete-time systems, possibly for simple low-order models.

5.1.2. Harmonic response peculiarities

Input forms A linear system's dynamic properties can be described independently of its input, using TF or state-space representations. Conversely, a nonlinear system's behaviour, be it stable, unstable, oscillatory or chaotic, may depend crucially on its *inputs*; a scenario depicted in any successful NL analysis technique, e.g. DFM (§.A.2.4.2).

5.1.2.1. Frequency response and jump resonance phenomena

Applying a sinusoidal input to a LTI system can only generate an amplified and phase-shifted sinusoidal output of the same frequency. With a NL system, however, the output:

- Might be periodic, but will generally contain higher harmonics of the input's fundamental frequency, instead of being purely sinusoidal.
- More generally, may contain subharmonic components of the input's frequency, or even incommensurate frequencies, associated with internal dynamical phenomena.
- Exhibits 'jump resonance' phenomenon, due to multi-valued frequency-response.

However, the above system is assumed to be non-limit-cycling. RID systems at subcritical speeds fall into this category, and yet there is *hypothetical* concern as to whether a LC might break out as discussed in what follows.

5.1.2.2. External frequencies and limit cycle parameter alterations

If an input external to the LTI subsystem is applied to a nonlinear system capable of self-oscillation, it will most likely interfere with LC dynamics: initiating, altering its parameters, or suppressing it altogether.

Frequency response, limit cycle induction and quenching The forced sinusoidal response of nonlinear systems is particularly interesting since a variety of modes of operation may exist and in some cases may be obtained simply by varying the input amplitude.

Apart from the normal forced response, which may possess unstable solutions, the possibility also exists that the input will excite an oscillation either at a frequency unrelated or related to that of the input. Not surprisingly investigations of the various situations proceed rather differently. The variations of gain to a signal through a nonlinearity, which may be produced by an unrelated second signal, are readily appreciated from the modified nonlinearity concept (see §7.2.1) so that physical situations where a sinusoidal input may induce an oscillation, or quench an existing one, are usually easily foreseen.

Incommensurate frequencies quenching limit cycles is a feature that is well documented (e.g. §A.2.4.4). It is also the basis for the successfully implemented signal stabilisation (§7.2.2.2) as well as linearising the highly nonlinear effects of friction (§7.2.2.1), albeit at high frequencies ratio. The fact that orthotropic bearings result in LTV coefficients at 2Ω , usually higher than thrice the RID LC frequency, may be advantageous for avoiding RID precession, and is planned for future investigation (§7.2.1).

5.2. Nonlinear analysis suitable for the RID problem

Unlike linear systems' analysis, there is not a unified nonlinear analysis or approach that applies across the whole spectrum of nonlinear systems. Rather, specific groups of problems have certain approaches that can be applied based on a set of assumptions; and solutions thus achieved usually correspond to preset functional conditions. A general nonlinear dynamic mechanical system can be described by:

$$\mathbf{M}\ddot{\mathbf{q}} + \mathbf{C}_g\dot{\mathbf{q}} + \mathbf{K}_g\mathbf{q} + \mathcal{F} = \mathbf{f} \quad (5.1)$$

where \mathcal{F} is the internal nonlinear force vector resulting from nonlinear elements (springs and dampers) whose inputs are the coordinates' relative displacements and/or velocities.

The nonlinear RID problem is that of a MIMO system with at least two nonlinearities. The objective here is to identify and adapt existing analysis techniques, which can accommodate the system's 1) Rotordynamic characteristics (§3.1.4) and 2) RID models/characteristics (§3.2.1.2). With these techniques, we are interested in examining:

1. Absolute stability of equilibrium
2. Self-induced precession or limit cycles (LCs)
 - Predict existence of limit cycles or lack thereof
 - Characterise the stability of predicted limit cycles
 - Identify the parameters of stable limit cycles; i.e. amplitude and frequency

3. Nonlinear Response to external forcing and its effect on possible limit cycles.

5.2.1. Various types of nonlinearities

Nonlinear functions may arise in dynamic systems' models either because they are intrinsic to the nature of the system or because they have been deliberately introduced for a specific purpose. Because there is a vast variety of possible nonlinearities to be encountered, it is worthwhile to classify them into some general categories, with features which permit (or preclude) the application of particular analytical methods.

5.2.1.1. Nonlinear Functions unrepresentative of friction

Simple analytic functions such as powers, sinusoids and exponentials of a single variable, or products of different variables is one common category of nonlinearities. Most significantly, these functions are smooth enough to possess convergent Taylor expansions at all points. Consequently, they can be linearised, rendering the full mathematical power of linear system analysis to hand.

Bilinear nonlinearities are another important class of systems, in which the only nonlinear terms consist of state variables multiplied by input variables, and are thus the simplest possible generalisation of linear systems, being linear in the state and input separately. Symmetry, however, is not considered a feature of such nonlinearities. If a system model contains only analytic nonlinearities, it also admits the possibility of using a special type of input-output representation, in which the output is expressed as a kind of generalised power (Volterra) series containing multiple convolution integrals of products of the input variables evaluated at different times.

5.2.1.2. Nonlinear Functions utilised in representing friction

Piecewise-linear approximation of nonlinearities is a very common and important (for defining $\mathcal{L}(x)$ of damping models *p.124*) type of nonlinear function, which consists of a set of linear relations valid in different regions. Such functions are not analytic at all points, since they contain discontinuities of value or gradient, but have the advantage of equations becoming linear in any particular region, and thus solutions for different regions can be joined at the boundaries.

Symmetric SVNL Functions of this type are widely used to model the behaviour of actuating devices, the simplest of which being ideal relays; a model describing dry Coulomb friction (3.68) as well. These are continuous in value, although not in slope, but discontinuous functions may also be employed. Although, as mentioned previously, care should

be exercised when employing discontinuous approximants, they arise quite frequently and naturally in many applications.

Multi-valued nonlinear Functions (*p.116*) MVNL are used principally for modelling hysteresis, gear trains' backlash, non-ideal behaviour of relay devices, etc. Such relations consist of two or more branches, together with a prescription for switching from one to another (e.g. Masing's rule and $\mathcal{L}(x)$), so output depends on its current value as well as on the history of input. Thus, a MVNL relation is effectively infinitely-many-valued and deemed a nonlinearity with memory. From the mathematical point of view, multi-valuedness does not necessarily raise any fundamentally new difficulty. It does, however, render state-space formulations substantially more complicated, since the system now has to be represented by a combination of several (possibly infinite) different state-spaces, corresponding to the various branches of the nonlinearities. Accordingly, if state-space formulations have to be utilised, it is preferable to use an alternative description, involving state-spaces of different dimensions corresponding to sticking and slipping modes, for instance [36].

5.2.2. Overview: Nonlinear systems stability analysis

The stability theory dates back to the 19th century. Nonlinear stability theory, in particular, has its origins in the work of Lyapunov [106] and Poincaré [143]—see [71] for a historical perspective and [126] for comprehensive coverage of absolute stability analysis.

Practical exact absolute stability analysis (§A.2.3) are frequency domain techniques based on separating the overall nonlinear system $\mathcal{S}_{NL} \stackrel{s}{\supset} \{\mathcal{S}_L, \mathcal{S}_N\}$ into a LTI subsystem and a nonlinear and/or time-varying subsystem, in a feedback formulation.

Frequency domain criteria are sufficient but not necessary conditions for stability, and thus results are often conservative due to the approaches' generality and minimal utilisation of \mathcal{N} nonlinearities' characteristics [12].

Suitability of exact methods for RID problem Although it is possible to model a rotor with RID in a feedback set-up separating sub-systems: 1) RID $\mathcal{N} \stackrel{\text{def}}{=} \mathcal{S}_N$ from \mathcal{S}_L (as well as time-varying parameters) and 2) LTI rotordynamics as in §3.2.2.3, the major hindrance in finding *exact* stability analysis suited to the RID problem is the *hard* and usually *multi-valued* character of RID models \mathcal{N} . This violates the usual *sector condition* (§.A.2, *def.A.2*, *fig.A.1*) pre-requisite on all nonlinearities $\forall \mathcal{N}_{ij} \in \mathcal{N}$.

Approximate methods largely adopt the general methodology of studying nonlinear systems, as far as possible, using linear techniques.

Linearisation around some nominal operating point, if possible, is usually the first step in dealing with a nonlinear system. Assuming that deviations from this operation condition are not large in practice, linearisation may well be adequate as a basis for analysis and design over a limited range of operation. Lyapunov's linearisation method draws conclusions about the *local stability* of nonlinear \mathbf{S} around an *equilibrium* state $\hat{\mathbf{p}}$ from the stability properties of the system's linear (Jacobian) state matrix \mathbf{A}_j approximation. System dynamics are written in terms of uniformly convergent Taylor series:

$$\dot{\mathbf{p}} = \left. \frac{\partial \mathbf{F}}{\partial \mathbf{p}} \right|_{\mathbf{p}=\mathbf{0}} + \mathbf{F}_{\text{hot}}(\mathbf{p}) \approx \mathbf{A}_j \mathbf{p} \quad (5.2)$$

where \mathbf{F}_{hot} represents higher-order terms in \mathbf{p} . Lyapunov's linearisation is a formalisation of the intuition that NL \mathbf{S} should behave similarly to its linearised approximation for small range motion; and represents the *theoretical justification* of linear modelling [169].

Tondl [177] used (§.2.4.3.4) system linearisation for *absolute* stability and response analysis of a Jeffcott rotor with nonlinear (hysteretic) RID as well as geometric nonlinearities. Results were deemed erroneous, on account of possible instability at subcritical speeds, and blamed on approximations of ignoring higher order terms.

Harmonic balance approximations When exact methods are inapplicable or inconclusive, conclusions about absolute stability may be drawn from LC analysis, which in the case of RID problem is the HBM or describing function method (§.5.3.1.2, 5.3.2.2).

Frequency response is a useful tool in NL analysis, mainly because the output's harmonic content is usually dominated by a few frequencies. It is often sufficient to consider only the fundamental frequency, in which case the input-output relation is represented by a nonlinear analog of the transfer function, namely the 'describing function', which depends on the input amplitude. Although this approximation must be used with care, as it may yield erroneous results, it is capable of predicting many nonlinear effects, including LCs and jump resonance phenomena. Furthermore, it can be extended to include more frequencies, to cover other effects such as the generation of subharmonics and LC quenching. The HBM is sometimes referred to as *harmonic linearisation*, since it constitutes another example of exploiting linear techniques for NL analysis benefit.

5.2.2.1. Limit cycle analysis

Exact analysis and criteria are well established for second order systems $\mathbf{S} \in \mathbb{R}^2$, e.g. the Van der Pol oscillator (a nonlinear SDOF); most celebrated of such criteria is the Poincaré-Bendixson theorem [62]. These criteria however, do not have generalisations to systems of order higher than second $\mathbf{S} \in \mathbb{R}^{l>2}$.

Limit cycle stability (boundedness) of nonlinear SISO systems (possibly higher order $\mathbf{S}_{NL} \in \mathbb{R}^{l>2}$) that fail the frequency domain absolute stability criteria (§A.2.3) can be concluded upon using the sector condition (*def. A.2*) and characteristics of \mathbf{A}_k . \mathbf{A}_k is the state matrix of \mathbf{S}_{kL} the equivalent linear system of the nonlinear scalar system \mathbf{S}_{NL} , and is arrived at in the following manner:

- On replacing the *sector-bounded* nonlinearity $\mathcal{N}(x) \in [k_l, k_u]$ with k , the equivalent linear system \mathbf{S}_{kL} ensues: $\mathbf{S}_{NL} \Rightarrow \mathbf{S}_{kL} \Rightarrow \mathbf{A}_k$.
- Provided that $\frac{\mathcal{N}(x)}{x} \rightarrow k \begin{cases} >k_l \\ <k_u \end{cases}$ as $x \rightarrow \infty$

If \mathbf{A}_k is Hurwitz, the only possible form of instability is a stable/bounded limit cycle. This result [182] for scalar \mathbf{S}_{NL} has a multivariable generalisation [11]. There are several results available, originally by Garber [53] for SISO \mathbf{S}_{NL} that were extended for MIMO \mathbf{S}_{NL} [48], which rule out the possibility of limit cycles with certain frequencies for these systems. *Such limit cycle criteria are not compatible with the RID problem as nonlinear RID models \mathcal{N} do not satisfy the sector condition.*

Approximate methods do exist for limit cycle analysis of higher order MIMO systems $\mathbf{S} \in \mathbb{R}^{l>2}$, which is the case for all real rotor-bearing systems. There are two popular approximate methods [79] for predicting limit cycle parameters, namely: The periodic averaging method and the Quasilinearisation concept (§A.2.4.2) that is primarily applied through the describing function method [9, 12, 54, 36].

The averaging method applies to systems of form:

$$\dot{\mathbf{p}} = \epsilon \mathbf{F}(t, \mathbf{p}, \epsilon) \quad (5.3)$$

where ϵ is a *small* positive parameter and $\mathbf{F}(t, \mathbf{p}, \epsilon)$ is T -periodic and is sufficiently smooth to possess continuous second order partial derivatives with respect to its arguments \mathbf{p}, ϵ . The method approximates the solution of (5.3) by the solution of the *autonomous* averaged system (5.4) that is obtained by averaging $\mathbf{F}(t, \mathbf{p}, \epsilon)$ at $\epsilon = 0$

$$\dot{\mathbf{p}} = \epsilon \mathbf{F}_{av}(\mathbf{p}) \quad \text{where} \quad \mathbf{F}_{av}(\mathbf{p}) = \frac{1}{T} \int_0^T \mathbf{F}(\tau, \mathbf{p}, 0) d\tau \quad (5.4)$$

The requirements for using the averaging method, i.e. smoothness and the modelling with small ϵ as in (5.3), make the method inappropriate for handling the RID problem.

The describing function method (§5.3) however is well suited to the RID problem as it: 1) Can handle hard and multi-valued \mathcal{N} characteristics in MIMO \mathbf{S}_{NL} 2) Mainly targets separable systems $\{\mathbf{S}_L, \mathbf{S}_N\} \stackrel{s}{\subset} \mathbf{S}_{NL}$ and 3) Essential requirement of rotordynamic \mathbf{S}_L having high-frequency-attenuation characteristics is generally well-satisfied.

5.3. Describing Function Method for RID problem

It is strongly recommended to refer to §.A.2.4 for detailed derivations and coverage.

5.3.1. DFM suitability for RID precession and forced response

The DFM can be used in its simple first order truncation guise for the MIMO RID precession analysis. However, a suitable initial guess (IG) for solving iteratively the NL algebraic equations is needed to converge at a solution, which is derived graphically as in §.5.3.2.2. Similarly, the DFM can be used for sinusoidally forced response at subcritical speeds, with IG derived from LTI system FRFs away from resonances. The same cannot be said about forced response at supercritical speeds, when precession may well occur, and at least SSDF have to be implemented for analysis to have any hope of conclusion.

5.3.1.1. The DFM/HBM for general stable MIMO mechanical system

Sinusoidal describing functions and their resulting quasilinear (stiffness or impedance) models have been used extensively to predict the sinusoidally forced response of a *slightly nonlinear stable mechanical structures* that are described by lumped-parameter EOMs:

$$\mathbf{M}\ddot{\mathbf{q}} + \mathbf{C}_g\dot{\mathbf{q}} + \mathbf{K}_g\mathbf{q} + \mathcal{F}(\mathbf{p}) = \Re(\mathbf{f}e^{i\omega_e t}) \quad (5.5a)$$

These systems typically satisfy the frequency ‘low-pass’ characteristic, and would generally incorporate smooth and hard nonlinearities, e.g. cubic stiffness and friction damping simultaneously. Although, in principle, the DFM can be applied to NL mechanical systems exhibiting LCs, e.g. gear trains with backlash; the widely successful DFM application is concerned with absolutely stable and slightly NL mechanical structures.

The foregoing justifies the underlying assumption that: Response is periodic, if not sinusoidal, with the fundamental frequency ω_e being of predominant amplitude. Response is understood to contain super- and possibly sub-harmonics of ω_e , which are *usually*

considered negligible, and first order DFs result in quasilinear stiffnesses $\mathbb{k} \in \mathbb{K}$:

$$\mathbf{q} \approx \mathbf{q}^1 = \Re(\mathbf{q}^1 e^{i\omega_e t}) \quad (5.5b)$$

$$\mathbf{M}\ddot{\mathbf{q}} + \mathbf{C}_g \dot{\mathbf{q}} + \mathbf{K}_g \mathbf{q} \approx \Re\left((\mathbf{K}_g - \omega_e^2 \mathbf{M} + i\omega_e \mathbf{C}_g) \mathbf{q}^1 e^{i\omega_e t}\right) = \Re\left(\mathcal{S}_{(i\omega_e)} \mathbf{q}^1 e^{i\omega_e t}\right) \quad (5.5c)$$

$$\mathcal{F}(\mathbf{p}) \approx \mathcal{F}^1 \simeq \Re(\mathbb{K} \mathbf{q}^1 e^{i\omega_e t}) \quad \text{where} \quad \mathbb{K} \stackrel{\text{def}}{=} \mathbb{K}(\mathbf{q}^1) \quad (5.5d)$$

which are used to setup the following nonlinear algebraic equations:

$$\mathcal{S}_{(i\omega_e)} \mathbf{q}^1 = \mathbf{f} - \mathbb{K} \mathbf{q}^1 \quad \text{and} \quad \left(\mathcal{S}_{(i\omega_e)} + \mathbb{K}\right) \mathbf{q}^1 = \mathbf{f} \quad (5.5e)$$

for the HBM and the DFM respectively. (5.5e) are solved iteratively, using e.g. Newton-Raphson method and given an appropriate initial guess \mathbf{q}_{IG}^1 , for each ω_e . Typically:

1. At $\omega_{e:1}$ of low FRF, away from the LTI system model resonance, $\mathbf{q}_{IG}^1 \stackrel{\text{def}}{=} \mathbf{q}_{LTI}$, where it is expected that $\mathbf{q}_{NL}^1 \approx \mathbf{q}_{LTI}$, and the first frequency response $\mathbf{q}_{\omega_{e:1}}^1$ is arrived at
2. For the following frequency $\omega_{e:2}$ at small increment $\Delta\omega_e$ from $\omega_{e:1}$, $\mathbf{q}_{IG}^1 \stackrel{\text{def}}{=} \mathbf{q}_{\omega_{e:1}}^1$
3. The above steps are repeated until the whole frequency range of interest is covered.

The ‘jump resonance phenomenon’ will reveal itself on comparing the solutions of sweeping the frequency range increasingly and decreasingly, when (5.5e) will yield different *stable* solutions $\mathbf{q}_{\omega_e}^1$ for the same ω_e around resonance. It is worthy of noting that: The DFM in (5.5e) is more favoured computationally to the HBM, as it reduces system order thus converging to a solution more efficiently.

5.3.1.2. The DFM for the MIMO NL RID problem

MIMO NL RID systems have inherent characteristics that distinguish them from structures (§.5.3.1.1) normally handled by the DFM/HBM, namely:

- LC oscillations at supercritical speeds are a common recurrence with RID systems, which seldom exist separately, except possibly in the unforced isotropic stator case.
- NL RID models have *hard* characteristics, varying which affects LCs markedly
- A symmetric rotor on anisotropic bearings (3.9) introduces LTV terms of stiffness (and possibly impedance) to (5.7) leading to oscillations at 2Ω . These have to be accounted for along with RID precession oscillations at supercritical speeds.
- A typical sinusoidal xy -frame force at ω_e translates to two forces at $\omega_e - \Omega$ and $\omega_e + \Omega$ in the $\xi\eta$ -frame (3.4) and their resulting oscillations, which have to be accounted for along with those from stator anisotropy and RID precession, if existent.

- Rotor imbalance translates to static loads in the ξ - and η -directions and results in constant deflections, which render RID precession oscillations *unsymmetrical*. This necessitates the use of SBDF, which is no small feat for Masing's joints (p.119)

Notes of Caution In order to implement the DFM neatly and effectively, only single-frequency oscillations should be considered, which is not always possible or prudent.

Inherent multiple frequencies derive from orthotropic bearings, gravity sag, etc. It is tempting to analyse rotors on orthotropic bearings as isotropic twice; once with each stiffness, to conclude on stability. However, this would prove rather unwise when oscillations of several frequencies exist, due to the significantly different internal dynamics. Although this is not addressed here, it certainly should be followed upon.

LC quenching by other-frequency oscillations is frequently observed in NL systems. In the RID precession case, this might prove rather beneficial as 2Ω oscillations may be easily introduced via orthotropic bearings. When linear analysis could not explain or justify it [33], this experimentally observed favourable effect of orthotropic bearings on suppressing RID precession can be easily explained by this NL phenomenon. However, to reproduce such observations analytically, LTV terms must correspond to models' input, i.e. \mathbf{q}_r for displacement (fig.3.2) and/or $\dot{\mathbf{q}}_r$ for velocity (fig.3.3) models. Fortunately, the DFM can be used for such predictions, albeit in the MIDF guise.

Ignored super-harmonics is another important issue when considering the hardness of \mathcal{N} and the corresponding harmonic content $\sum_{m=1}^{\infty} \mathcal{F}^m(\tau)$ of its output $\mathcal{F}(\tau)$ (A.17). The ideal relay odd-symmetric SVNL representing Coulomb RID is a good simple example, because it is the building block for most NL RID models. The resulting odd super-harmonics have magnitudes $|\mathcal{F}^m| = \frac{1}{m} |\mathcal{F}^1| \forall m \in \{3,5,7,\dots\}$ (A.20). Although friction damping models are a common recurrence in the DFM for general structures, they do not necessarily have a dramatic impact on the structures's stability and behaviour. Normally, a general structure's FR characteristics would attenuate super-harmonics, so at $\frac{1}{3}$ magnitude and $3\omega_e$ the first super-harmonic is certainly negligible. However, all is not the same when considering rotor FR characteristics in the rotating frame. Other than the debate about non-minimum-phase TF characteristics (§.4.1.2.3), the transformed resonances at $-(\omega_b - \Omega)$ occur at higher frequencies and with higher magnitudes (fig. 4.9), which is a serious concern as aero-engines have wide operating speeds spectra.

LC predictions in NL feedback systems is one of the principal DFM applications. Experimentation and simulation show that NL RID can cause ω_p -periodic precession, which

is largely dominated by its fundamental frequency. The low-pass system's LTI part attenuates significantly higher harmonics $m\omega_p$ to negligible levels. Isotropic rotors' RID precession observed in both $\xi\eta$ - and xy -frames can be approximated by single frequency:

$$\mathbf{q}_r \approx \mathbf{q}_r^1 = \Re(\mathbf{q}_r^1 e^{i\omega_p t}) \Rightarrow \mathbf{q} \approx \mathbf{q}^1 = \Re(\mathbf{q}^1 e^{i(\Omega + \omega_p)t}) \quad (5.6)$$

That justifies first order \mathbb{k} (§.5.3.1.3) use in place of the NL elements \mathcal{N} of (3.75). It is assumed: LC oscillations (5.6) may exist, thus \mathcal{F}, \mathcal{N} of (3.75) are approximated as:

$$\mathcal{N} = \begin{bmatrix} \mathcal{N}_\xi(\xi) & 0 \\ 0 & \mathcal{N}_\eta(\eta) \end{bmatrix} \approx \Re \left(\begin{bmatrix} \mathbb{k}_\xi(\text{amp}(\xi^1)) & 0 \\ 0 & \mathbb{k}_\eta(\text{amp}(\eta^1)) \end{bmatrix} \mathbf{q}_r e^{i\omega_p t} \right) \quad (5.7a)$$

$$\approx \Re(\mathbb{K}(\bar{\mathbf{q}}_r) \mathbf{q}_r e^{i\omega_p t}) = \Re(\mathbb{K} \mathbf{q}_r e^{i\omega_p t})$$

↓

$$\mathcal{F} \approx \mathcal{F}^1 \simeq \Re(\mathbb{K} \mathbf{q}_r e^{i\omega_p t}) \quad (5.7b)$$

It is assumed that RID precession of the *autonomous and balanced* 2DOF isotropic rotor is adequately approximated by sinusoids, and (3.86) is approximated using (5.7) as:

$$\begin{aligned} \mathcal{S}(i\omega_p) \mathbf{q}_r(i\omega_p) &= -\mathbb{K}(\bar{\mathbf{q}}_r) \mathbf{q}_r(i\omega_p) \\ (\mathcal{S} + \mathbb{K}) \mathbf{q}_r &= 0 \quad \leftarrow \end{aligned} \quad (5.8)$$

which is pre-multiplied by FRM $\mathbf{H}_r(i\omega)$ for iterations to converge faster avoiding possible singularities on account of diagonal \mathbb{K} :

$$(\mathbf{I} + \mathbf{H}_r \mathbb{K}) \mathbf{q}_r = 0 \quad (5.9)$$

Should there be interest in accounting for imbalance, where:

$$\mathbf{f} = \Re(\mathbf{f} e^{i\Omega t}) \Rightarrow \mathbf{f}_r = \Re(\mathbf{f}_r e^{i\Omega t}) = \Re(\mathbf{f}_r) \stackrel{\text{def}}{=} \text{phased vector of constant bias} \quad (5.10)$$

results in $\xi\eta$ -frame constant deflections, the SBDF should be used for displacement macro-/micro-slip models, which dictates serious reconsideration of Masing's joints.

NL algebraic equations iterations (5.8,5.9) were solved (Matlab Optimisation Toolbox) for precession amplitude and frequency $\mathbf{q}_r \neq 0 \neq \omega_p$, using an IG of their values. This IG should be as close as possible to the final solution and is derived from graphical LC predictions of the complex SISO system (§.5.3.2.2). Eigenvalues of system (5.8,5.9) with the achieved solution provide a check for predicted precession stability, and should *ideally* yield marginally stable modes. Further eigen-analysis are carried out with amplitude (and

frequency for completeness and added reliability) perturbations of solution. If the system is absolutely stable [unstable] with positive [negative] perturbations, then the achieved solution represents a sustainable [unsustainable] precession.

Validity of solutions achieved was assessed using (Matlab Simulink) time-marching of isotropic- and orthotropic-bearings (3.86, 3.9) rotors with *ideal relay* representing Coulomb damping. Results of isotropic rotor were in excellent agreement with simulations. Furthermore, orthotropic-bearings rotor simulations showed similar precession behaviour, since there are no LTV terms associated with \mathbf{q}_r , which is the relays' input.

Forced response iterations for isotropic rotors (3.86) with SVNL and DVNL RID were carried out, after validating the iterative technique against linear RID models, which were in excellent agreement. As with the general application of the DFM (§.5.3.1.1), iterations converged successfully at subcritical speeds using IG as detailed (p.192). *However*, as speed approached critical, convergence to a solution became rather inefficient and failed totally just before it and for all higher speeds. This can be related to a jump resonance and/or the possible *coexistence* of precession at different frequency. This alters system dynamics significantly and may involve other issues e.g. LC suppression.

5.3.1.3. Characteristics of RID models' describing functions

Describing functions for RID models of §.3.2.1.2 (figs.3.2, 3.3) are discussed here.

Real DFs of SVNL RID models (fig.3.2) are used in conjunction with mobility FRFs. While Coulomb damping (ideal relay) results in a *monotonically decreasing* $\mathbb{k}_{\text{relay}}(\bar{v})$ with increased velocity amplitude $\bar{\zeta}$, the parabolic damping model results in a non-monotonic $\mathbb{k}_{\text{parab}}(\bar{v})$ having a *minimum* at some velocity ($\bar{\zeta} = 1.531\text{m/s}$ in fig.5.1). For elaboration purposes, both $\mathbb{k}_{\text{relay}}, \mathbb{k}_{\text{parab}}$ are compared to linear RID $c_i = 75\text{Ns/m}$, which causes instability at $\Omega = 800$ but not 500rad/s . As shown in §.5.3.2.2, the non-monotonicity of $\mathbb{k}_{\text{parab}}$ results in two LC predictions (fig.5.5) which are represented here by its two intersections with $\frac{-1}{\min(\Re(H_{rc}^v(i\omega)))}$ at $\Omega = 800\text{rad/s} > \Omega_c$. The $\min(\mathbb{k}_{\text{parab}})$ is what causes the second intersection to reflect an *absolutely unstable* LC, as $\mathbb{k}_{\text{parab}}$ increases thereafter.

Complex DFs of DVNL RID models (fig.3.3) are used in conjunction with receptance FRFs. For comparative elaboration, the *imaginary* linear hysteretic RID (*id*) with $\kappa = 0.025$, which causes instability at both $\Omega = 800$ and 500rad/s is plotted on fig.5.2. Also, Coulomb damping is represented by the DVNL relay with hysteresis, and results in a *purely imaginary* \mathbb{k}_{col} that decreases monotonically with amplitude \bar{X} . DVNL macro/micro-slip

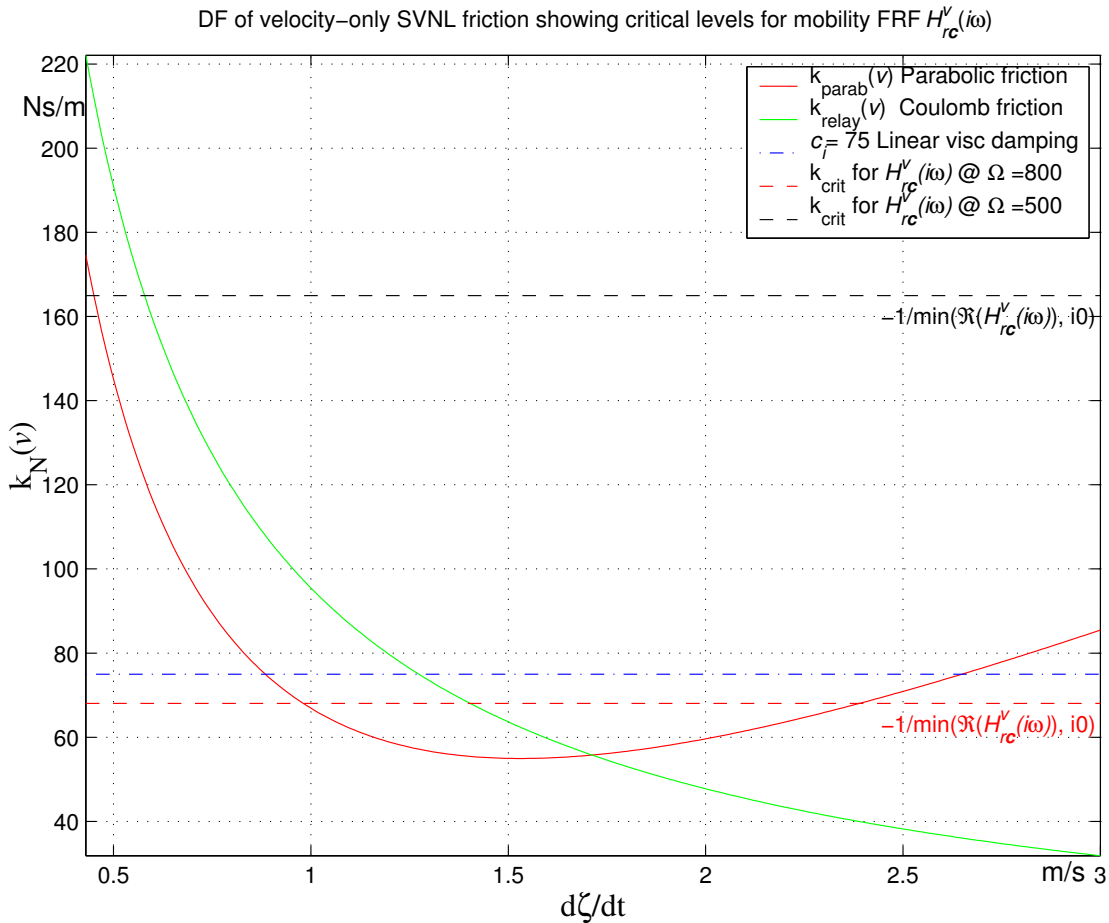


Figure 5.1.: Real DFs of SVNL friction models for mobility FRFs

RID models (*fig.3.3*) yield complex DFs (*fig.5.2*), whose imaginary parts decrease monotonically with \bar{X} as with k_{col} . However, their real parts are non-monotonic exhibiting *maxima*, as opposed to the minima of k_{parab} . Conversely with k_{parab} , this suggests the possibility of two LCs; an unstable first, and a neutrally stable second.

5.3.2. Graphical predictions with complex SISO RID problem

Throughout §.5.3.2, the parameters and numerical values of (4.2) are used.

5.3.2.1. Nyquist criterion adapted for RID instability problem

The Nyquist criterion is a simple semi-graphical method used in control engineering for the design and stability analysis of LTI SISO *real* closed-loop feedback system, by investigating the frequency response properties of the loop TF. This criterion's use in conjunction with describing functions is a common and straightforward means of investigating the existence and stability of limit cycles in a similar system with one nonlinearity. This method is adapted here to handle the RID instability problem of a *complex* SISO system

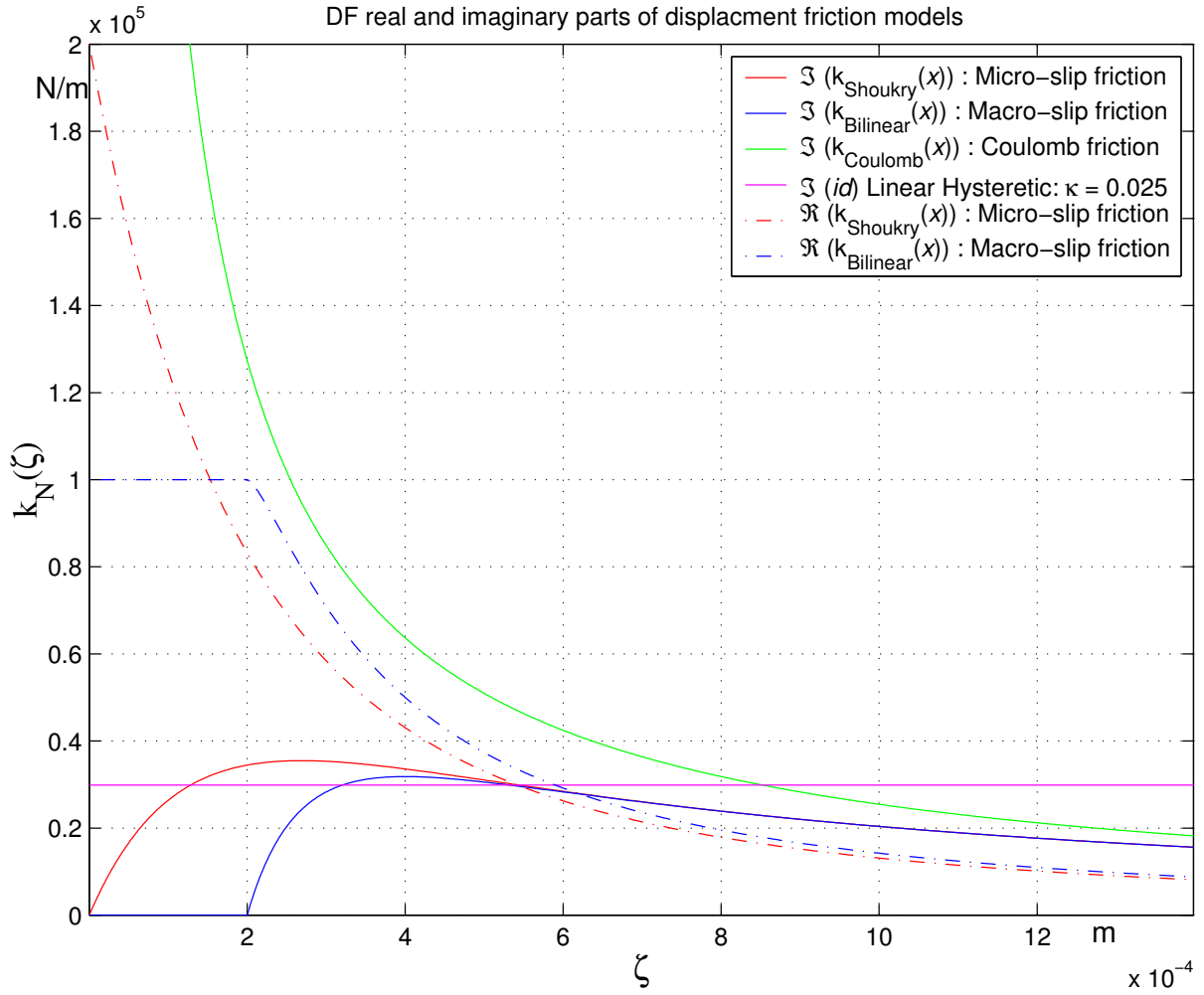


Figure 5.2.: Complex DFs of DVNL friction models for receptance FRFs

using its analytical or experimental FRF $H_c(\omega)$ prior to introducing RID, be it linear or nonlinear, in the feedback loop. This is carried out so as to:

1. Prove graphically that RID instability cannot exist at $\Omega < \Omega_c$ sub-critical speeds in the case of nonlinear RID as well as linear and particularly hysteretic RID.
2. Test for the possible existence of several limit cycles, their stability and properties.
3. Derive initial guesses (IG) for the iterative solution of real MIMO RID system.
4. Elaborate on system's relative stability or degree of instability, depending on combinations of $\frac{\text{internal}}{\text{external}}$ damping ratio and coefficients. Accordingly, the method can be used as a design tool, and can indicate means of enhancing stability if needed.
5. Extend using SBDF to predict graphically the imbalance effect on RID precession.

In order to utilise the simplicity of Nyquist criterion, it is necessary to analyse a SISO system model, hence the use of complex rotor formulations. Naturally, the multivariable

rotordynamic systems can be modelled as a fully controllable and observable SISO system as discussed on *p.109*. However:

- In order to model RID as a feedback matrix for design and stability analysis purposes, at least two outputs ξ, η need be considered/observed.
- Point TFs (3.28) have +ve real zeros $\forall \Omega > \Omega_c$ (3.57a) thus non-minimum-phase (§.4.1.2.3), rendering the following simple version of Nyquist criterion inapplicable.

For LTI MIMO systems, there are Nyquist-like criteria (3.88), however, the diagonal dominance constraint placed on $\mathbf{H}(\omega)$ renders the technique not readily amenable.

Nyquist criterion for minimum-phase TFs in real SISO feedback system whose overall (closed-loop) TF is:

$$G(s) = \frac{H(s)}{1 + H(s)B(s)} \quad (5.11)$$

If its loop TF $H(s)B(s)$ has minimum-phase characteristics, then the Nyquist criterion for minimum-phase TFs, which is a special case of the general Nyquist criterion (§A.2.2), can be applied. In such case, the criterion requires that locus Γ_{HB} —the plot of $H(s)B(s)$ corresponding to Nyquist locus Γ_s , i.e. resulting from mapping $\Gamma_s \xrightarrow{H(s)B(s)} \Gamma_{HB}$ —must not encircle the critical point ($s_c = -1 + i0$) for system (5.11) to be stable. Since the criterion was developed for real and proper TFs, only the +ve ω -axis $s : [i0 \triangleright i\infty]$ referred to as Nyquist path needs be considered, which results in the Nyquist plot of $H(i\omega)B(i\omega)$. In such case, $s_c = -1 + i0$ must lie to the left of Nyquist plot as it is traversed.

Adaptations of Nyquist criterion for the complex SISO rotordynamic system in $\xi\eta$ -frame modelled with linear RID has an overall (closed-loop) TF:

$$G_{rc}(s) = \frac{H_{rc}(s)}{1 + H_{rc}(s)B_c(s)} \quad (5.12a)$$

$$\leftrightarrow G_{rc}^d(s) = \frac{H_{rc}^d(s)}{1 + sc_i H_{rc}^d(s)} \quad \text{or} \quad G_{rc}^v(s) = \frac{H_{rc}^v(s)}{1 + c_i H_{rc}^v(s)} \quad \leftrightarrow \quad (5.12b)$$

where $H_c(s)$ is a complex TF of the rotor without RID, and $B_c(s)$ is the appropriate complex representation of linear viscous RID, all in the rotating frame. In (5.12), $G_{rc}(s)$ can be defined as the overall mobility TF $G_{rc}^v(s)$, in which case $H_c(s) \stackrel{\text{def}}{=} H_c^v(s)$ is mobility TF without RID (4.9) and accordingly, $B_c(s) \stackrel{\text{def}}{=} c_i$. Alternatively, an overall receptance TF $G_c(s) \stackrel{\text{def}}{=} G_c^d(s)$ requires $H_c(s) \stackrel{\text{def}}{=} H_c^d(s)$, which in turn dictates the suitable $B_c(s) \stackrel{\text{def}}{=} sc_i$ RID modelling. The rotordynamic TFs $H_c^d(s), H_c^v(s)$ have been shown to have minimum-phase characteristics, so the loop TFs in (5.12), namely $sc_i H_{rc}^d(s), c_i H_{rc}^v(s)$ are also minimum-phase ones. Accordingly, the *Nyquist criterion for minimum-phase* TFs is conceptually

viable as well as being an ideal choice due to its straightforwardness. However, because $H_{rc(s)}B_c(s)$ is now complex, the Nyquist path and preferably the critical point need be modified for the successful application of this *modified Nyquist criterion*:

The critical point $s_c \stackrel{\text{def}}{=} \frac{-1}{B_c(s)}$, although not a stringent requirement, is necessary to identify intersections of $\frac{-1}{k}$ and $H_{rc(i\omega)}$ when using DF (p.200) for limit cycle analysis.

FRFs used directly be they experimentally or analytically-derived (§.4.1.2.5), instead of $\Gamma_{HB(i\omega)}$. This elucidates the following significant opposites between super and subcritical speeds with direct implications on stability in each case. At $\Omega < \Omega_c$:

- $H_{rc(i\omega)}$ has +ve $i\omega$ for its quasi-circle around $(\omega_f - \Omega)$, where $s_c \stackrel{\text{def}}{=} \frac{-1}{k}$ is required.
- The mobility $H_{rc}^v(i\omega)$ has both quasi-circles around the -ve $(\omega_b - \Omega)$ and +ve $(\omega_f - \Omega)$ on the same right-hand H -plane on account of the TF's zero $o \stackrel{\text{def}}{=} s = 0$.

The Nyquist path to cover the entire $i\omega$ -axis: $\langle -i\infty \triangleright i\infty \rangle$ as in §.4.1.2.5 and §.4.2.2.2 since poles/zeros of complex TFs are generally not complex conjugates.

Adapted Nyquist criterion for absolute stability analysis of linear RID system Figs.5.3, 5.4 use the $\xi\eta$ -frame mobility $H_{rc}^v(i\omega)$ and receptance $H_{rc}^d(i\omega)$ FRFs respectively at the subcritical $\Omega = 200_{\text{rads/s}}$ and the supercritical $\Omega = 500, 800_{\text{rads/s}}$ speeds against the relevant critical points s_c . Whilst FRFs at 500/800_{rads/s} have -ve $i\omega$, the 200_{rads/s} FRFs have a +ve $i\omega$ range surrounding $\omega_f - \Omega$ and reflected in the corresponding quasi-circle.

Viscous RID: Criterion validated against instability conditions of §.4.2.1.2, which were modal-analysis-validated and exemplified in §.4.2.1.3 and figs.4.14, 4.15. Fig.5.3 shows $s_c \stackrel{\text{def}}{=} \frac{-1}{c_i}$ (-ve real) for viscous RID against mobility FRF. Obviously, $H_{rc}^v(i\omega)$ will never encircle $\frac{-1}{c_i}$ at any $\Omega < \Omega_c$ as both its quasi-circles are on the right-hand H -plane with +ve real axis. For $\Omega > \Omega_c$, absolute instability might occur depending on c_i and $\min(\Re(H_{rc}^v(i\omega)))$, which in turn depends on Ω, c, ω_{f_u} —see (4.22). Figs.4.14, 5.3 are in agreement, indicating stable operation at $\Omega = 500 > \Omega_c$ and absolute instability at $\Omega = 800 > \Omega_c$ for $c_i = c = 75$, thus validating the criterion.

Hysteretic RID: Criterion validates eigen-analysis of §.4.2.3.2. As elaborated in §.4.2.3.3, the hysteretic RID model must account for $\text{sgn}(\omega)$ as in (3.64), i.e. replaced by its complex conjugate $-id$ (3.65) when used in conjunction with -ve $i\omega$ FRF portions. Fig.5.4 shows the -ve imaginary $s_c \stackrel{\text{def}}{=} \frac{-i}{d} \equiv \frac{-1}{(id)^*}$ for two hysteretic RID $\kappa = \frac{d}{k} = 0.2$ and 0.25. The +ve imaginary $s_c \stackrel{\text{def}}{=} \frac{-1}{id}$ suitable for the +ve $i\omega$ FRF portion at $\Omega = 200_{\text{rads/s}}$ is

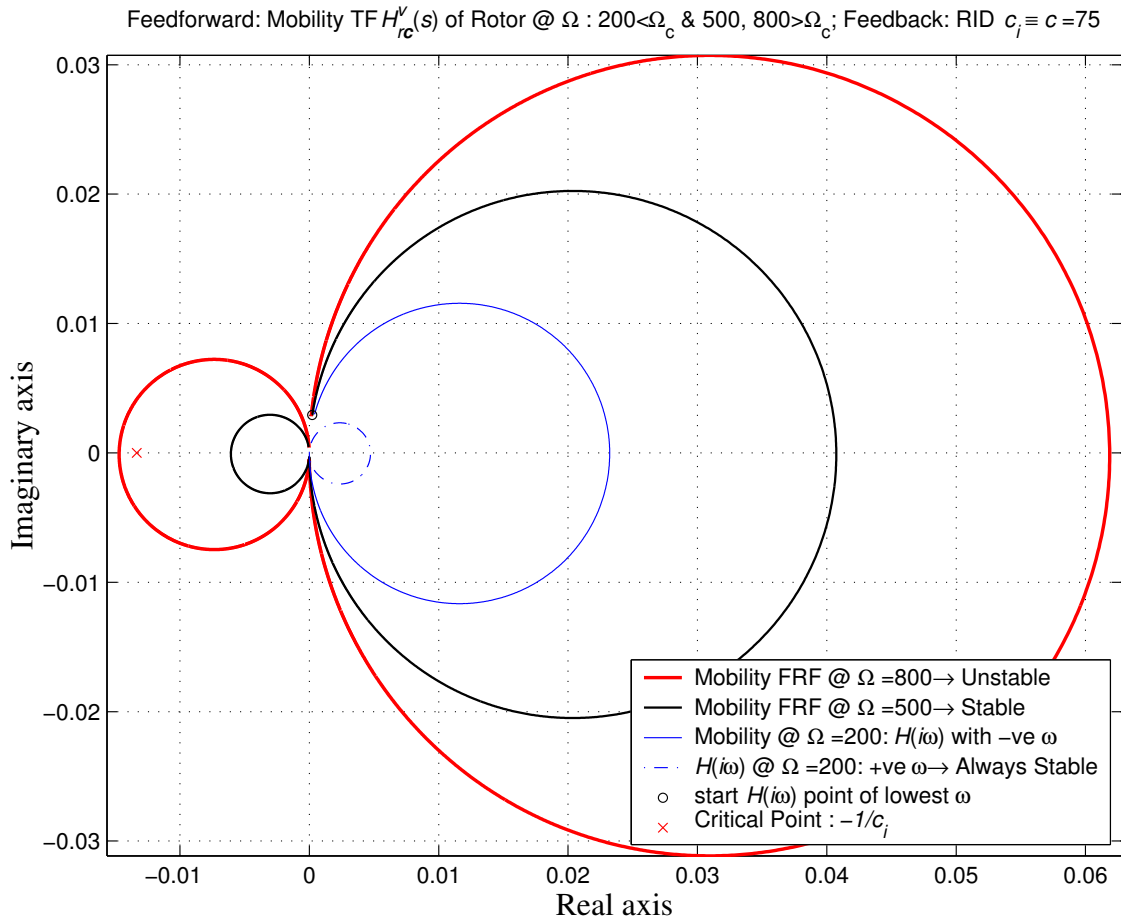


Figure 5.3.: Nyquist criterion adapted for *complex* linear viscous RID system *mobility* FRFs in $\xi\eta$ -frame: The effect of sub/supercritical speeds on instability

not shown for clarity. It is clear that $H_{rc}^d(\omega)$ at any $\Omega < \Omega_c$ will never encircle the relevant s_c as it lies in the opposite (upper/lower) half- H -plane to where the corresponding (+ve/-ve) ω FRF portion (indicated by quasi-circles) lie; as is exemplified by $\Omega = 200 < \Omega_c$. At supercritical speeds $\Omega > \Omega_c$, absolute instability might occur depending on $\frac{1}{\omega d}$ and $\min(\Im(H_{rc}^d(\omega)))$. While $\kappa = 0.25$ renders both supercritical speeds' operation unstable, $\kappa = 0.20$ renders neither unstable, of course in turn depending on Ω, c, ω_{fu} and possibly c_i if accounted for as should be in the FRFs. Figs.4.19, 5.4 are in agreement, thus validating the approach adopted for hysteretic RID in §4.2.3.2.

5.3.2.2. Extended Nyquist criterion for RID precession predictions

It is assumed here that RID precession (LC) is the only oscillation taking place in system (fig.3.5), and that it can be adequately approximated by a single-frequency sinusoid.

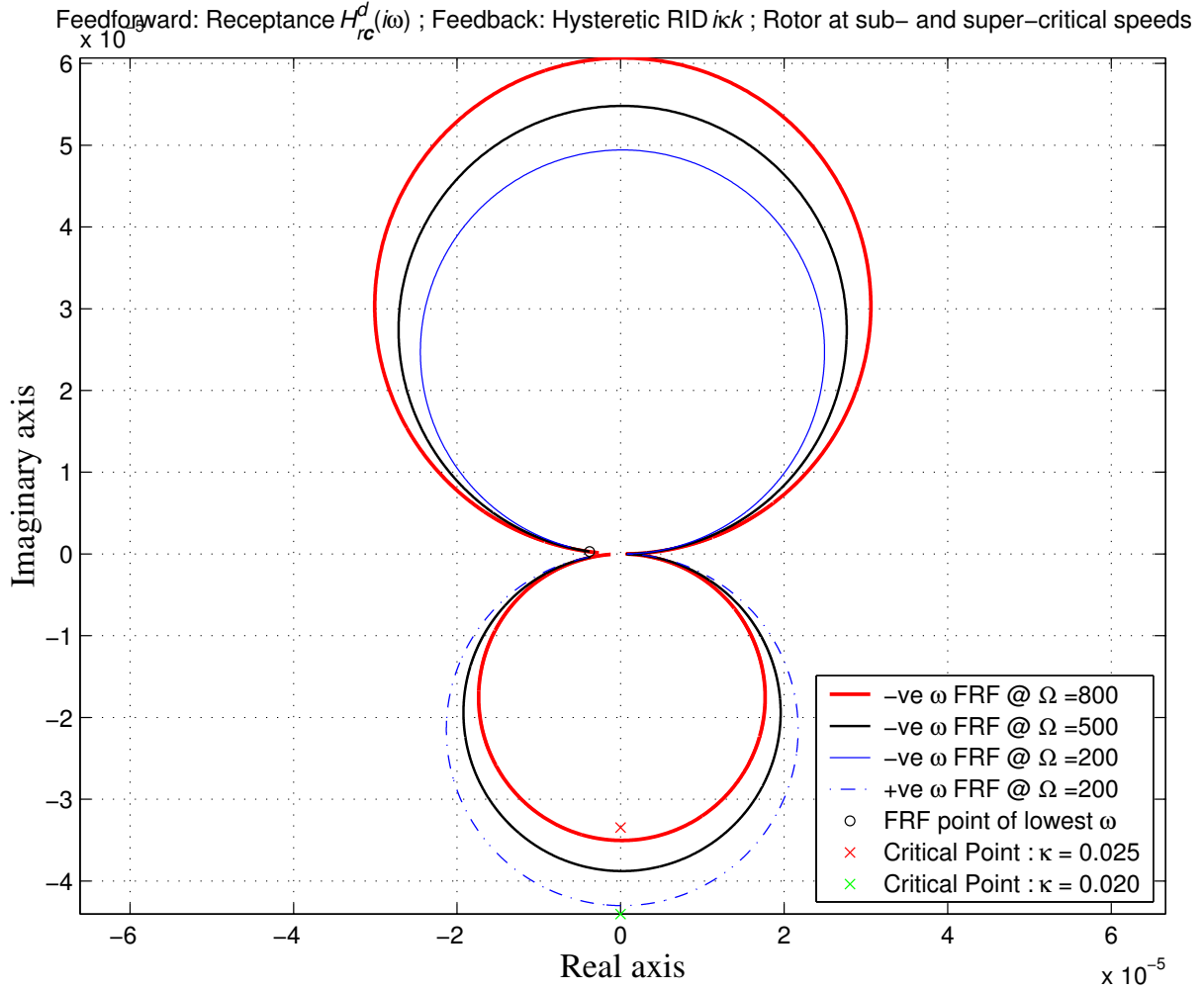


Figure 5.4.: Adapted Nyquist criterion for complex *hysteretic* RID system *receptance* FRFs in $\xi\eta$ -frame: Infeasibility of instability at subcritical speeds

DF LC predictions assume an unbiased sinusoidal input into SVNL or DVNL RID models, as would exist in a perfectly balanced unforced rotor. Precession and its stability predictions at two super-critical speeds as well as the *impossibility* of RID precession at subcritical speeds are illustrated and discussed. Only FRF quasi circles around $\omega_f - \Omega$ are shown (*figs. 5.5, 5.6*) as it will be obvious these are the only regions necessary for analysis, which explains why RID precession occurs at frequencies close to ω_f .

By (5.13, 5.14, 5.16), RID precession is predicted to exist if there is an intersection between loci $H_{rc}(i\omega)$ and $\frac{-1}{i\kappa^*}$ (for -ve ω) in the complex H -plane, both of which can be plotted independently since they depend on different variables. Precession frequency and amplitude are obtained from these independent variables' values at points of intersection. Furthermore, conclusions about precession neutral stability or instability are arrived at graphically from the direction in which $\frac{-1}{i\kappa^*}$ crosses $H_{rc}(i\omega)$ as amplitude increases, reflecting the Loeb condition [112]. Graphically, this can be rationalised by considering amplitude

perturbations. A small amplitude increase should take the predicted stable [unstable] limit cycle into the region of stable [unstable] system configuration in accordance with the normal Nyquist criterion (*figs.5.3, 5.4*). Accordingly, if $\frac{-1}{\mathbb{k}^*}$ crosses $H_{rc}(i\omega)$ from inside the quasi-circle to outside as amplitude increases, then the predicted precession is neutrally stable, otherwise it is unstable. Since the DF method is approximate, any results and conclusions arrived at from the extended Nyquist criterion should be scrutinised thoroughly. Most significantly, the actual existence of a predicted limit cycle would rely on the nature of loci intersection. If the $\frac{-1}{\mathbb{k}^*}$ and $H_{rc}(i\omega)$ loci cross perpendicularly, then it is certain the predicted LC will exist. As Loci move away from perpendicular to semi-tangential intersection, the possibility of predicted LC diminishes.

SVNL DF predictions apply to relative velocity-only RID models (*fig.3.2*), which may be used to represent spline couplings especially un-piloted ones. Input to and output of the RID SVNL model are related and approximated by their first order components:

$$\begin{aligned} \dot{\zeta}(t) &= -H_{rc}^v(s)\mathcal{F}_{\zeta}(t) \\ 1^{st} \text{ order truncated: } \bar{\zeta} \cos \omega t &= -\Re(H_{rc}^v(i\omega) \mathbb{k}(\bar{\zeta}) \bar{\zeta} e^{i\omega t}) \quad \leftrightarrow \quad (5.13) \\ \text{and rearranged as: } H_{rc}^v(i\omega) &= \frac{-1}{\mathbb{k}(\bar{\zeta})} \end{aligned}$$

SVNL RID models result in +ve real $\mathbb{k}(\bar{\zeta})$, thus locus $\frac{-1}{\mathbb{k}(\bar{\zeta})}$ will always be on the -ve real axis of the H -plane, where intersection with $H_{rc}^v(i\omega)$ may occur. Accordingly (*fig.5.5*):

- Precession can not occur at subcritical speeds, since there are no intersection points on account of FRF (both quasi-circles) existing solely in the right-half H -plane.
- At supercritical speeds, all loci intersections are perpendicular at $\min(\Re(H_{rc}^v(i\omega)))$, reflecting *imminent* LCs with $\omega \simeq \omega_f - \Omega \ \forall \Omega > \Omega_c$. When transformed to the stationary xy -frame, these LCs translate to FWD mode precession at around ω_f .

Whilst Coulomb damping models yield DFs $\mathbb{k}_{\text{relay}}(\bar{\zeta})$ that are *monotonically decreasing* with increased $\bar{\zeta}$ (see §.5.3.1.3, *fig.5.1*), the parabolic model yields *non-monotonic* $\mathbb{k}_{\text{parab}}(\bar{\zeta})$ that exhibits a *minimum* ($\min(\mathbb{k}_{\text{parab}}(\bar{\zeta}))$), which suggests an unstable LC on account of *more-than-linearly increasing* \mathbb{k} and hence force. Coulomb damping results in one neutrally stable LC prediction, as its $\frac{-1}{\mathbb{k}_{\text{relay}}(\bar{\zeta})}$ intersects once with $H_{rc}^v(i\omega)$ moving from within the FRF quasi-circle outwards, i.e. from unstable to stable regions. On the other hand, the $\frac{-1}{\mathbb{k}_{\text{parab}}(\bar{\zeta})}$ locus intersects $H_{rc}^v(i\omega)$ twice predicting two LCs, one stable and one unstable. As velocity amplitude increases from 0 to $\bar{\zeta} \leq 1.531_{\text{m/s}}$, $\frac{-1}{\mathbb{k}_{\text{parab}}(\bar{\zeta})}$ decreases along the -ve real axis, and then flips direction and increases along the -ve real axis $\forall \bar{\zeta} > 1.531_{\text{m/s}}$. The first

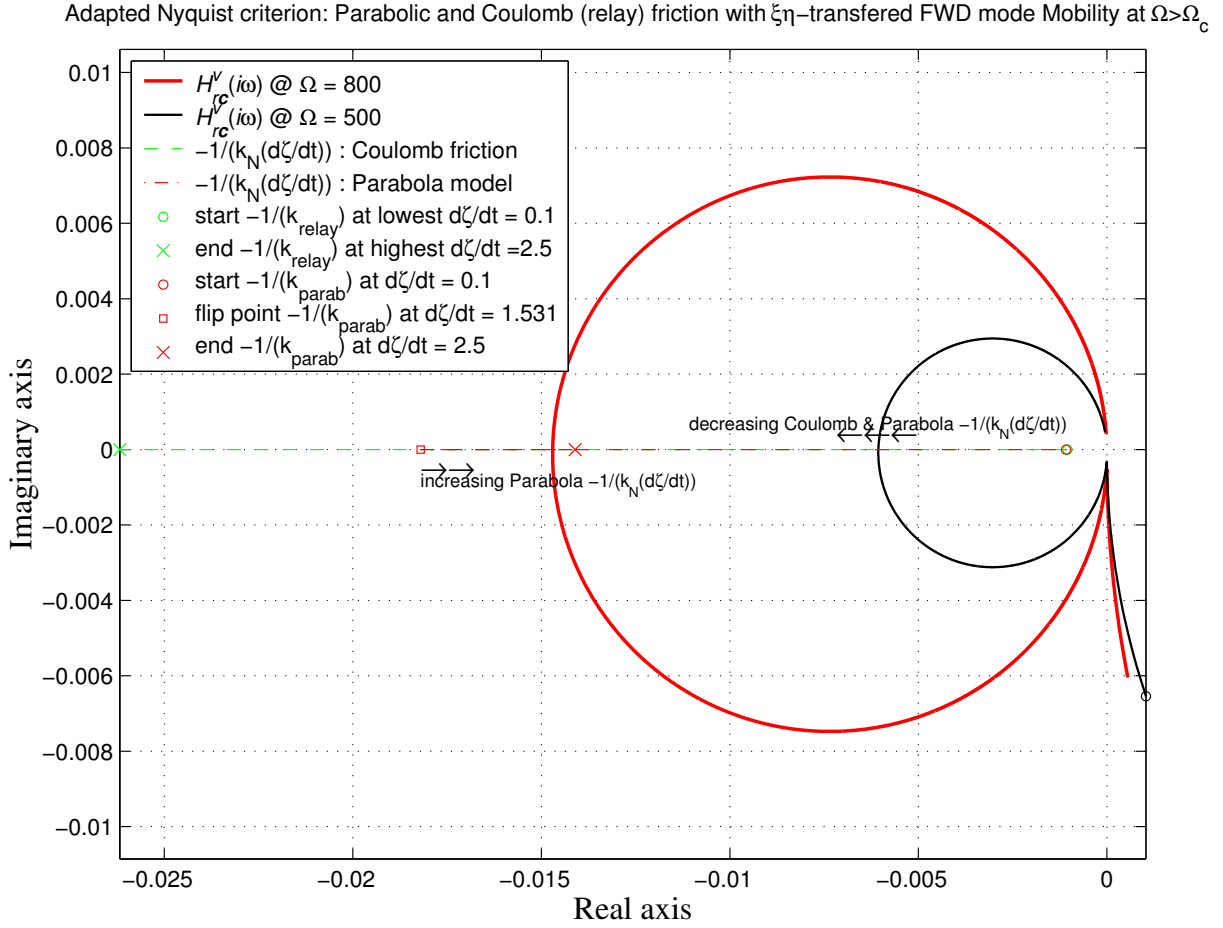


Figure 5.5.: Graphical prediction of SVNL RID precession: Bounded and unbounded

LC is viewed as neutrally stable, because a small increase in $\bar{\zeta}$ along the $\frac{-1}{k_{parab}(\bar{\zeta})}$ locus moves the system into a stable region as with Coulomb damping. However, the second LC is predicted to be unstable, because a small $\bar{\zeta}$ increase moves the system into the unstable region.

To elaborate, consider the specific k_{parab} characteristics in *fig.5.1*, which shows the important flip point ‘ $\min(k_{parab}(\bar{\zeta}))$ ’ at $\bar{\zeta} = 1.531_{m/s}$. A small $\dot{\zeta}$ perturbation (e.g. $0.1_{m/s}$) up to but below $1.531_{m/s}$, results in the first stable LC. If a significant $\dot{\zeta}$ perturbation (e.g. $1.6_{m/s}$) is experienced, the second absolutely unstable LC will kick in. This scenario is exemplified for $\Omega = 800_{rad/s}$ in *fig.5.1* where LCs intersections are easier to visualise.

DVNL DF predictions apply to displacement RID models with nonlinear stiffness and damping characteristics (*fig.3.3*), which are representative of rotors with tight couplings. Input to the DVNL model is $\zeta(t)$, which is approximated as $\zeta(t) \approx \Re(\vec{\zeta}e^{i\omega t})$. As elaborated in §.4.2.3.3 and applied to Hysteretic RID *p.201*, $k(\bar{\zeta})$ must account for $\text{sgn}(\omega)$, i.e.

5. Nonlinear analysis: Stability, Limit Cycles and Forced Response

replaced by its complex conjugate $\mathbb{k}^*(\bar{\zeta})$ when considering -ve ω :

$$\zeta(t) = -H_{rc}^d(s)\mathcal{F}_\zeta(t)$$

$$1^{st} \text{ order truncated: } \bar{\zeta} \cos \omega t = -\Re(H_{rc}^d(i\omega) \mathbb{k}(\bar{\zeta}) \bar{\zeta} e^{i\omega t}) \quad \leftrightarrow \quad (5.14)$$

$$\text{accounting for sgn } \omega : \quad H_{rc}^d(i\omega) = \frac{-1}{\mathbb{k}(\bar{\zeta})} \quad \forall +ve \omega \quad \text{and} \quad H_{rc}^d(i\omega) = \frac{-1}{\mathbb{k}^*(\bar{\zeta})} \quad \forall -ve \omega$$

Coulomb damping is a DVNL without stiffness—relay with hysteresis—with a purely imaginary \mathbb{k}_{col} , which yields identical LC predictions as the ideal relay's \mathbb{k}_{relay} in (fig.5.5), and is included in (fig.5.6) to elaborate the must of accounting for $\text{sgn}(\omega)$.

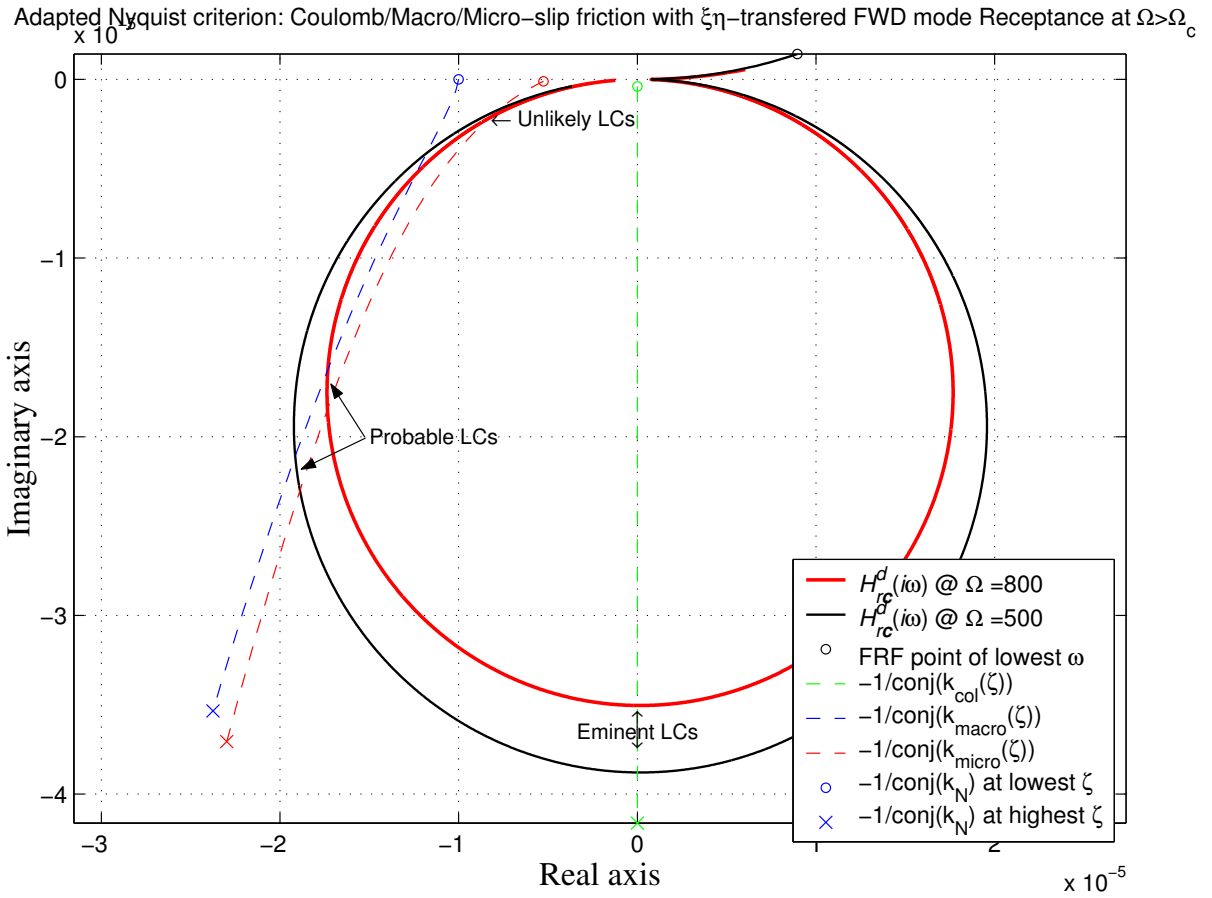


Figure 5.6.: Graphical prediction of DVNL RID precession: Probable or unlikely

Complex DFs (fig.5.2) of DVNL RID are non-monotonic, exhibiting maxima as opposed to the minima, which suggests the possibility of two LCs; an unstable first jumping to a neutrally stable second at higher $\bar{\zeta}$. However, because $\frac{-1}{\mathbb{k}^*(\bar{\zeta})}$ is now complex as opposed to purely real or imaginary, intersections with $H_{rc}^d(i\omega)$ do not occur perpendicularly. Fig.5.6 shows the first intersections to be almost tangential, thus predicted LCs' have a virtually nil probability of existence. The second set of predicted LCs' intersections has a better chance of actually existing, albeit far from imminent. Such predictions are in line with

actual tight-couplings rotors' behaviour, and thus far more realistic than SVNL or linear RID models.

SBDF predictions assume a biased LC sinusoidal input into displacement DVNL RID models, as would exist in an unforced rotor with imbalance $\bar{f}_\zeta e^{i0} \Rightarrow \bar{\zeta}_0 e^{i\psi}$. Since, imbalance has 'zero' effect on mobility $H_{rc}^v(\omega)$, LC analysis (5.13) of SVNL RID models (*fig.3.2*) is unaffected. SBDF use with extended Nyquist criterion is detailed (5.15, 5.16) but not implemented as the effect of bias $\bar{\zeta}_0$ on hysteresis-derived MVNL has to be studied carefully. Input to MVNL RID models is $\zeta(t) \approx \bar{\zeta}_0 + \Re(\bar{\zeta} e^{i\omega t})$:

$$\zeta(t) = H_{rc}^d(s)(f_\zeta - \mathcal{F}_\zeta(t)) \quad (5.15a)$$

$$\zeta_0 = \Re\left(H_{rc}^d(0)(\bar{f}_\zeta - \mathbb{k}_{0(\zeta_0, \bar{\zeta})} \zeta_0)\right) \quad , \quad \bar{\zeta} \cos \omega t = -\Re\left(H_{rc}^d(i\omega) \mathbb{k}_{(\zeta_0, \bar{\zeta})} \bar{\zeta} e^{i\omega t}\right) \quad (5.15b)$$

$$\Leftrightarrow \quad H_{rc}^d(0) = \frac{\zeta_0}{\bar{f}_\zeta - \mathbb{k}_{0(\zeta_0, \bar{\zeta})} \zeta_0} \quad \text{and} \quad H_{rc}^d(i\omega) = \frac{-1}{\mathbb{k}^*(\zeta_0, \bar{\zeta})} \quad \forall \text{-ve } i\omega \quad \Leftrightarrow \quad (5.15c)$$

The first of (5.15c) yields a functional relation between bias and sinusoidal inputs, $\zeta_0 = F(\bar{\zeta})$, which is used in conjunction with the second of (5.15c) to define:

$$\tilde{\mathbb{k}}(\bar{\zeta}) \equiv \mathbb{k}(F(\bar{\zeta}), \bar{\zeta}) \equiv \mathbb{k}(\zeta_0, \bar{\zeta}) \quad \Rightarrow \quad H_{rc}^d(i\omega) = \frac{-1}{\tilde{\mathbb{k}}^*(\bar{\zeta})} \quad \forall \text{-ve } i\omega \quad (5.16)$$

which, in turn, is used in a similar fashion to (5.14) and *fig.5.6*.

Summing up conclusions It has been shown that whirling cannot occur at $\Omega < \Omega_c$ for any of the RID models presented. However, Coulomb and the assumed parabolic RID models *always predict an imminent LC* for any remotely reasonable rotor at $\Omega > \Omega_c$, on account of an infinite $\mathbb{k}(\dot{x} = 0)$ (*fig.5.1*) due to lack of flexibility. In this case, MVNL micro-slip models portray a more realistic scenario, where whirling *might* occur depending on LTI properties, an may be avoided totally by increasing the stabilising external damping level. On the other hand, the micro-slip models used cannot account for the experimental findings of MTI (§.2.3.5) where $\Im(\mathbb{k}(x))$ assumed a curve of higher than quadratic order. The proposed parabolic RID model, when stacked in series with a stiffness as in the bilinear element (3.69), should go further to better emulate MTI results, which is planned for future investigation.

5.3.2.3. Forced response and Jump phenomenon

Assumes a sinusoidal input into displacement/velocity RID models, as would exist in a forced perfectly balanced rotor without LC $\bar{f}_\zeta e^{i\tau} \Rightarrow \bar{\zeta} e^{i(\tau+\psi_d)}, \bar{\zeta} e^{i(\tau+\psi_v)}$. Input to DVNL

5. Nonlinear analysis: Stability, Limit Cycles and Forced Response

RID models is $\zeta(t) \approx \Re(\vec{\zeta} e^{i\omega_e t})$ used with $H_{rc}^d(s)$ and $\dot{\zeta}(t) \approx \Re(\dot{\vec{\zeta}} e^{i\omega_e t})$ used with $H_{rc}^v(s)$:

$$\zeta(t) = H_{rc}^d(s)(f_{\zeta}(t) - \mathcal{F}_{\zeta}(t)) \quad \text{and} \quad \dot{\zeta}(t) = H_{rc}^v(s)(\dot{f}_{\zeta}(t) - \mathcal{F}_{\dot{\zeta}}(t)) \quad (5.17a)$$

$$\hookrightarrow (\mathcal{S}_{rc}(i\omega) + \mathbb{k}(\bar{\zeta}))\bar{\zeta} = \bar{f}_{\zeta} e^{-i\psi_d} \quad \text{and} \quad (\mathcal{V}_{rc}(i\omega) + \mathbb{k}(\bar{\zeta}))\dot{\bar{\zeta}} = \dot{\bar{f}}_{\zeta} e^{-i\psi_v} \quad \leftrightarrow \quad (5.17b)$$

Of course \mathbb{k}^* is used \forall -ve $i\omega$. In contrast with the LC scenario, frequency is now a given parameter, associated with the external force and not generated within the system. Solving the NL algebraic equations thus yields a kind of *generalised frequency response* (FR) for the closed-loop system.

6. Experimental validations

In this chapter, experimental validations for the analytical work developed are presented:

- The follower force rationale (§.2.4.2) is demonstrated using modal parameters.
- The RID micro-slip behaviour (figs.3.3, 5.2) is demonstrated through stationary and rotordynamic modal testing using damping estimates of quasi-linearised FRFs.
- The effect of *linear* RID on FWD and BWD modal (§.4.2.1.1) and FRF (fig.4.17) characteristics is demonstrated using controlled-response sine sweep modal tests.
- The stabilising effect of increased *linear* RID coefficients at subcritical speeds (fig.4.15) is demonstrated on increased subsynchronous vibration amplitudes.
- The largely speed-independent nature of RID, emphasising an appropriate mix of *linear* hysteretic and viscous RID coefficients (fig.4.19), is demonstrated.
- The CCW Nyquist plot is presented as the basis for EAST as well a demonstration of the effect of unstable right-half s -plane poles (4.6b, figs.4.16 ,4.17).

6.1. Experimental Set-up

The experimental set-up was built with two objectives in mind:

1. Fulfil the ROSTADYN project requirement of providing experimental estimates of RID, using different joints, in isolation from external damping mechanisms under rotating and non-rotating conditions. That was fairly straightforward, as described later, utilising vertical rotors of the same global geometry with different joints.
2. Allow for a flexible and versatile approach to control those variables (§.1.1.2.2) believed to influence the RID instability/whirling behaviour. Accordingly, an experimental parametric study on the effects of changing these variables was to be conducted: 1) To verify results of previous analytical research hypothesising on the effects of such variables, and 2) to observe the, as yet, unstudied thoroughly variables, with an objective to develop a model representative of their behaviour.

As such, this research would have been rather experimentally oriented. However, due to ROSTADYN partners changes of interest regarding responsibilities for experimental and analytical work, the author's efforts were redirected to concentrate more on analytical aspects of the phenomenon and cut down on the experimental investigations. The previous experimentation plan is mentioned (§.6.2.4) briefly for possible future use.

6.1.1. Safety, applicability and limitations

Safety considerations are of paramount importance while experimenting with instability phenomena of rotors since a lot of kinetic energy is involved. A means of enhancing safety could be to lower the natural frequency of the rotor, and hence the critical speeds around which we are interested in observing the rotor (with lower kinetic energy from rotation) behaviour, which eventually leads to a safer operation. On the other hand, that would have implicated a rather lengthy and slender rotor whose handling and operation would be unrealistic.

A satisfactory compromise between safety and a test rotor that is representative of a real rotor has been reached with a natural frequency and critical speeds that can be tolerated when the safety devices are operative. Orienting the rotor vertically avoided its running in bearings, which would introduce significant external damping that could mask (prevent) the RID instability at speeds close to the critical speed. This, on the other hand, introduced the limitation of not observing the rotor in a horizontal orientation or the effects of stator asymmetries. Other limitations included: the un-accounted-for friction damping introduced from fastening the quill to the rotor's upper end, and from tightening the accelerometers- and force gauge-mounted rider bearing—introducing damping from the ball bearing and from the variable friction due to the un-precise torque applied to its fastening nut—to the rotor's bottom end (fig. 6.4); and the inability to observe the rotor's free behaviour above critical speed without forcing. The latter limitation resulted from the necessity of the shaker to act as a damper due to the strong unbalance, inadequate straightness of the rotor and misalignment of the shrink fits. The strong amplitude of unbalance synchronous vibration caused by the non-precise fabrication of rotors, made the extraction of the forced subsynchronous vibration frequency component rather difficult, and hence distorted the FRF Nyquist plots above the critical speed.

6.1.2. Test pieces

The philosophy adopted for test pieces design was to be able to run a quasi-realistic rotor post critical, at around half the maximum speed of the driving motor without compromising on safety while maintaining the functionality of the friction joints in flexing.

The macro geometry of the rotors was arrived at using the FE package ANSYS and an in-house rotordynamic analysis package developed under a concurrent BRITE/EURAM project (fig. 6.1). After several trial and error attempts to comply with safety, applicability, physical constraints and market availability, the shaft diameter was selected to be 20 mm. The three discs were manufactured to the same dimensions for convenience.

The middle disc was intended to:

- Be the main source of Gyroscopic effects especially at the first bending mode, hence the shifted location from mid span.
- Place the various friction joints at a rotor station with a relatively large displacement in the first forward bending mode (fig. 6.2).

The three discs were required to:

- Provide three balancing planes for two rigid body modes and one bending mode.
- Remove the first mode shape nodes away from the central disc and friction joint by placing two heavy masses at the ends of the shaft.
- Provide for vibration monitoring stations using probes without cascading to avoid cross-talk.

According to the FEA results, the first FWD mode-shape remains virtually unchanged with increased (sub- and supercritical) speed and modal frequency. The almost speed-independent mode-shape feature is a requirement to ensure the unchanged response amplitude—resulting from applying controlled excitation to the bottom end of the rotor, while running at different speeds—at specific points along the rotor. This is especially important at the mid disc, where the friction producing joint was located. The modal properties of the flange-coupled rotor were virtually identical to those of the reference rotor (fig. 6.3).

6.1.3. Rotordynamic Test rig

Vertical rotors' operation (*fig. 6.4*) was recommended to avoid their running in bearings, thus eliminating a significant source of external damping, and lending credibility to the assumption that experimentally estimated system damping was a fair measure of RID. A flexible quill was also used to minimise damping introduced from the drive motor.

Configuration The rotor was vertically hung at its end tap (*fig. 6.3*) by a laterally-flexible quill that is driven by a brush-less DC servomotor. An electromagnetic shaker provided excitation (input), which was generally controlled and measured off a force gauge. Two accelerometers in quadrature orientation (perpendicular directions) measured response (acceleration) signal. Both excitation and response were applied and measured at the lower end of the rotor utilising a rider bearing to ensure avoiding modal nodes.

The Quill was intended to bear the rotor weight and to be the drive link between motor and rotor while maintaining sufficient lateral flexibility to de-couple the lateral vibration of the rotor from the lateral stiffness of the rig's truss and motor. Although the 0.9 mm diameter silver steel quill was strong enough to bear the rotor's weight and inertia at low acceleration, it often sheared under torsional fatigue at one of its ends where screw heads were welded. The quill diameter was increased to 1.1 mm, 1.6 mm, 2.1 mm and finally to 2.35 mm, with which systematic experimentation was carried out.

Safety Two sliding blocks, each housing a controlled variable diameter snubber bearing, were the main safety feature providing for orbit limitation and fail-safe operation. Initially, the snubber bearings were to be used as fast clamp-on devices in case of failure; and were modified, subsequently, to be used as bearings (when lubricated) while running the rotor up to the required speed and through the critical speed. That was to avoid the possible amplitude build-up—due to rigid body modes on commencement of rotation, and due to resonance at the critical speed—which could not be accommodated without sufficient external stiffness.

6.1.4. Hardware

The rig control system is PC-based, selected for its low noise power supply unit so as not to interfere with measured signals, with software developed for communication via the two serial ports and the PCI DAQ¹ cards. The control software for the main drive motor and the stepper motors controlling the snubber bearings was written in MS Qbasic for the possibility of easy alterations by other users. The motors operational parameters and commands were downloaded via the two serial ports. The use of the DSP and DAQ cards, intended for excitation signal generation and vibration monitoring respectively, was postponed in accordance with the change in research plans.

Motors and drives :

Main (drive) motor: SEM HD70 brush-less DC servomotor with resolver

¹PCI:Peripheral Component Interconnect, DAQ:Data Acquisition, DSP: Digital Signal Processing

Main motor drive & control board: HMK+ELGO 1306 servomotor amplifier

Snubber control motors: Two RS high torque/resolution stepper-motors

Stepper-motors control board: RS dual-axis stepper-motor control board

Excitation and response pick-ups

For sine sweep tests One B&K force gauge and two B&K accelerometers in perpendicular directions, were mounted on a small aluminium frame, housing a small ball bearing that was interference-fitted to the end of the rotor (fig. 6.4). The frame was prevented from rotating by the shaker's stinger which was attached to the force gauge.

Bentley Nevada capacitance probes for prospective horizontal rotor rig:

Six 11 mm dia.; 5mm Peak-Peak max. linear sensitivity : two per disk perpendicular to disc face. Intended to be in quadrature around the circumference to monitor the rigid disk (one nodal diameter) mode.

Two 8 mm Dia.; 2mm Peak-Peak max. linear sensitivity : 16 mm stagger along shaft length to avoid cross-talk. Intended to sweep monitor the lateral shaft vibration.

SOLARTRON analysers driven by ICATS software (MODAQ) :

SOLARTRON 1254: Sine Sweep with controlled response or input force

SOLARTRON 1220: for hammer testing and FFT monitoring during Sine Sweep testing

Charge amplifier GW 4 channel rack

Shakers :

LING Electronics LDS V408 22LbF 0.5" Pk-Pk

GW M20b ;virtually zero axial damping and stiffness,1.5" peak to peak: Intended for nonlinear modal properties investigations.

DAQ and DSP National Instruments cards :

DAQ AT-MIO-64E-3; 333 kHz. Sampling frequency, 32 dual ended channels, full software control (no Jumpers): For acquiring and sampling probes and transducer output.

DSP AT-DSP-2200 ; 51.2 kHz sampling frequency per channel, 256 Kwords onboard RAM: Intended for uninterrupted signal generation and Real time signal processing

Dampers Two B&K Aero-viscous dampers intended to investigate the effect asymmetric external damping when using the GW friction-less shaker.

6.2. Experimental Modal Analysis and Testing

6.2.1. Standard Modal Testing

6.2.1.1. Investigative benchmark Modal Testing

A damping-less simple beam was suspended at its first mode nodes and modal tested (hammer and sine-sweep) to:

- Gain insight into the difficulties of modal testing virtually undamped systems, e.g. reference rotor with soldered discs. Hammer testing proved to be rather tricky, especially with a hard nib to excite higher modes.
- Investigate the effect of suspension on damping estimates. The resulting FRFs along with software used yielded 0.05% hysteretic damping estimates, which were indicative of zero-damping benchmark as well as an estimate accuracy threshold.
- Investigate the differences of FRFs and modal values obtained via hammer- and sine-sweep-testing.

The TURBOMECA $\Delta 2$ rotor supplied (without blades) was examined for representative RID values and nonlinear behaviour of an actual industrial rotor. This helicopter aero-engine is built-up of five short segments, held together by Curvic couplings and a tie-bolt.

As expected, the $\Delta 2$ rotor exhibited both cyclic asymmetry and relatively low linear damping (0.45% hysteretic). Damping and asymmetry were least at the design tension of the tie bolt. On loosening the tie bolt, asymmetry was more pronounced and the rotor exhibited a typical friction damping behaviour.

6.2.1.2. Reference test rotor

The rotor, with un-soldered shrink-fitted discs (*fig. 6.3*) was examined whilst stationary:

Analytical modal characteristics validated The rotor was suspended horizontally by long elastics at its first bending mode nodes. Hammer-testing showed it had the modal frequencies and shapes it was designed for (*figs. 6.1, 6.2, 6.3, 6.5*). It also presented the reference rotor as very lightly damped (0.1% hysteretic); since hammering did not exercise the shrink fit's nonlinear damping properly.

In vertical orientation frequencies of the reference rotor have virtually unchanged when suspended by the quill at its upper end (*fig. 6.4*). Although the rotor upper end was close to being an anti-node for all modes, the quill's high lateral flexibility de-coupled the rotor modes from the rig successfully.

Nonlinear RID characteristics of test rotors (reference and flange-coupled disc rotor—*fig. 6.3*) were examined, while hanging by the quill at their upper end, using controlled force and response sine sweeps applied at their bottom end (*fig. 6.4*). A very fine frequency step (0.01 Hz.) was needed to have at least 5 FRF points between half power points, since the test rotors were very lightly damped.

Modal tests with controlled response and with controlled force revealed the nonlinear nature of the rotor's damping. The equivalent damping estimate increased with increased vibration amplitude (*fig. 6.6*) and hence was concluded to be resulting from joint friction (the shrink-fit). This is typical micro-slip friction behaviour (*figs. 3.3, 5.2*), where damping estimates increase with increased amplitude, up to a peak and then decrease on further increase of amplitude, depending on the regions of micro/macro slip. The equivalent damping estimate, in the reference rotor, could never be made to reach its peak value and drop down again on increased amplitude. This is because the vibration amplitude could not be increased beyond the shaker's 0.5 inch Pk-Pk; a value that is not excessive for a long, unrestrained structure as a hanging rotor. Damping estimates for both the reference and flange-coupled rotors were very close which led to the conclusion that the major source of rotor damping was the disc shrink-fit. Rotor joints' micro-slip friction behaviour has been demonstrated previously (§.2.3.5) [185] using static and dynamic (modal) tests on non-rotating rotors.

6.2.2. Rotordynamic Modal Testing

Testing rotating rotors validated FE model results at various speeds (*fig. 6.5*), and corroborated modal (§.4.1.1.2, *fig. 4.4*) and FRF (§.4.1.2.1, *fig. 4.8*) characteristics.

6.2.2.1. Friction RID effect on experimentally acquired modal characteristics

FRFs exhibited the expected gyroscopic split as separated 1st FWD and BWD modes of increasing and decreasing resonant frequency respectively (*fig. 6.5*). However, no beating, sub- or super-harmonics of forcing frequency were observed during experimentation.

The RID follower force effect Contrary to the case of rotor void of RID (§.4.1.1.2, *fig. 4.4*), modal damping estimates increased for the BWD mode and decreased for the FWD one as speed was increased, albeit mildly, while the reverse was true for receptance

peak at both modes. This is in tandem with the findings of (§.4.2) demonstrating the effect of *linear* RID on FWD and BWD modal (§.4.2.1.1) and FRF (*fig.4.17*) characteristics. These modal constant and damping estimates are considered measures of the *follower force* increased strength with speed; counteracting external damping for FWD modes and complementing it for BWD modes (§.2.4.2) at sub-critical speeds.

The nonlinear character of friction RID corroborates linear predictions Increased damping with response-controlled amplitude was exhibited in *both* BWD and FWD modes. Increased amplitude of quasi-linearised FRFs at subcritical speeds resulted in an increased equivalent hysteretic damping $\Im(\mathbb{k}_{\text{micro}})$. This reflects the stabilising effect of increased *linear* RID coefficients at subcritical speeds (*fig.4.15*), demonstrated here on increased subsynchronous vibration amplitudes. The largely speed-independent nature of RID, further emphasised by modal damping results of (*fig.6.9*), dictates an appropriate mix of hysteretic and viscous RID coefficients (*fig.4.19*), resulting in qualitative agreement with eigenvalues when hysteretic RID κ is increased.

6.2.2.2. Modal tests at supercritical speeds

FRFs at supercritical speeds exhibited a counter-clockwise (CCW) Nyquist plot, which was loosely termed *negative damping*, explained by (4.6) §.4.1.2.1, exemplified (§.4.2.2.3, *fig.4.18*) and was the basis for EAST (§.4.3). However, no subsynchronous precession (LC) was observed, which is related to the forcing frequency LC-quenching (§.5.1.2.2).

The CCW Nyquist plot was discovered on examining its sense of direction—tracing indices of FRF points, evaluated at increasing frequency increments—which turned out to be CCW (*fig.6.7*). Examining the real and imaginary parts of acquired FRFs (*fig.6.8*), all with similar quasi even-symmetric real parts but with positive imaginary parts at sub-critical speeds and negative imaginary parts at supercritical speeds, confirmed the CCW Nyquist plots representing unstable modes.

The validity of negative damping reference to a CCW Nyquist plot is based on the hypothetical SDOF EOM with a negative damping coefficient (4.27). This EOM will result in a dynamic stiffness with negative imaginary (quadrature stiffness) term, i.e. response (output) leads force (input), which does not exist naturally in a stand-alone physical system. The resulting receptance FRF will thus have the usual even-symmetric real part and a positive (as opposed to the usual negative) odd-symmetric imaginary part, and will trace a CCW polar plot, which applies equally to the ω $[-\omega^2]$ phased mobility [accelerance]. Negative damping is hypothetical on two counts: 1) Barring perpetual devices, by definition, damping is never negative; 2) Negative damping implies an unstable system, of which an FRF cannot not be experimentally acquired.

Physical interpretation and explanation of CCW Nyquist plot Experimentally, a measured FRF (*figs. 6.7, 6.8*) exhibiting a CCW Nyquist plot simply means that the system measured (first FWD mode) has more energy than that of its input (shaker excitation). This extra energy is postulated to flow from the shaft rotation (rigid-body-mode) into its first FWD mode. This scenario reflects an unstable system whose transfer function has at least one pole in the right-half s -plane, thus its FRF should have been impossible to measure experimentally, yet has been obtained successfully. The whole test rig (including the truss, motor and shaker, as well as the rotating rotor) was clearly stable. However, as elucidated in (§.4.3.2, 4.3.4 and *figs. 4.21, 4.22*), the FRF acquired was that of the de-coupled rotor subsystem, since the quill isolated the rotor from the whole structure, and the excitation and response measured were those of the isolated rotor. The rotor subsystem contributed a destabilising influence, that was overwhelmed by the stabilising external damping from the heavily damped shaker. The CCW Nyquist plot proved the possibility of unbounded instability due to RID, had there been no added external damping from the shaker, but could not characterise the instability adequately on account of complex nonlinear dynamics.

6.2.2.3. Follower force represented by modal values at different speeds

Caution when using traditional modal analysis for said representation should be exercised in conjunction with rotating rotors as the mode shapes-dependant modal constants are consequently speed-dependent. As soon as the rotor rotates, the modal constant is about halved between the FWD and BWD modes; a reasonable consequence of the zero-speed bending mode being the summation of the zero-speed FWD and BWD modes.

Although our FEA results showed that the first bending mode shapes at different speeds (*fig. 6.2*) are virtually identical, modal constants of FWD modes increased minimally, while those of BWD modes decreased notably on increasing subcritical speeds well below critical. Accordingly, the summation of modal constants of both FWD and BWD modes at one speed keeps decreasing, with increased speed, from the zero-speed modal constant. We can adopt the foregoing rationale of the destabilising [stabilising] effect of RID on FWD [BWD] modes, along with the FEA results, so as to rationalise the contrary-to-standard behaviour of the experimentally acquired FRFs.

The decreasing modal constant of the first BWD mode of decreasing frequency with increased speed, which is expected to have increasing receptance, is postulated to be the result of the increased stabilising RID effect. The opposite happens for FWD modes which ought to have a decreasing receptance with increased speed, yet their modal constant is virtually invariant at speeds well below the first critical. Furthermore, the FWD modal constant increased significantly on approaching the critical speed, and more dramatically

at supercritical speeds. Further insight into modal constant changes with speed is required before a concrete method for quantifying the follower force destabilising strength is reached.

6.2.3. Systematic experimentation

Some of the relevant observations from the systematic experimentation conducted at Imperial College (1994-97), are described briefly here. The ROSTADYN team at Imperial College carried out modal tests on both the actual built-up $\Delta 2$ turboshaft rotor and several simpler test specimens representing some of the components on an industrial rotor, e.g. shrink fits, flanged couplings and a Curvic coupling.

6.2.3.1. Standard modal tests on stationary test rotors

These were in general agreement with those of MTI (§.2.3.5) [185]. Curvic couplings produced very low damping coefficients. These were practically amplitude-independent when the coupling halves were properly mated and fastened with their high tension Tie bolt, which is analogous to the TURBOMECA $\Delta 2$ rotor. Shrink fits produced relatively higher damping estimates in comparison to Curvic and flanged couplings, particularly at higher amplitudes. When the shrink-fitted discs were soldered on the shafts, the damping level dropped to around 0.015% hysteretic (about 10% of its original value), and was fairly linear.

6.2.3.2. Rotordynamic modal tests

These showed a systematic decrease [increase] of damping estimates and increase [decrease] of resonant amplitude for FWD [BWD] modes with increased speed (*fig. 6.5*). This trend was more pronounced in the case of the shrink-fitted disc, which exhibited the CCW Nyquist plot at 2300 rpm, ≈ 500 rpm above critical. The RID destabilising effect generally grew with speed, with receptance and damping values serving as its measures, and would overcome the external damping from the shaker leading to total instability of the system.

6.2.3.3. Reservations on experimental results

Experimental results acquired by the ROSTADYN team ought to be considered with several reservations in mind, primarily due to the less-than-satisfactory test rotors fabrication. Accordingly, the speed-dependence/-independence of damping estimates for the shrink-fitted and Curvic-coupled rotors, are to be considered in a trend-observing manner. Furthermore, analytical limitations of software used, which was not suitable for analysing

very lightly-damped structures that might be unstable, yielded inconsistent modal parameters at supercritical speeds.

Imperfect fabrication of test pieces The test pieces used were sourced from tubes/bars stock suppliers, and fabricated at Imperial workshops:

- Discs cut-out and shrink-fitted or solder-welded onto the shafts (bars) supplied
- Tie-bolts holding the two part-shafts (tubes), each with one mating-part of the coupling soldered on—Curvic coupling parts were manufactured at Turbomeca.

Imperial workshops are not specialised in precision shrink-fits and solders of discs on shafts; this being a rather intricate procedure that is important to:

- Minimise force and moment imbalances resulting from geometric (let alone mass) off-centring and askew discs (not in a plane perpendicular) with shaft axis.
- Avoid any shaft distortion due to cooling and/or heating
- Ensure proper and uniform interference of the joint with the shaft

The above factors influence RID instability behaviour rather seriously, and should be as enforced as possible for successful parametric experimentation, which was not the case.

The dominant imbalance vibration component speeds just above critical, resulted in distorted Nyquist plots. Improper fabrication of the Curvic-coupled rotor emphasised the unfavourable effects of lack of above factors strongly. This first rotor could not be run safely at a supercritical speeds, and displayed severe instability destroying the rotor, the shaker, the snubber bearings of safety devices and even the drive motor was affected. Improper fabrication is also *the reason why the second Curvic-coupled rotor could not be tested super-critically (fig. 6.9)*.

Improper shrink-fits There was no control on, or estimate of the amount of interference between the shaft and the shrunk-on discs, or its repeatability with other shrunk-on discs. Indeed, while experimenting with the rotating flange-coupled rotor, the lower (short) shaft part of the rotor fell off, disconnecting from the part of the flange coupling that was shrunk-fitted onto it.

The cooled discs had to be fitted rather quickly to specified points on the length of the shaft, which left no time for adjusting precisely the plane of the disc to be orthogonal to the shaft axis. This not only resulted in moment unbalance, but also, resulted in the non-uniform interference of the joint along its 20 mm of length, which impacts significantly on macro/microslip characteristics. As for flanges-coupled two-shaft rotors, the flanges' planes' non-orthogonality yielded a bent rotor with a slope discontinuity at the coupling.

Improper soldering Soldering discs onto shafts solved some of the shortcomings of shrink-fits like the non-uniformity of interference and joint looseness, along with eliminating the shrink-fits as a source of friction damping, hence allowing for the study of the other friction sources. Soldering also introduced a different set of shortcomings such as: 1) Heat effect on shafts' straightness, and 2) Scruffy solder finish at joint interface with shaft contributing to imbalance, asymmetry, and decentred askew discs. In order for the solder to overcome the problem of non-uniform interference, the disc had to be bored at the centre to a diameter that is wider than the shaft diameter so as to allow the solder to flow all the way through. Centring the disc—without necessary jigs—and keeping it orthogonal to the shaft axis was a difficult task to achieve. The result of this exercise was a bent Curvic coupling rotor with a slope discontinuity at the coupling.

Bent rotors Other than the aforementioned causes of a bent rotor, the following also contributed to the lack of straightness of the shaft. The tie-bolt used with the Curvic coupling rotor, to keep its two parts together, was tensioned by turning the nut at its end. The tension in the bolt was estimated based on Young's modulus and the pitch of the thread on the bolt. The tension in the bolt was varied by varying the number of turns of the nut. This means of tension estimation is rather rough and it is believed that a higher bolt tension than the cylindrical shaft could withstand was achieved, with the result of buckling the cylindrical shaft.

The shafts used were circular bars sourced from bars' stock supplier, thus not well suited for rotordynamic instability studies. They were simply not straight enough, especially when considering the distorting effect of cutting long bar stocks (20mm dia.) to lengths of about 800 mm.

Software limitations The software used (MODAQ) to control the FRA (SOLARTRON 1254) and acquire the experimental data (accelerance and phase angle), was well suited for the application. The software used to analyse the acquired experimental data (MODENT & MODENT NL), although highly specialised and suited for the experimental modal analysis of most structures, was not well suited for the application because of:

Very lightly damped rotors Using any available experimental modal analysis package would have not been well suited for the estimation of the rotors modal damping; where the margin of error in the estimate may well be around 50%. This is because, even with a very fine frequency step of 0.01 Hz., there could be a maximum of five FRF points between and including the half-power points. This renders the estimation procedure very dependent on the analyst's choice of points to fit a circle through so as to acquire estimates modal parameters.

Software not prepared to deal with a CCW Nyquist plot hence the circle fitted to the Nyquist plot will be, literally, far removed from the measured points, resulting in modal estimates that are, probably, not very representative of the vibration characteristics. Minor alterations to the software can solve this problem.

6.2.4. Future plan for flexible experimentation

Although the experimental work covered in this chapter demonstrated various aspects of the RID instability phenomenon, the work plan was less than rigorous with some shortcomings, e.g. fabrication inadequacies; and it fell short of examining numerous aspects, e.g.: anisotropic bearings effect on suppressing precession, as well as the effect of other system parameters. This calls for a flexible experimental programme, which replicates the instability behaviour (§.1.1.2.1); and allows for investigating the numerous parameters (§.1.1.2.2) affecting it, as well as implementing either linearisation/stabilisation with fast modal control algorithms derived from geometric (Clifford) algebra.

The intent is to start with observing parameters influencing RID whirling, whilst isolated from external damping using non-contacting excitation/measurement and develop a model for it. Close experimental scrutiny of free- and various forced-response levels whilst controlling those variables believed to influence RID and its effects precession, would have portrayed adequately the different mechanisms behaviour. Suitable RID models would then be adapted, compared and validated for representative response prediction against experimental results, using both frequency and time domain analysis.

Vibration monitoring would be via sets of inductance probes positioned at different shaft stations (initially the discs)—in at least three non perpendicular directions in the plane perpendicular to the rotor axis—to observe the stations' orbits. A sliding staggered set of probes, or alternatively, a Laser Doppler Vibrometer would be used to scan the shaft under stationary or stable rotation tests, so as to extract the mode shape and hence, the amplitude of vibration and bending moment at the joint. Monitoring would be in a range of speeds extending from below the first to above the second critical speeds.

Excitation and level control would be initially from the high-amplitude friction-less shaker to investigate the character of nonlinear friction damping. Later, Active Magnetic Bearings (AMBs) would have been used not only for excitation but also for controlling some of the variables mentioned previously. AMBs provide the capability of software controlling the input force and bearing stiffness and damping along with vibration response. As such nonlinear and more importantly rotating forces can be applied to the rotor along with studying the effects of asymmetric nonlinear support properties on insta-

6. *Experimental validations*

bility with minimum effort and no hardware alteration. This could have been very useful in simulating the effect of rotating damping forces that are generated in a flexing rotating rotor hence separating the various effects resulting from the uncontrollable true RID. That should enable the proper validation of the models by representing isolated damping mechanisms rather than observing the collective effect of all operative damping mechanisms. Despite the obvious advantages of using AMBs, their price can be prohibitive (£50,000 / pair).

Avoidance of shrink-fit imperfections Care should be exercised so as to avoid such imperfections by not using a shrink-fit for interference. Rather, a circular wedge whose clamping force on the shaft can be varied continuously using a threaded ring, is to be used instead.

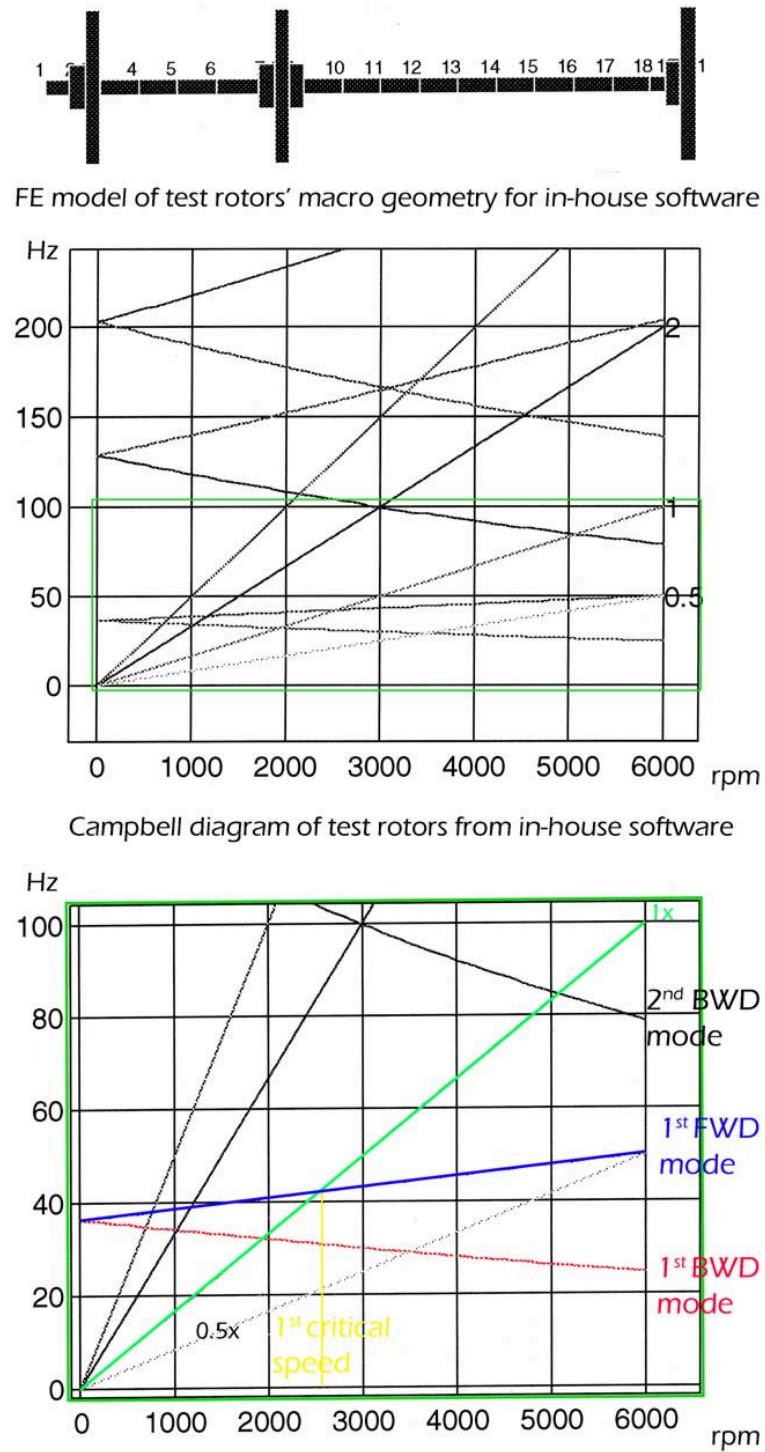


Figure 6.1.: FE model and Campbell diagram of the test rotors' macro geometry

6. Experimental validations

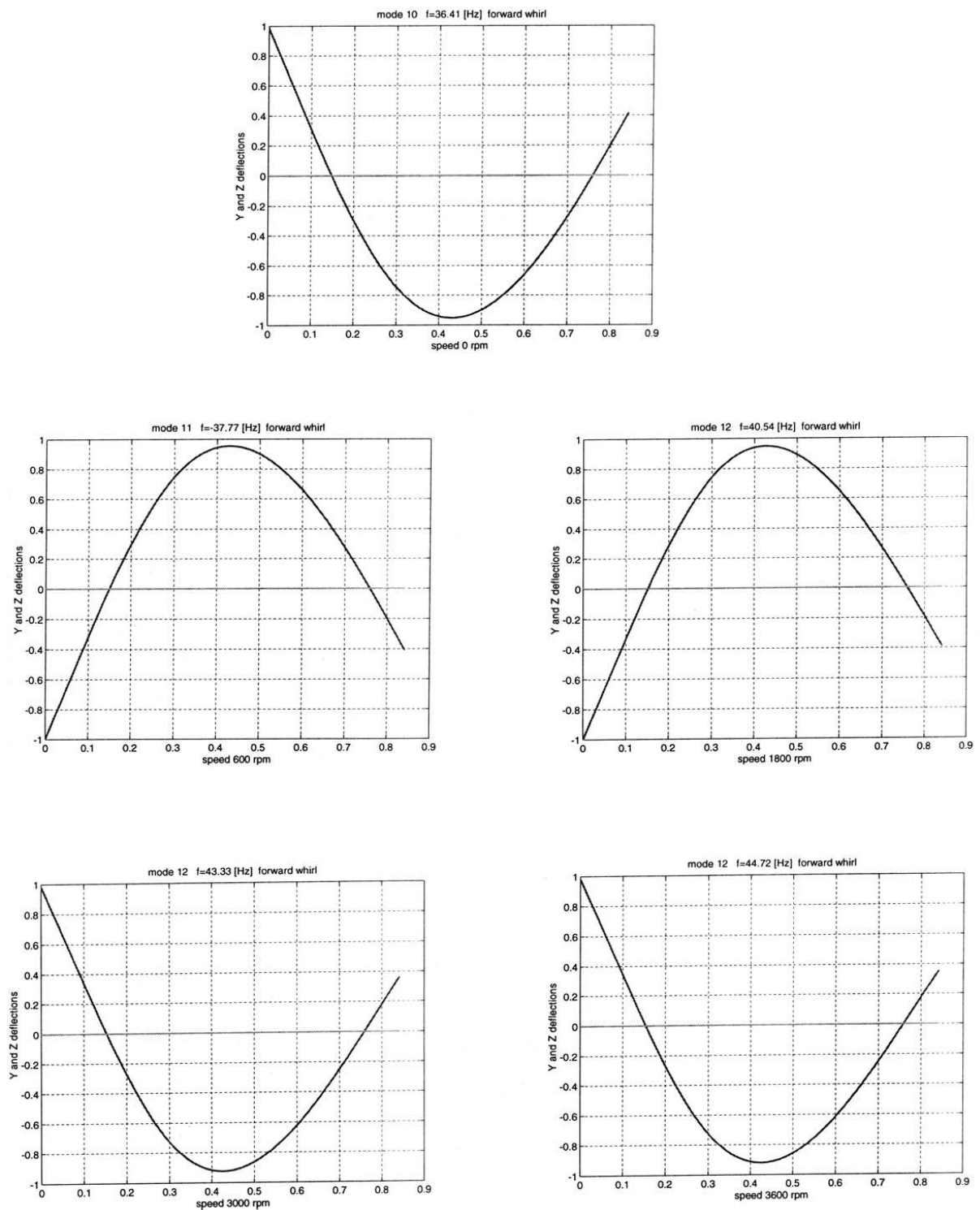


Figure 6.2.: 1st FWD Mode shape and frequency of reference rotor at various speeds: 0, 600, 1800, 3000, 3600 rpm. Modes' ID numbers may vary slightly for each analysis

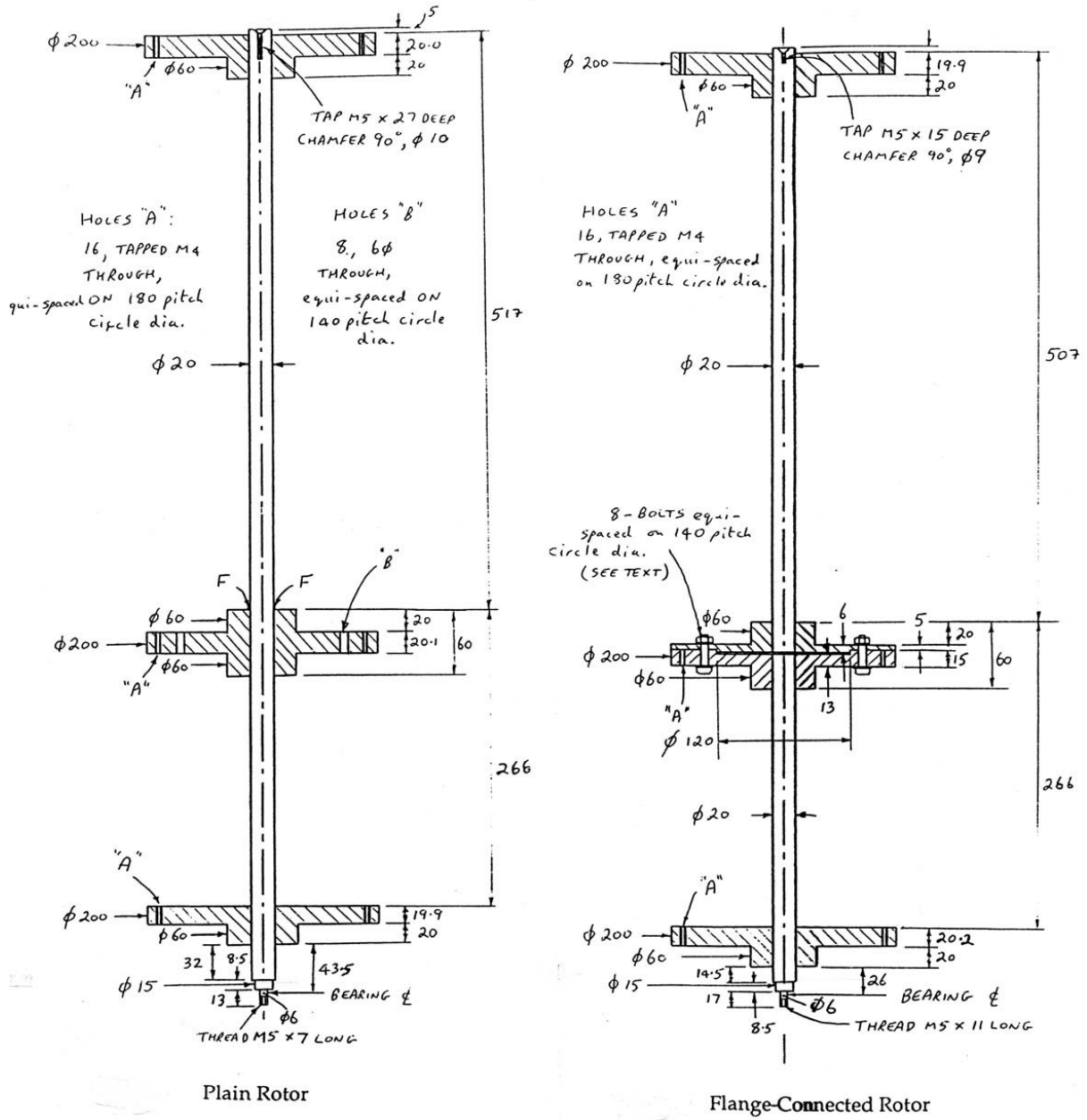


Figure 6.3.: Plain and flange-coupled test rotors

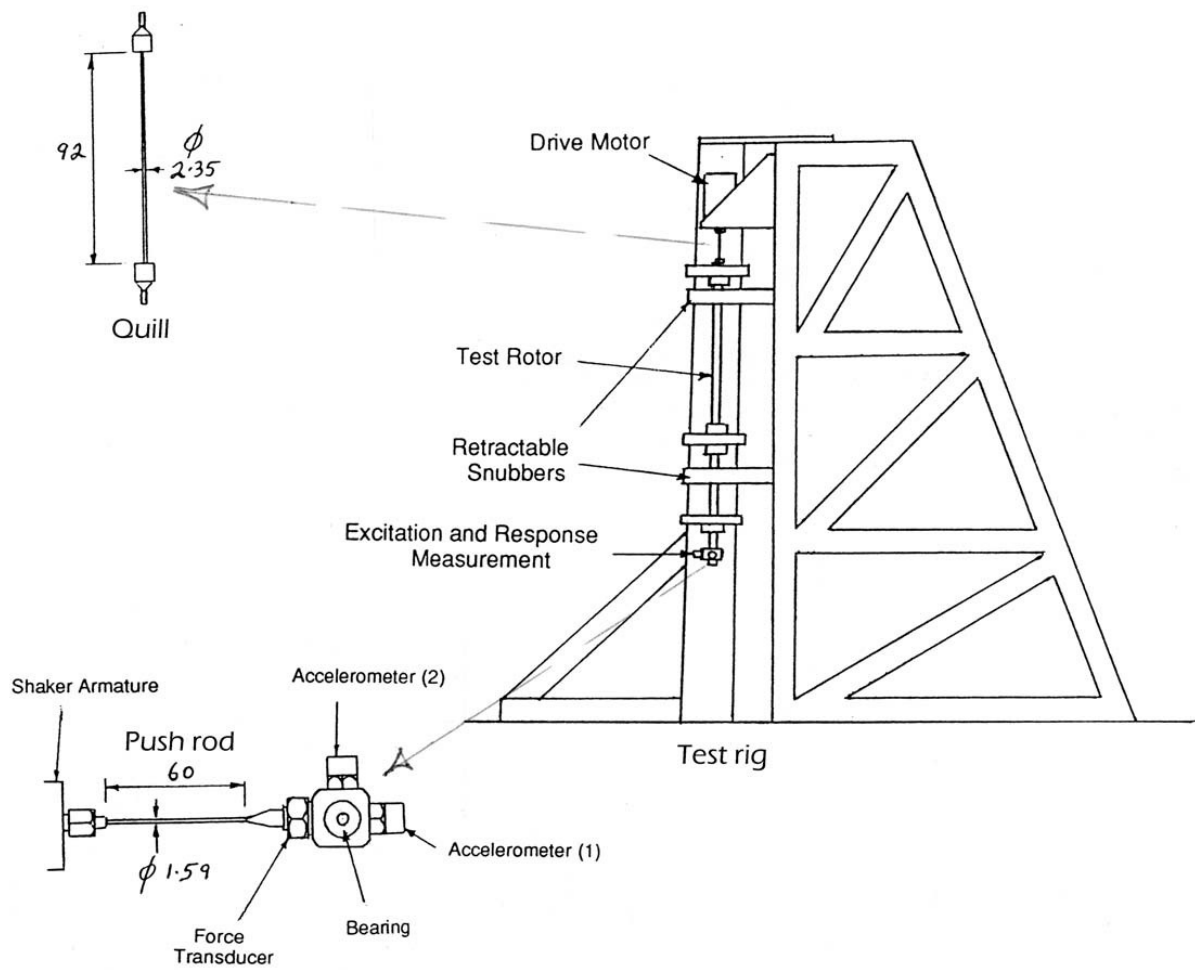


Figure 6.4.: Test rig, quill and rider bearing

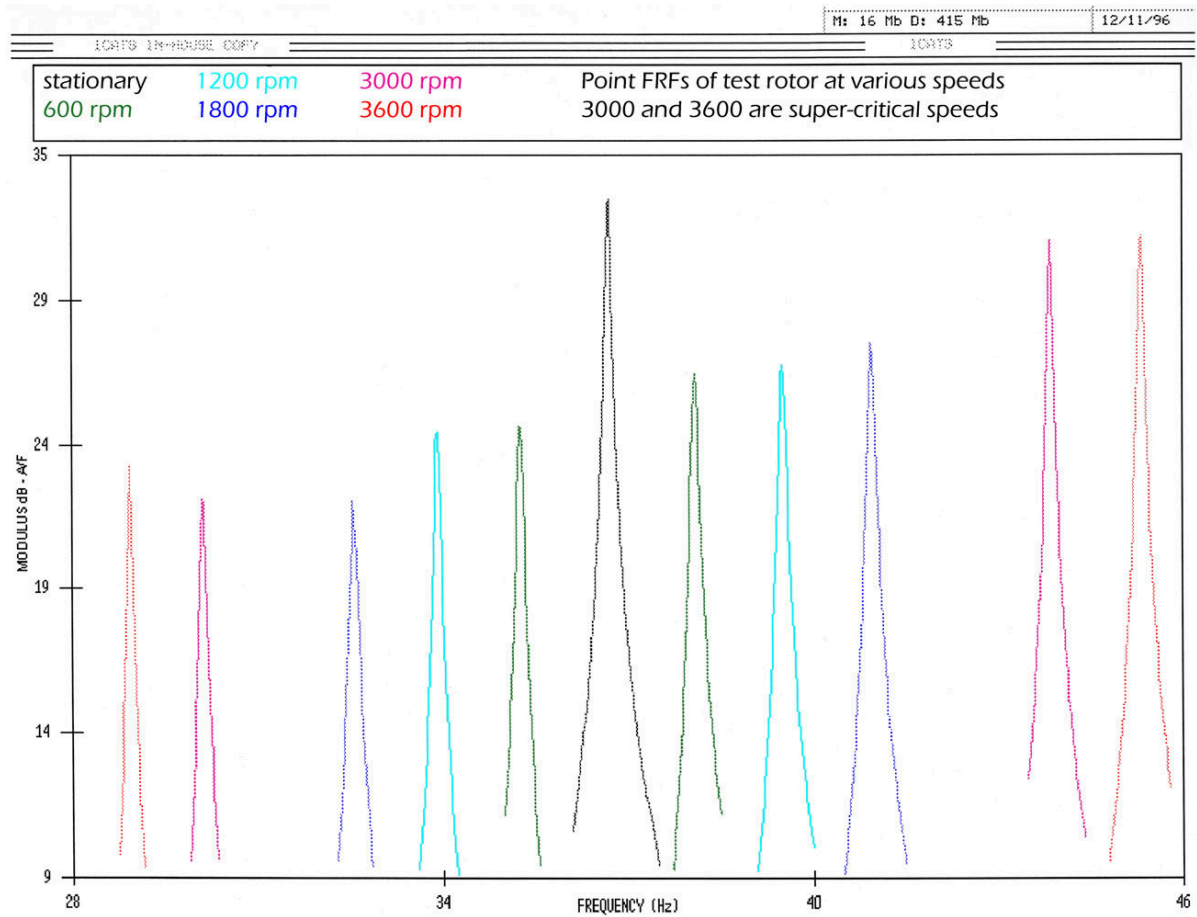
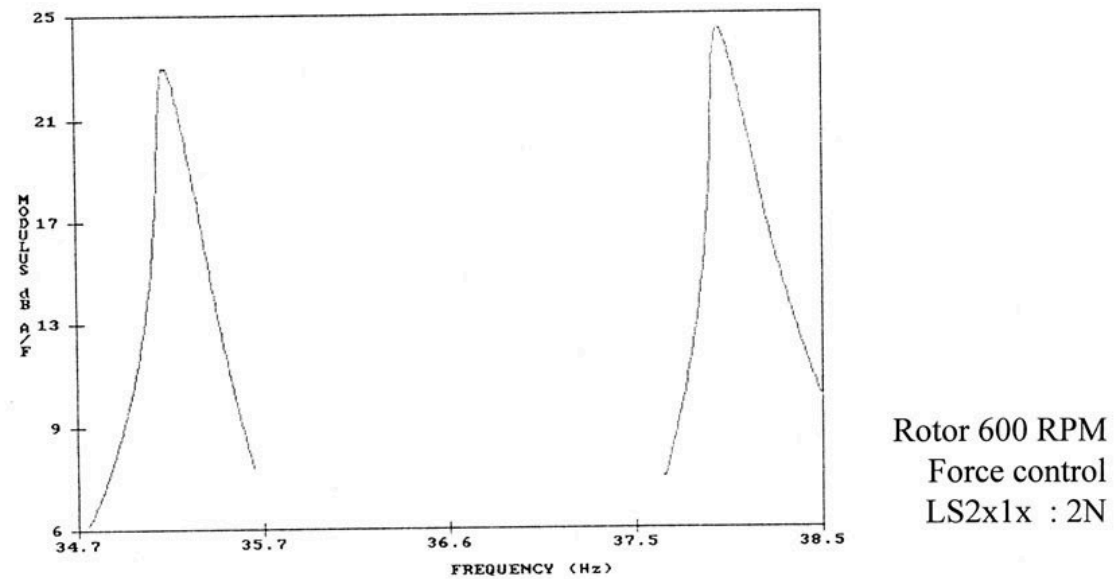
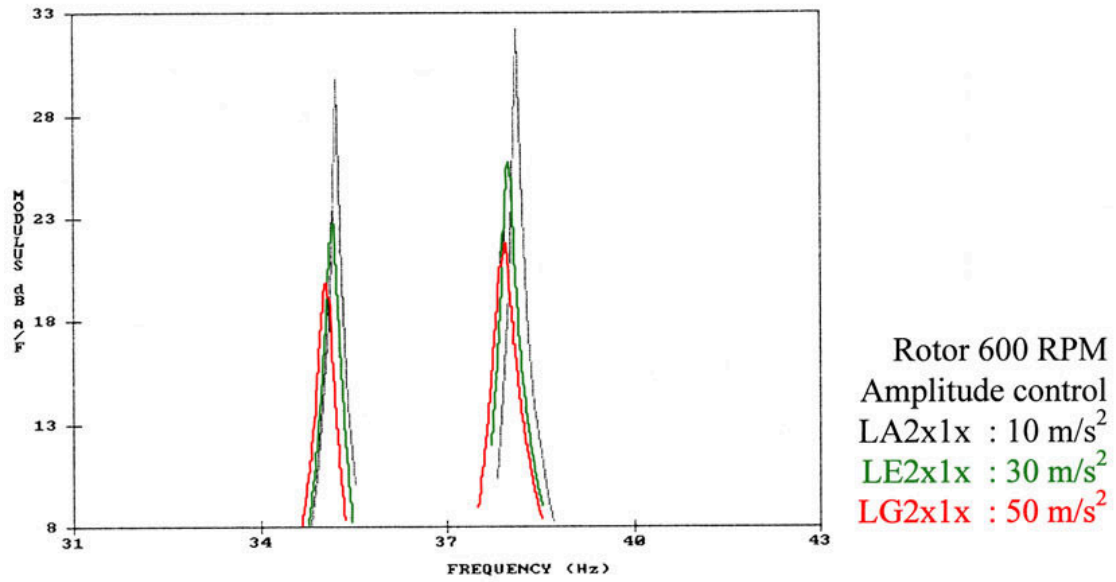
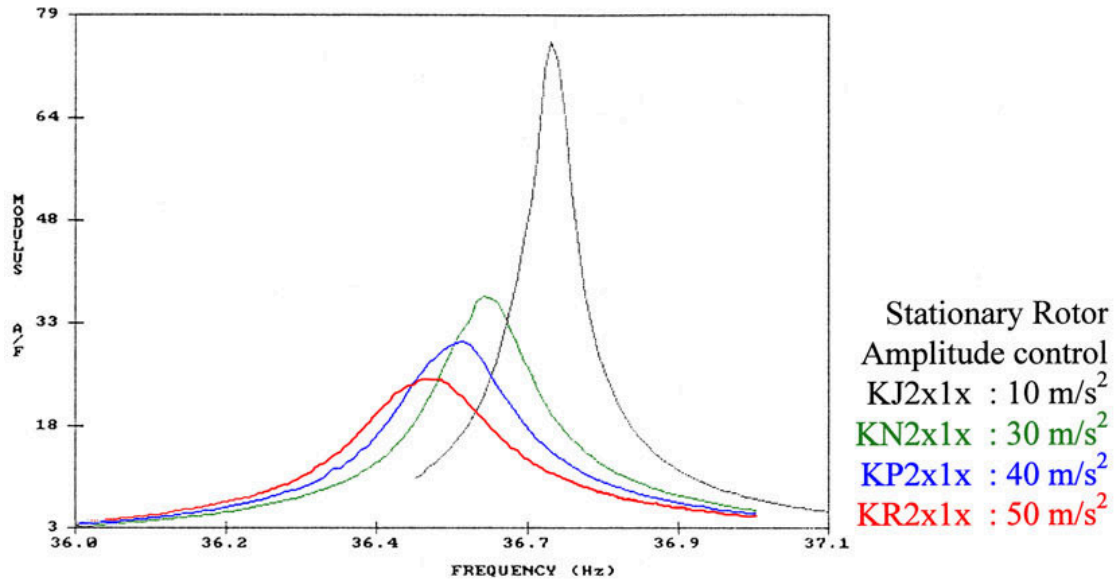


Figure 6.5.: FRFs of the test rotor at increasing speeds from stationary to supercritical

6. Experimental validations



FRF

file name (e.g. KJ2x1x) and its controlled parameter are coloured as corresponding plot.

Figure 6.6.: Flanged-rotor: Controlled FRFs exhibit typical friction damping behaviour

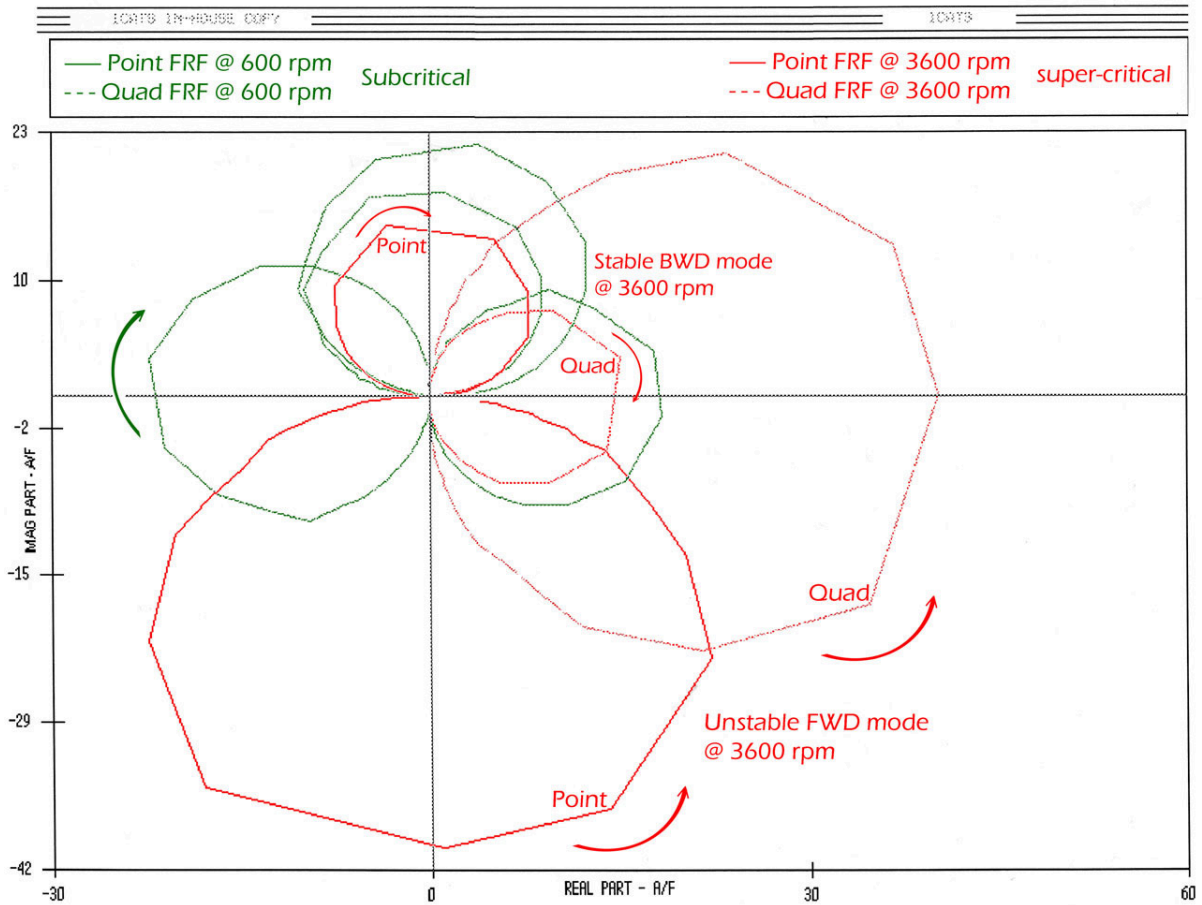


Figure 6.7.: Overlaid Nyquist plots of stable and unstable mode-dominated FRFs Experimental FRFs at sub-(600) and supercritical(3600) speeds of flanged rotor. The unstable mode-dominated FRF traces a CCW Nyquist plot emulating a -ve damper.

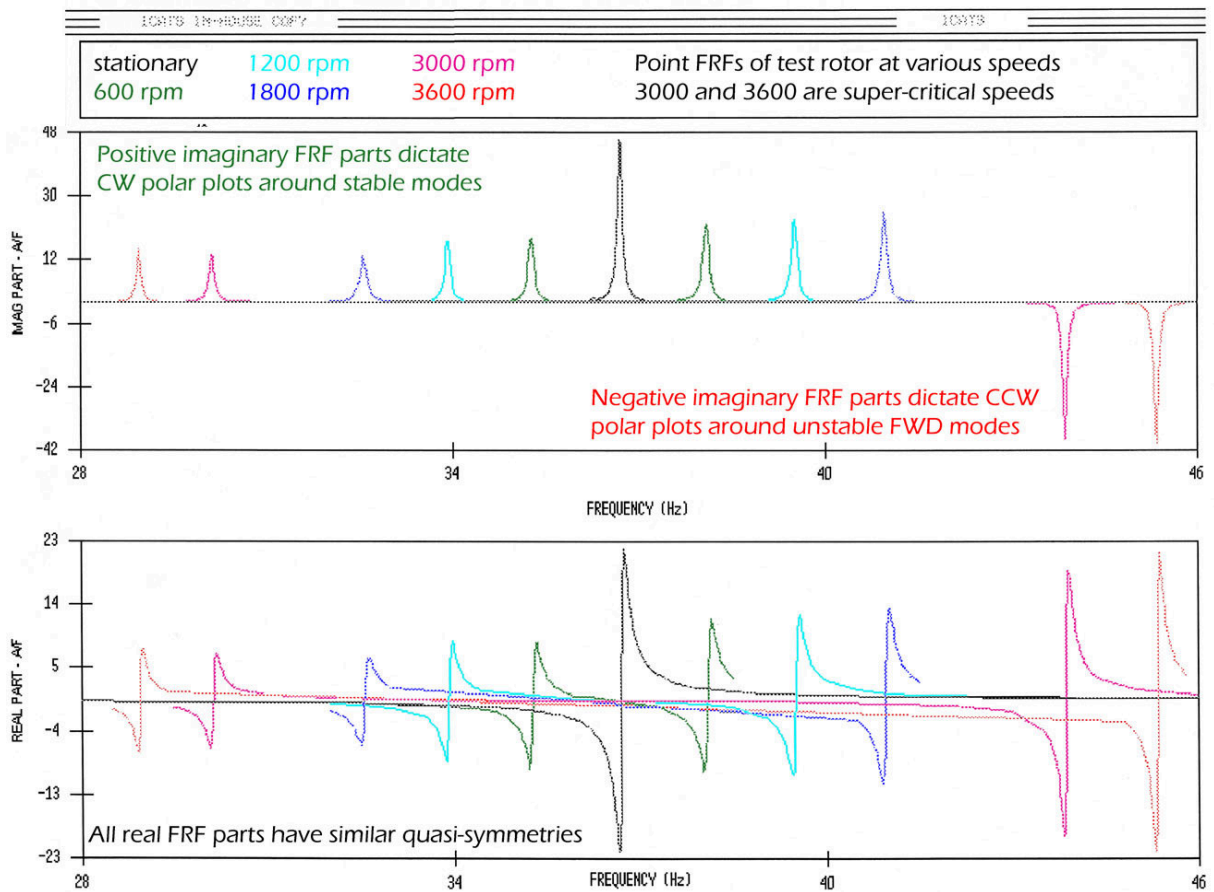


Figure 6.8.: \Re & \Im parts of stable and unstable mode-dominated FRFs at various speeds Flanged rotor FRFs at 0, 600, 1200, 1800, 3000, 3600 rpm. The -ve imaginary parts of FRFs at supercritical speeds 3000 and 3600 rpm, elaborate their CCW Nyquist plots.

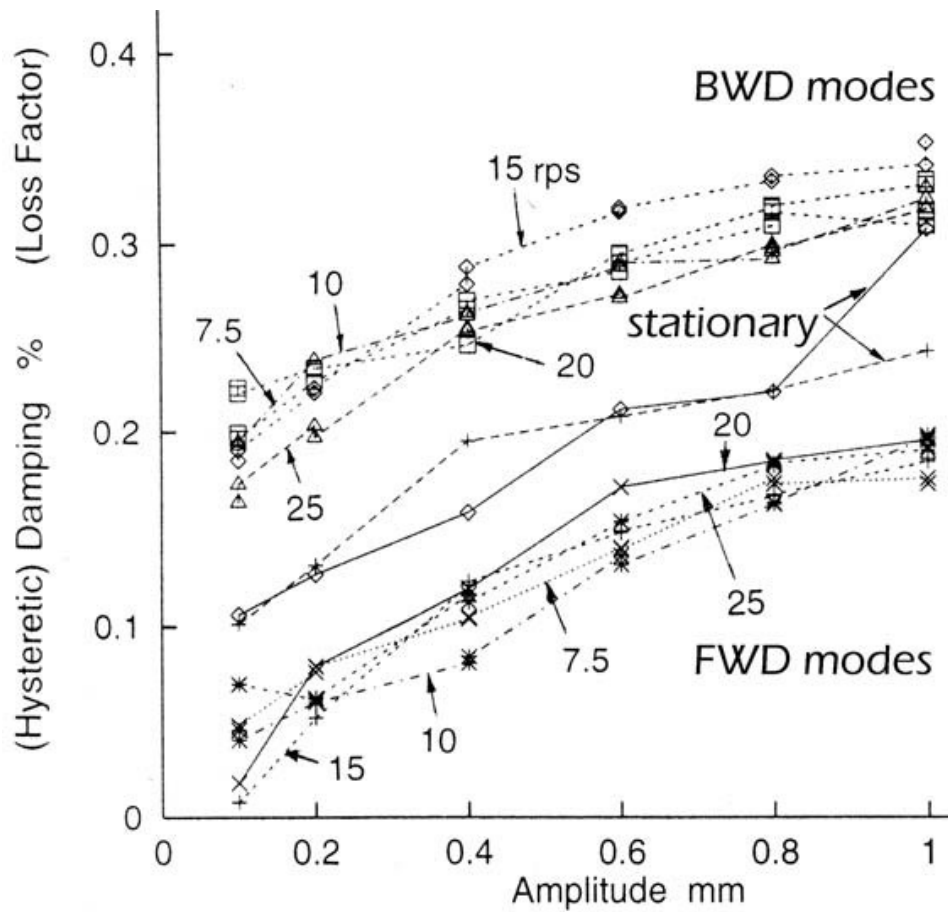


Figure 6.9.: Modal damping at various speeds: Curvic-coupling rotor controlled FRFs

7. Conclusions and Future work

Rotor Internal Damping instability, which was the first recognised over a century ago, has become a formidable problem for supercritically-operated rotating machinery. Currently, even regular rotors, let alone advanced aero-engines, are of an increasingly assembled design encouraging joint slippage, and hence RID whirling. For the purposes of effective design: the simplistic, unrepresentative or industrially-inapplicable analysis tools; and empirically-implemented hardware fixes, are no longer sufficient. It was concluded that:

- Accurate and efficient, linear and nonlinear, analytical techniques for parametric design evaluations, coupled with
- Appropriately implemented RID models, yielding representative predictions of whirling behaviour, and finally
- Safe and conclusive experimental stability testing of operational rotor prototypes.

are in virtual absentia, yet are required to live comfortably with RID whirling, as opposed to totally avoiding it. Consequently, these main issues were addressed by developing the basis of three applicable analytical techniques, which were corroborated experimentally. Further extending the functionality of these techniques and applying them to actual rotors is proposed for future work, along with implementing *dither system linearisation and stabilisation*; being the logical consequence of NL analysis developed.

7.1. Developments and Contributions

Analytical and experimental contributions in this work are meant to address the current industrial problem (§.1.1.1.4) with RID and cover most of its related gaps (§.1.1.3), inline with the defined research scope (§.1.2).

7.1.1. Main industrially-applicable techniques basis

Three analytical techniques are developed, along with their several leading and peripheral contributions, and corroborated experimentally. They form the basis, which is to be expanded upon and fine-tuned to arrive at industrial and research tools for the design, testing and analysis of RID systems.

7.1.1.1. The extended Nyquist criterion: Graphical predictions of RID whirling

This is a frequency response method (§.5.3.2) borrowed from control engineering, modified to suit the complex SISO nonlinear RID problem in the rotating frame, and extended to be used in conjunction with the DFM. The Nyquist criterion is adapted (§.5.3.2.1) to the problem for whirling stability analysis (§.5.3.2.2). Amplitude-dependant curves (derived from complex-conjugate DFs) of several RID joint input-output models (as opposed to geometric modelling) are used to assess their effect on whirling behaviour.

This technique may be used for parametric studies of both joint characteristics and rotordynamics, including the necessary level of stabilising external damping to avoid RID whirling. Although exemplified using a simple 2DOF rotor, it should be applicable to industrial rotors, whose FRF in the rotating frame can be acquired either analytically or experimentally. As compared to time-marching analysis (TMA), this technique:

- Avoids coding and analysing a masing-type joint model, which is costly in TMA.
- Provides immediate visual appreciation of system's behaviour, hence allowing for intuitive parametric changes, which will yield an acceptable system in very few trials. This, as opposed to the brute force of TMA, which dictates numerous blind runs just to get a stable system, albeit the final verdict for system performance, in which case one final run is sufficient.
- Requires comparable set-up time and toil for any rotor (2-20,000DOF) to that of a 2DOF rotor TMA.

7.1.1.2. Experimentally applicable stability test: EAST

EAST is developed to assess safely and conclusively the modal stability (and its margins) of a *target* rotordynamic system, which may become unstable when operated under various conditions. This is accomplished by analysing experimental FRFs of the quasi-linearised target system whilst operational, but *included as a subsystem* in an overall-stable system—§.4.3.

7.1.1.3. The proper use of ideal Hysteretic RID model

Hysteretic RID, appropriately implemented with $\text{sgn } \omega$ for frequency response and Eigen/modal analysis in the rotating frame, is presented in §.4.2.3. With the proper mix of viscous and hysteretic RID coefficients, eigenvalues-based stability predictions §.4.2.3.2 are realistic, albeit abrupt around the critical speed, and in tandem with experimental observations. This is as opposed to the unrealistic and possibly erroneous results from

industry standard Hysteretic RID models [200]. Necessary Hysteretic RID model adaptations for the more appropriate frequency response stability analysis (§.4.2.2.2, 5.3.2.1, 5.3.2.2), which involves negative frequency ranges, are presented in §.4.2.3.3.

7.1.2. Peripheral contributions to main techniques

These are necessary tools developed for use in conjunction with the main techniques.

Relation of Eigensolutions in stationary and rotating frames (3.48) used to:

- Relate analysed modes in the rotating frame to FWD/BWD modes in the stationary frame and conclude on their stability. Essential for complex stiffness RID.
- Arrive at the critical speed expression (3.44) for rotor with gyroscopic effect

Complex stiffness use in conjunction with negative frequencies is necessary for the analysis of complex representation of rotors with (Hysteretic or describing functions) RID in the rotating frame, as well as other mechanisms analysis. Complex conjugates of said stiffness are to be used with negative frequencies for appropriate phasing (*p.175*).

Nyquist criterion adapted for RID instability problem Adapted for complex SISO transfer functions with negative frequency poles, to handle complex stiffness feedback, as opposed to real SISO minimum phase TF (§.5.3.2.1).

The effect of different RID models on whirling behaviour patterns (§.5.3.2.2) is important to have in the background whilst designing or analysing a RID system. While properly implemented linear RID models cause absolute instability after an onset speed (*fig.4.19*), nonlinear RID models have a markedly different effect on sustainable whirling. Dry friction (SVNL) models (*fig.3.2*) will *always* result in whirling at any speed above critical, regardless of external damping (*fig.5.5*). While Coulomb damping yields stable whirling, a parabolic model yields initially stable whirling, which may take another unbounded solution as in the case of spline couplings, depending on external disturbances (*p.203*). Conversely, microslip (DVNL) models (*fig.3.3*) may yield a vaguely sustainable whirling or may not altogether (*fig.5.6*) depending on external damping.

7.1.2.1. Leading contributions to main techniques

Identification of modal directionality from polar plots §.4.1.2.4 along with its physical significance classify modes to conclude on their stability, and avoid confusion with unstable modes-dominated FRF portions that have distinctive characteristics.

Right/left-half s -plane poles and zeros effect on FRF angle sweep explains (4.6) their influence on FRFs mappings (*fig.4.5*), especially the counter-clockwise (CCW) polar plots around unstable poles in the right-half s -plane (§.4.2.2.1).

Polar plot FRFs of an unstable rotor are CCW quasi-circles in unstable modes' frequencies (§.4.2.2.3) vicinities, on account of well-separated and moderately damped modes, which are frequently *mistakenly assumed to reflect negative damping!*

7.1.3. Experimental contributions

Other than analytical confirmations, contributions to existing experimental work are:

Stabilising effect of increased subsynchronous vibration amplitude on both BWD and FWD modes, corroborated the effect of increased hysteretic and viscous RID coefficients. Increased amplitude of quasi-linearised FRFs at subcritical speeds resulted in an increased equivalent hysteretic damping $\Im(k_{\text{micro}})$. The experimental modal damping results of (*fig.6.9*) are in qualitative agreement with those of linear Eigenvalues (*fig.4.19*), when hysteretic RID κ is increased.

The CCW Nyquist plot (*figs.6.7,6.8*) is not only an interesting demonstration of the effect of unstable right-half s -plane poles (4.6b, §.4.1.2.1, *figs.4.16,4.17*); but is also the basis for EAST method to identify experimentally the existence of instability—under safe operation—and possibly quantify its strength and behaviour on varying its influencing parameters. An increased receptance and a decreased damping estimate suggest a stronger instability in the super-critical region, or a more pronounced effect of the follower force in overcoming external damping in the sub-critical region.

RID micro-slip behaviour during a rotordynamic test was demonstrated using damping estimates of quasi-linearised FRFs at increased response amplitudes and various speeds (*figs.6.6,6.8*). Rotor joints' micro-slip friction behaviour has been demonstrated previously (§.2.3.5) [185] using static and dynamic (modal) tests on non-rotating rotors.

Follower force rationale presented for RID in §.2.4.2 as destabilising [stabilising] to FWD [BWD] modes with increased speed was demonstrated (§.6.2.2.1, 6.2.2.3, *fig.6.5*) using modal damping and constants from quasi-linearised modal tests at various sub- and supercritical speeds. When finally developed, this approach (§.6.2.2.3), should be equally applicable to the follower force rationale of any self-induced instability mechanism.

7.1.4. Fundamentals' elaboration

RID-specific analytical expressions and conclusions

Linear viscous RID

- Effect on BWD and FWD modes stability is elaborated in §.4.2.1.1 and derived from analysing (4.14) the imaginary expression (4.13b) under square root in eigenvalues (4.12) of complex rotor representation
- Conditions for RID instability (§.4.2.1.2) in terms of damping ratio $\frac{\text{internal}}{\text{external}}$ relative to system parameters (4.20), and operating speed (4.19, 4.21) are arrived at using Routh's array and Routh-Hurwitz criterion for complex equations (4.16, 4.17)
- Onset speed of instability is expressed in terms of the *undamped* FWD modal frequency and $\frac{\text{internal}}{\text{external}}$ damping ratio (4.22), for intuitive design purposes, and is exemplified (*figs.4.14, 4.15*) along with expressions above.
- Gyroscopic effects deter, and may totally avoid RID instability (*p.162*)
- Static (4.24) as well as dynamic forced response is affected by RID (§.4.2.2.2)

Other RID models

- Hysteretic Vs. viscous RID effect on BWD and FWD modal stability (§.4.2.3.2)
- The assigned parabolic friction model (*fig.3.2*) explains (*p.203*) spline coupling RID whirling behaviour (*fig.5.5*) jump from stable to asymptotically unbounded.
- Microslip friction models (*fig.3.3*) explain the possible avoidance of tight couplings RID whirling or its behavioural (*fig.5.6*) change from unstable to stable/bounded.
- Incommensurate 2Ω -frequency quenching a LC explains the experimentally-observed favourable effect of support anisotropy (3.9) on suppressing RID instability (*p.193*).
- No proper RID model predicts instability or whirling at subcritical speeds (§.5.3.2)

Critique of RID analysis

- Suitability of various NL analysis to the RID problem (*Ch.5*): Characteristics of both linear rotordynamics and NL RID models dictate the use of quasilinearisation.

- The *erroneous* conclusion of hysteretic RID being destabilising at any speed even subcritical [200] derives from utilising it in a similar manner to viscous RID in the stationary frame. The basis of such analysis, as per (§.2.4.2) leading to (2.32), is invalid without accounting for $\text{sgn } \alpha_h$ in (2.45), which is inappropriate (§.2.4.6.2) when considering subcritical operation, BWD modes or even non-circular whirling. Hysteretic RID is a complex frequency response model that is not best suited for stability analysis except with serious caution (§.4.2.3). Also, unlike viscous RID that is constitutively represented by real coefficients that can be transferred seamlessly between frames of reference, the *single*-frequency hysteretic RID model needs to account for *multiple*-frequency responses on reference-frame transfer.

Rotordynamic contributions

- Modal directionality classified §.3.1.3.1 p.103
- Eigen-analysis closed-form expressions of 2DOF rotor with gyroscopic effect in stationary and rotating frames (§.3.1.3.2) leading to critical speed (3.44)
- Invariance of modal vectors in stationary and rotating frames (3.51)
- Modal damping factors characteristics in stationary and rotating frames §.4.1.1.2
- Peculiarities of rotor point transfer function and FRF in the rotating frame §.4.1.2.3.
- Effect of complex stiffness on eigenvalues p.173

7.2. Proposed future work

Extending the functionality of techniques developed herein, and expanding into the field of dither system linearisation and stabilisation, being their logical consequence, is proposed for future work. Other than the necessary corroborations, experimental work as detailed in (§.6.2.4), is planned on rotors with modifiable friction joints, and utilising non-contacting DAQ/DSP and control systems

- emphasising Active Magnetic Bearings for profiled signal stabilisation and orthotropic stiffness/damping variations
- and implementing fast geometric algebra-derived modal control algorithms.

as well as to formalise the follower force quantification via modal constants and damping, and EAST parameters. Another issue worthy of consideration is the effect of shearing rotor segments on RID whirling behaviour.

7.2.1. Extended Nyquist criterion with modified nonlinearities

As it stands, the extended Nyquist criterion (§.5.3.2.2) can handle SVNLD/DVNL RID models using DFs, which assume a single sinusoid. Naturally, all rotors exhibit some imbalance and support-anisotropy reflected by rotating-frame LTV coefficients, both of which result in biased sinusoidal inputs into the RID joint. As pointed out (§.A.2.4.3), the MIDF of MIMO RID systems should be able to handle such scenario, albeit with some complexity. However, the MIDF analysis will face the same problem of DFM MIMO analysis, namely: arriving at an initial guess for iterations of whirling solution and stability, which was one of the main reasons for developing the extended Nyquist criterion.

The functionality of extended Nyquist criterion is to be enhanced, so as to handle a further biased sinusoid, thus solving the above problem. This would be accomplished by using what is termed a modified nonlinearity \mathcal{N}_M , which yields a single DF \mathbb{k}_M for \mathcal{N} with multiple inputs, usually biased dual sinusoids. Consequently, \mathbb{k}_M^* is used in a similar manner as \mathbb{k}^* with LTI complex rotor FRF in the rotating frame. The concept of \mathcal{N}_M started with the SBDF (5.16) and is easily extended to bias plus unrelated dual sinusoid, which usually are a LC and a forcing sinusoid. Basically, $\mathcal{N}(x)$ having $\mathbb{k}(x)$ is modified by another input (e.g. bias) to another nonlinearity $\mathcal{N}_M(\dot{x})$ characteristic, for which a single DF \mathbb{k}_M can be derived when excited by a second sinusoid.

Applications of the two-sinusoidal input describing function (SSDF) and the incremental describing function (IDF), which include aspects such as *the induction and quenching of limit cycles, jump resonance, signal stabilisation and sub-harmonic oscillations* have been researched thoroughly. The SSDF, a special case of MIDF, is of significant importance for the forced RID problem or that with time-varying coefficients. For incommensurate frequencies, the SSDF is proven to be the same as the DF of $\mathcal{N}_M(\dot{x})$. The IDF, a special case of SSDF, is the DF for one of the sinusoids as its amplitude tends to zero. Again the incommensurate frequencies case gives the same result as \mathbb{k}_M as well as the DF for the bias in the SBDF as the bias tends to zero.

This proposed enhancement is necessary to:

- examine the effect of orthotropic supports, yielding LTV terms, on altering LC parameters or quenching it altogether as discussed (§.5.1.2.2)
- probe the possibility of LCs at subcritical speeds (§.5.1.2.2) due to sinusoidal forcing
- furnish the base for its logical extension: signal stabilisation using dither (§.7.2.2.2).

7.2.2. Dither system linearisation and stabilisation

The SSDF, \mathbb{k}_M and other theories show how the DF for a particular signal is modified by the presence of another signal and the marked effect this can have on system behaviour. The introduction of external signals to modify nonlinear system performance is therefore a logical consequence of such observation. High frequency dither signals have been used for about fifty years to compensate for the effects of coulomb friction, dead zones in hydraulic valves and hysteresis effects. The dither signal is normally introduced immediately prior to the nonlinear element, whose response to the system signal is to be varied, and is chosen so that a negligible component of it is fed back to the nonlinearity.

The major disadvantage of introducing dither is the excessive wear it may cause to system components. However, dither is required at a high frequency for two reasons: 1) to ensure that the amount of perturbation it causes to the desired system outputs, and thus also feeds back to the nonlinearity input, is small; 2) to justify substitution of the modified nonlinearity for the original characteristic in transient calculations, the dither frequency should be several times higher than the signal component frequencies.

7.2.2.1. System linearisation

Even if the system is known to be nonlinear, its initial design is based on a linearised model, and one then has the problem of assessing how actual nonlinearities will affect its performance. Although nonlinear behaviour may be acceptable, it is generally undesirable since it can cause performance degradation and instability. If this is intolerable, one approach is to inject dither into the nonlinear element, with the aim of effectively smoothing it out, so that the system behaviour becomes more nearly linear. This is effected by causing the operating point to sweep repeatedly over a certain range around its nominal position, on a timescale much shorter than that of system dynamics. *This technique is often profitably employed for the purpose of linearising the highly nonlinear force-velocity effects of friction.*

There are three main dither $w(t)$ forms, which induce a kind of *averaging* of the nonlinearity, depending on the nature of the oscillatory signal:

(1) Square-wave dither is the simplest, where $w(t)$ takes constant values W and $-W$ alternately, each being held for a half-period $\frac{T_o}{2}$, with T_o much smaller than system time constants. As a result, the effective value of \mathcal{F} , the output of the nonlinear element, can be written as $\check{\mathcal{F}} = \frac{\mathcal{N}(x+W) + \mathcal{N}(x-W)}{2}$, i.e. the arithmetic mean of the values corresponding to the two levels of the dither signal.

(ii) Sinusoidal dither $w(t) = W \sin(\frac{2\pi t}{T_o})$ is another simple possibility, where again T_o is chosen so small that the angular frequency $2\pi/T_o$ is much greater than any other involved in the operation of the system. In this case, the effective value of \mathcal{F} is its average over a

complete period of the dither oscillation, namely

$$\check{\mathcal{F}} = \frac{1}{2\pi} \int_0^{2\pi} \mathcal{N}(x + W \sin \theta) d\theta$$

which can also be regarded as the bias component of a Fourier expansion in multiples of the dither frequency. The approximation thus corresponds to the neglect of all harmonic terms, including the fundamental.

(iii) Triangular-wave (saw-tooth) is another popular dither signal, where $w(t)$ varies linearly with respect to time from $-W$ to W and then back again. Because of the constancy of \dot{w} on each upward and downward sweep, averaging over t is equivalent to averaging over w , and so the effective value of \mathcal{F} becomes

$$\check{\mathcal{F}} = \frac{1}{2W} \int_{-W}^W \mathcal{N}(x + w) dw$$

which is independent of the speed at which w actually changes. Thus, it is not in fact necessary that the times taken by the two linear sections of the oscillation should be the same, provided that the total period T_o is small enough, in the same sense as before. However, if $\mathcal{N}(x)$ is multivalued, the upward and downward averages may be different, and then $\check{\mathcal{F}}$ is given by their weighted mean value, with weighting factors proportional to the durations of the corresponding sweeps.

It follows from the discussion of the effect of artificial dither that ideal-relay (Coulomb friction) characteristic, as well as various hysteresis effects, can be manipulated. Thus a practical means for altering the properties of a feedback loop is that of simply changing the waveform of an additive dither signal. In two of the three cases shown, the effect of this dither is to linearise the nonlinearity for small input signals, the triangular dither providing a larger linear region than the sinusoidal dither.

7.2.2.2. Signal stabilisation

Since injecting dither has the effect of altering the nonlinear system characteristics, it is reasonable to expect that limit cycles in nonlinear systems can be turned on, altered, turned off, and, in general, controlled by proper choice of dither waveshape. The use of dither to turn limit cycles off is referred to as signal stabilisation. Oldenburger et al. [134, 135, 136, 137], was among the first to discover this phenomenon experimentally, and subsequently provide analytical justification, after extensive investigation.

Investigation of signal stabilisation via describing function theory can be executed as a two-stage process. First, by use of \mathbb{k}_M theory, the dither and original nonlinear element \mathcal{N} are replaced with an equivalent nonlinear element \mathcal{N}_M whose form implicitly accounts for

the presence of dither, but which no longer explicitly displays the dither signal. Second, the resulting system is made the object of a DF analysis to reveal the presence or absence of a limit cycle (§.5.3.2.2).

Analysis is subject to the usual DF and \mathbb{k}_M limitations, such as the assumption of a single time-invariant loop nonlinearity, the absence of nonlinearity subharmonic generation, and satisfaction of the filter hypothesis. In addition, it is a convenience if only a negligible amount of dither returns via the feedback loop to the nonlinearity input. As a rule of thumb, Oldenburger et al. suggest that the dither frequency be at least ten times the highest possible limit cycle frequency, an assumption that is readily verified during analysis. This is roughly the same rule of thumb which ought to be used in design of a limit-cycling system, where the frequency ratio of 10 there refers to limit cycle frequency over highest significant input frequency. The analytic study of signal stabilisation as described above is contingent upon our ability to determine DFs \mathbb{k}_M for the equivalent nonlinear element \mathcal{N}_M under consideration. No difficulty is likely to arise in obtaining \mathcal{N}_M itself. Occasionally, \mathbb{k}_M can be readily determined analytically, as in the case of the ideal relay, and can also be done for odd polynomial nonlinearities.

A. Reference material

A.1. Complex formulations

In rotordynamics, it is often beneficial to use the complex notions:

$$\mathbf{z} = \mathbf{x} + \imath\mathbf{y} \quad \text{and} \quad \mathbf{f}_c = \mathbf{f}_x + \imath\mathbf{f}_y \quad (\text{A.1})$$

A.1.1. General complex EOMs

With the notation of (2.4), we can rewrite (3.1) as:

$$\mathbf{M}_f \ddot{\mathbf{z}} + \mathbf{M}_b \ddot{\mathbf{z}}^* + \mathbf{C}_f \dot{\mathbf{z}} + \mathbf{C}_b \dot{\mathbf{z}}^* + \mathbf{K}_f \mathbf{z} + \mathbf{K}_b \mathbf{z}^* = \mathbf{f}_c \quad (\text{A.2a})$$

where

$$\begin{aligned} 2\mathbf{M}_f &= (\mathbf{M}_{xx} + \mathbf{M}_{yy}) - \imath(\mathbf{M}_{xy} - \mathbf{M}_{yx}) \\ 2\mathbf{M}_b &= (\mathbf{M}_{xx} - \mathbf{M}_{yy}) + \imath(\mathbf{M}_{xy} + \mathbf{M}_{yx}) \\ 2\mathbf{C}_f &= (\mathbf{C}_{xx} + \mathbf{C}_{yy}) - \imath(\mathbf{C}_{xy} - \mathbf{C}_{yx}) \\ 2\mathbf{C}_b &= (\mathbf{C}_{xx} - \mathbf{C}_{yy}) + \imath(\mathbf{C}_{xy} + \mathbf{C}_{yx}) \\ 2\mathbf{K}_f &= (\mathbf{K}_{xx} + \mathbf{K}_{yy}) - \imath(\mathbf{K}_{xy} - \mathbf{K}_{yx}) \\ 2\mathbf{K}_b &= (\mathbf{K}_{xx} - \mathbf{K}_{yy}) + \imath(\mathbf{K}_{xy} + \mathbf{K}_{yx}) \end{aligned} \quad (\text{A.2b})$$

and the sub-matrices of (A.2b) (e.g. $\mathbf{K}_{xx}, \mathbf{K}_{xy} \subset \mathbf{K}_g$; $\mathbf{M}_{yy}, \mathbf{M}_{yx} \subset \mathbf{M}$) are related to their main matrices in (3.1) by:

$$\mathbf{M} = \begin{bmatrix} \mathbf{M}_{xx} & \mathbf{M}_{xy} \\ \mathbf{M}_{yx} & \mathbf{M}_{yy} \end{bmatrix}, \quad \mathbf{C}_g = \begin{bmatrix} \mathbf{C}_{xx} & \mathbf{C}_{xy} \\ \mathbf{C}_{yx} & \mathbf{C}_{yy} \end{bmatrix}, \quad \mathbf{K}_g = \begin{bmatrix} \mathbf{K}_{xx} & \mathbf{K}_{xy} \\ \mathbf{K}_{yx} & \mathbf{K}_{yy} \end{bmatrix} \quad (\text{A.2c})$$

A.1.2. Complex formulation for isotropic rotors

Isotropic rotors can be viewed as those rotors whose *response directionality is the same as their rotating excitation directionality*. Whence in (A.2), isotropic rotors have:

$$\mathbf{M}_b = \mathbf{C}_b = \mathbf{K}_b = \mathbf{0} \quad (\text{A.3a})$$

which leads to

$$\begin{aligned} \mathbf{M}_{xx} = \mathbf{M}_{yy} &= \mathbf{M}_1 & \mathbf{M}_{xy} = -\mathbf{M}_{yx} &= \mathbf{M}_2 \\ \mathbf{C}_{xx} = \mathbf{C}_{yy} &= \mathbf{C}_1 & \mathbf{C}_{xy} = -\mathbf{C}_{yx} &= \mathbf{C}_2 \\ \mathbf{K}_{xx} = \mathbf{K}_{yy} &= \mathbf{K}_1 & \mathbf{K}_{xy} = -\mathbf{K}_{yx} &= \mathbf{K}_2 \end{aligned} \quad (\text{A.3b})$$

Introducing (A.3) to (A.2) results in:

$$\mathbf{M}_c \ddot{\mathbf{z}} + \mathbf{C}_c \dot{\mathbf{z}} + \mathbf{K}_c \mathbf{z} = \mathbf{f}_c \quad (\text{A.4a})$$

where

$$\mathbf{M}_c = \mathbf{M}_1 - i\mathbf{M}_2, \quad \mathbf{C}_c = \mathbf{C}_1 - i\mathbf{C}_2, \quad \mathbf{K}_c = \mathbf{K}_1 - i\mathbf{K}_2 \quad (\text{A.4b})$$

A.1.3. Formula for the square root of a complex quantity

$$\sqrt{a + ib} = \sqrt{\frac{a + \sqrt{a^2 + b^2}}{2}} + i\sqrt{\frac{-a + \sqrt{a^2 + b^2}}{2}} \quad \text{for } b > 0 \quad (\text{A.5a})$$

$$= \sqrt{\frac{a + \sqrt{a^2 + b^2}}{2}} - i\sqrt{\frac{-a + \sqrt{a^2 + b^2}}{2}} \quad \text{for } b < 0 \quad (\text{A.5b})$$

where a and b are real quantities that can generally be +ve or -ve.

A.2. Adapted Control theorems and applications

A.2.1. The Principle of the Argument: A Mapping application

The ‘‘principle of the argument’’ is a well known mapping theorem (*Th.A.1*) in complex variables theory, on which the Nyquist stability criteria, as well as EAST, are based.

Theorem A.1 (The ‘‘principle of the argument’’) *can be stated as:*

Let $H(s)$ be a single-valued rational polynomial function, e.g. (3.53), with l poles and u zeros in the s -plane (e.g. fig.4.7). Let Γ_s be an arbitrary closed path in the s -plane that does not go through any poles or zeros of $H(s)$. The mapping $\Gamma_s \xrightarrow{H(s)} \Gamma_H$ yields the closed locus Γ_H , which encircles the origin of the H -plane as many times ‘ N_e ’ as the difference ‘ $u_e - l_e$ ’ of $H(s)$ zeros and poles that are encircled by Γ_s in the s -plane:

$$N_e = u_e - l_e \quad ; \quad \text{where } 0 \leq u_e \leq u, \text{ and } 0 \leq l_e \leq l$$

A point or region in a complex plane, e.g. s -plane or $H(s)$ -plane, is said to be encircled by a closed path if it is found inside the path. The Γ_s path can be traversed in an arbitrarily chosen direction, i.e. CCW \odot or CW \ominus directions. Depending on the numbers of encircled zeros and poles, u_e and l_e , N can be +ve (-ve) indicating that Γ_H is traversed in the same (opposite) direction as Γ_s . For FR analysis purposes, (*part of*) the imaginary ω -axis of the s -plane can be considered as a segment of a closed path Γ_s that encircles the entire right- or left-half- s -plane, which is comprised of the infinite ω -axis $\omega \in (-\infty, \infty)$ and a semi-circle of infinite radius. Then we can adopt concept (A.1) [92]:

Concept A.1 (An enclosure concept) *A point or region is said to be enclosed by a closed path if it is encircled in the CCW direction; or equally, if the point/region lies to the left of a path when that path is traversed in the prescribed direction e.g. fig. 4.5.*

Accordingly, the ω -axis with $\omega: (-\infty \triangleright \infty)$ encloses the left-half- s -plane.

FRF features of minimum-/non-minimum-phase (real) TFs (H_{\min} and H_{nmin}) are stated here as the +ve ω -axis is swept from ω_0 to ω_∞ only, i.e. $\omega : [0 \triangleright \infty)$. Since the poles/zeros of real TFs occur in either complex-conjugates or real format, the FRF

$$H_{ij}(\omega) = |H_{ij}(\omega)|e^{j\psi(\omega)} = \frac{\bar{q}_i e^{j(\omega t + \psi)}}{f_j e^{j\omega t}} \quad \text{where} \quad \psi = \angle H_{ij}(\omega) = \tan^{-1} \frac{\Im(H_{ij}(\omega))}{\Re(H_{ij}(\omega))}$$

of $H_{ij}(s)$ with $p_{1,\dots,l}, o_{1,\dots,u}$ has these magnitude $|H_{ij}(\omega)|$ and phase shift $\angle H_{ij}(\omega)$ features:

1. The total phase variation $\Delta \angle H_{\min} = -\frac{\pi}{2}(l-u)$, excluding poles and zeros at the origin ($p, o \equiv s = 0$)
2. Phase angle at $\omega = \infty$: $\angle H_{\min}(\infty) = -\frac{\pi}{2}(l-u)$, while $\angle H_{\text{nmin}}(\infty) \neq -\frac{\pi}{2}(l-u)$
3. The absolute magnitude: $|H_{\min}(\omega)| \neq \{0, \infty\} \forall \omega \neq \{0, \infty\}$
4. For $H_{\min}; |H_{\min}(\omega)| \Leftrightarrow \angle H_{\min}(\omega)$ which is not necessarily the case for H_{nmin}
5. Both $H_{\min}, H_{\text{nmin}}$ have a slope of log-magnitude curve as $-20(l-u)$ db/decade at $\omega = \infty$

The above features are elucidated by the heuristic arguments and illustrations of §.4.1.2.1.

A.2.2. The general Nyquist criterion

The stability of a real LTI SISO closed-loop feedback system whose overall TF is:

$$G(s) = \frac{H(s)}{1 + H(s)B(s)} \quad (\text{A.6})$$

requires its characteristic equation to have no roots in the right-half s -plane. Since the characteristic equation is arrived at by setting the denominator: $1 + H(s)B(s) = \check{D}(s) = 0$, the stability condition is equivalent to requiring that the $1 + H(s)B(s)$ has no zeros in the right-half s -plane.

In examining whether the above stability condition is satisfied as an application of ‘the principle of the argument’ (*Th.A.1*), the general Nyquist stability criterion:

1. Sets a closed path (Nyquist locus) Γ_s defined to be a semicircle with an infinite radius and the entire ω -axis ($-\omega_\infty \triangleright \omega_\infty$) for a diameter so as to encircle the entire right-half s -plane.
2. Examines the resulting $\Gamma_{\check{D}}$ locus that is mapped $\Gamma_s \xrightarrow{\check{D}(s)} \Gamma_{\check{D}}$ into the $\check{D}(s)$ plane.

According to (*Th.A.1*), locus $\Gamma_{\check{D}}$ must encircle the s -plane origin ($s = 0$) a number of times $N_e = -l_{\text{rhsp}}$ that is equal to the number of $\check{D}(s)$ poles in the right-half s -plane, and in the opposite direction to that of Γ_s , for system (5.11) to be stable. Alternatively and similarly, the number and direction that critical point ($s_c = -1 + j0$) is encircled by the mapping Γ_{HB} of loop TF $H(s)B(s)$ can be considered.

A.2.3. Practical Absolute stability criteria

Definition A.2 (Sector condition) A continuous scalar function \mathcal{N} of x that is a real SVNL is said to be sector bounded $\mathcal{N}(x) \in [k_l, k_u]$ if there exists two non-negative numbers k_l and k_u such that

$$x \neq 0 \Rightarrow k_l \leq \frac{\mathcal{N}(x)}{x} \leq k_u \tag{A.7a}$$

$$k_l x^2 \leq x\mathcal{N}(t, x) \leq k_u x^2, \quad \forall t \geq 0, \forall x \in [x_- \dots x_+] \tag{A.7b}$$

if (A.7) holds $\forall x \in (-\infty, \infty)$ then the sector condition holds globally.

Equations (A.7) imply that $\mathcal{N}(0) = 0$ and $x\mathcal{N}(x) \geq 0$ so \mathcal{N} lies between xk_l and xk_u in the first or third quadrant of (fig.A.1).

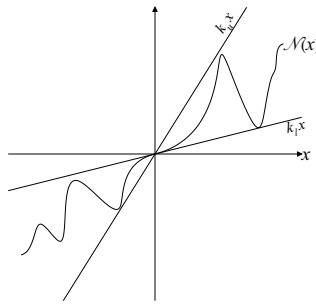


Figure A.1.: Sector bounded nonlinearity $\mathcal{N}(x, t)$

The most general Lyapunov analysis had provided some satisfactory results for a few systems, usually SISO with simple polynomial-type nonlinearities \mathcal{N} . However, there was not a systematic solution procedure for the types of \mathcal{N} that were actually encountered, which could be applied in a straightforward manner. One nonlinear system, based on an auto-pilot problem, which received intensive study in the former USSR is the feedback SISO \mathcal{S}_{NL} (fig.A.2). Letov [99] and Lur'e [105] initially used a Lyapunov function to handle this Letov-Lur'e problem. However, it was not until Popov's work [145] in 1960 on this problem, using frequency domain methods for practically applicable stability analysis, that a theory of nonlinear system design began to emerge.

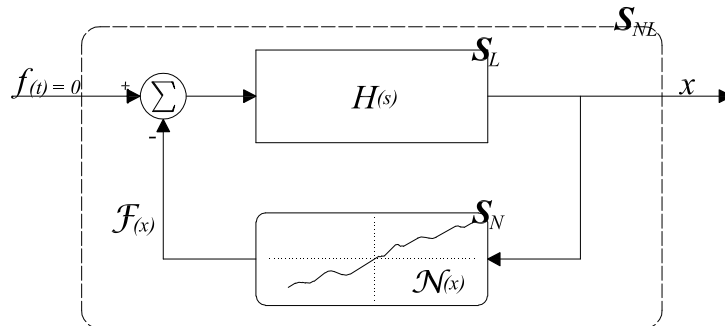


Figure A.2.: Letov-Lur'e problem: A nonlinear SISO feedback system

SISO analysis Utilising frequency response methods for autonomous systems, Popov's work [145] spurred renewed interests in the stability of nonlinear systems. Several theorems that were proven using functional analysis followed, allowing stability to be ascertained for the autonomous system with a bounded input $f(t)$ i.e. BIBO stability.

Popov criterion Using Lyapunov's direct method, Popov [146] provided a simple sufficient stability criterion for \mathbf{S}_{NL} of *fig.A.2*. The Popov stability criterion is formulated in terms of a *modified frequency response* $L_P(i\omega)$ for \mathbf{S}_L , and $\mathcal{N} \in [0, k_u]$ (*def.A.2*). Popov Locus $L_P(i\omega) = \Re(H(i\omega)) + i\omega\Im(H(i\omega))$ is a distorted version of the Nyquist locus. This stability criterion requires that $L_P(i\omega)$ lies to the right of a straight *Popov line* that passes through the point $(\frac{-1}{k_u}, i0)$. Restrictions when using Popov criterion are:

- \mathbf{S}_{NL} has to be autonomous
- $\mathbf{S}_L \stackrel{\text{def}}{=} \text{Hurwitz}$, i.e. strictly stable and controllable
- single-valued \mathcal{N} in sector $[0, k_u < \infty]$ as in (A.7)

Even if RID \mathcal{N} is SVNL, as in Coulomb damping, \mathcal{N} belongs to the sector $[0, k_u = \infty]$. Even a *softer* approximation of Coulomb damping $\Rightarrow k_u \approx \infty$, which renders the method useless, as it is already rather conservative.

The circle criterion Like Popov's criterion, the circle criterion can be proven using the integration by parts procedure for finding a Lyapunov function. This criterion, however, is a more direct generalization of Nyquist criterion to nonlinear systems. Here, the critical point $-\frac{1}{k}$ in Nyquist criterion is replaced by (blown up to) a circle with diameter on negative real axis of the complex plane from $-1/k_u$ to $-1/k_l$, with respect to which the Nyquist theorem is applied. Also, proof using functional analysis methods allows for the conclusion on BIBO stability for non-autonomous \mathbf{S}_{NL} . However, this criterion is more conservative [169] than Popov's and requires $\mathcal{N} \in [k_l, k_u]$ (A.7).

Practical MIMO system analysis being extensions of their SISO versions, are frequency domain-based separating \mathbf{S}_{NL} into $\mathbf{S}_L, \mathbf{S}_N$ in a feedback set-up. The MIMO analysis, which is even more conservative than for SISO [12], will thus depend on characteristics of subsystems \mathbf{S}_L and $\mathbf{S}_N \stackrel{\text{def}}{=} \mathcal{N}$ as well as those of $\mathcal{N}_{ij} \in \mathcal{N}$. Important characteristics of $\mathbf{H}(s)$ representing the LTI \mathbf{S}_L are: Positive realness PR/SPR, normality and diagonal dominance; which were discussed in §3.1.4. Important characteristics of $\mathbf{S}_N \stackrel{\text{def}}{=} \mathcal{N}$, the nonlinear block in feedback loop, are: Diagonality of \mathcal{N} and sector conditions (A.7) of each $\mathcal{N}_{ij} \in \mathcal{N}$. Dynamic and high frequency attenuation properties of each $H_{ij} \in \mathbf{H}(s)$, as well as the superharmonic frequency content in output \mathcal{F}_i from each \mathcal{N}_{ij} are important characteristics for the approximate harmonic balance methods.

Considerable efforts were devoted to extending several SISO absolute stability criteria to MIMO systems. Successful attempts were largely those with the feedback \mathcal{N} being diagonal, i.e. $i \neq j \Rightarrow \mathcal{N}_{ij} = 0$, as the otherwise limited criteria for a general \mathcal{N} are overly conservative [12]. The first two of such extension results were those of Jury and Lee [77], and Falb et al. [50]. Recent results largely present extensions or different interpretations of such results so as to obtain less conservative ones [12]. The Jury and Lee result is an

extension of Popov criterion to MIMO systems with diagonal \mathcal{N} where each \mathcal{N}_{ii} satisfies the sector condition. The result of Falb et al. is a simple extension of the eigenvalue criterion for the stability of MIMO LTI systems, to \mathbf{S}_{NL} with sector condition imposed on the diagonal \mathcal{N} . A further restriction is that the TFM \mathbf{H} describing \mathbf{S}_L must be *normal*. Papers [113] followed to show how to apply this method to systems where the normality condition can be levied. Popov developed a multivariable generalisation of his work on the Lur'e-Letov problem for which he coined the title “*Hyper-stability*” [147]. The MIMO feedback loop could accommodate \mathcal{N} block with nonlinear time-varying entries. However, a SPR condition must be imposed on the TFM \mathbf{H} .

A.2.4. The approximate Describing Functions Method

A.2.4.1. Time periodicity and Fourier series approximations

The exploitation of time periodicity is widely implemented in dynamic system analysis, and leads straightforwardly to frequency-domain descriptions, via Laplace or Fourier transformation, of LTI systems. Although oversimplicity is sacrificed where nonlinear systems are concerned, the technique is no less important, albeit in an approximate sense, since periodic phenomena (e.g. limit cycles) are among the more prominent features of said systems. Fourier series is the natural framework for analysing periodic behaviour, e.g. the periodic scalar function $\mathcal{F}(\tau)$, which is represented by the simple infinite series:

$$\mathcal{F}(\tau) = a_0 + \sum_{m=1}^{\infty} a_m \cos m\tau + b_m \sin m\tau = a_0 + \sum_{m=1}^{\infty} \mathcal{F}^m(\tau) \quad (\text{A.8})$$

$$a_0 = \frac{1}{2\pi} \int_{-\pi}^{\pi} \mathcal{F}(\tau) d\tau \quad , \quad a_m = \frac{1}{\pi} \int_{-\pi}^{\pi} \mathcal{F}(\tau) \cos m\tau d\tau \quad , \quad b_m = \frac{1}{\pi} \int_{-\pi}^{\pi} \mathcal{F}(\tau) \sin m\tau d\tau$$

Fourier series (A.8) is rather important for nonlinear system analysis because it:

1. Decomposes the general periodic output $\mathcal{F}(\tau)$ into a set of terms, each retaining its sinusoidal form under the operation of any linear system element.
2. Is naturally amenable to an approximation scheme by truncating to n -finite series.

$$\mathcal{F}_n(\tau) = a_0 + \sum_{m=1}^{m=n} a_m \cos m\tau + b_m \sin m\tau \quad (\text{A.9})$$

which generates the best approximation of $\mathcal{F}(\tau)$ by minimising the mean squared-error:

$$\text{mean } (e^2) = \frac{1}{2\pi} \int_0^{2\pi} \left(\mathcal{F}(\tau) - \mathcal{F}_n(\tau) \right)^2 d\tau \quad \text{where} \quad e = \mathcal{F}(\tau) - \mathcal{F}_n(\tau) \quad (\text{A.10})$$

Furthermore, a general class of *almost-periodic* functions is defined by the *generalised Fourier series* in which terms have arbitrary frequencies of the form:

$$\mathcal{F}(\tau) = a_0 + \sum_{m=1}^{\infty} a_m \cos \omega_m \tau + b_m \sin \omega_m \tau \quad (\text{A.11})$$

where the frequencies ω_m may be incommensurable. This extends the method to cover situations where signals are approximated by a combination of sinusoids of unrelated

frequencies, which is naturally appropriate for analysing oscillations in periodically- (or almost-periodically) forced nonlinear systems.

The foregoing leads to the Harmonic Balance Method (HBM) or the Describing Function Method (DFM) for the approximate analysis of periodic phenomena, where every dynamic variable is approximated by a finite sum of periodic terms, usually a single sinusoid, possibly with a constant bias. Any nonlinear component of the system is then approximately represented by its action on sinusoids just as though it were linear, so that the method involves a kind of *quasi-linearisation*. These methods can be generalised beyond the strictly periodic case, since the foregoing does not prerequisite all the terms in Fourier series being at multiples of the same fundamental frequency.

A.2.4.2. Quasilinearisation and Describing functions

The basic idea is to represent a nonlinear element by a kind of ‘transfer function’, derived from its effects on sinusoidal input signals or combinations thereof. Quasilinearisation is a choice to represent (*replace*) the nonlinear element model \mathcal{N} by the *best* equivalent linear gain $\mathbb{k} = \mathbb{k}(x)$ approximation, that is optimum in some sense of error e minimisation. With \mathcal{F} being the output of the nonlinearity \mathcal{N} that is subjected to input x :

$$\mathcal{F} = \mathcal{N}(x) \quad \Rightarrow \quad \mathcal{F} \approx \mathbb{k}x \quad \Rightarrow \quad \mathcal{F} - \mathbb{k}x = e \quad (\text{A.12})$$

The optimum value of \mathbb{k} will depend on:

- The criterion of optimality, i.e. the criterion chosen for defining the *best approximation*. The usual criterion is one that minimises the mean squared error.
- The *form* of the input x , i.e. sinusoidal, random, bias and combinations thereof
- The nonlinear characteristic \mathcal{N}

Naturally, as \mathbb{k} is an approximate representation, the error e will vanish only when x is a constant (bias) input or when \mathcal{N} is actually linear. This notion can be extended to \mathcal{N} having multiple input signals $\mathbf{x}_{1 \times n} = \{x_1, x_2, \dots, x_n\}$.

$$\mathcal{F} = \mathcal{N}(\mathbf{x}) = \mathcal{N}(x_1, x_2, \dots, x_n) \quad (\text{A.13})$$

In such a situation each input is represented by a separate equivalent gain $\mathbb{k}_1, \mathbb{k}_2, \dots, \mathbb{k}_n$ with $\mathbb{k}_j = \mathbb{k}_j(\bar{\mathbf{x}}) = \mathbb{k}_j(\text{amp}(x_1), \dots, \text{amp}(x_n))$, $j = 1, \dots, n$.

$$\mathcal{F} \approx \mathbb{k}_1 x_1 + \mathbb{k}_2 x_2 + \dots + \mathbb{k}_n x_n \quad (\text{A.14})$$

Describing Functions are the relationships that yield gain \mathbb{k} for nonlinearity \mathcal{N} (§.A.2.4.3).

This concept of quasilinearisation is the basis for both: 1) The HBM, which describes nonlinearities’ output of specific frequencies by an external quasilinear force vector, and 2) The DFM, which describes nonlinearities by their (internal) quasilinear stiffness elements $\mathbb{k} \in \mathbb{K}$ matrix. The latter being the more numerically efficient method.

Input signal assumptions With the HBM/DFM, input and output must be treated consistently, i.e. if the input is taken to be a pure sinusoid, the Fourier series (A.8) for

the output should be truncated (A.9) at first order $m = 1$. By the foregoing, the form of input x to a nonlinear element \mathcal{N} must be known in order to obtain a quasilinear model \mathbb{k} for \mathcal{N} . This is rarely the case since a NL system x is a function of: 1) Characteristics of nonlinearity \mathcal{N} , 2) External inputs to the system (forces \mathbf{f}), as well as 3) LTI frequency attenuation characteristics. Accordingly, a specific input form must be assumed.

Assigning a certain form of input signal x to \mathcal{N} for NL systems' behavioural predictions is an issue of particular importance, and one that develops from observation and experience. Most real systems, especially slightly nonlinear mechanical systems, have transfer functions with good high frequency attenuation (low-pass) characteristics. Since low-pass filtering of any periodic signal tends to make it sinusoidal, periodic signals within the system might be (rightly) expected to be approximately sinusoidal at the input to \mathcal{N} . Also, low-pass filtering of any random signal tends to render it more Gaussian. Accordingly, there are three basic forms of a nonlinearity inputs that are assumed for Describing Functions calculations, namely: 1) Bias (constant), 2) Sinusoid and 3) Gaussian random. Generally, it is necessary to assume various combinations of these basic input forms for Describing Functions calculations. Our main concern is with nonlinearities having pure sinusoidal input for RID self-induced precession analysis (DF), pure sinusoidal *plus* bias inputs when considering the effect of imbalance (SBDF), and dual-sinusoid for combined forced response and limit cycle analysis (SSDF).

Describing Function Definitions are outcomes of attempts to extend linear FRF analysis to NL systems. Describing functions may be defined as complex ratios of constants and sinusoids, or more generally, via correlation and mean squared-error criteria. The latter two definition criteria are applicable to deterministic and random inputs.

The most widely used Describing Function is the DF defined for a single sinusoidal input into \mathcal{N} , e.g. $x(t) = \Re(\vec{X}e^{i\tau})$. The complex ratio \mathbb{k} of output's fundamental component \mathcal{F}^1 to the sinusoidal input $\bar{X} \cos \tau$ was the original definition of a DF, due to the physically-motivated extension of FRF technique, i.e \mathbb{k} is a complex stiffness:

$$\mathbb{k} = \mathbb{k}(\bar{X}) = \frac{\mathcal{F}^1(\tau)}{\bar{X} \cos \tau} = \frac{\vec{\mathcal{F}}^1 e^{i(\tau+\theta_1)}}{\bar{X} e^{i\tau}} = \frac{\vec{\mathcal{F}}^1}{\bar{X}} \equiv \frac{\vec{\mathcal{F}}^1}{\bar{X}} \quad (\text{A.15})$$

Minimising (A.10) yields \mathbb{k} that is identical to that defined by the complex ratio. Also, it is important here to define a sinusoid's amplitude probability density function $\wp(x)$:

$$\wp(x) = \left(\pi \sqrt{\bar{X}^2 - x^2} \right)^{-1} \quad (\text{A.16})$$

A.2.4.3. Describing Functions evaluation

Effect of \mathcal{N} symmetry and SVNL characteristics on Fourier series coefficients Considering an \mathcal{N} with input $\bar{X} \cos \tau$ and periodic output $\mathcal{F}(\tau)$ Fourier-expanded as:

$$\mathcal{F}(\tau) = a_0 + \sum_{m=1}^{\infty} \mathcal{F}^m(\tau) \quad (\text{A.17a})$$

$$\begin{aligned} \mathcal{F}^m(\tau) &= a_m \cos m\tau + b_m \sin m\tau = \Re((a_m - ib_m)e^{im\tau}) = \Re(\vec{\mathcal{F}}^m e^{im\tau}) \\ \vec{\mathcal{F}}^m &= \bar{\mathcal{F}}^m e^{i\theta_m}, \quad \bar{\mathcal{F}}^m = |\vec{\mathcal{F}}^m| = \sqrt{a_m^2 + b_m^2} \\ \theta_m &= \arctan\left(\frac{\Im(\vec{\mathcal{F}}^m)}{\Re(\vec{\mathcal{F}}^m)}\right) = -\tan^{-1}\left(\frac{b_m}{a_m}\right) \end{aligned} \quad (\text{A.17b})$$

Deductions about the series' coefficients are made depending on symmetry and SVNL:

Odd symmetry if $\mathcal{F}(\tau)$ is an odd function of $x(t)$, then changing $\tau \rightarrow \tau + \pi$ changes $x \rightarrow -x$ and $\mathcal{F} \rightarrow -\mathcal{F}$, which implies that $a_m = b_m = 0 \forall m = 0, 2, 4, \dots$ in both SVNL and DVNL. Otherwise, a_m and b_m can be non-zero only if m is odd.

Even symmetry if $\mathcal{F}(\tau)$ is an even function of $x(t)$, then reversing the sign of $x(t)$ leaves $\mathcal{F}(\tau)$ unaltered, and $a_m = b_m = 0 \forall m = 1, 3, 5, \dots$ (odd m)

SVNL $\mathcal{F}(\tau) \stackrel{\text{def}}{=} \text{single-valued function of } x(t) \Rightarrow a_m = 0 \forall \text{ even } m, b_m = 0 \forall \text{ odd } m.$

In the above scenarios, if the input is unbiased sinusoid (no constant term), the DFM approximation will only be consistent if the output is also unbiased, which is ensured only if the nonlinearity has odd symmetry. However, there is no need to assume a SVNL, since a DVNL is allowed for by the presence of both sine and cosine terms in the output.

RID models (§.3.2.1.2) fall in the odd symmetric SVNL/DVNL class where:

$$\begin{aligned} \mathcal{N}(x) &= -\mathcal{N}(-x) && \text{for SVNL with input } x \stackrel{\text{def}}{=} v \text{ relative velocity (fig.3.2)} \\ \mathcal{N}_+(x) &= -\mathcal{N}_-(-x) && \text{for DVNL with displacement input (fig.3.3), when:} \\ \mathcal{F} &= \mathcal{N}_+(x) && \text{for } \frac{dx}{d\tau} > 0 \quad \text{where } \mathcal{N}_+(x) \stackrel{\text{def}}{=} \mathcal{N}_r(x) \\ \mathcal{F} &= \mathcal{N}_-(x) && \text{for } \frac{dx}{d\tau} < 0 \quad \text{where } \mathcal{N}_-(x) \stackrel{\text{def}}{=} \mathcal{N}_u(x) \end{aligned} \quad (\text{A.18})$$

Accordingly, only odd symmetric nonlinearities are considered. However, it is useful for further analysis to define the symmetric odd $\mathcal{N}_{\Re}(x)$ and even $\mathcal{N}_{\Im}(x)$ averaging functions:

$$\mathcal{N}_{\Re}(x) = \left(\mathcal{N}_+(x) + \mathcal{N}_-(x)\right)/2 \quad \text{and} \quad \mathcal{N}_{\Im}(x) = \left(\mathcal{N}_+(x) - \mathcal{N}_-(x)\right)/2 \quad (\text{A.19})$$

The DF is the Describing Function for \mathcal{N} having a sinusoidal input $x(t) = \Re(\bar{X} e^{i\tau})$ which will not be phased, without loss of generality, as $x(t) = \bar{X} \cos \tau$ with $\psi_x = 0$. Accordingly, we only consider the fundamental sinusoid of the output $\mathcal{F}^1(\tau)$.

For \mathcal{N} being SVNL all $b_m = 0$, hence $\mathbb{k} \stackrel{\text{def}}{=} \text{real}$, $a_0 = 0$ and $\forall a_{m \in \{m=1,3,\dots\}}$

$$a_m = \frac{4}{\pi} \int_0^{\pi/2} \mathcal{F}(\tau) \cos m\tau d\tau$$

$$\mathbb{k}(\bar{X}) = \frac{\mathcal{F}^1(\tau)}{\bar{X} \cos \tau} = \frac{a_1}{\bar{X}} = \frac{4}{\bar{X}\pi} \int_0^{\pi/2} \mathcal{F}(\tau) \cos \tau d\tau \quad (\text{A.20a})$$

$$\text{or alternatively, in terms of input } x: \quad = \frac{4}{\bar{X}^2} \int_0^{\bar{X}} x \mathcal{N}(x) \wp(x) dx \quad (\text{A.20b})$$

For \mathcal{N} being DVNL $a_0 = 0$ some $b_{m \in \{m=1,3,\dots\}} \neq 0$ hence $\mathbb{k} \stackrel{\text{def}}{=} \text{complex}$.

$$a_m = \frac{2}{\pi} \int_0^{\pi} \mathcal{F}(\tau) \cos m\tau d\tau, \quad \text{or} \quad a_1 = \frac{4}{\bar{X}} \int_0^{\bar{X}} x \mathcal{N}_{\Re}(x) \wp(x) dx \quad (\text{A.21a})$$

$$b_m = \frac{2}{\pi} \int_0^{\pi} \mathcal{F}(\tau) \sin m\tau d\tau, \quad \text{or} \quad b_1 = \frac{4}{\pi \bar{X}} \int_0^{\bar{X}} \mathcal{N}_{\Im}(x) dx \quad (\text{A.21b})$$

$$\mathbb{k}(\bar{X}) = \frac{2}{\bar{X}\pi} \int_0^{\pi} \mathcal{F}(\tau) e^{-i\tau} d\tau = \frac{\Re((a_1 - ib_1)e^{i\tau})}{\Re(\bar{X}e^{i\tau})} = \frac{a_1 - ib_1}{\bar{X}} \quad (\text{A.21c})$$

Here, $\Im(\mathbb{k}) = \pm \frac{\Delta}{\pi \bar{X}^2}$, $b_1 = \mp \frac{\Delta}{\bar{X}\pi}$ where $\Delta \stackrel{\text{def}}{=} \text{area inside DVNL loop}$, in tandem with linear damping. The \pm sign reflects the CW/CCW loop traverse directionality respectively.

The SBDF is the immediately obvious generalisation of the DF, where the input to \mathcal{N} is assumed to be a biased (plus constant) sinusoid, the output is approximated by its fundamental sinusoid and a constant, and the the SBDF has two components \mathbb{k}_0 and \mathbb{k} .

$$x(t) = \bar{X}_0 + \bar{X} \cos \tau, \quad \mathcal{F}(\tau) \approx a_0 + \mathcal{F}^1(\tau) \quad \Rightarrow \quad \mathbb{k}_0 = \frac{a_0}{\bar{X}_0}, \quad \mathbb{k} = \frac{\bar{\mathcal{F}}^1}{\bar{X}} \quad (\text{A.22})$$

where both the real \mathbb{k}_0 and the complex \mathbb{k} are functions of X_0 as well as \bar{X} :

$$\mathbb{k}_0(X_0, \bar{X}) = \frac{1}{2\pi \bar{X}_0} \int_{-\pi}^{\pi} \mathcal{F}(X_0 + \bar{X} \cos \tau) d\tau \quad \text{and}$$

$$\mathbb{k}(X_0, \bar{X}) = \frac{1}{\pi \bar{X}} \int_{-\pi}^{\pi} \mathcal{F}(X_0 + \bar{X} \cos \tau) e^{-i\tau} d\tau \quad (\text{A.23})$$

or written in terms of input x , using the averaging functions:

$$a_0 = \int_{-\bar{X}}^{\bar{X}} \mathcal{N}_{\Re}(x + X_0) \wp(x) dx \quad \text{and} \quad (\text{A.24})$$

$$a_1 = \frac{2}{\bar{X}} \int_{-\bar{X}}^{\bar{X}} x \mathcal{N}_{\Re}(x + X_0) \wp(x) dx, \quad b_1 = \frac{2}{\pi \bar{X}} \int_{-\bar{X}}^{\bar{X}} \mathcal{N}_{\Im}(x + X_0) dx$$

As in the case of DF: if $\mathcal{N} \stackrel{\text{def}}{=} \text{SVNL}$ then \mathbb{k} is real, while if $\mathcal{N} \stackrel{\text{def}}{=} \text{DVNL}$ then $\Im(\mathbb{k}) = \pm \frac{\Delta}{\pi \bar{X}^2}$. Also, the optimum linear model for SVNL is: $\mathcal{N} \approx \bar{X} \mathbb{k}(X_0, \bar{X}) + X_0 \mathbb{k}_0(X_0, \bar{X})$.

Several inputs into a nonlinearity The above formulations can be generalised further, by retaining more terms in the Fourier series and defining higher-order (HODF) and multiple-input (MIDF) describing functions.

HODF are used in an attempt to improve accuracy, particularly for hard \mathcal{N} e.g. Coulomb friction, which may yield notable commensurate superharmonics. Generally, the increased accuracy achieved does not justify the significant mathematical complications incurred, which diminishes the DFM attractiveness [51].

MIDF are used to analyse systems with incommensurate frequencies e.g. from precession combined with forced response or oscillatory terms at 2Ω (3.9) from anisotropic bearings, or gravity sag at $\Omega/2$. MIDF are useful in such applications where some prior idea as to the frequencies, which are likely to be significant, is at hand. An alternate version of the MIDF is the *describing function matrix*, obtained by truncating an infinite matrix which relates the infinite-dimensional vectors formed from the Fourier coefficients of the input and output signals, respectively. The almost-periodic, rather than periodic, output raises major difficulties in computing the generalised Fourier coefficients, unless the nonlinearity has a simple analytic form.

A.2.4.4. MIDF illustrates Limit cycle quenching in Van der Pol oscillator

If an external input is applied to a limit-cycling system, it will generally interfere with the dynamics and alter the LC parameters, or even suppress it altogether. To demonstrate this, the Van der Pol oscillator is arranged in the configuration of *fig.A.2*, with the forcing sinusoid $f(t) = \bar{f} \sin \omega t$ entering at the input to the linear component. The EOM is:

$$\ddot{x} + \epsilon(3x^2 - 1)\dot{x} + x = \epsilon \bar{f} \omega \cos \omega t \quad (\text{A.25})$$

which is just Van der Pol's equation with a forcing term. Now, if the driving frequency ω is unrelated to the LC frequency ω_l , it is reasonable to take the approximation

$$x(t) \approx X_l \sin \omega_l t + X_e \sin(\omega t + \psi) \quad (\text{A.26})$$

$$x^3 \approx \frac{3}{4} X_l (X_l^2 + 2X_e^2) \sin \omega_l t + \frac{3}{4} X_e (2X_l^2 + X_e^2) \sin(\omega t + \psi) \quad \leftrightarrow \quad (\text{A.27})$$

Hence, applying the HBM to terms at frequencies ω_l and ω , we obtain:

$$\begin{aligned} [H^{-1}(i\omega_l) + \frac{3}{4}(X_l^2 + 2X_e^2)]X_l &= 0 \\ [H^{-1}(i\omega) + \frac{3}{4}(2X_l^2 + X_e^2)]X_e e^{i\psi} &= \bar{f} \\ \text{where } H^{-1}(i\omega) &= \frac{i}{\epsilon} \left(\omega - \frac{1}{\omega} \right) - 1 \end{aligned}$$

so that the first equation gives $\omega_l = 1$ (assuming $X_l \neq 0$), and $X_l^2 + 2X_e^2 = \frac{4}{3}$ whence, by substitution into the second equation,

$$\left\{ \frac{1}{\epsilon^2} \left(\omega - \frac{1}{\omega} \right)^2 + \left(\frac{9X_l^2}{8} - \frac{1}{2} \right)^2 \right\} \left(\frac{2}{3} - \frac{X_l^2}{2} \right) = \bar{f}^2$$

after eliminating ψ . It is thus clear that, for any given value of ω , there is a bound on the magnitude of f for which a solution of this type is possible; if this bound is exceeded, then the only possibility is that $X_l = 0$ in which case the component of the solution at the LC frequency disappears entirely. This is sometimes expressed by saying that, for a certain range of values of the input amplitude and frequency, the limit cycle is *quenched*. In that case, the only remaining component, in this approximation, is at the frequency of the driving signal, and its parameters can be calculated by applying harmonic balance at this frequency alone.

A.2.4.5. Describing Function Method precautions

The DFM is an intuitively appealing, convenient and relatively simple analysis technique, particularly when using the simple first order DFs, which:

- gives the designer a relatively quick appreciation of the systems behaviour
- indicates methods by which systems may be modified to meet performance criteria

Difficulties with the Describing Function Method include:

- The DFM/HBM for MIMO systems involves solving a set of nonlinear algebraic equations (5.5e) iteratively, which requires an initial guess solution (IG). Although this initial guess can be derived from LTI system FRFs for forced response, especially away from resonances, it is not readily available for LC analysis. In such situations, reliance on graphical techniques is necessary, which are not in abundance for MIMO systems and manipulations such as those in §.5.3.2 are necessary.
- Solving the system of NL algebraic equations may yield several solutions, and it is necessary to investigate their stability. In so doing, various perturbations' possibilities must be considered.
- Existence of a stable solution does not guarantee its actual occurrence as the actual solution depends on initial conditions and history as well as system parameters.
- Experience is a powerful ally, due to lack of precise methods for estimating solutions' accuracy.

The validity of Describing Functions approximations is important to bear in mind on account of limitations, which arise from their approximate nature. The DFM depends crucially on the irrelevance of the neglected higher harmonics, and can thus be expected to perform best when the:

- Nonlinearity is smooth, which does not really reflect RID models
- LTI system component has '*low pass*' characteristics, which is generally satisfied

The latter condition means that the pass-band of the linear element, regarded as a filter, should be narrow enough to effectively suppress response/LC components of high frequency, thus excluding all signals at multiples of the fundamental frequency.

Limit cycles predictions reliability Unless some system low-pass condition is satisfied, not only will the quantitative estimates be unreliable, but it is quite possible the DFM predicts LCs which do not exist, or fails to predict those which do. In order to make the predictions more reliable, it is necessary to take into account further details of both linear and nonlinear system elements. This is achieved by constructing ‘*error bands*’ around intersecting loci, to allow for the effects of truncating the Fourier series.

Assessing LCs stability using the DFM may be regarded as more unreliable than their existence, since this involves not only Fourier series truncation, but also assumptions the DFM is still valid even when applied to exponentially growing or decaying signals. Generally, such predictions ought to be regarded as rough indications of what to expect. Often however, it may be clear on other grounds whether or not an oscillation is likely to be stable, and if this expectation is reinforced by graphical predictions, then it should be reliable; otherwise, a deeper analysis is called for, which is usually no easy matter.

Limit sets predictions as opposed to LCs, e.g. strange attractors, is another avenue where the DFM fails because they cannot be practically represented by simple harmonic balance approximations. Nevertheless, some indication of their presence may be provided when there are multiple solutions, suggesting several LCs. If these lie close together, they may not actually exist as such, but are some form of chaotic behaviour.

A.2.4.6. Notes and references

The DFM is covered in many texts, particularly detailed treatments being found in Gelb and Vander Velde (1968) and Atherton (1975). Several authors, notably Mees (1972) extended the DFM to incorporate multiple harmonics. Prediction of oscillations in feedback systems with several nonlinearities can be found in Freeman and Barney (1963), and Gray and Taylor (1979). Construction of error bands in the DFM graphical formulation is detailed by Mees (1984). Examples where the describing function approximation fails have been given by Holtzman (1970), Rapp and Mees (1977) and Mees and Sparrow (1981). The determination of limit cycle stability, for both free and forced systems, based on the so-called incremental describing function (IDE) can be found in Choudhury and Atherton (1974). A study of forced systems, including the topics of jump phenomena, subharmonic oscillations and the suppression of limit cycles, is contained in Lawden (1967). Incidentally, the occurrence of subharmonic solutions, in the large-parameter form of Van der Pol’s equation, provided the setting for the earliest studies of chaotic behaviour, by Cartwright and Littlewood (1945) and Levinson (1949).

Bibliography

- [1] *MATLAB 5.3*.
- [2] Z. Abduljabbar, M.M. ElMadany, and A.A. AlAbdulwahab. Active vibration control of a flexible rotor. *Computers and Structures*, 58(3):499 – 511, 1996.
- [3] M. Ahmadian and D. J. Inman. Some stability results for general linear lumped-parameter dynamic systems. *J. Applied Mechanics*, 53:10–14, 1986.
- [4] Amde M. Amde and Amir Mirmiran. A new hysteresis model for steel members. *International journal for numerical methods in Engineering*, 45:1007–1023, 1999.
- [5] Hongrui Ao, Hongyuan Jiang, and A.M. Ulanov. Dry friction damping characteristics of a metallic rubber isolator under two-dimensional loading processes. *Modelling and Simulation in Materials Science and Engineering*, 13(4):609 – 620, 2005.
- [6] S. T. Ariaratnam and N. Namachchivaya. Periodically perturbed nonlinear gyroscopic systems. *J. Structural Mechanics*, 14:153–175, 1986.
- [7] A.F. Artiles. Effects of friction in axial splines on rotor system stability. In *International Gas Turbine And Aeroengine Congress And Exposition*, Orlando, FL, Usa, 3-6 Jun 1991.
- [8] A.F. Artiles. Effects of friction in axial splines on rotor system stability. *Journal Of Engineering For Gas Turbines And Power*, 115(2):272–278, Apr 1993.
- [9] D. P. Atherton. *Nonlinear Control Engineering: Describing function analysis and design*. Van Nostrand Reinhold, London, 1975.
- [10] D. P. Atherton. An overview of nonlinear systems theory. In Billings et al. [22].
- [11] D. P. Atherton and D. H. Owens. Boundedness properties of nonlinear multivariable feedback systems. *Electronics Letters*, 15:559–61, 1979.
- [12] Derek P. Atherton. *Stability of Nonlinear Systems*. Research Studies Press, 1981.
- [13] R.H. Bannister. Methods for modelling flanged and curvic couplings for dynamic analysis of complex rotor constructions. *ASME J. Of Mechanical Design*, 102(1):168–176, 1980.
- [14] Jerome Bastien, Michelle Schatzman, and Claude-Henri Lamarque. Study of an elastoplastic model with an infinite number of internal degrees of freedom. *European Journal of Mechanics, A/Solids*, 21(2):199 – 222, 2002.
- [15] I.C. Begg. Friction induced rotor whirl - a study in stability. *ASME, J. Engineering For Industry*, 96, May 1974.

- [16] R. Bell and M. Burdekin. A study of the stick-slip motion of machine tool feed drives. *Proc Instn Mech Engrs*, 184(30):543–555, 1969-70.
- [17] D. Bently and A Muszynska. Rotor internal friction instability. In *Instability In Rotating Machinery*, Carson City, Nv, Usa, 10-14 Jun 1985. Conf. Code 07687.
- [18] D.E. Bently. The re-excitation of balance resonance regions by internal friction. *ASME*, Pet-49, September 1972.
- [19] R. A. Billet. Shaft whirl induced by dry friction. *Engineer*, 220(5727), 1965.
- [20] R. A. Billet. Effects of symmetrical nonlinear bearing flexibility of shaft whirl. *Journal Mech. Engineering Science*, 8(2), 1966.
- [21] R. A. Billet. Experimental studies of the effects of a nonlinear bearing stiffness of a shaft whirl. *Instn. Mech. Engrs. Appl. Mech. Convention*, (29), 1966.
- [22] S. A. Billings, J. O. Gray, and D. H. Owens, editors. *Nonlinear system design*. IEE Control Engineering Series 25. Peter Peregrinus Ltd., London, 1984.
- [23] R.E.D. Bishop and D.C. Johnson. *The Mechanics of Vibration*. Cambridge University Press, 1960.
- [24] H. F. Black. The stabilizing capacity of bearing of flexible rotors with hysteresis. *J. Engineering For Industry*, 98:87, Feb 1976.
- [25] V. V. Bolotin. *Non-Conservative Problems of The Theory Of Elastic Stability*. Pergamon Press, 1961. English trans: 1963.
- [26] R. W. Brockett. Path integrals, Lyapunov functions and quadratic minimisation. *J. Basic Eng., ASME paper 62-JACC-5*, 5(1), 1966.
- [27] Ll Bucciarelli. On the instability of rotating shafts due to internal damping. *ASME Transactions: Journal Of Applied Mechanics*, 49(2):425–428, Jun 1982.
- [28] M. Burdekin, A. Cowley, and N. Back. An elastic mechanism for the microsliding characteristics between contacting machined surfaces. *Journal of Mechanical Engineering Science*, 20(3):121–7, 1978.
- [29] Yu.P. Busarov. The rayleigh-masing mathematical model of hysteresis and its modifications as solutions to second-order differential equations. *Izvestiya Vysshikh Uchebnykh Zavedenii, Mashinostroenie*, (12):31 – 7, 1976//.
- [30] C.O. Chang and J.W. Cheng. Nonlinear dynamics and instability of a rotating shaft-disk system. *Journal Of Sound And Vibration*, 160(3):433–454, Jan 1993.
- [31] L. Chen and D. M. Ku. Analysis of whirl speeds of rotor-bearing systems with internal damping by c0 finite elements. *Finite Elements In Analysis And Design*, 9(2):169–176, 1991.
- [32] Dar-Yun Chiang. Generalized masing models for deteriorating hysteresis and cyclic plasticity. *Applied Mathematical Modelling*, 23(11):847 – 863, 1999.

- [33] D. Childs. *Turbomachinery Rotordynamics*. J. Wiley & Sons, New York, 1993.
- [34] D. W. Childs. Space shuttle main engine high-pressure fuel turbopump rotordynamic instability problem. *Journal of Engineering for Power, Transactions ASME*, 100(1):48 – 57, 1978.
- [35] H.-J. Christ and H. Mughrabi. Cyclic stress-strain response and microstructure under variable amplitude loading. *Fatigue and Fracture of Engineering Materials & Structures*, 19(2-3):335 – 348, 1996.
- [36] P. A. Cook. *Nonlinear Dynamical Systems*. Prentice-Hall, 2nd edition, 1994.
- [37] S. H. Crandall. The hysteretic damping model in vibration theory. *Proc. IMechE, J. of Mechanical Engineering Science*, 205:23–28, 1991.
- [38] S. H. Crandall et al. *Dynamics of Mechanical and Electromechanical Systems*. Krieger Publishing Co., Malabar, 1982.
- [39] S.H. Crandall. Physical explanations of the destabilizing effect of damping in rotating parts. Cp 2133, NASA, May 1980.
- [40] S.H. Crandall. The influence of material creep on rotor dynamics. In *Proc. International Conf. On Vibration Problems In Engineering*, pages 43–50, 1986.
- [41] F. M. Dimentberg. *Flexural Vibrations of Rotating Shafts*. Butterworths, London, 1959. English trans: 1961.
- [42] M.F. Dimentberg. Vibration of a rotating shaft with randomly varying internal damping. *Journal of Sound and Vibration*, 285(3):759 – 765, 2005.
- [43] M.F. Dimentberg, B. Ryzhik, and L. Sperling. Random vibrations of a damped rotating shaft. *Journal of Sound and Vibration*, 279(1-2):275 – 284, 2005.
- [44] Q. Ding and J.E. Cooper. Hopf bifurcation analysis of a rotor/seal system. *Proceedings of the 25th International Conference on Noise and Vibration Engineering, ISMA*, pages 1019 – 1025, 2000.
- [45] F.F. Ehrich. Shaft whirl induced by rotor internal damping. *Journal Of Applied Mechanics*, pages 279–282, 1964.
- [46] F.F. Ehrich. Role of bearing support stiffness anisotropy in suppression of rotordynamic instability. In *12th Biennial Conference On Mechanical Vibration And Noise, Rotating Machinery Dynamics*, Montreal, Que, Canda, 17-21 Sep 1989. ASME.
- [47] F.F. Ehrich et al. *Handbook of Rotordynamics*. McGraw-Hill, 1992.
- [48] A. K. El Sakkary and D. P. Atherton. Computer graphics methods for nonlinear multivariable systems. In *IFAC Computer Aided Design Symposium*, pages 447–52, Zurich, 1979.
- [49] D. J. Ewins. *Modal Testing: Theory, Practice and Application*. Research Studies Press Ltd., second edition, 2000.

- [50] P.L. Falb et al. Input-output stability—a general viewpoint. In *4th IFAC congress, paper 41.3*, Warsaw, 1969.
- [51] Janito Vaqueiro Ferreira. *Dynamic Response Analysis of Structures with Nonlinear Components*. PhD thesis, Department of Mechanical Engineering, Imperial College, London, SW7 2BX, UK, May 1998.
- [52] Vicente C. Gallardo. Stability of a rotor with alford forces under the influence of non isotropic support stiffness and gyroscopic moments. *American Society of Mechanical Engineers (Paper)*, pages 1 – 14, 1993.
- [53] E. D. Garber. Frequency criteria for absence of periodic modes. *Automatic and Remote Control*, 28(11):1776–80, 1967.
- [54] Arthur Gelb and Wallace E. Vander Velde. *Multiple-Input Describing Functions and Nonlinear System Design*. McGraw-Hill, Inc., 1968.
- [55] J. Genin. Effect of nonlinear material damping on whirling shafts. *Applied Scientific Research*, 15(1, Sec A):1 – 11, 1965.
- [56] J. Genin and J.S. Maybee. Stability in the three dimensional whirling problem. 4(3):205 – 15, 1969.
- [57] J. Genin and J.S. Maybee. External and material damped three dimensional rotor system. *International Journal of Non-Linear Mechanics*, 5(2):287 – 97, 1970/06/.
- [58] J. Genin and J.S. Maybee. Whirling motion of a viscoelastic continuous shaft. *International Journal of Engineering Science*, 8(8):671 – 86, 1970/08/.
- [59] J. Genin and J.S. Maybee. The role of material damping in the stability of rotating systems. *Journal of Sound and Vibration*, 21(4):399 – 404, 1972/04/22.
- [60] Henning Grafe. *Model Updating of Large Structural Dynamics Models Using Measured Response Functions*. PhD thesis, Department of Mechanical Engineering, Imperial College, London, SW7 2BX, UK, October 1998.
- [61] J. O. Gray and L. S. Brown. Harmonic analysis of feedback systems. In Billings et al. [22].
- [62] J. Guckenheimer and P. Holmes. *Nonlinear Oscillations, Dynamical Systems and Bifurcations of Vector Fields*. Springer-Verlag, 1983.
- [63] E.J. Gunter. *Dynamic Stability Of Rotor-Bearing Systems*. NASA Sp-113, 1966.
- [64] E.J. Gunter. The influence of internal friction on the stability of high speed rotors. *ASME J. Of Engineering For Industry*, 89(4):683–688, 1967.
- [65] E.J. Gunter and P. R. Trumpler. The influence of internal friction on the stability of high speed rotors with anisotropic support. *ASME J. Of Engineering For Industry*, 91:1105–1113, 1969.

- [66] U. Gutzler, W. Seemann, and P. Hagedorn. Nonlinear structural damping described by the masing model and the method of slowly varying amplitude and phase. *American Society of Mechanical Engineers, Design Engineering Division (Publication) DE*, 84(3 Pt A/1):773 – 779, 1995.
- [67] Y. Haomin. The stability of rotating shafts when distributed gyroscopic effects are taken into account. In *11th Biennial Conference On Mechanical Vibration & Noise*, volume 1 of *Rotating Machinery Dynamics*, Boston, Massachusetts, 1987. ASME Design Technology Conferences.
- [68] W. Hauger. Stability of a gyroscopic non-conservative system. *J. Applied Mechanics*, 42:739, 1975.
- [69] S.L. Hendricks. The effect of viscoelasticity on the vibration of a rotor. *Journal Of Applied Mechanics*, 53:412–416, 1986.
- [70] I. Herrera. Dynamic models for masing type materials and structure. *Boletin Sociedad Mexicana De Ingenieria Sismica*, 3:1–8, 1965.
- [71] J. C. Hsu and A. U. Meyer. *Modern Control Principles and Applications*. McGraw-Hill, New York, 1968.
- [72] Y. Ishida and T. Yamamoto. Forced oscillations of a rotating shaft with nonlinear spring characteristics and internal damping (1/2 order subharmonic oscillations and entrainment). *Nonlinear Dynamics*, 4(5):413–431, Oct 1993.
- [73] W. D. Iwan. On a class of models for the yielding behaviour of continuous and composite systems. *ASME: Journal of Applied Mechanics*, 64:612–7, 1967.
- [74] H. R. Jhansale. New parameter for the hysteretic stress-strain behavior of metals. *Journal of Engineering Materials and Technology, Transactions of the ASME*, 97 Ser H(1):33 – 38, 1975.
- [75] D. I. Jones. The impulse response function of a damped single degree of freedom system. *J. of Sound and Vibration*, 106:353–356, 1986.
- [76] D. I. Jones. Reflections on damping technology at the end of the twentieth century. *J. of Sound and Vibration*, 190(3):449–462, 1996.
- [77] E. I. Jury and B.W. Lee. The absolute stability of systems with many nonlinearities. *Automatic and Remote Control*, 26:913–6, 1965.
- [78] N Khader. Stability of rotating shafts loaded by follower axial force and torque load. *Journal Of Sound And Vibration*, 182(5):759–773, 1995.
- [79] Hassan K. Khalil. *Nonlinear Systems*. Prentice-Hall, 2nd edition, 1996.
- [80] A. L. Kimball. Internal friction theory of shaft whirling. *General Electric Rev.*, 27:224–251, 1924.
- [81] A. L. Kimball. Internal friction as a cause of shaft whirling. *Phil. Magazine*, 49(S6):724–727, 1925.

- [82] A. L. Kimball. Measurement of internal friction in a revolving deflected shaft. *General Electric Rev.*, 28:554–558, 1925.
- [83] A. L. Kimball and D. E. Lovell. Internal friction in solids. *Trans. ASME*, 48:479, 1926.
- [84] V. N. Kirsanova. The shear compliance of flat joints. *Machines and Tooling*, XXXVIII:30–34, 1967.
- [85] W. Kliem, C. Pommer, and J. Stoustrup. Stability of rotor systems: a complex modelling approach. *Zeitschrift für Angewandte Mathematik und Physik*, 49(4):644 – 55, 1998/07/.
- [86] E. Kramer. *Dynamics of Rotors and Foundations*. Springer-Verlag, Berlin, 1993.
- [87] Jm Krodkiewski and Za Parszewski. Gyroscopic effect in rotor-bearing parametric instability. In *Proceedings Of The Sixth World Congress On The Theory Of Machines And Mechanisms*, New Delhi, India, 15-20 Dec 1983. Conf. Code 5752.
- [88] C.-P.R. Ku, J.F. Jr Walton, and J.W. Lund. Dynamic coefficients of axial spline couplings in high-speed rotating machinery. *Journal Of Vibration And Acoustics*, 116(3):250–256, Jul 1994.
- [89] C.-P.R. Ku, J.F.Jr Walton, and J.W. Lund. An experimental investigation of the dynamic characteristics of an axial spline coupling in high speed rotating machinery. In *14th Biennial Conf. On Mechanical Vibration And Noise*, Albuquerque, New Mexico, September 19-22 1993.
- [90] C.-P.R. Ku, J.F.Jr Walton, and J.W. Lund. An investigation of angular stiffness and damping coefficients of an axial spline coupling in high-speed rotating machinery. In *Rotordynamic Instability Problems in High Performance Turbomachinery*. Texas A&M University (TAMU), Lewis Research center, 1993.
- [91] C.-P.R. Ku, J.F.Jr Walton, and J.W. Lund. A theoretical approach to determine angular stiffness and damping coefficients of an axial spline coupling in high speed rotating machinery. In *14th Biennial Conf. On Mechanical Vibration And Noise*, Albuquerque, New Mexico, September 19-22 1993.
- [92] Benjamin C. Kuo. *Automatic Control Systems*. Prentice Hall, Inc., 7th edition, 1995.
- [93] M.Y. Kushul'. *The self-induced Oscillations of Rotors*. Consultants Bureau, New York, 1964. Trans. from Russian.
- [94] J. P. La Salle. Some extensions of lyapunov's second method. *IRE Trans. Circuit Theory*, CT-7(4):520–527, December 1960.
- [95] J. P. La Salle and S. Lefschetz. *Stability by Lyapunov's Direct Method with Applications*. Academic Press, New York, 1961.
- [96] M. Lalanne and G. Ferraris. *Rotordynamics Prediction in Engineering*. J. Wiley & Sons, England, 1993.

- [97] C.W. Lee. *Vibration Analysis of Rotors*. Kluwer Academic Publishers, Dordrecht, 1993.
- [98] J. C. Lee. On stability of high speed rotors with internal friction. Master's thesis, University Of Florida, 1972. Engineering.
- [99] A. M. Letov. *Stability in Nonlinear Control Systems*. Princeton University Press, 1961.
- [100] Rongming Lin. *Identification of the Dynamic Characteristics of Nonlinear Structures*. PhD thesis, Department of Mechanical Engineering, Imperial College, London, SW7 2BX, UK, December 1990.
- [101] Wenjie Liu. *Structural Dynamic Analysis and Testing of Coupled Structures*. PhD thesis, Department of Mechanical Engineering, Imperial College, London, SW7 2BX, UK, October 2000.
- [102] I Lottati and I Elishakoff. On a new 'destabilization' phenomenon: Effect of rotary damping. *Ingenieur-Archiv*, 57(6):413–419, 1987.
- [103] J. W. Lund. Stability and damped critical speeds of a flexible rotor in fluid film bearings. *J. Engineering For Industry*, 96(2):509–517, May 1974.
- [104] J.W. Lund. Destabilization of rotors from friction in internal joints with micro slip. In *Proc. The International Conf. On Rotordynamics*, pages 487–491, Tokyo, Sept. 14-17 1986.
- [105] A. I. Lur'e. *Some Nonlinear Problems in the theory of automatic control*. HMSO, London, 1957.
- [106] A. M. Lyapunov. *Probleme general de la stabilité du mouvement*. Kharkov (1947 Princeton University Press), 1892.
- [107] R. A. Marmol. Engine rotor dynamics, synchronous and nonsynchronous whirl control. Report Usartl Tr-79-2, U.S. Army, Feb 1979.
- [108] R.A. Marmol, A.J. Smalley, and J.A. Tecza. Spline coupling induced nonsynchronous rotor vibrations. *ASME, J. Mechanical Design*, 102, Jan 1980.
- [109] J. A. C. Martins, J. T. Oden, and F. M. F. Simone. A study of static and kinetic friction. *International Journal of Engineering Science*, (1):29–91, 1990.
- [110] V.V. Matveev and A.P. Bovsunovskii. Analysis of methods of determining the damping capacity of a material under two-frequency loading. *Problemy Prochnosti*, 20(7):79 – 85, 1988/07/.
- [111] E Medgyesi. Stability of a simple rotor with nonlinear internal damping. In *ASME 13th Biennial Conference On Mechanical Vibration And Noise*, Miami, Fl, Usa, Sep 1991.
- [112] A.I. Mees and D.P. Atherton. Domains containing the field of values of a matrix. *Linear Algebra and Its Applications*, 26:289–296, 1979.

- [113] A.I. Mees and P.E. Rapp. Stability criteria for multi-loop nonlinear feedback systems. In *IFAC symposium on Multivariable Technology Systems*, pages 983–8, Canada, 1977.
- [114] C. H. Menq, J. H. Griffin, and J. Bielak. The influence of a variable normal load on the forced vibration of a frictionally damped structure. *ASME J. of Engineering for Gas Turbines and Power*, 108:300–5, 1986.
- [115] Mindlin.R.D. Compliance of elastic bodies in contact. *ASME J. of Applied Mechanics*, 16:259–68, 1949.
- [116] N. Minorsky. *Nonlinear Mechanics*. Edwards, Ann Arbor, 1947.
- [117] N. Minorsky. *Nonlinear Oscillations*. Van Nostrand Reinhold, Princeton, 1962.
- [118] P.G. Morton. Aspects of coulomb damping in rotors supported on hydrodynamic bearings. In *Rotordynamic Instability Problems In High-Performance Turbomachinery*, Tex, Usa, 10-12 May 1982. College Station.
- [119] G.V. Moskvitin. On additional possibilities of using general masing’s principle equations. *Vestnik Moskovskogo Universiteta, Seriya 1 (Matematika Mekhanika)*, (4):47 – 53, 1994.
- [120] Hael Mughrabi and Hans-Juergen Christ. Cyclic deformation and fatigue of selected ferritic and austenitic steels: Specific aspects. *ISIJ International*, 37(12):1154 – 1169, 1997.
- [121] Grigori Muravskii. On description of hysteretic behaviour of materials. *International Journal of Solids and Structures*, 42(9-10):2625 – 2644, 2005.
- [122] A. Muszinska. Non linear excited and self excited processional vibrations of symmetrical rotors. In *Proceedings Of The Iutam Symposium*, Lyngby, Denmark, 1974.
- [123] A. Muszynska. An analysis of the motion of a shaft with nonlinear characteristic of elasticity & damping. *Biul. Pan Ser. Sci. Techn.*, 16(7), 1968.
- [124] A. Muszynska. Motion of a shaft with nonlinear elastic and internal damping properties. *Nonlinear Vibration Problems*, 17:189–224, 1976.
- [125] N. O. Myklestad. The concept of complex damping. *J. of Applied Mechanics*, 19:284–286, 1952.
- [126] K. S. Narendra and J. Taylor. *Frequency Domain Methods for Absolute Stability*. Academic Press, New York, 1973.
- [127] C Nataraj, Hd Nelson, and N Arakere. Effect of coulomb spline on rotor dynamic response. In *Bently. Symp. On Instability In Rotating Machinery*, Carson City, Nv, Usa, 10-14 Jun 1985.
- [128] Frederick C. Nelson. Rotor dynamics - instabilities. *S V Sound and Vibration*, 36(9):8 – 10, 2002.

- [129] H.D. Nelson. A finite rotating shaft element using timoshenko beam theory. *J. Mechanical Design*, 102:793, Oct 1980.
- [130] B. L. Newkirk. Shaft whipping. *General Electric Rev.*, 27:169–178, 1924.
- [131] Ali Salehzadeh Nobari. *Identification of the Dynamic Characteristics of Structural Joints*. PhD thesis, Department of Mechanical Engineering, Imperial College, London, SW7 2BX, UK, December 1991.
- [132] R. L. Norwood. *Studies On The Motion Of Continuous Viscoelastic Rotors*. PhD thesis, Univ. Of Illinois At Urbana-Champaign, 1980.
- [133] Katsuhiko Ogata. *Modern Control Engineering*. Prentice Hall, Inc., 1985.
- [134] R. Oldenburger. Signal stabilization of a control system. *Trans. ASME*, 79:1869–1872, August 1957.
- [135] R. Oldenburger and R. C. Boyer. Effects of extra sinusoidal inputs to nonlinear systems. *J. Basic Eng., Trans. ASME ser. D*, 84(4), 1962.
- [136] R. Oldenburger and C. C. Liu. Signal stabilization of a control system. *Trans. AIEE*, 78:96–100, May 1959.
- [137] R. Oldenburger and T. Nakada. Signal stabilization of self-oscillating systems. *IRE Trans. Automatic Control*, AC-6(3), 1961.
- [138] P. C. Parks. Stability criteria for nonlinear systems—a survey. In Billings et al. [22].
- [139] O. Pinkus. Experimental investigation of resonant whip. In *Trans. ASME*, volume 78, pages 975–983. 1956.
- [140] S.R. Pisani and J.J. Rencis. Investigating curvic coupling behavior by utilizing the two-and three-dimensional boundary and finite element methods. In *International Conference On Boundary Element Methods*, Worcester, Ma,USA, Aug 10-13 1993.
- [141] A. Plumtree and H.A. Abdel-Raouf. Relationship between cyclic stress-strain response and substructure. *Low Cycle Fatigue and Elasto-Plastic Behaviour of Materials*, pages 279 – 84, 1998//.
- [142] A. Plumtree and H.A. Abdel-Raouf. Cyclic stress-strain response and substructure. *International Journal of Fatigue*, 23(9):799 – 805, 2001.
- [143] H. Poincaré. *Les methodes nouvelles de la mecanique celeste*. Gauthier-Villars, Paris, 1892.
- [144] J. Polak, F. Fardoun, and S. Degallaix. Analysis of the hysteresis loop in stainless steels. i. austenitic and ferritic steels. *Materials Science & Engineering*, A297(1-2):144 – 53, 2001/01/15.
- [145] V. M. Popov. Nouveaux criteriums de stabilité pour les systemes automatiques non-lineares. In *Revue d'Electrotechnique et d'Energetique*, volume 5, Romania, 1960.

- [146] V. M. Popov. Absolute stability of nonlinear control systems of automatic control. *Automatic and Remote Control*, 22:957–8, 1962.
- [147] V. M. Popov. *Hyperstability of Automatic Control Systems*. Springer Verlag, 1973.
- [148] R. Pyrz. Stability of motion of a viscoelastic rotating shaft. Report 237, Danish Center For Applied Mathematics And Mechanics, April 1982.
- [149] Saeed Ziaei Rad. *Methods for Updating Numerical Models in Structural Dynamics*. PhD thesis, Department of Mechanical Engineering, Imperial College, London, SW7 2BX, UK, June 1997.
- [150] J. Rayleigh. *The Theory of Sound*, volume 1. London: Mc Millan, 1877. Last reprint 1944.
- [151] Y. Ren. *The Analysis and Identification of Friction Joint Parameters in the Dynamic Response of Structures*. PhD thesis, Department of Mechanical Engineering, Imperial College, London, SW7 2BX, UK, 1992.
- [152] Y. Ren and C.F. Beards. Generalized method for modelling interfacial microslip in joints. *American Society of Mechanical Engineers, Petroleum Division (Publication) PD*, 52:219 – 224, 1993.
- [153] Y. Ren and C.F. Beards. Two algorithms for calculating nonlinear force from the response of a masing type friction related element. *American Society of Mechanical Engineers, Petroleum Division (Publication) PD*, 52:213 – 218, 1993.
- [154] D. Robertson. Whirling of a shaft with skew stiffness. *Engineer*, 156, 1933.
- [155] D. Robertson. The whirling of shafts. *Engineer*, 158:216–228, 1934.
- [156] D. Robertson. Hysteretic influences on whirling of rotors. In *Proc. Of The Inst. Of Mech. Eng.*, pages 513–531, 1935.
- [157] D. Robertson. Transient whirling of a rotor. *Phil. Magazine*, 20(S7), 1935.
- [158] M. Roseau. *Vibrations in Mechanical Systems*. Springer-Verlag, Berlin, 1984. trans. from French: 1987.
- [159] M. Roseau. Roseau report for rostadyn. *Internal reports*, 1997.
- [160] V. I. Rosenblum. Stability of the rectilinear mode of a rotating shaft under conditions of material creep. *Problems Of The Mechanica Of The Continuous Media*, (1), 1970.
- [161] K.Y. Sanliturk. Personal communications and internal reports. Internal, Vibration UTC, Dynamics section, Mechanical Engineering, Imperial College London, 1999.
- [162] D. G. Schultz and J. E. Gibson. The variable gradient method of generating Lyapunov functions. *AIEE paper*, pages 62–81, 1962.
- [163] A.S. Sekhar and Jayant Kumar Dey. Effects of cracks on rotor system instability. *Mechanism and Machine Theory*, 35(12):1657 – 1674, 2000.

- [164] J. Shaw and S.W. Shaw. Instabilities and bifurcations in a rotating shaft. *Journal Of Sound & Vibration*, 132(2):227–244, 1989.
- [165] J. Shaw and S.W. Shaw. Nonlinear interactions between resonance and instability in a symmetric rotor. In *Proc. Of 3rd Int. Symp. On Transport Phenomena And Dynamics Of Rotating Machinery Isromac-3*, 1990.
- [166] J. Shaw and S.W. Shaw. Non linear resonance of an unbalanced rotating shaft with internal damping. *Journal Of Sound & Vibration*, 147(3):435–451, 1991.
- [167] S. N. Shoukry. A mathematical model for the stiffness of fixed joints between machine parts. In *Proceedings of the NUMETA 85 Conference*, pages 851–8, Swansea, UK, 1985.
- [168] P. K. Sinha. *Multivariable Control*. Marcel Dekker, Inc., New York, 1984.
- [169] J.-J. E. Slotine and Weiping Li. *Applied Nonlinear Control*. Prentice-Hall, 1991.
- [170] D. M. Smith. The motion of a rotor carried by a flexible shaft in flexible bearings. In *Proc. Royal Society (London)*, volume 142 of A, pages 92–118, 1933.
- [171] C. R. Soderberg. On the subcritical speeds of rotating shafts. *Journal Of Applied Mechanics*, 54:45–50, 1932.
- [172] H. Svensson. Dynamics of composite rotors, with special reference to influence of imperfections and internal damping. pages 129p –, 1993.
- [173] G. P. Szego. On the application of the Zubov method for the construction of Lyapunov functions for nonlinear control systems. *J. Basic Eng., ASME paper 62-JACC-5*, 5,1, 1963.
- [174] J.A. Tecza. Stability model and analysis for spline coupling induced nonsynchronous rotor vibrations. Report Mti-78tr9, Mechanical Technology Incorporated, October 1977.
- [175] J.A. Tecza. Stability analysis of a spline coupling test rig. Report Mti-78tr78, Mechanical Technology Incorporated, May 1978.
- [176] T. Theodorsen and I. E. Garrick. Mechanism of flutter, a theoretical and experimental investigation of the flutter problem. Technical Report 685, NACA, 1940.
- [177] A. Tondl. *Some Problems of Rotor Dynamics*. Chapman & Hall, London. Trans. from Czech: 1965.
- [178] A. Tondl. Notes on the identification of subharmonic resonances of rotors. *J. Sound And Vibration*, 31:119–127, 1973.
- [179] B. J. Torby. The effect of structural damping upon the whirling of rotors. *J. Applied Mechanics*, 46:469, 1979.
- [180] J.M. Vance. *Rotordynamics of Turbomachinery*. Wiley, New York, 1993.

- [181] J.M. Vance and J. Lee. Stability of high speed rotors with internal friction. *ASME, J. Engineering For Industry*, 96, August 1974.
- [182] W. G. Vogt and J. H. George. On Aizerman's conjecture and boundedness. *IEEE transactions, Automatic Control*, AC-12:338–9, June 1967.
- [183] James F. Walton, Roger C.-P. Ku, and Jorgen W. Lund. Experimental investigation of the dynamic characteristics of an axial spline coupling in high-speed rotating machinery. *American Society of Mechanical Engineers, Design Engineering Division (Publication) DE*, 60:265 – 270, 1993.
- [184] J.f. Walton and M. Martin. Internal rotor friction induced instability in high-speed rotating machinery. In *14th Biennial ASME Design Technical Conference On Mechanical Vibration And Noise*, pages 297–305, Albuquerque, 1993.
- [185] J.F.Jr Walton, A. Artiles, J.W. Lund, J. Dill, and E. Zorzi. Internal rotor friction instability. Report 88tTR39, Mechanical Technology Incorporated, 968 Albang Shaker road, Latham, New York, 12110, march 1990.
- [186] Zhirui Wang and C. Laird. Relationship between loading process and masing behavior in cyclic deformation. *Materials Science & Engineering A (Structural Materials: Properties, Microstructure and Processing)*, 101:1 – 5, 1988/05/.
- [187] Hakan Wettergren. *Rotordynamic Analysis with Special Reference to Composite Rotors and Internal Damping*. PhD thesis, Division of Machine Design, Dept. of Mechanical Engineering, Linköping University, S-581 83 Linköping, Sweden, 1996.
- [188] H.L. Wettergren and K.-O. Olsson. Dynamic instability of a rotating asymmetric shaft with internal viscous damping supported in anisotropic bearings. *Journal of Sound and Vibration*, 195(1):75 – 84, 1996.
- [189] M.F. White and S.H. Chan. Proposed forcing mechanisms and non-linear effects on subsynchronous vibrations in high performance turbomachinery. *American Society of Mechanical Engineers (Paper)*, pages 8 –, 1997.
- [190] I. R. Whiteman. On the deviation of the stress-strain diagram from a statistical approach. *Aerospace Engineering*, 21:69–73, 1962.
- [191] R. Jr. Williams and R. Trent. The effects of nonlinear assymmetric supports on turbine engine rotor stability. *SAE Trans.*, 79:1010–1020, 1970.
- [192] H. Wittke, J. Olfe, and K.-T. Rie. Description of stress-strain hysteresis loops with a simple approach. *International Journal of Fatigue*, 19(2):141 – 149, 1997.
- [193] S.M. Yang and C.D. Mote. Stability of non-conservative linear discrete gyroscopic systems. *J. Sound And Vibration*, 147(3):453–464, 1991.
- [194] Z. Yin, Y. Ou, B.A. Hu, and Y. Li. Influencis of curvic coupling connection and variable axial forces. *Journal Of Aerospace Power/Hangkong Dongli Xuebao*, April 1994.

- [195] Z. Yin, Y. Ou, Y. Li, and Q. Mei. Dynamic characteristic analysis for axially prestressed rotor systems with curvic couplings. *Journal Of Aerospace Power/Hangkong Dongli Xuebao*, April 1994.
- [196] Z. Yin, Y. Ou, Y. Li, D. Yang, and Q. Mei. Stiffness of a shaft section with curvic coupling and its effect on dynamic characteristic of a rotor. *Zhendong Gongcheng Xuebao/Journal Of Vibration Engineering*, 6(1):63, 1993.
- [197] Wen Zhang. On dynamic instability of rotating viscoelastic shafts. *Fudan Journal (Natural Science)*, 23(4), Dec 1984.
- [198] Wen Zhang. Dynamic stability of the rotating shaft made of boltzmann viscoelastic solid. *ASME J. Applied Mechanics*, 53:424, 1986.
- [199] Wen Zhang. A general theory for viscoelastic rotor dynamics. In *11th Biennial Conference On Mechanical Vibration & Noise*, volume 1 of *Rotating Machinery Dynamics*, Boston, Massachusetts, 1987. ASME Design Technology Conferences.
- [200] E.S. Zorzi and H.D. Nelson. Finite element simulation of rotor-bearing systems with internal damping. *J. Engineering For Power*, 99(Ser. A #1):71, Jan 1977.